Modeling, Dynamics, and Control of Tethered Satellite Systems

Joshua R. Ellis

Dissertation submitted to the Faculty of the
Virginia Polytechnic Institute and State University
in partial fulfillment of the requirements for the degree of

Doctor of Philosophy
in
Aerospace Engineering

Christopher D. Hall, Chair
Craig A. Woolsey
Mayuresh J. Patil
Scott L. Hendricks

March 23, 2010
Blacksburg, Virginia

Keywords: tethered satellite systems, verification and validation, finite element method,
Floquet theory, sliding mode control.

Modeling, Dynamics, and Control of Tethered Satellite Systems

Joshua R. Ellis

(ABSTRACT)

Tethered satellite systems (TSS) can be utilized for a wide range of space-based applications, such as satellite formation control and propellantless orbital maneuvering by means of momentum transfer and electrodynamic thrusting. A TSS is a complicated physical system operating in a continuously varying physical environment, so most research on TSS dynamics and control makes use of simplified system models to make predictions about the behavior of the system. In spite of this fact, little effort is ever made to validate the predictions made by these simplified models.

In an ideal situation, experimental data would be used to validate the predictions made by simplified TSS models. Unfortunately, adequate experimental data on TSS dynamics and control is not readily available at this time, so some other means of validation must be employed. In this work, we present a validation procedure based on the creation of a top-level computational model, the predictions of which are used in place of experimental data. The validity of all predictions made by lower-level computational models is assessed by comparing them to predictions made by the top-level computational model. In addition to the proposed validation procedure, a top-level TSS computational model is developed and rigorously verified.

A lower-level TSS model is used to study the dynamics of the tether in a spinning TSS. Floquet theory is used to show that the lower-level model predicts that the pendular motion and transverse elastic vibrations of the tether are unstable for certain in-plane spin rates and system mass properties. Approximate solutions for the out-of-plane pendular motion are also derived for the case of high in-plane spin rates. The lower-level system model is also used to derive control laws for the pendular motion of the tether. Several different nonlinear control design techniques are used to derive the control laws, including methods that can account for the effects of dynamics not accounted for by the lower-level model. All of the results obtained using the lower-level system model are compared to predictions made by the top-level computational model to assess their validity and applicability to an actual TSS.

Contents

List of Figures

List of Tables

Chapter 1

Introduction

In recent years tethered satellite systems (TSS) have been proposed for a number of space applications including formation control of satellite clusters, orbital maneuvering of satellites, and numerous scientific applications such as observations of Earth's upper atmosphere and magnetic field. Tethered satellite systems are not a new concept, however, and in fact have been studied since well before the dawn of human space flight. In addition to the various theoretical studies of TSS that have been performed in the past, a number of TSS missions have already flown in space, providing a solid foundation for the design of future missions and the further development of the theory underlying the behavior of TSS.

1.1 A Brief History of Tethered Satellite Systems

The concept of a TSS was first proposed by Tsiolkovsky in 1895.[5] In his work, Tsiolkovsky proposed a means of generating artificial gravity that involves connecting a spacecraft to a counterweight with a long chain and spinning the entire system. The length of the tether in Tsiolkovsky's study was 0.5 km. The first practical application of a TSS was conducted during NASA's Gemini program in the 1960's.[5] On the Gemini 11 flight in 1966, the Gemini spacecraft was connected to the Agena target vehicle by a 30 m tether. The purpose of connecting the two spacecraft was to test in-space docking maneuvers, as well as to test the possibility of using a TSS to generate artificial gravity as proposed by Tsiolkovsky. Similar experiments were also performed on the Gemini 12 flight later the same year.

After the Gemini program, activities related to TSS went relatively quiet for roughly a decade. In 1975, Colombo et al.[13] reignited interest in TSS by proposing a "Shuttle-borne Skyhook" as a means of performing a wide range of on-orbit scientific experiments. The basic idea put forth by Colombo et al. was to deploy a probe from the Space Shuttle (which was still in the development stage at the time) using a 100 km long tether. Assuming that the Shuttle orbits at an approximate altitude of 200 km, a probe deployed upward along the local

vertical could be used to make electromagnetic measurements in Earth's magnetosphere, and a downward deployed probe could be used to make high-altitude atmospheric measurements. In addition, both the upward and downward deployed configurations could be used to study the effects of gravity-gradient of large space structures.

Actual missions involving TSS began again in the 1980's. In the early 1980's, a joint US-Japanese effort launched a series of TSS experiments on sounding rockets, known as the Tethered Payload Experiment (TPE) series.[20] At a particular point in the flight of each sounding rocket, the payload separated into two pieces connected by a tether. After the separation, various experiments were conducted related to the electrodynamic properties of the system. Three different flights were conducted, with successful deployment of the tether and data collection achieved on each flight. The longest tether deployment was achieved on the third and final flight in 1983, during which the tether was deployed to a length of 418 m.

The Canadian Space Agency launched the OEDIPUS-A spacecraft in 1989[15] (OEDIPUS stands for Observations of Electric-field Distribution in the Ionospheric Plasma–a Unique Strategy). The purpose of the mission was to use a TSS to make measurements of Earth's magnetic field in the auroral ionosphere. The system consisted of two payloads connected by a tether, which was deployed to a length of 958 m during the mission. A second spacecraft, OEDIPUS-C, was launched in 1995.[15] The OEDIPUS-C mission has similar scientific goals as OEDIPUS-A, but also supported the Tether Dynamics Experiment (TDE), which was designed to further develop the theory and computational tools associated with TSS dynamics. The tether on OEDIPUS-C was deployed to a length of 1,174 km during the mission.

Perhaps the most well-known TSS missions are NASA's TSS-1 and TSS-1R missions.[15] The TSS-1 mission was launched in 1992, and consisted of an Italian spacecraft deployed vertically from the Space Shuttle to a distance of 268 m. The spacecraft remained completely deployed and in a stable configuration for over 20 hours, successfully demonstrating the concept of long-term gravity-gradient stability of TSS. Following the success of TSS-1, the TSS-1R mission was launched in 1996. The mission once again consisted of an Italian spacecraft deployed vertically from the Space Shuttle. The tether was successfully deployed to a length of 19.7 km, but was unfortunately severed before the entire mission could be completed. However, during the time before the tether broke numerous experiments were conducted and measurements were taken that demonstrated the feasibility of using electrodynamic propulsion with TSS.

Before the TSS-1R mission, NASA's two Small Expendable Deployer System (SEDS) missions were used to demonstrate the feasibility of deploying a tether to large distances on-orbit.[15] The SEDS-1 mission was launched in 1993 as a secondary payload on a Delta-II rocket, and open-loop control was used to deploy a 20 km long tether. The SEDS-2 mission was launched in 1994, also as a secondary payload on a Delta-II rocket. Unlike SEDS-1, SEDS-2 used closed-loop control to deploy a 20 km long tether. In both missions, the tether was completely deployed, demonstrating the feasibility of in-space deployment of long tethers.

One of the first spacecraft designed to demonstrate the feasibility of electrodynamic propulsion of TSS was NASA's Plasma Motor Generator (PMG) spacecraft,[15] which was launched in 1993. As with the SEDS spacecraft, the PMG spacecraft was launched as a secondary payload on a Delta-II rocket, and was successfully deployed from the Delta-II to a length of 500 m. Once deployed, the spacecraft made successful measurements of the voltage induced across the system and the resulting current generated in the tether.

The Tether Physics and Survivability Spacecraft (TiPS) was launched by the Naval Research Laboratory (NRL) in 1996.[15] Up to that point in time, all TSS missions had been conducted over relatively short time spans, so the picture of the long-term behavior and survivability of TSS was still relatively incomplete. The TiPS mission was designed to study these unresolved issues, and to further the development of the theory of long-term TSS dynamics. The system consisted of two end bodies connected by a 4 km long tether, which was successfully deployed once the system was on orbit. The TiPS spacecraft is notable because it consisted of two end bodies of similar size and mass (dubbed Ralph and Norton), whereas previous TSS consisted of an end body connected to a second, much more massive, spacecraft (such as the Space Shuttle).

Another TSS mission designed by the NRL was the Advanced Tether Experiment (ATEx),[21] which was launched in 1998. The ATEx mission was designed to demonstrate the deployment and survivability of a new kind of tether design, and to perform various controlled libration maneuvers. Before ATEx, all tethers had been rope-like in design, and ATEx was to test a new flat, tape-like tether design. The system consisted of two end bodies and a 6.05 km long tether. Unfortunately, the tether deployment failed after only 22 m of the tether had been deployed, at which point the tether was jettisoned from the system. The exact cause of the failure is not known, but it is known that the tether went slack during deployment, triggering the jettison of the tether.

One of the most recent TSS missions was the ESA's Young Engineers Satellite 2 (YES 2), which was launched in 2007. The YES 2 spacecraft was designed and built entirely by students and young engineers with the mission objective of deploying a 30 km long tether and delivering a payload attached to the end of the tether safely back to Earth. A sensor failure during deployment meant that an accurate measurement of the total deployed length of tether could not be made; however, a post-mission analysis indicated that the full 30 km of tether was deployed, making the YES 2 tether the longest tether ever deployed in space.

In addition to the TSS missions described above that have already been conducted, several other missions have been proposed for development in the future. Perhaps the most promising of these proposed missions is NASA's Momentum eXchange Electrodynamic Reboost (MXER) system.[6,24] The MXER system consists of a roughly 100–150 km long tether nominally spinning in the plane of a low-Earth orbit. Payloads bound for higher orbits are launched from Earth via rocket into low-Earth orbit, at which point they are captured by one end of the spinning tether. At a specified time and location in its orbit, the tether releases the payload, transferring some of its momentum to the payload and sending it on

a trajectory toward a higher orbit. The loss of momentum by the tether causes its orbit to decay, and the system uses electrodynamic propulsion to raise its orbit back up to the desired level. The power required for electrodynamic propulsion is collected by solar panels, making the system almost completely autonomous and self-sustaining.

1.2 Fundamentals of Spinning and Electrodynamic Tethered Satellite Systems

While a portion of the work presented in this dissertation is applicable to TSS in general, much of the work is focused on the dynamics and control of spinning and electrodynamic TSS, with systems such as the MXER system discussed in the previous section serving as the primary motivation. The proposed configuration of MXER consists of two spacecraft–or end bodies as they can also be called–connected by a single tether, so we confine our attention to these types of systems. We do note that many other types of system configurations exist that consist of three or more end bodies connected in various geometric arrangements using multiple tethers. The interested reader is referred to Ref. [15] for a more general discussion of various types of TSS configurations and their applications.

As mentioned in the previous section, the MXER system is intended to spin in the orbit plane and utilize electrodynamic propulsion during portions of its operation. In this section, we present a qualitative discussion of some of the key concepts associated with the dynamics and control of spinning and electrodynamic two-body TSS. Understanding these concepts, at least on a qualitative level, is a crucial first step in the theoretical analysis or design of any TSS. Once again, the reader is referred to Ref. [15] for a more general discussion of TSS dynamics and control.

1.2.1 Spinning Tethered Satellite System

One of the principal reasons for using a TSS for a given application is that the gravity-gradient acting over the length of the tether serves to maintain the tether in a tensioned state throughout the course of its operation. The fact that the tether is tensioned means that it remains deployed and relatively straight during the operation of the system, with the tension providing some resistance against tether elastic vibrations induced by external perturbations. For relatively short tethers or systems consisting of less massive end bodies, however, the gravity-gradient effect is not as significant, and external perturbations can lead to the tether becoming slack. A slack tether is typically undesirable, and would most likely result in the failure of the mission (as occurred in the ATEX mission discussed previously.)

One of the simplest methods of reducing the possibility of the tether becoming slack during the operation of the system is to spin the system in the orbit plane, thus turning the system

into a spinning TSS. The spinning motion of the system creates a "centrifugal force" along the tether that serves to increase the tension in the tether above that of a non-spinning system, making the tether more resistant to external perturbations that can cause slackness. The increased tension therefore allows for more flexibility in choosing the length of the tether and the masses of the end bodies in the system.

The spinning motion of a spinning TSS also has a number of advantages over non-spinning systems in addition to the decreased probability of tether slackness. One such advantage is that the system goes through a much wider range of orientations during its operation than a non-spinning system. The spinning motion allows the tether to be oriented at any angle relative to the local vertical, whereas a non-spinning system is constrained to orientations in the direct vicinity of the local vertical. Spinning TSS can therefore be used to perform a wider range of scientific measurements over a larger spatial range than their non-spinning counterparts. Another advantage possessed by spinning TSS is that their spinning motion can be utilized to perform orbit transfers of satellites. As discussed in relation to MXER earlier in this chapter, the spinning motion can be used to "throw" a satellite onto a transfer orbit, thus reducing propellant requirements for the satellite. For all of these reasons discussed above, spinning TSS have a much broader range of applicability than non-spinning systems.

There are several aspects of the dynamics of a spinning TSS that can have a significant impact on the operation of the system. Understanding these dynamics is a critical part of the design or analysis of any spinning TSS. The various aspects of the system dynamics are illustrated in Fig. 1.1, and include the orbital motion of the system, the motion of the tether, and the attitude motion of the end bodies.

The orbital motion of the system defines the state of some reference point in the system relative to the central body. The reference point is typically chosen as the system mass center, or some convenient point on one of the end bodies. The orbital motion is affected by a number of different influences, including the gravity of the central body, the distributed mass of the system, and any external forces acting on the system such as atmospheric drag and electrodynamic forcing. The relative influence of each of these factors depends on the specific spinning TSS and its operational regime.

The motion of the tether can be decomposed into two parts, as illustrated in Fig. 1.1. The first part of the tether motion is a pendular mode that defines the motion of the line connecting the ends of the tether. This pendular mode can be thought of as the attitude motion that the tether would display if it were a rigid rod, and is affected by the mass properties of the system and the external forces acting on the system. For a typical spinning TSS, the pendular motion is ideally a rotation in the orbit plane; however, external perturbations will result in small out-of-plane deviations for the nominal planar motion. The pendular motion of the tether can therefore be viewed as a combination of an in-plane rotation and small out-of-plane librations. The second component of the tether motion is the elastic vibrations of the tether, which can be divided into transverse and longitudinal vibrations. The tether

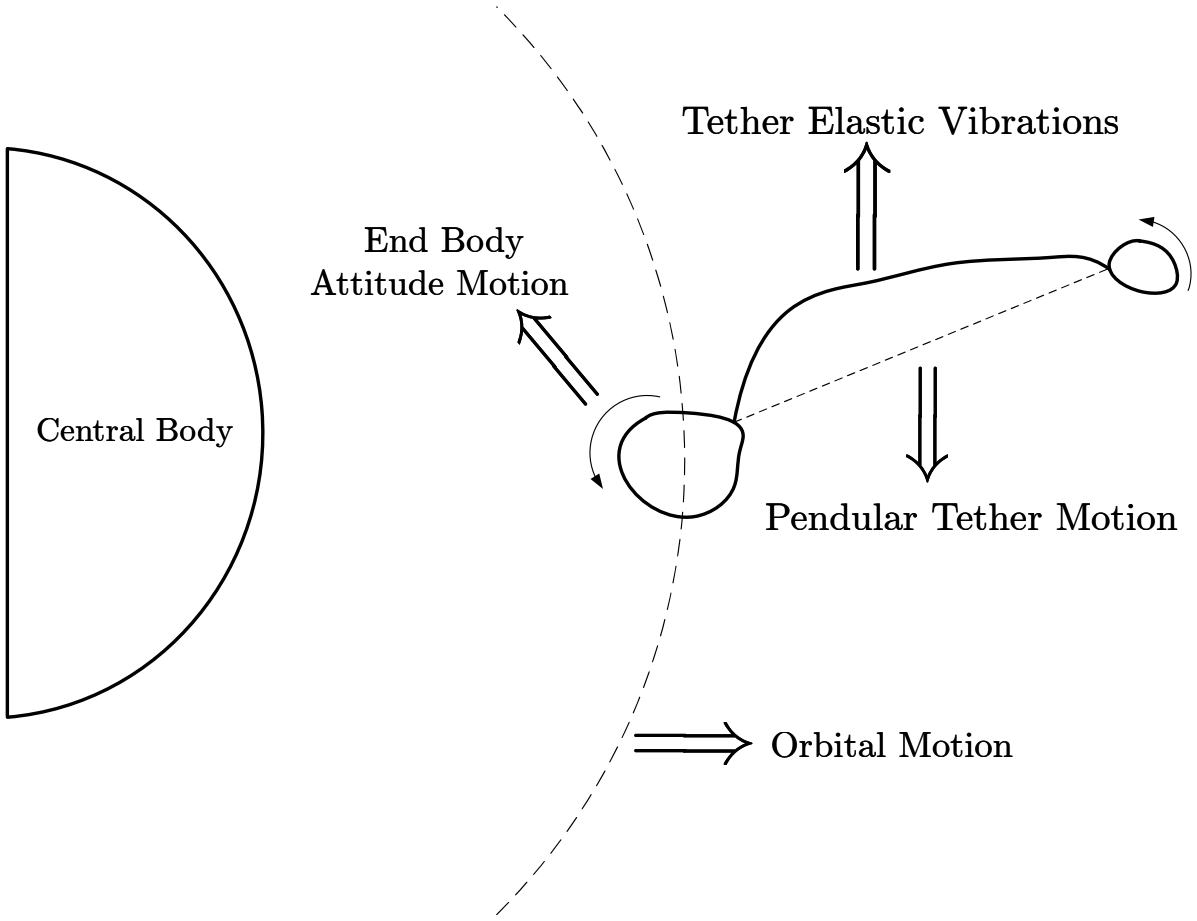

Figure 1.1: Illustrations of the various aspects of spinning TSS dynamics

elastic vibrations are affected by the external forces acting along the tether as well as the physical and material properties of the tether. Note that the pendular motion and the elastic vibrations of the tether are coupled, in that neither is independent of the other.

The final component of the system dynamics is the attitude motion of the end bodies, which is dependent upon the inertia properties of the end bodies and driven by the external moments acting on the end bodies. A component of the external moment acting on each end body is due to the tensions applied by any tethers attached to the body, so the attitude motion of the bodies is affected by the motion of the tether. Likewise, the motion of the tethers is affected by the attitude motion of the end bodies, because motion of the end bodies affects the conditions at the ends of the tethers. Similarly, the orbital motion of the system affects both the tether motion and the attitude motion of the end bodies and vice versa, so all of the motions of a spinning TSS are coupled to one another. This coupling makes analyzing the dynamics of a spinning TSS quite difficult, but also means that spinning TSS dynamics are quite rich and interesting. One of the principle objectives of the work presented in this dissertation is to analyze several of the key aspects of spinning TSS dynamics.

1.2.2 Electrodynamic Tethered Satellite System

The primary difference between an electrodynamic TSS and a conventional TSS is that the tether in an electrodynamic TSS is electrically conductive and intended to carry an electrical current. The current in the conductive tether interacts with the magnetic field of the central body, resulting in a distributed force along the length of the tether. This force provides a form of propellantless propulsion for the system that can be used to affect all aspects of the system dynamics.

An illustration of a two-body electrodynamic TSS and the fundamental principles underlying its operation is shown in Fig. 1.2. At any point in time, a differential tether length element, $d\vec{\mathbf{l}}$, has a velocity $\vec{\mathbf{v}}$ relative to the local magnetic field vector $\vec{\mathbf{B}}$. Note that the local magnetic field vector is generated by the central body. Because the tether is electrically conductive, its motion relative to the local magnetic field induces an electrical potential across its ends equal to

$$\Phi = \int_L (\vec{\mathbf{v}} \times \vec{\mathbf{B}}) \cdot d\vec{\mathbf{l}} \tag{1.1}$$

where the integration is performed over the length of the tether. The induced potential can be used to drive an electrical current through the tether, provided that the ends of the tether are allowed to make electrical contact with the ambient plasma environment. If contact with the ambient plasma is achieved, a current loop forms through the tether and ambient plasma as shown in Fig. 1.2. The electrical current at $d\vec{\mathbf{l}}$, which is denoted i, then interacts with the local magnetic field to create a force on $d\vec{\mathbf{l}}$ equal to

$$d\vec{\mathbf{F}}_{\mathrm{ED}} = i\, d\vec{\mathbf{l}} \times \vec{\mathbf{B}} \tag{1.2}$$

The total force acting on the tether is found by integrating Eq. (1.2) over the length of the tether

$$\vec{\mathbf{F}}_{\mathrm{ED}} = \int_L i \, d\vec{\mathbf{l}} \times \vec{\mathbf{B}} \tag{1.3}$$

Using the process described above an electrodynamic TSS can generate propulsion without the need for any propellant. The force generated by an electrodynamic TSS is inherently low, but it can nonetheless be used to alter various aspects of the system dynamics.

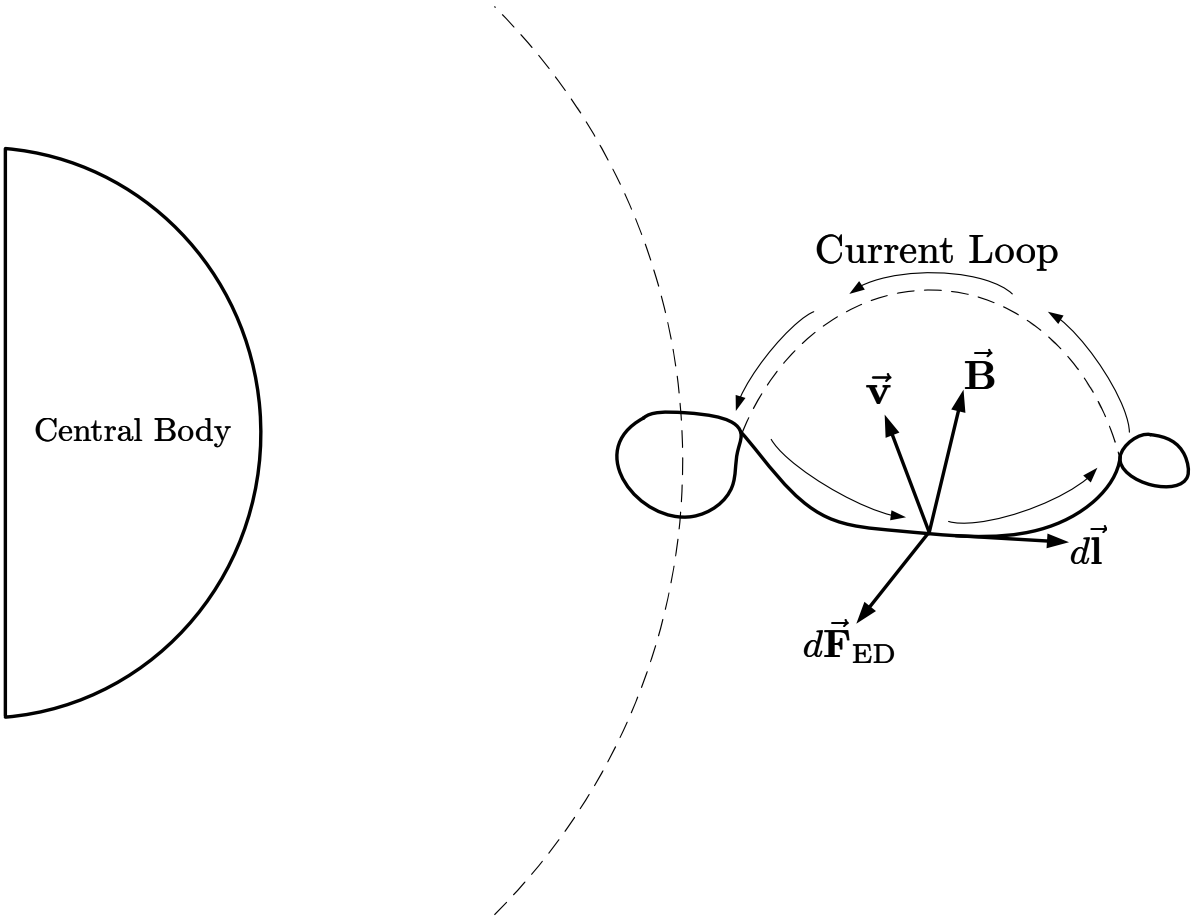

Figure 1.2: Illustrations of the operational principles of an electrodynamic tether system

For Earth-orbiting electrodynamic TSS, the strength of Earth's magnetic field limits the operational regime of the system to low-Earth orbit (LEO). At higher orbit altitudes the magnetic field is too weak to allow for the generation of a useful electrical current, and the ambient plasma is not dense enough to allow for the reliable formation of a current loop. In LEO, the system orbits with a velocity greater than that of the local magnetic field, so $\vec{\mathbf{v}}$ in Eq. (1.1) is roughly in the direction of the system orbital motion. From Eq. (1.1), the induced voltage across the system is positive, meaning that the end of the tether at a higher

orbit altitude is at a higher electric potential than the end of the tether at a lower orbit altitude. If a current loop is formed through the tether and ambient plasma, the current is naturally driven in the direction shown in Fig. 1.2–from the lower end body to the upper end body. According to Eq. (1.2), the electrodynamic force generated on the tether is therefore acting in the direction opposite the orbital motion, and serves to decay the system orbit. However, no power is required to generate the current in the tether because it is driven by the naturally induced voltage, and the current can therefore be used to charge a power source if one is placed in the current loop. Because of this fact, an electrodynamic TSS operating as described above is said to be operating in the "generator mode." In this operational mode, electrical energy is gained in the form of a charged power source at the expense of the mechanical energy of the system.

In addition to being charged if the system is operating in the generator mode, a power source can be used to reverse the naturally occurring induced voltage such that the lower end body is at a higher electric potential than the upper end body. The electrical current therefore flows from the upper end body to the lower end body, and the resulting electrodynamic force is in the same direction as the system orbital motion. In this case the electrodynamic force serves as a thrust force that raises the system orbit, and an electrodynamic TSS operating in such a manner is therefore said to be operating in the "thruster mode." In this operational mode, the mechanical energy of the system is increased at the expense of electrical energy in the form of an applied power source. The discussion presented above applies to electrodynamic TSS orbiting bodies other than Earth; however, we must note that the generator and thruster modes can be slightly different for systems orbiting other central bodies, and there can even be some overlap between the two modes. For example, the magnetic field of Jupiter is still quite strong at altitudes above its synchronous altitude, so Jupiter-orbiting electrodynamic TSS can operate above the synchronous altitude. This means that the velocity of the system relative to the magnetic field is opposite the system motion, and a force in the direction of the system orbital motion can be generated using the naturally induced voltage. It is therefore possible for a Jupiter-orbiting electrodynamic TSS to generate a thrust force that raises the system orbit while simultaneously charging a power source.

As with any TSS, the primary aspects of the dynamics of an electrodynamic TSS are the system orbital motion, the tether motion, and the attitude motion of the end bodies. The characteristics of these aspects of the system dynamics are similar to those described for an spinning TSS in § 1.2.1. With an electrodynamic TSS, however, perhaps the most important aspect of the system dynamics is the effect of the electrodynamic force on the various components of the system motion.

The main effect of the electrodynamic force on the orbital motion of the system is to increase or decrease the orbit radius, depending on whether the system is operating in the thruster or generator mode. The change in the orbit radius is slow due to the relatively low magnitude of the electrodynamic force, but over long enough time scales significant changes in the orbit radius can be achieved. The electrodynamic force also changes the orientation in space of the system orbit, but these changes are much slower than the change in the orbit radius.

The electrodynamic force affects both the pendular and flexible modes of the tether motion. For local vertically aligned systems, the electrodynamic force drives both in- and out-of-plane librations of the system about the nominal alignment with the local vertical. For spinning systems, the electrodynamic force can either increase or decrease the in-plane spin rate depending on the direction of the force, and also drives out-of-plane librations that are deviations from the nominal planar spinning motion. Because the electrodynamic force acts tangent to the tether, only the transverse elastic vibrations of the tether are directly affected by the electrodynamic force. However, the transverse vibrations are coupled to the longitudinal vibrations of the tether, so the electrodynamic force affects all aspects of the tether elastic vibrations.

Th electrodynamic force only acts along the tether, so it does not directly affect the attitude motion of the end bodies. As with a spinning TSS, however, the end body attitude motion in an electrodynamic TSS is affected by the tether motion and the system orbital motion, so the electrodynamic force has an indirect affect on the end body attitude motion.

From the discussions presented in this section it is evident that the dynamics of spinning and electrodynamic TSS can be quite complicated and rich. The analysis and design of any TSS mission requires more than the qualitative insights discussed thus far, and the literature contains a vast amount of detailed analysis of various types of TSS. In the next section, we present a review of the most relevant studies related to the dynamics and control of spinning and electrodynamic TSS.

1.3 Review of Relevant Literature

Dating back to Tsiolkovsky, literally hundreds of studies of TSS dynamics and control have been published in the literature. Two excellent survey articles on the topic of non-electrodynamic TSS dynamics and control are those written by Misra and Modi,[41] and Kumar.[30] The former article provides a survey of works published prior to 1986, while the latter provides a survey of works published after 1986.

As mentioned previously, some of the work presented in this dissertation applies to TSS in general, but we are mostly concerned with the dynamics and control of spinning and electrodynamic TSS, with systems such as the MXER system discussed in §1.1 are our primary motivation. The proposed configuration of MXER consists of two spacecraft connected by a single tether, so we confine our survey of the relevant literature to studies that have considered these types of systems. In addition, we are specifically interested in the dynamics and control of the system in its operational configuration, meaning that we are not concerned with deployment or retrieval of the tether. We therefore also confine our review of the relevant literature to studies of systems in their operational configuration. We do point out that in this section a more thorough review of the literature on electrodynamic TSS is presented than is presented for other systems. This is due to the fact that several survey articles on

non-electrodynamic TSS have been published in the past, while no such survey exists for electrodynamic TSS. We hope that the literature review presented in this section may serve as a useful introduction to the dynamics and control issues associated with electrodynamic TSS.

1.3.1 Spinning Tethered Satellite Systems

The literature contains a large number of studies on the dynamics of spinning TSS dating back to the early years of human spaceflight. The earliest studies of spinning TSS dynamics were motivated by their possible use for generation of artificial gravity in space. Tai and Loh[63] studied the dynamics of a space-station connected to a counterweight by a flexible cable. The spinning motion of the system was confined to the orbital plane, and numerical simulations were used to analyze the system dynamics. Chobotov[12] studied a spinning TSS by modeling the system as two point masses connected by a massless linear spring. The system mass center remained on an unperturbed circular orbit and the motion of the system was confined to the orbital plane. Numerical solutions were used to study the system dynamics. Crist and Eisley[16] studied a system similar to that studied by Chobotov, but included some effects due to orbital eccentricity. A Floquet analysis was used to study the stability properties of the planar motion of the system.

Stabekis and Bainum[60] studied a spinning TSS consisting of two finite, rigid end bodies connected by an extensible, massless tether. As in previous studies, the system mass center was constrained to a circular orbit and the motion was restricted to the orbital plane. The nonlinear equations of motion were linearized about equilibrium configurations and the Routh-Hurwitz criterion was used to analyze the stability of the planar motion.

Three-dimensional motion of a spinning TSS was considered by Bainum and Evans[2] using a model similar to that used in Ref. [60]. However, gravity-gradient effects were not included in the model, so the motion of the system was torque-free. Bainum and Evans[3] later extended their analysis to include the effects of the gravity-gradient torque acting on the system. The nonlinear equations of motion were linearized about a nominal spin in the orbit plane, and possible resonances were identified. Some resonances in the attitude motion of the end bodies were demonstrated using numerical simulations, and all of the simulations indicated small out-of-plane motion of the tether. A rigorous stability analysis was not performed, although Floquet theory was suggested.

Another study of the three-dimensional motion of a spinning TSS was conducted by DeCou.[17] Several system configurations were considered, but all consisted of point masses connected by massless, fixed-length tethers with the system mass center constrained to a circular orbit. The system was nominally spinning in a plane with an arbitrary orientation relative to the orbital frame. Expressions were derived for the accelerations of the end bodies due to the gravity-gradient, and these expressions were used to derive differential equations governing the out-of-plane motion of the end masses and the deviation of the spin rate from a nominal

value. The differential equation governing the out-of-plane motion contained periodic, time-varying coefficients that were assumed to be negligible to simplify the analysis. The resulting linear, constant-coefficient differential equation was solved, and the solution for the out-of-plane motion was a combination of various sinusoidal terms. These solutions assumed that there was no initial out-of-plane motion, such that the motion remains planar if the desired spin plane is the orbital plane.

Breakwell and Janssens[8] studied the transverse vibrations of a two-body spinning TSS by assuming that the tether is inextensible and that the elastic vibrations of the tether have no effect on the attitude motion of the tether. The system was assumed to be spinning in the orbit plane at a rate equal to the orbital rate, and the stability of small transverse oscillations was analyzed using Floquet theory. The transverse vibrations were found to be unstable for certain configurations of the system mass distribution, and methods of selecting the masses of the end bodies that avoid the instabilities are presented.

A rather extensive study of spinning TSS dynamics can be found in the book by Beletsky and Levin.[5] Massless and massive tethers are considered, but in all cases the system mass center is constrained to an unperturbed circular orbit. The planar motion of systems with massless tethers is completely characterized, and bounds are placed on the possible out-of-plane motion for non-planar systems. The planar motion of massive tethers is studied by assuming that the tether is flexible, but the elastic vibrations of the tether do no affect the pendular motion of the tether. The elastic vibrations are thus superimposed upon the pendular motion of a rigid tether. In addition, the longitudinal vibrations of the tether are ignored and only transverse vibrations are considered. A Floquet analysis is used to show that the transverse vibrations are unstable for certain in-plane spin rates and system mass properties. The results of this analysis are an extension of those presented by Breakwell and Janssens,[8] in that different in-plane spin rates are considered.

Somewhat surprisingly, the literature contains few studies on the control of two-body spinning TSS in their operational configuration. Most studies of the control of two-body spinning TSS relate to deployment and retrieval of the tether, which is not the focus of the work presented in this dissertation. The interested reader is referred to Refs. [41] and [30] for more information of these topics. Most modern studies of spinning TSS control focus on controlling large formations of satellites, such as triangular or diamond-shaped configurations. An excellent reference for work on these types of systems is the book by Levin,[34] in which the dynamics and control of various types of TSS is studied related to specific TSS missions. As mentioned previously, we are only concerned with two-body systems, so works related to different spinning TSS configurations are not discussed here.

1.3.2 Electrodynamic Tethered Satellite Systems

Research on electrodynamic TSS is a relatively new branch of TSS research, having only begun during the past several decades. In general, the research on the dynamics and control

of electrodynamic TSS can be divided into two main categories, each focusing on a particular aspect of the system dynamics. The first category deals with the change in the system orbit due to the electrodynamic force, and how the force can be used to control the system orbit. The second category deals with the motion of the tether and how it is specifically affected by the electrodynamic force.

Orbital Maneuvering

One of the first studies on the effect of the electrodynamic force on the system orbit was conducted by Beletsky and Levin.[5] In their work, Beletsky and Levin considered a two-body electrodynamic TSS consisting of point mass end bodies connected by a flexible tether. The magnetic field of the central body was modeled as a non-tilted, non-rotating dipole. Approximations of the average rates-of-change of the orbital inclination, right-ascension of the ascending node, and orbital parameter were derived and analyzed. The average changes in the inclination and right-ascension of the ascending node were found to be quite small, even over relatively long time spans. However, over similar time spans the variation of the orbit parameter was found to be significant, reaching approximately 50 km over 100 orbits for a typical system.

Tragessear and San[64] developed a simple guidance scheme for the orbital motion of a two-body electrodynamic TSS consisting of two point mass end bodies connected by a rigid tether. The magnetic field of the central body was modeled as a non-tilted, non-rotating dipole, and the electrodynamic force was assumed to have a negligible influence on the tether attitude motion. The system was therefore assumed to remain aligned with the local vertical throughout its motion such that the orbital motion of the system comprised the only degrees of freedom. The time-averaged Gauss variational equations were used to develop guidance laws for the osculating orbit elements of the system mass center, with the variation of the electrodynamic force achieved by modulating the current in the tether. Numerical simulations were used to demonstrate the performance of the guidance laws.

The results of Tragessear and San were extended by Williams[66] to include the effects of the pendular motion of the tether. Optimal control laws for the osculating orbit elements of the system mass center were developed using the current in the tether as the control input. The performance of the optimal control laws was demonstrated using numerical simulations and compared to the results of Tragesser and San. In certain cases, the inclusion of the pendular motion of the tether in the guidance scheme led to improved performance over the guidance scheme that did not include the pendular motion.

Another extension of the work of Tragesser and San was made by Sabey and Tragesser.[54] The attitude dynamics of the tether were included in the system dynamics by assuming that the attitude was controlled about a nominal periodic trajectory, and a similar procedure as that used in Ref. [64] was used to determine guidance laws for the osculating orbit elements of the system mass center.

Lanoix et al.[31] considered the orbital dynamics of a more complicated and physically realistic system model than the studies discussed previously. The system consisted of two point mass end bodies connected by an axially extensible tether. The magnetic field of the central body was represented using the International Geomagnetic Reference Field model, which expresses the field in terms of a spherical harmonic series. Aerodynamic and thermal effects on the dynamics of the tether were also considered in the system model, and numerical simulations were used to analyze the orbital motion of the system.

A recent study of electrodynamic TSS orbital maneuvering was conducted by Stevens and Wiesel.[62] As in previous studies, the system was modeled as two point mass end bodies connected by a rigid tether. The magnetic field of the central body was modeled as a non-tilted, non-rotating dipole, and atmospheric drag was included in the tether dynamics model. As in the studies of Tragesser and San and Sabey and Tragessear, the time-averaged Gauss form of the variational equations for the osculating orbit elements of the system mass center were considered and used to develop optimal control laws for the orbital motion of the system. The control laws presented were for maximum final altitude, maximum final inclination change, and minimum time orbital maneuvers.

Tether Dynamics and Control

Previous studies of the tether dynamics of electrodynamic TSS have typically focused on either the pendular motion of the system or the elastic vibrations of the tethers. Some of the earliest studies of the pendular motion of electrodynamic TSS were conducted by Levin[33] and Beletsky and Levin.[5] In these studies, the system consists of two point mass end bodies connected by a flexible, massless tether, with the system mass center constrained to an unperturbed circular orbit. The magnetic field of the central body is modeled as a non-tilted, non-rotating dipole and the orbit of the system was confined to the plane of the magnetic equator. The current in the tether is assumed constant throughout the motion. Because the tether is massless and the system orbit is in the magnetic equatorial plane, the shape of the tether can be determined at any moment in time such that the tether attitude angles are the only degrees of freedom of the system. Equilibrium configurations for the tether attitude angles are determined and their linear stability is analyzed. The stability analysis shows that the operational equilibrium configurations of a two-body electrodynamic TSS are always unstable under a constant current. The instabilities are attributed to a constant pumping of energy into the pendular motion of the tether by nonconservative components of the electrodynamic force.

The studies of Levin and Beletsky and Levin were extended to electrodynamic TSS systems on inclined circular orbits by Pelaez et al.[47] In this study, the system consists of two point mass end bodies connected by a massive, rigid tether, and the magnetic field of the central body is modeled as a non-tilted, non-rotating dipole. The current in the tether is once again assumed to be held constant. Unlike the previous studies, the circular orbit on which the

system mass center is constrained is allowed to have an inclination relative to the plane of the magnetic equator. As a result, the electrodynamic force varies periodically with a period equal to the orbital period, and equilibrium configurations for the tether attitude can no longer be determined. However, periodic solutions are determined and their stability is analyzed using Floquet theory. As with systems confined to the magnetic equator, the periodic solutions of two-body electrodynamic TSS on inclined orbits are always unstable under the action of a constant current. The instabilities are once again attributed to a constant pumping of energy into the system by the electrodynamic force.

Several further extensions of the work in Ref. [47] were performed to consider a much larger family of periodic tether attitude trajectories[46] and systems on elliptical inclined orbits.[45] In each of these studies the tether attitude motion was once again found to always be unstable due to the same energy pumping mechanism discussed previously.

One of the earliest studies of the elastic vibrations of an electrodynamic TSS was conducted by Belestsky and Levin.[5] In this study, the system consists of two point mass end bodies connected by a flexible, massive tether, with the system mass center constrained to a circular orbit. The magnetic field of the central body is modeled as a non-tilted, non-rotating dipole and the system orbit is confined to the plane of the magnetic equator. Planar equilibrium configurations are determined for the case of constant current in the tether, and the linear stability of the equilibrium configurations is analyzed. As with the attitude motion of a two-body electrodynamic TSS in the plane of the magnetic equator, the elastic vibrations are always unstable under a constant current. The instability occurs in both the transverse and longitudinal vibrations due to the coupling between those two motions, and is once again attributed to energy pumping by the electrodynamic force.

The transverse vibrations of a two-body electrodynamic TSS on an inclined circular orbit were considered by Pelaez et al.[48] The magnetic field is modeled as a non-tilted, non-rotating dipole and the current in the tether is held constant. The transverse vibrations of the tether are modeled by assuming that the tether is comprised of two articulated rigid rods. Periodic trajectories for the system dynamics are determined and their linear stability is analyzed numerically. Two different system configurations are studied: one in which only a portion of the tether carries an electrical current; and another in which the entire length of the tether carries an electrical current. For both types of systems, the periodic motions are found to always be unstable.

Somenzi et al.[59] studied the transverse vibrations of a two-body electrodynamic TSS consisting of two point mass end bodies connected by a flexible, but inextensible, tether. The system mass center is constrained to a circular inclined orbit, and the magnetic field is modeled using the International Geomagnetic Reference Field model. Some effects on the current in the tether due to the ambient plasma environment and average solar activity are also included in the dynamic model. The tether transverse vibrations are expanded in normal modes, and the system equations of motion are linearized about an alignment with the local vertical. A linear stability analysis is performed considering only the first two modes

of the transverse vibrations, and shows that the system is always unstable.

The studies discussed above indicate that the tether dynamics of electrodynamic TSS are inherently unstable. As mentioned previously, the instability is due to a constant pumping of energy into the system by non-conservative components of the electrodynamic force. Because the pendular motion and elastic vibrations of the tether are coupled, any instability in one aspect of the tether motion is transmitted to the other. The inherent instability in the tether motion means that successful operation of any electrodynamic TSS requires some means of controlling both the pendular motion and elastic vibrations of the tether.

Corsi and Iess[14] considered the control of the pendular motion of an electrodynamic TSS for satellite deorbiting applications. The system considered in the study consists of two point mass end bodies connected by a rigid tether. A Lyapunov function is used to derive a control law that keeps the in- and out-of-plane motions of the tether within pre-defined bounds, and the performance of the control law is demonstrated with numerical simulations. The control law is based on a simple on-off switching of the electrical current in the tether (and thus the electrodynamic force) that is demonstrated to keeps the tether attitude motion bounded.

Libration control of a system model similar to that considered by Corsi and Iess was considered by Pelaez and Lorenzini.[25] The system is modeled as two point masses connected by a rigid tether, and the system mass center is assumed to remain fixed on an inclined circular orbit. The latter assumption means that the influence of the electrodynamic force on the orbital motion is considered negligible for the systems and time scales considered in the study. The magnetic field of the central body is modeled as a non-tilted, non-rotating dipole. Simple feedback control laws are derived that control the attitude motion of the tether about periodic trajectories for a constant current in the tether. The control of the tether attitude motion is achieved by adding "appropriate forces" into the system model, so no physical mechanism for providing the control inputs is given. Floquet theory is used to determine stability boundaries that are related to the control gains used in the control laws, and numerical simulations are used to demonstrate the effectiveness of the control laws.

Williams[67] also considered the control of the tether attitude motion about a periodic trajectory. The model considered by Williams is identical to that studied by Pelaez and Lorenzini.[25] Control about the periodic trajectory is achieved by modulating the current in the tether based on feedback measurements of the system Hamiltonian relative to the Hamiltonian of the desired periodic trajectory. Stability boundaries are determined using Floquet theory as functions of the control gain of the control law, and a numerical simulation is used to demonstrate the performance of the control law.

Zhou et al.[71] developed control laws for the tether attitude motion by using the rate-of-change of the tether length as an additional control input. The system considered consists of two point mass end bodies connected by a rigid tether, and the magnetic field is modeled as a non-tilted, non-rotating dipole. Feedback linearization is used to determine control laws for the tether current and rate-of-change of length that regulate the attitude motion about the local vertical. Numerical simulations are used to demonstrate the performance of the

control laws.

A recent study by Williams[69] considers the control of the tether attitude motion about a periodic trajectory using what the author calls "time-delayed predictive control." The control of the attitude motion is achieved using modulation of the current in the tether as the only control input. The system is modeled as two point mass end bodies connected by a rigid tether. Numerical simulations are used to demonstrate the performance of the controller for the case of the system constrained to a circular orbit about a central body with a non-tilted dipole magnetic field. Several numerical simulations are also performed for systems in which the orbital variations due to the electrodynamic force are included in the model, and the magnetic field is modeled as a tilted dipole that rotates with the central body. In these cases, the controller cannot drive the tether attitude motion exactly to the desired periodic trajectory, but it does stabilize the attitude motion in the sense that the attitude motion remains bounded and "close" to the desired periodic trajectory for all time.

Equilibrium-to-equilibrium maneuvers of electrodynamic TSS are considered by Mankala and Agrawal.[35] The system model used in the study consists of two point mass end bodies connected by a rigid tether, with the system constrained to a circular orbit. The magnetic field of the central body is modeled as a non-tilted, non-rotating dipole and the motion of the system is confined to the plane of the magnetic equator. Equilibrium configurations for the planar tether attitude angle are determined, and control laws for the current in the tether are determined using feedback linearization. These control laws drive the system from one equilibrium configuration to another, and their performance is demonstrated using numerical simulations. Another study by Mankala and Agrawal[36] considers equilibrium-to-equilibrium maneuvers of flexible electrodynamic TSS. The system model is identical to that used in Ref. [35], with the exception that the tether is modeled as flexible, but massless. Once again, feedback linearization is used to derive control laws that drive the system from one equilibrium configuration to another.

All of the studies of electrodynamic TSS control discussed to this point have only considered control of the pendular motion of the tether. However, several studies have also considered control of the elastic vibrations of the tether. Beletsky and Levin[5] considered tether vibration control of a system consisting of two point mass end bodies connected by a flexible tether. Control laws based on modulations of the current in the tether were determined that regulate small tether elastic vibrations about a nominal equilibrium configurations. These control laws are determined assuming that the magnetic field of the central body is a nontilted dipole, and that the motion of the system takes place entirely in the plane of the magnetic equator.

Hoyt[22] develops two different feedback control laws for the elastic vibrations of a two-body electrodynamic TSS. The first control method is based on measurements of the position of the tether at various points along its length. These measurements are made by beacons that must be attached to various points along the tether. The second control method does not require any knowledge of the tether motion, and only requires knowledge of the relative acceleration of the end bodies. Numerical simulations are used to demonstrate that the

control laws are successful in stabilizing the tether elastic vibrations over relatively long time spans.

Watanabe et al.[65] use input shaping to control the elastic vibrations of a two-body electrodynamic TSS. A lumped mass model in which the tether is modeled as a finite number of point masses connected by springs is used to account for the flexibility of the tether. The magnetic field is modeled as a non-tilted, non-rotating dipole and the system mass center is constrained to a circular orbit in the plane of the magnetic equator. Numerical simulations are used to demonstrate that the control method is successful in reducing the amplitude of the tether elastic vibrations relative to those seen in an uncontrolled system.

Control of a continuum tether model is considered by Williams et al.[70] The electrodynamic TSS considered in this study is a two-body system with the system mass center constrained to a circular orbit. The magnetic field of the central body is modeled as a non-tilted, non-rotating dipole. Control laws are developed for the tether transverse vibrations by assuming that the transverse vibrations are governed by the linear, one-dimensional wave equation and applying principles of wave-absorbing control design. The control is applied by movement of the tether attachment point at one of the end bodies. The transverse vibration control is combined with a tether pendular control law to provide complete control of the tether motion. The performance of the control is demonstrated using numerical simulations for stationkeeping, deployment, and retrieval of the tether.

1.3.3 Spinning Electrodynamic Tethered Satellite Systems

A number of studies contained in the literature consider two-body TSS that are both spinning and utilizing electrodynamic propulsion. Pearson et al.[44] proposed using spinning electrodynamic TSS for orbital maneuvering and showed that they can generally provide much greater performance than local-vertical aligned systems. Several minimum-time orbit maneuvers utilizing spinning electrodynamic TSS were also computed and demonstrated numerically.

Williams[68] studied spinning electrodynamic TSS orbital maneuvering by considering a system consisting of two point mass end bodies connected by a rigid tether. The magnetic field of the central body was modeled as a non-tilted, non-rotating dipole, and the entire system was assumed to spin at a constant rate in the orbital plane. This last assumption means that the effects of the electrodynamic force on the attitude dynamics of the tether are neglected. The methods used by Tragesser and San are used to develop guidance laws for the system orbital motion, and numerical simulations are used to demonstrate the performance of the guidance laws. As done by Pearson et al., Williams concluded that spinning electrodynamic TSS are generally more effective orbit transfer vehicles than vertically aligned systems.

A relatively detailed study of the dynamics and control of two-body spinning electrodynamic TSS is contained in the book by Levin.[34] In this work, the system is modeled as two point

mass end bodies connected by a massive, flexible tether. The basic operation of the system is analyzed by determining how the electrodynamic force varies as the system spins, and how the current in the tether can be modulated to produce a net force in a desired direction. The evolution of the spin rate and axis of the system due to the electrodynamic force and gravity-gradient torque is also considered. Levin finds that an appropriate modulation of the current in the tether can eliminate any average effects that the electrodynamic force has on the system spin rate, and the spin axis is only affected by the gravity-gradient torque if the spin plane is not the same as the orbit plane.

Small transverse vibrations of the tether in the two-body spinning electrodynamic TSS are also considered by Levin. The rotation of the system is assumed uniform in this study, and the effects of the gravity-gradient are neglected. The primary result of the study is that spinning electrodynamic TSS are preferable to vertically aligned electrodynamic TSS because they can operate at higher thrust levels due to the fact that the tether is in a higher state of tension. Because the tether is at a higher tension, it is more resistant to external forces, and can thus be exposed to larger magnitude electrodynamic forcing without "inducing any catastrophic dynamic responses."

The final area of two-body spinning electrodynamic TSS dynamics and control considered by Levin is that of orbital maneuvering. A current scheduling procedure is introduced that allows for maximum orbit boost, orbit de-boost, and rotation of the orbit plane. Methods of performing the fastest possible in-plane orbit transfers and orbit plane changes are also analyzed.

1.4 Contributions of the Present Study

Although a great deal of research has already been conducted on the dynamics and control of spinning and electrodynamic TSS, including numerous studies on spinning and electrodynamic TSS, there exist a number of topics that remain to be addressed. The purpose of this dissertation is to address several of these open areas of study, and in this section we present an overview of the original contributions made by this work.

1.4.1 Validation of Computational Models

In the literature review presented in the previous section a fair amount of attention was paid to the various modeling assumptions used to analyze the given TSS. Any TSS is a fairly complicated physical system, and as the literature review shows, it is common practice to use greatly simplified system models to study the dynamics and control of the system. The mathematical models associated with these simplified models are often relatively simple, and in many cases lend themselves to a rigorous analytical treatment. This practice of using simplified models is entirely justifiable, because the analysis of a system model that takes

into account every conceivable aspect affecting the system dynamics would be completely intractable, even using numerical analysis techniques. However, the validity and practical applicability of results obtained using simplified system models should not be taken for granted. It is entirely possible that the assumptions implicit in the simplified models remove critical aspects affecting the behavior of the system such that the predictions made by these models have no resemblance whatsoever to the behavior of the actual physical system.

In an ideal situation, results obtained using simplified system models would be compared to experimental data to test their validity. If the results compare favorably to the experimental data according to some objective metric, then the results are said to be validated. The experimental data used in the validation process is typically only available for a small subset of the intended operational regime of the actual physical system, and the validated results obtained from the simplified system model are used to make predictions about the behavior of the system for cases in which experimental data is not available. This type of process is commonly used in fields such as fluid and solid mechanics in which experimental data is readily available.

Unfortunately, the above described process cannot be applied to results obtained related to TSS dynamics and control because experimental data is virtually nonexistent. This means that no results can be truly validated at the current point in time; however, it does not mean that some form of validation cannot be performed. In this dissertation we propose a method of validating results obtained from simplified system models when experimental data is not available, as in the case of a TSS. The validation procedure requires the construction of what we term a "top-level system model," and an associated "top-level computational model." The top-level system model is a model of the system containing as few simplifying assumptions as possible. It is intended that this model capture all of the relevant behaviors of the system, but can still be analyzed in a practical way. The top-level computational model contains all of the tools used to make predictions about the behavior of the system using the top-level system model. Because of the complicated nature of the top-level system model, the predictions made by the top-level computational model are in the form of numerical solutions which take the place of experimental data. All results obtained using simplified system models are compared to the predictions made by the top-level computational model as a means of validation. If the results do not compare favorably, then the simplified system model must be altered in some way so that it compares more favorably to the predictions of the top-level computational model.

In addition to the proposed computational model validation procedure, one of the major contributions of this work is the development of a top-level computational model that can be used to perform validation of results obtained using simplified system models. This model is developed with spinning and electrodynamic TSS specifically in mind; however, the model can be applied to a variety of other types of TSS as well. Most likely because of the lack of experimental data, validation of results obtained using simplified system models is seldom, if ever, performed in the field of TSS dynamics and control. It is the hope of the author that the validation method proposed in this work, combined with the availability of the top-level

computational model presented in this work, makes it much easier for other researchers to validate their results and better gage their practical applicability.

1.4.2 Verification of Computational Models

Because the numerical solutions produced by the top-level computational model act in place of experimental data in the validation method we propose, the accuracy of the computer codes written to produce the numerical solutions must be rigorously verified. Errors in these codes, no matter how small, will lead to inaccurate numerical solutions that can be used to make false claims about the validity of a result obtained from a simplified system model. The method we use in this work to verify the computer codes written for the top-level computational model is the method of manufactured solutions, which is more commonly used in the fields of fluid and solid mechanics. To the author's knowledge, this work constitutes the first instance in which the method of manufactured solutions is used to verify the computational model of a TSS. We believe that the work presented herein demonstrates the relative ease with which the method is applied to a TSS, and we hope that this work encourages other researchers in the field of TSS dynamics and control to apply the method to their work whenever applicable. Verification of computational models is another practice that is uncommon in TSS dynamics and control research, and we believe that this work demonstrates its necessity.

1.4.3 Dynamics of Spinning Tethered Satellite Systems

As discussed in §1.3.1, most of the previous research on the dynamics of spinning TSS has used simplified system models in which the out-of-plane pendular motion of the tether is neglected. A typical spinning TSS nominally spins in the orbit plane, so it is reasonable to neglect the out-of-plane motion in a preliminary study of spinning TSS dynamics; however, a complete picture of spinning TSS dynamics requires a rigorous analysis of the out-of-plane pendular motion of the system. Such an analysis is one of the main contributions of this work. A simplified system model is used to study the stability of small out-of-plane pendular motion of the tether, and to determine approximate solutions for stable out-of-plane pendular motion. These results obtained using a simplified system model are validated using numerical solutions determined using the top-level computational model.

The transverse vibrations of the tether in a spinning TSS are also studied using a simplified system model, and conditions for unstable transverse vibrations are determined. These results on the stability of spinning TSS transverse vibrations are not an original contribution, as they duplicate results obtained in Refs. [5] and [8]. The original contribution made in this work is the application of the model validation procedure to these results. We use the procedure to show that the instabilities predicted by the simplified system model are not predicted by the top-level computational model, meaning that the results obtained using

the simplified model cannot be used to make predictions about an actual spinning TSS. We also present an analysis of the reasons behind the lack of agreement with the top-level computational model, and propose ways in which the simplified system model can be changed to yield better agreement with the top-level computational model.

1.4.4 Control of Spinning Tethered Satellite Systems

In addition to the thorough analysis of the pendular motion of the tether in a spinning TSS, we also consider several methods of controlling the pendular motion. As discussed in the literature review in §1.3.1, the literature contains surprisingly few studies on control of spinning TSS, most likely because all TSS that have flown to date have been local-vertically aligned systems. The control analysis presented in this work therefore constitutes an original contribution to the field of spinning TSS dynamics and control. A simplified system model is used along with several nonlinear control design techniques to derive control laws that allow the pendular motion of the tether to track a desired planar reference motion. Two of the control laws we develop are based upon principles of sliding mode control, which allow for tracking of a reference trajectory in the presence of unmodeled dynamics (which are certainly present for a simplified system model). Several of the control laws are applied to the top-level computational model to assess their effectiveness and feasibility when applied to a more physically realistic system model.

1.5 Organization of the Dissertation

The remainder of this dissertation is organized as follows. In Ch. 2, we present some fundamental concepts of system modeling, along with the validation procedure that we propose for use on systems for which experimental data is not available. The top-level system model used in the validation procedure is presented in Ch. 3. All aspects of the top-level system model are thoroughly developed, and several examples of the output of the top-level computational model are presented. A detailed dynamic analysis of the motion of the tether in a spinning TSS is presented in Ch. 4. The analysis makes use of a lower-level system model so that a number of analytical results pertaining to both the pendular motion and elastic vibrations of the tether can be determined. All of these results are compared to numerical solutions obtained using the top-level computational model to assess their applicability to an actual TSS. In Ch. 5, various methods of controlling the pendular motion of the tether in a spinning TSS are investigated, including the possibility of controlling the pendular motion using only electrodynamic forcing. The control law developments in Ch. 5 make use of a lower-level computational model, although several of the control laws take into account the effects of unmodeled dynamics. Several of the control laws are applied to the top-level computational model to assess their performance on a more realistic system model. Concluding remarks and recommendations for future work are offered in Ch. 6.

Chapter 2

Validation of Computational Models

In this chapter we present a procedure for validating the predictions made by computational models when experimental data is not available, as in the case of a TSS. Many of the concepts and much of the terminology presented in this chapter are adapted from the material in Refs. [43] and [51]. We first present some fundamental concepts related to modeling of physical systems and model validation as motivation for the development of the procedure. The validation procedure is then outlined in detail, and we discuss how it is applied to the work related to the dynamics and control of TSS presented in the remainder of this dissertation.

2.1 Fundamental Concepts of System Modeling

The first step in the analysis of any physical system is the careful and thoughtful development of a system model. The system model is the vehicle through which an actual physical system is represented by a form that is suitable for scientific and engineering analysis. The wise and careful development of the system model can result in the gain of a great deal of insight into the behavior of the physical system, while a poor or uninformed development of a system model can lead to incorrect predictions and erroneous results.

The various aspects of any system model can be arranged in the hierarchy shown in Fig. 2.1. At the top of the hierarchy sits the actual physical system that is being considered. The physical system consists of real components and hardware operating in a real physical environment. As an example, the work presented in this dissertation is focused on the dynamics and control of spinning and electrodynamic TSS, so the physical system for any system model we consider could be MXER, or any other similar TSS. Below the physical system in the hierarchy are the three elements that make up the system model: 1) the conceptual model; 2) the mathematical model; and 3) the computational model. The objective of developing the system model is to produce accurate predictions about the behavior of the actual

physical system, as illustrated in Fig. 2.1. In the remainder of this section we discuss the role of each of the three separate elements in the system model.

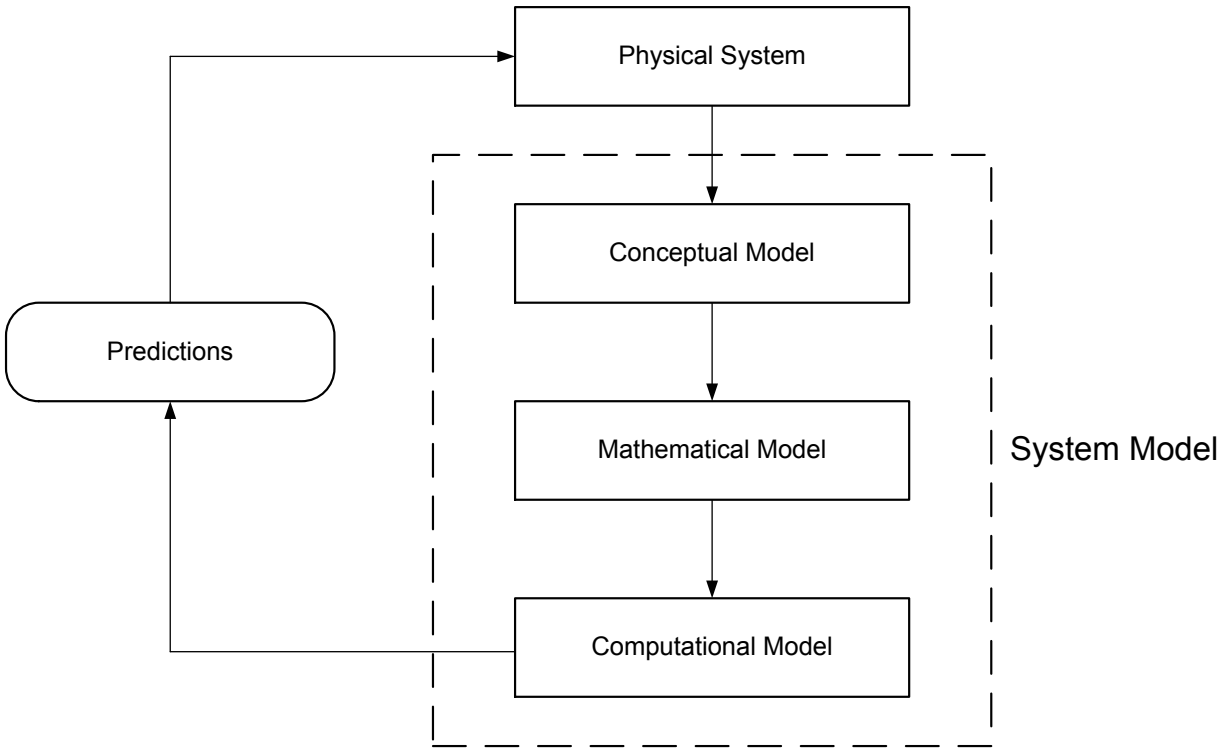

Figure 2.1: Diagram of the system modeling hierarchy

2.1.1 Conceptual Model

The conceptual model is an abstraction of the physical system that is used to study a particular behavior or behaviors of the system. Because every detail of the physical system cannot be considered in the conceptual model without it becoming prohibitively complex, the features of the physical system deemed to have a negligible influence on the behaviors of interest are not included in the conceptual model. These features can be related to the physical components of the system or the physical environment. In this sense, the conceptual model is a collection of assumptions about the physical system that removes all features that have, or are believed to have, an insignificant influence on the behaviors of interest.

The conceptual model is an idealization of the physical system that is suitable for scientific and engineering analysis. Note that there is a great deal of freedom involved in creating a conceptual model for a given physical system. The validity of various assumptions is open

to a great deal of debate, and two different "experts" can come up with two very different conceptual models that are intended to model a specific behavior for an identical physical system.

2.1.2 Mathematical Model

The mathematical model is a set of mathematical equations that govern the behavior of the conceptual model. These equations can consist of differential equations and algebraic relationships. The mathematical model includes the equations of motion for all of the degrees of freedom associated with the conceptual model, along with any required constitutive relations. It is important to note that the mathematical model gives a mathematical description of the conceptual model, not the physical system. However, the conceptual model is intended to be a sufficiently accurate approximation of the physical system, so it is also intended that the mathematical model provides a sufficiently accurate description of the physical system. The mathematical model does not include any exact or approximate solutions to the equations governing the behaviors of the system being studied, and only consists of the governing equations themselves; however, the mathematical model can include solutions to any aspects of the system motion that are constrained by the assumptions implicit in the conceptual model. For example, constraining a system to follow an unperturbed circular orbit provides a "solution" to the orbital motion that is included in the mathematical model. Any solutions to the governing equations for the behaviors of interest are contained in the computational model.

2.1.3 Computational Model

The computational model consists of all of the tools used to analyze the mathematical model, and thus make predictions about the behavior of the physical system. In this sense, the computational model is the key component of the system model, because its output is actually applied to the physical system. For system models with relatively simple mathematical models, the computational model can contain, or consist entirely of, exact or approximate analytical solutions to the governing equations. For most system models, however, the associated mathematical model is relatively complicated and does not allow for any form of analytical treatment. In this case, the computational model consists of the tools required to produce approximate numerical solutions of the governing equations. These tools include a discretized form of the governing equations along with any computer codes used to solve these discretized equations. Note that the governing equations are often partial differential equations, so a temporal and a spatial discretization scheme must be used to form the discretized equations of motion.

If the computational model contains computer codes used to produce approximate numerical solutions to the governing equations, then the accuracy of these computer codes must be rigorously verified before the numerical solutions can be used to make predictions about

the behavior of the physical system. Recall that the computer codes produce approximate numerical solutions to a discretized form of the governing equations. The verification of the computer codes involves demonstrating in some way that they produce numerical solutions that approach the true solution of the governing equations as the discretization level is refined. There are numerous different verification methods that can be applied to a computer code depending on the form of the discretized equations; however, the important point is that the accuracy of the codes must be verified before their outputs can be used to make predictions about the physical system.

One final important point to make about the computational model is that there is no guarantee that it will produce accurate predictions of the behavior of the physical system. The code verification process is purely mathematical, and only tests whether the computer codes produce accurate solutions to the governing equations contained in the mathematical model. The assessment of the accuracy and predictive capability of the computational mode is called validation. The relationship between code verification, computational model validation, and the various components of the system model is illustrated for an ideal situation in Fig. 2.2. In this ideal situation, experimental data collected on the actual physical system, or on a scale model of the actual physical system, is used to validate solutions produced by the computational model. If there is acceptable agreement between the computational solutions and the experimental data, then the model is validated and can be used to make predictions about the behavior of the physical system. If the computational solutions do not agree with the experimental data to an acceptable degree, than the model is not validated, and a new system model must be developed starting with a new conceptual model of the physical system. The results of the validation procedure can be used to determine in what ways the conceptual model must be altered to produce better agreement between the output of the computational model and the experimental data. For some physical systems, such as a TSS, experimental data is not available, and the above described situation cannot be used to validate the computational model. In the next section, we propose a procedure for validating computational models in the absence of experimental data.

2.2 Validation of Computational Models in the Absence of Experimental Data

When experimental data is not available we must resort to some other means of validating a computational model. The validation procedure proposed in this dissertation is illustrated in Fig. 2.3. In place of experimental data we define a "top-level" system model and all of its corresponding components. The solutions produced by the top-level computational model serve as the actual replacement of the experimental data. The top-level system model contains as few simplifying assumptions as possible, and is assumed to accurately capture all of the relevant behaviors of the physical system. Because of the nature of the top-level system model, its associated mathematical model will be quite complicated, and the com-

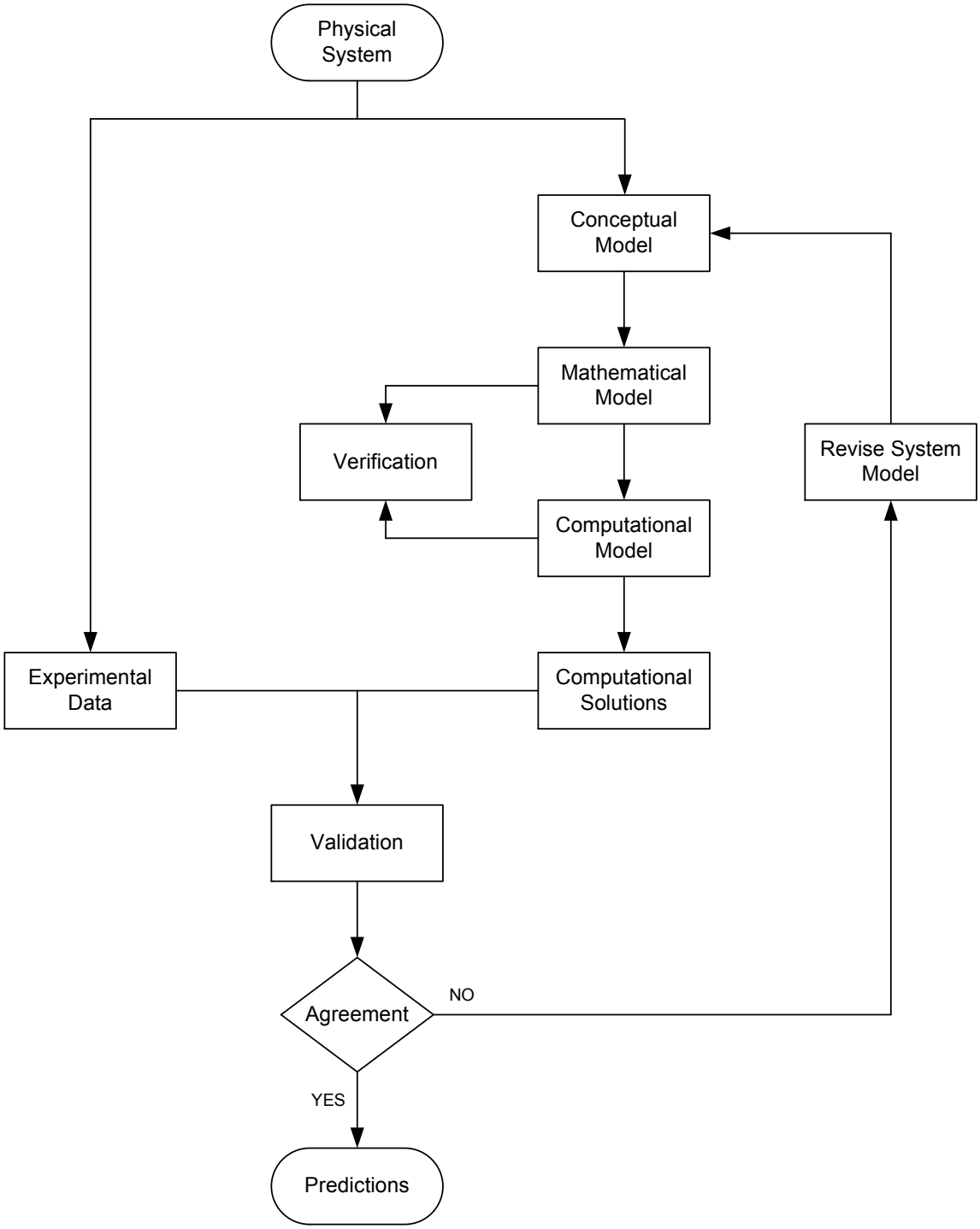

Figure 2.2: Diagram illustrating the ideal situation for computational model validation

putational model consists entirely of tools used to generate approximate numerical solutions of the mathematical model. It is important to note at this point that the top-level system model cannot be so complicated as to render the generation of numerical solutions using the computational model impractical. These numerical solutions serve as the replacement for experimental data, so it is imperative that they can be generated in a reasonable amount of time. We must also note that the computer codes used to generate the numerical solutions for the top-level computational model must be rigorously verified. Because these solutions serve as the basis for validation tests, there can be no doubt that they are accurate solutions of the top-level mathematical model.

The complicated nature of the top-level system model makes it necessary to develop other, less complicated, system models. As shown in Fig. 2.3, we call these simplified system models "lower-level" system models. Any lower-level system model can be viewed as a simplification of the top-level system model in that the lower-level model is developed using assumptions in addition to those used to develop the top-level model. Note that all of the assumptions used to develop the top-level system model must also be used to develop the lower-level system model. The primary reason for developing a lower-level system model is that the simplified nature of the lower-level model makes analysis using its computational model much easier and more practical than analysis using the top-level computational model. In fact, the lower-level computational model may contain analytical solutions that can be used to make predictions about the behavior of the physical system for the entire range of system physical parameters. In any case, being able to make predictions about the behavior of the physical system using a lower-level system model is almost always preferable to using the top-level system model due to the relative simplicity and ease of analysis using the former. Most of the previous research on TSS dynamics and control presented in §1.3 is based on the analysis of lower-level computational models.

Because they are based on simplified system models, the results obtained from any lower-level computational model may or may not be applicable to the actual physical system. In the absence of experimental data, the applicability of these results is tested by comparing them to numerical solutions generated using the top-level computational model. If the predictions made by the two computational models are in acceptable agreement, then we consider the lower-level computational model validated and its predictions can be applied to the actual physical system. If the predictions made by the two computational models are not in acceptable agreement, then the lower-level computational model is not validated. In this case, we must use the results of the validation test to alter the lower-level system model such that the predictions made by its computational model are in better agreement with those made by the top-level computational model. This process is repeated until the two models are in sufficient agreement, at which point the lower-level computational model is validated and can be used to make predictions about the actual physical system.

At this point we must stress the relative importance of the top-level system model in the validation procedure that we propose. The fundamental idea underlying the use of the top-level system model in place of experimental data is that it is a sufficiently accurate

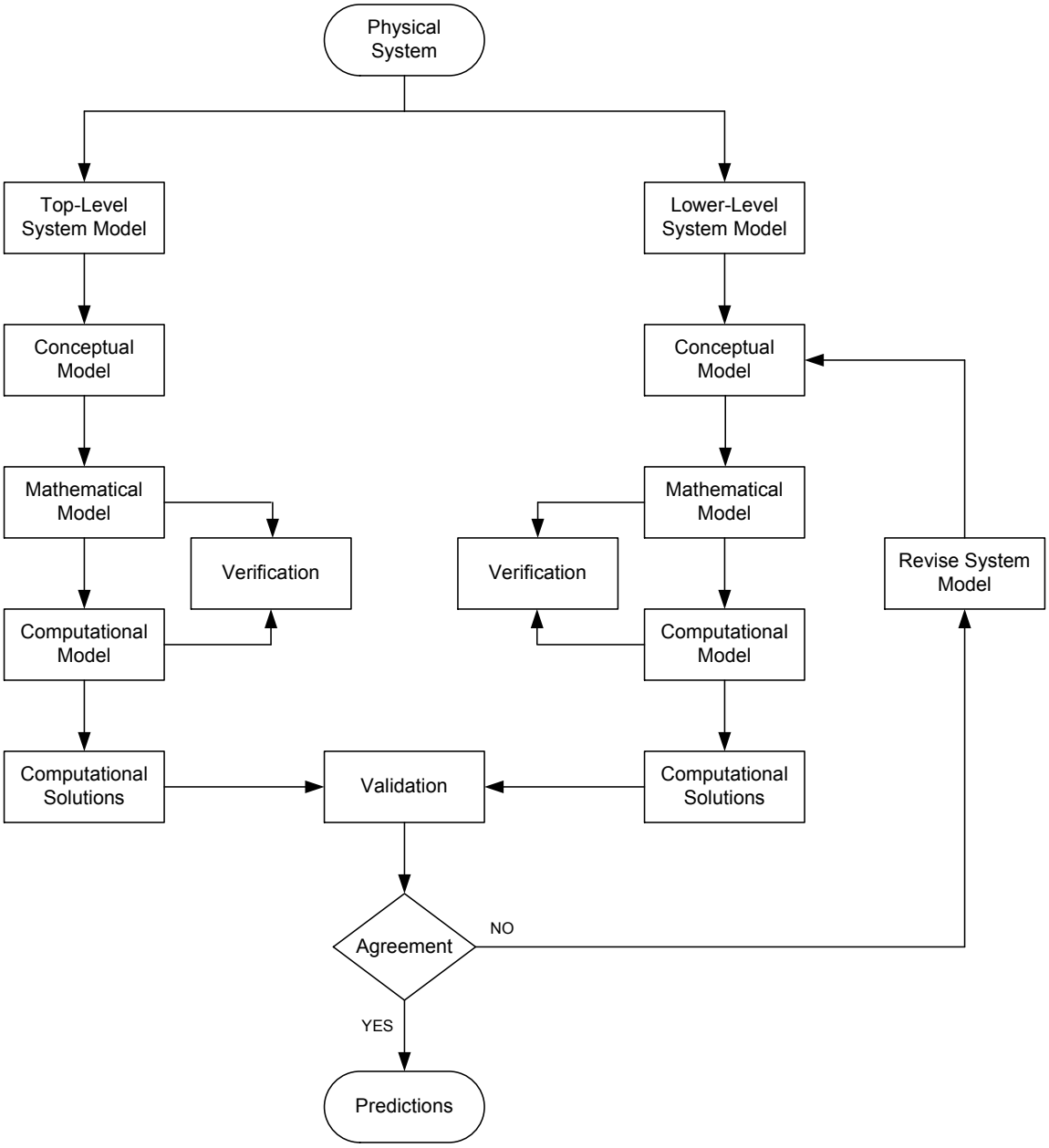

Figure 2.3: Diagram illustrating the computational model validation procedure for the case of no experimental data

representation of the actual physical system. A poor choice of the top-level system model therefore throws off the entire process, and makes any conclusions related to the validity of lower-level computational models practically meaningless. This is one of the main weaknesses of the proposed validation procedure. Another weakness of the procedure is that there is no way to test the validity of the top-level system model. Even a fairly complicated top-level model may not capture all of the relevant behaviors of the actual physical system, and there is no way to determine whether this is the case because there is no experimental data available with which to validate the top-level computational model. Despite these weaknesses, we believe that the validation procedure proposed in this chapter is the best way of performing some means of validation on results obtained from simplified system models when experimental data is unavailable.

2.3 Application of the Proposed Validation Procedure

In the remaining chapters of this dissertation, the validation procedure proposed in this chapter is applied to various problems related to TSS dynamics and control. The top-level system model and all of its components are developed in Ch. 3, in which we also verify the accuracy of the computer codes used to produce the numerical solutions for the top-level computational model. In Chs. 4 and 5, we derive a number of results related to TSS dynamics and control using lower-level system models. The validity of all of these results is examined by applying the validation procedure presented in this chapter.

Chapter 3

Top-Level System Model

In this chapter we present the various components of the top-level system model used in this work to study the dynamics and control of spinning and electrodynamic TSS. The modeling assumptions that comprise the conceptual model are presented and discussed, and the mathematical model that describes the system dynamics is derived. The mathematical model contains partial differential equations that govern the elastic vibrations of the tether, and two different computational models based on different methods of spatially discretizing these partial differential equations are developed. The first computational model is based on the assumed modes method, and the second is based on the finite element method. The method of manufactured solutions is used to verify both of the computational models, and the two models are compared to determine which is better suited to spinning and electrodynamic TSS dynamics and control applications. We conclude the chapter by presenting two examples of the output generated by the top-level computational model: 1) an example for a spinning TSS; and 2) an example for an electrodynamic TSS[1].

3.1 Physical System and Conceptual Model

The physical system under consideration is a TSS in orbit around an arbitrary central body. The system consists of two end bodies connected by a single tether. The central body has a magnetic field, and the tether is conductive and capable of producing and electrodynamic force.

Several modeling assumptions are made related to the physical environment of the system. We first assume that the central body is spherical with a homogeneous mass distribution, and therefore acts as a point mass. By making this assumption we are assuming that the Newtonian component of the gravitational field of the central body is the dominant

[1]The material presented in this chapter is also presented in Ref. [18].

component, and all of the higher-order components of the field due to the non-spherical shape and non-uniform mass distribution of the central body have a negligible influence on the system dynamics. We next assume that the magnetic field of the central body is a tilted dipole that is centered at the center of the central body and fixed to the central body as it rotates. This assumption means that we are considering any higher-order harmonics of the magnetic field of the central body to be negligible relative to its dipole component. The final environmental assumption we make is that the gravitational force of the central body and the electrodynamic force acting on the tether are the only external forces acting on the system. By making this assumption, we are assuming that all other external forces other than the gravity of the central body and the electrodynamic force, such as atmospheric drag and solar radiation pressure, have a negligible influence on the system dynamics.

The modeling assumptions related to the actual TSS are as follows. Both of the end bodies in the system are treated as finite rigid bodies, meaning that any elastic vibrations that they undergo during operation are considered negligible. Because the tether in a typical TSS is long and thin, we model the tether as an elastic string that can only resist axial stretching. This assumption implies that the tether cannon support any amount of compression, and has negligible bending and torsional stiffness.

3.2 Mathematical Model

Using the modeling assumptions outlined above we develop the mathematical model for the dynamics of the top-level system model. A diagram of the system is shown in Fig. 3.1. The end bodies are denoted $\mathcal{A}$ and $\mathcal{B}$, where $\mathcal{A}$ is the primary end body and $\mathcal{B}$ is the secondary end body. The mass centers of $\mathcal{A}$ and $\mathcal{B}$ are denoted G_A and G_B, respectively. The tether attaches to $\mathcal{A}$ at the point P_A, and attaches to $\mathcal{B}$ at the point P_B. The center of the central body is denoted O, which is taken as an inertial point.

Because $\mathcal{A}$ is the primary end body, the state of $\mathcal{A}$ is used to represent the orbital motion of the system. The state of $\mathcal{A}$ is parameterized using a set of osculating classical orbit elements

$$\mathbf{e} = \begin{pmatrix} a & e & \Omega & I & \omega & \nu \end{pmatrix}^{\mathrm{T}} \tag{3.1}$$

where a is semimajor axis, e is eccentricity, Ω is right-ascension of the ascending node (RAAN), I is inclination, ω is argument of periapsis, and ν is true anomaly. At any moment in time, $\mathbf{e}$ defines an instantaneous Keplerian orbit, known as the osculating orbit, that can be used to determine the position and velocity of G_A relative to O. Let $\vec{\mathbf{r}}_{\mathrm{A}}$ be the position of G_A relative to O. The position of P_A relative to G_A is denoted $\vec{\mathbf{p}}_{\mathrm{A}}$. Let ds be a differential tether length element located at an arclength s along the tether measured from P_A, and let $\vec{\mathbf{r}}$ be the position of ds relative to P_A. The position of P_B relative to G_B is denoted $\vec{\mathbf{p}}_{\mathrm{B}}$.

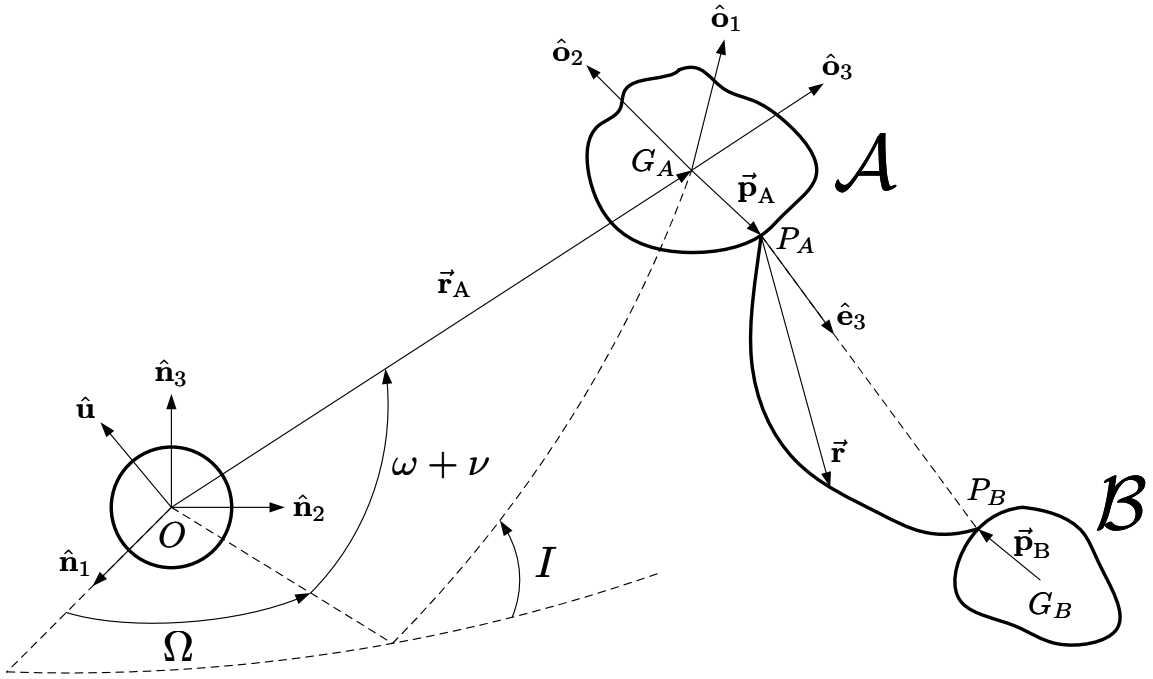

Figure 3.1: Diagram of top-level system model

3.2.1 Coordinate Frames and Kinematics

Let $\mathcal{F}_N$ be the inertial frame with coordinate axes $\hat{\mathbf{n}}_\mathrm{i}$. Note that $\mathcal{F}_N$ is centered at O, as shown in Fig. 3.1. The $\hat{\mathbf{n}}_3$ axis is aligned with the spin axis of the central body, and the $\hat{\mathbf{n}}_1 - \hat{\mathbf{n}}_2$ plane is the same as the equatorial plane of the central body. For Earth-orbiting systems, a logical choice for $\mathcal{F}_N$ would be the Earth-centered inertial frame; however, any desired inertial coordinate frame can be used for $\mathcal{F}_N$.

Let $\mathcal{F}_O$ be the orbital frame of the osculating orbit of G_A with coordinate axes $\hat{\mathbf{o}}_\mathrm{i}$. The $\hat{\mathbf{o}}_3$ axis points from O to G_A, $\hat{\mathbf{o}}_2$ is in the direction of the instantaneous angular momentum vector of the osculating orbit, and $\hat{\mathbf{o}}_1$ completes the right-handed triad. The inertial frame is transformed into the orbital frame by performing a 3-1-3 Euler rotation sequence through the angles Ω, I, and $\theta = \omega + \nu$, followed by a permutation to align the coordinate axes in the proper directions. The direction cosine matrix (DCM) that maps $\mathcal{F}_N$ to $\mathcal{F}_O$ is

$$\mathbf{R}^{\mathrm{ON}} = \begin{pmatrix} -\cos\Omega\sin\theta - \cos I\cos\theta\sin\Omega & \cos I\cos\theta\cos\Omega - \sin\theta\sin\Omega & \cos\theta\sin I \\ \sin I\sin\Omega & -\cos\Omega\sin I & \cos I \\ \cos\theta\cos\Omega - \cos I\sin\theta\sin\Omega & \cos I\cos\Omega\sin\theta + \cos\theta\sin\Omega & \sin I\sin\theta \end{pmatrix} \quad (3.2)$$

The angular velocity and acceleration of $\mathcal{F}_O$ relative to $\mathcal{F}_N$ are

$$\begin{aligned}\vec{\boldsymbol{\omega}}_{\mathrm{O/N}} &= \frac{\sqrt{\mu p}}{r_A^2}\hat{\mathbf{o}}_2 \\ &= \dot{\theta}\hat{\mathbf{o}}_2\end{aligned} \tag{3.3}$$

$$\begin{aligned}\dot{\vec{\boldsymbol{\omega}}}_{\mathrm{O/N}} &= -\frac{2\mu e \sin\nu}{r_A^3}\hat{\mathbf{o}}_2 \\ &= \ddot{\theta}\hat{\mathbf{o}}_2\end{aligned} \tag{3.4}$$

where μ is the gravitational parameter of the central body, and the quantities p and r_A are defined as

$$p = a(1-e^2) \tag{3.5}$$

$$r_A = \frac{p}{1+e\cos\nu} \tag{3.6}$$

Note that p is the orbital parameter of the osculating orbit, and r_A is the instantaneous orbit radius of G_A.

Let $\mathcal{F}_A$ be a body-fixed principal coordinate frame for $\mathcal{A}$, with coordinate axes $\hat{\mathbf{a}}_{\mathrm{i}}$. Similarly, let $\mathcal{F}_B$ be a body-fixed principal coordinate frame for $\mathcal{B}$, with coordinate axes $\hat{\mathbf{b}}_{\mathrm{i}}$. The orientations of $\mathcal{F}_A$ and $\mathcal{F}_B$ relative to $\mathcal{F}_O$ are defined using the quaternions

$$\begin{aligned}\bar{\mathbf{q}}_{\mathrm{A}} &= \begin{pmatrix} q_{A1} & q_{A2} & q_{A3} & q_{A4} \end{pmatrix}^{\mathrm{T}} \\ &= \begin{pmatrix} \mathbf{q}_{\mathrm{A}}^{\mathrm{T}} & q_{A4} \end{pmatrix}^{\mathrm{T}}\end{aligned} \tag{3.7}$$

$$\begin{aligned}\bar{\mathbf{q}}_{\mathrm{B}} &= \begin{pmatrix} q_{B1} & q_{B2} & q_{B3} & q_{B4} \end{pmatrix}^{\mathrm{T}} \\ &= \begin{pmatrix} \mathbf{q}_{\mathrm{B}}^{\mathrm{T}} & q_{B4} \end{pmatrix}^{\mathrm{T}}\end{aligned} \tag{3.8}$$

Note that a quaternion is defined as

$$\bar{\mathbf{q}} = \begin{pmatrix} \mathbf{q}^{\mathrm{T}} & q_4 \end{pmatrix}^{\mathrm{T}} \tag{3.9}$$

$$\mathbf{q} = \mathbf{a}\sin\left(\frac{\Phi}{2}\right) \tag{3.10}$$

$$q_4 = \cos\left(\frac{\Phi}{2}\right) \tag{3.11}$$

where $\mathbf{a}$ contains the components of the unit principal rotation axis and Φ is the principal rotation angle. We choose a quaternion to parameterize the orientation of both $\mathcal{F}_A$ and $\mathcal{F}_B$ relative to $\mathcal{F}_O$ because we want the mathematical model to be valid for arbitrary attitude motion of the end bodies. Because a quaternion is a nonsingular attitude parameterization, we do not have to place any bounds on the end body attitude motion to avoid the mathematical singularities associated with singular attitude parameterizations, such as Euler angles.

The DCM for a general quaternion is

$$\mathbf{R} = (q_4^2 - \mathbf{q}^{\mathrm{T}}\mathbf{q})\mathbf{1} + 2\mathbf{q}\mathbf{q}^{\mathrm{T}} - 2q_4\mathbf{q}^{\times} \tag{3.12}$$

where $\mathbf{1}$ is the identity matrix and

$$\mathbf{q}^{\times} = \begin{bmatrix} 0 & -q_3 & q_2 \\ q_3 & 0 & -q_1 \\ -q_2 & -q_1 & 0 \end{bmatrix} \tag{3.13}$$

The DCMs that map $\mathcal{F}_O$ to $\mathcal{F}_A$ and $\mathcal{F}_O$ to $\mathcal{F}_B$ are therefore

$$\mathbf{R}^{\mathrm{AO}} = (q_{A4}^2 - \mathbf{q}_{\mathrm{A}}^{\mathrm{T}}\mathbf{q}_{\mathrm{A}})\mathbf{1} + 2\mathbf{q}_{\mathrm{A}}\mathbf{q}_{\mathrm{A}}^{\mathrm{T}} - 2q_{A4}\mathbf{q}_{\mathrm{A}}^{\times} \tag{3.14}$$

$$\mathbf{R}^{\mathrm{BO}} = (q_{B4}^2 - \mathbf{q}_{\mathrm{B}}^{\mathrm{T}}\mathbf{q}_{\mathrm{B}})\mathbf{1} + 2\mathbf{q}_{\mathrm{B}}\mathbf{q}_{\mathrm{B}}^{\mathrm{T}} - 2q_{B4}\mathbf{q}_{\mathrm{B}}^{\times} \tag{3.15}$$

respectively. Let $\vec{\boldsymbol{\omega}}_{\mathrm{A/O}}$ be the angular velocity of $\mathcal{F}_A$ relative to $\mathcal{F}_O$, and let $\boldsymbol{\omega}_{\mathrm{A/O}}$ contain the components of $\vec{\boldsymbol{\omega}}_{\mathrm{A/O}}$ expressed relative to $\mathcal{F}_A$. Similarly, let $\vec{\boldsymbol{\omega}}_{\mathrm{B/O}}$ be the angular velocity of $\mathcal{F}_B$ relative to $\mathcal{F}_O$, and let $\boldsymbol{\omega}_{\mathrm{B/O}}$ contain the components of $\vec{\boldsymbol{\omega}}_{\mathrm{B/O}}$ expressed relative to $\mathcal{F}_B$. The time derivatives of $\bar{\mathbf{q}}_{\mathrm{A}}$ and $\bar{\mathbf{q}}_{\mathrm{B}}$ can then be expressed as

$$\dot{\bar{\mathbf{q}}}_{\mathrm{A}} = \frac{1}{2}\mathbf{B}(\bar{\mathbf{q}}_{\mathrm{A}})\boldsymbol{\omega}_{\mathrm{A/O}} \tag{3.16}$$

$$\dot{\bar{\mathbf{q}}}_{\mathrm{B}} = \frac{1}{2}\mathbf{B}(\bar{\mathbf{q}}_{\mathrm{B}})\boldsymbol{\omega}_{\mathrm{B/O}} \tag{3.17}$$

where

$$\mathbf{B}(\bar{\mathbf{q}}) = \begin{bmatrix} \mathbf{q}^{\times} + q_4\mathbf{1} \\ -\mathbf{q}^{\mathrm{T}} \end{bmatrix} \tag{3.18}$$

Let $\mathcal{F}_E$ be a tether-fixed coordinate frame with coordinate axes $\hat{\mathbf{e}}_i$. The orbital frame is transformed to $\mathcal{F}_E$ by performing a 2-1 Euler rotation sequence through the angles α and $-\beta$, as shown in Fig. 3.2. The DCM that maps $\mathcal{F}_O$ to $\mathcal{F}_E$ is

$$\mathbf{R}^{\mathrm{EO}} = \begin{bmatrix} \cos\alpha & 0 & -\sin\alpha \\ -\sin\alpha\sin\beta & \cos\beta & -\cos\alpha\sin\beta \\ \sin\alpha\cos\beta & \sin\beta & \cos\alpha\cos\beta \end{bmatrix} \tag{3.19}$$

and the angular velocity of $\mathcal{F}_E$ relative to $\mathcal{F}_O$ is

$$\vec{\boldsymbol{\omega}}_{\mathrm{E/O}} = \dot{\beta}\hat{\mathbf{e}}_1 + \dot{\alpha}\cos\beta\hat{\mathbf{e}}_2 + \dot{\alpha}\sin\beta\hat{\mathbf{e}}_3 \tag{3.20}$$

The axis $\hat{\mathbf{e}}_3$ points from P_A to P_B such that $\mathcal{F}_E$ defines the orientation of the undeformed tether line relative to $\mathcal{F}_O$. The angles α and β can therefore be viewed as the in- and out-of-plane attitude angles of the tether relative to $\mathcal{F}_O$. The evolution of α and β over time defines the pendular mode of the tether motion.

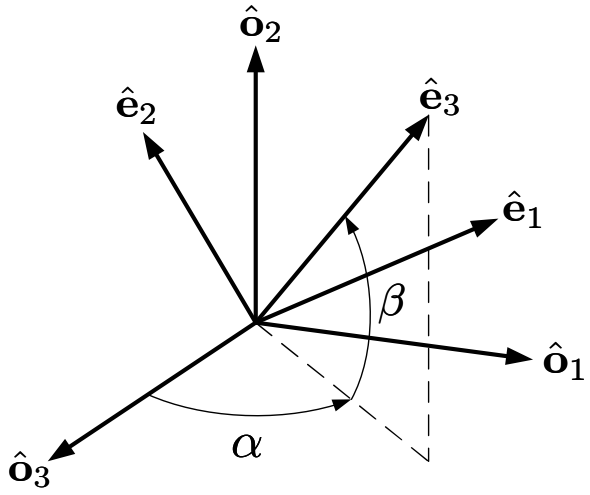

Figure 3.2: Diagram illustrating orientation of $\mathcal{F}_E$ relative to $\mathcal{F}_O$

3.2.2 Tether Geometry and Constitutive Relation

Recall that a differential tether length element, ds, is located an arclength s along the tether, measured from P_A, and the vector $\vec{\mathbf{r}}$ defines the position of ds relative to P_A. The vector $\vec{\mathbf{r}}$ is a function of both time and s, so $\vec{\mathbf{r}} = \vec{\mathbf{r}}(s,t)$. As the tether vibrates and deforms, s changes as the length of the tether expands and contracts. We would like to avoid defining $\vec{\mathbf{r}}$ using a time-varying spatial coordinate like s, so we must define a new spatial coordinate that is time-independent.

The time-independent spatial coordinate that we use is the unstretched arclength, $\bar{s}$. The relationship between s and $\bar{s}$ is illustrated in Fig. 3.3. When the tether is unstretched it lies entirely along the $\hat{\mathbf{e}}_3$ axis, and an unstretched differential length element, $d\bar{s}$, is located an unstretched arclength $\bar{s}$ from P_A. The unstretched length of the tether is L, such that $\bar{s} \in [0, L]$. When the tether stretches and deforms, it no longer lies along $\hat{\mathbf{e}}_3$, and its length deviates from L. The unstretched element $d\bar{s}$ becomes the stretched element ds, and the position of ds relative to $d\bar{s}$ is $\vec{\mathbf{u}}$. The displacement of ds from its unstretched state can be expressed as a function of $\bar{s}$, so $\vec{\mathbf{u}} = \vec{\mathbf{u}}(\bar{s},t)$, and we have

$$\vec{\mathbf{r}}(\bar{s},t) = \bar{s}\hat{\mathbf{e}}_3 + \vec{\mathbf{u}}(\bar{s},t) \tag{3.21}$$

The expression for $\vec{\mathbf{r}}$ given by Eq. (3.21) is in terms of independent spatial and temporal domains, so it is in the form we desire. The displacement vector $\vec{\mathbf{u}}$ can be conveniently expressed relative to $\mathcal{F}_E$ as

$$\vec{\mathbf{u}} = U(\bar{s},t)\hat{\mathbf{e}}_1 + V(\bar{s},t)\hat{\mathbf{e}}_2 + W(\bar{s},t)\hat{\mathbf{e}}_3 \tag{3.22}$$

where U and V are the transverse displacements of the tether, and W is the longitudinal displacement of the tether. Using Eq. (3.22), we can express $\vec{\mathbf{r}}$ relative to $\mathcal{F}_E$ as

$$\vec{\mathbf{r}}(\bar{s},t) = U\hat{\mathbf{e}}_1 + V\hat{\mathbf{e}}_2 + (\bar{s}+W)\hat{\mathbf{e}}_3 \tag{3.23}$$

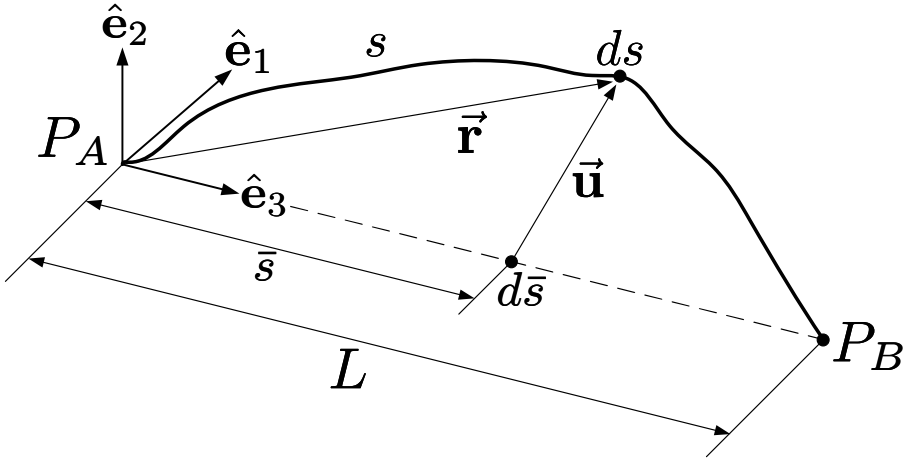

Figure 3.3: Diagram illustrating the relationship between the unstretched and stretched tether

The unit tangent vector at any point along the tether is defined as

$$\hat{\boldsymbol{\tau}}(s,t) = \frac{\partial\vec{\mathbf{r}}(s,t)}{\partial s} \tag{3.24}$$

Rewriting Eq. (3.24) as a function of $\bar{s}$, we obtain

$$\hat{\boldsymbol{\tau}}(\bar{s},t) = \frac{\partial\vec{\mathbf{r}}(\bar{s},t)}{\partial\bar{s}}\frac{\partial\bar{s}}{\partial s} \tag{3.25}$$

Because $\hat{\boldsymbol{\tau}}$ is a unit tangent vector, it must be true that

$$\frac{\partial s}{\partial\bar{s}} = \left\|\frac{\partial\vec{\mathbf{r}}(\bar{s},t)}{\partial\bar{s}}\right\| \tag{3.26}$$

The strain in the tether is defined as

$$\begin{aligned}\varepsilon &= \frac{ds - d\bar{s}}{d\bar{s}} \\ &= \frac{\partial s}{\partial\bar{s}} - 1\end{aligned} \tag{3.27}$$

Using Eq. (3.26), the strain at any point in the tether is expressed as a function of $\bar{s}$ as

$$\varepsilon(\bar{s},t) = \left\| \frac{\partial \vec{\mathbf{r}}(\bar{s},t)}{\partial \bar{s}} \right\| - 1 \tag{3.28}$$

Differentiating Eq. (3.28) with respect to time, the strain rate at any point along the tether is expressed as a function of $\bar{s}$ as

$$\dot{\varepsilon}(\bar{s},t) = \frac{1}{1+\varepsilon} \left[\frac{\partial \vec{\mathbf{r}}(\bar{s},t)}{\partial \bar{s}} \cdot \frac{\partial \dot{\vec{\mathbf{r}}}(\bar{s},t)}{\partial \bar{s}} \right] \tag{3.29}$$

The tension in the tether is modeled using the linear Kelvin-Voigt law of viscoelasticity, which expresses the axial stress in the tether, σ, in terms of the strain and strain rate as

$$\sigma = E(\varepsilon + c\dot{\varepsilon}) \tag{3.30}$$

where E is the Young's modulus of the tether material and c is a structural damping constant. Because the tether is modeled as an elastic string, the tension is only due to the axial stress, and is given by

$$T = EA(\varepsilon + c\dot{\varepsilon}) \tag{3.31}$$

where A is the cross-sectional area of the tether. Note that $T = T(\bar{s},t)$ because the strain and strain rate vary along the tether. In general, the cross sectional area may also vary along the length of the tether. Another consequence of the assumption that the tether is an elastic string is that the tension must be in the direction of the tether unit tangent vector, so the tension vector at any point in the tether is

$$\begin{aligned} \vec{\mathbf{T}} &= T\hat{\boldsymbol{\tau}} \\ &= EA(\varepsilon + c\dot{\varepsilon})\hat{\boldsymbol{\tau}} \end{aligned} \tag{3.32}$$

Using Eqs. (3.28) and (3.29) in Eq. (3.32) yields an expression for the tension vector in terms of the geometry of the tether.

One final point to note about the mathematical model of the tension in the tether is that the tension cannot be a compressive force. This fact is yet another consequence of the assumption that the tether is an elastic string. To account for this fact, we set the tension magnitude equal to zero at any point it is calculated to be negative using Eq. (3.31),

$$T = \begin{cases} EA(\varepsilon + c\dot{\varepsilon}), & \varepsilon + c\dot{\varepsilon} > 0 \\ 0, & \varepsilon + c\dot{\varepsilon} < 0 \end{cases} \tag{3.33}$$

Modeling the tension in this manner does not account for buckling of the tether at points where it becomes slack, and it also does not prevent the length of the tether from becoming less than the unstretched length L when portions of the tether become slack. However, typical TSS, and spinning TSS in particular, are expected to operate in a configuration in which the tether remains completely tensioned, so the fact that the tension model does not completely account for the effects of slackness is not a concern in this work.

3.2.3 Magnetic Field Model and Electrodynamic Force

The magnetic field of the central body is modeled as a dipole centered at O with strength μ_M and unit dipole axis $\hat{\mathbf{u}}$. The magnetic field vector at an arbitrary position $\vec{\mathbf{R}}$ relative to O is therefore

$$\vec{\mathbf{B}} = \frac{\mu_M}{R^3}\left[\hat{\mathbf{u}} - \frac{3(\hat{\mathbf{u}}\cdot\vec{\mathbf{R}})\vec{\mathbf{R}}}{R^2}\right] \tag{3.34}$$

where R is the magnitude of $\vec{\mathbf{R}}$.

We assume that the magnetic field is fixed to the central body as it rotates, with $\hat{\mathbf{u}}$ tilted relative to the spin axis of the central body, the inertial $\hat{\mathbf{n}}_3$ axis, by a constant angle Γ. The geometry of the unit dipole axis is illustrated in Fig. 3.4. The angle Θ defines the angle of rotation of the $\hat{\mathbf{u}} - \hat{\mathbf{n}}_3$ plane relative to the $\hat{\mathbf{n}}_1 - \hat{\mathbf{n}}_3$ plane, and can be viewed as the local sidereal time of the unit dipole axis. Assuming that the central body rotates at a constant angular rate ω_c, Θ can be expressed as a function of time as

$$\Theta = \Theta_0 + \omega_c t \tag{3.35}$$

where Θ_0 is the value of Θ at $t = 0$. Using Θ and Γ, we can express $\hat{\mathbf{u}}$ relative to the inertial frame as

$$\hat{\mathbf{u}} = \cos\Theta\sin\gamma\hat{\mathbf{n}}_1 + \sin\Theta\sin\gamma\hat{\mathbf{n}}_2 + \cos\Gamma\hat{\mathbf{n}}_3 \tag{3.36}$$

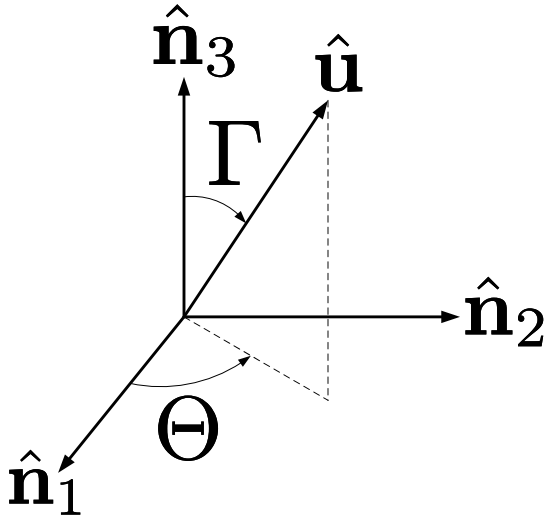

Figure 3.4: Geometry of the unit dipole axis $\hat{\mathbf{u}}$

The electrodynamic force acting on a stretched differential tether element is

$$\vec{\mathbf{F}}_{\mathrm{ED}} = i\frac{\partial\vec{\mathbf{r}}}{\partial s}ds \times \vec{\mathbf{B}} \tag{3.37}$$

where i is the electrical current in the tether. Noting that

$$\frac{\partial \vec{\mathbf{r}}}{\partial s} ds = \frac{\partial \vec{\mathbf{r}}}{\partial \bar{s}} d\bar{s} \tag{3.38}$$

we can also express the electrodynamic force in terms of the unstretched arclength as

$$\vec{\mathbf{F}}_{\mathrm{ED}} = i \frac{\partial \vec{\mathbf{r}}}{\partial \bar{s}} d\bar{s} \times \vec{\mathbf{B}} \tag{3.39}$$

In this study we are only concerned with the effects of the electrodynamic force on the system dynamics, and not with the actual physical mechanisms responsible for the generation of the electrodynamic force. We therefore assume that the current in the tether can be controlled to be any desired value. Recall that for an uncontrolled system the current in the tether is dependent on the motion of the tether through the magnetic field of the central body. Because of this dependence, the current naturally varies throughout the motion of the system. We are not concerned with these naturally occurring variations because it is always possible to include a separate power source in the system that can be used to control the current to a desired value. For this reason, we do not include a relationship such as Eq. (1.1) in the mathematical model of the electrodynamic force.

3.2.4 Equations of Motion of $\mathcal{A}$

The complete set of equations of motion for the primary end body, $\mathcal{A}$, consists of equations governing the evolution of the osculating orbit of G_A, and equations governing the rotation of the body-fixed coordinate frame $\mathcal{F}_A$ relative to $\mathcal{F}_O$. The latter set of equations govern the attitude motion of $\mathcal{A}$ relative to the orbital frame.

The orbital equations for G_A are determined by applying Newton's Second Law to $\mathcal{A}$,

$$m_A \ddot{\vec{\mathbf{r}}}_{\mathrm{A}} = \vec{\mathbf{F}}_{GA} + \vec{\mathbf{T}}(0,t) \tag{3.40}$$

where m_A is the mass of $\mathcal{A}$, $\vec{\mathbf{F}}_{GA}$ is the gravitational force of the central body acting on $\mathcal{A}$, and $\vec{\mathbf{T}}(0,t)$ is the tether tension acting on $\mathcal{A}$ at the attachment point P_A. Because the central body is treated as a point mass, the gravitational force is given by Newton's Law of Universal Gravitation as

$$\vec{\mathbf{F}}_{\mathrm{GA}} = -\frac{m_A \mu}{r_A^3} \vec{\mathbf{r}}_{\mathrm{A}} \tag{3.41}$$

Note that Eq. (3.41) also implies that $\mathcal{A}$ is a point mass, despite that fact that we have modeled $\mathcal{A}$ as a finite body. However, because $\mathcal{A}$ is small relative to its distance from O, any additional gravitational effects due to its finite dimensions are negligible relative to the Newtonian component of the gravitational force, and Eq. (3.41) is a sufficient approximation. Using Eq. (3.41) in Eq. (3.40), the orbital equation of motion for G_A is written as

$$\ddot{\vec{\mathbf{r}}}_{\mathrm{A}} = -\frac{\mu}{r_A^3} \vec{\mathbf{r}}_{\mathrm{A}} + \frac{\vec{\mathbf{T}}(0,t)}{m_A} \tag{3.42}$$

Defining the disturbance acceleration

$$\vec{\mathbf{a}}_{\mathrm{DA}} = \frac{\vec{\mathbf{T}}(0,t)}{m_A} \tag{3.43}$$

we can rewrite Eq. (3.44) in the perturbation form

$$\ddot{\vec{\mathbf{r}}}_{\mathrm{A}} + \frac{\mu}{r_A^3}\vec{\mathbf{r}}_{\mathrm{A}} = \vec{\mathbf{a}}_{\mathrm{DA}} \tag{3.44}$$

If $\vec{\mathbf{a}}_{\mathrm{DA}} = \vec{\mathbf{0}}$, then Eq. (3.44) has the form of the equation of motion of a point mass on a Keplerian orbit. Note that Eq. (3.44) approaches this case as m_A approaches infinity. When the disturbance acceleration is not zero, the disturbance acceleration causes perturbations away from a Keplerian orbit.

The effects of the disturbance acceleration on the orbit of G_A are quantified in terms of changes in the osculating orbit elements of G_A. Express the disturbance acceleration relative to $\mathcal{F}_O$ as

$$\vec{\mathbf{a}}_{\mathrm{DA}} = a_{DA1}\hat{\mathbf{o}}_1 + a_{DA2}\hat{\mathbf{o}}_2 + a_{DA3}\hat{\mathbf{o}}_3 \tag{3.45}$$

where a_{DA1}, a_{DA2}, and a_{DA3} are the disturbance acceleration components in the local horizontal, orbit normal, and local vertical directions of the osculating orbit, respectively. Using Eq. (3.45), the evolution of the osculating orbit elements under the action of the disturbance acceleration is governed by the Gauss form of the orbit variational equations,[4,55]

$$\dot{a} = \frac{2a^2}{h}\left[(e\sin\nu)a_{DA3} + \left(\frac{p}{r_A}\right)a_{DA1}\right] \tag{3.46}$$

$$\dot{e} = \frac{(p\sin\nu)a_{DA3} + [(p+r_A)\cos\nu + r_A e]a_{DA1}}{h} \tag{3.47}$$

$$\dot{I} = \frac{(r_A\cos\theta)a_{DA2}}{h} \tag{3.48}$$

$$\dot{\Omega} = \frac{(r_A\sin\theta)a_{DA2}}{h\sin I} \tag{3.49}$$

$$\dot{\omega} = \frac{-(p\cos\nu)a_{DA3} + [(p+r_A)\sin\nu]a_{DA1}}{he} - \frac{(r_A\sin\theta\cos I)a_{DA2}}{h\ I} \tag{3.50}$$

$$\dot{\nu} = \frac{h}{r_A^2} + \frac{(p\cos\nu)a_{DA3} - [(p+r_A)\sin\nu]a_{DA1}}{he} \tag{3.51}$$

where $h = \sqrt{\mu p}$ is the specific angular momentum of the osculating orbit. Equations (3.46–3.51) completely define the translational motion of G_A relative to O, and thus the orbital motion of the system. One important point we must note about Eqs. (3.46–3.51), however, is that they contain mathematical singularities for $e = 0$ and $\sin I = 0$, which correspond to circular and equatorial orbits, respectively. These singularities are due to the well-known

fact that ω is undefined for circular orbits and Ω is undefined for equatorial orbits. A non-singular set of osculating orbit elements, such as the equinoctial elements, could be used in place of the classical orbit elements, but the classical elements are sufficient for our purposes because an actual TSS is unlikely to ever be on exactly a circular or equatorial orbit.

Th rotational equations of motion of $\mathcal{A}$ are determined by applying Euler's rotational equations to $\mathcal{A}$,

$$\vec{\mathbf{I}}_{\mathrm{A}} \cdot \dot{\vec{\boldsymbol{\omega}}}_{\mathrm{A/N}} + \vec{\boldsymbol{\omega}}_{\mathrm{A/N}} \times \vec{\mathbf{I}}_{\mathrm{A}} \cdot \vec{\boldsymbol{\omega}}_{\mathrm{A/N}} = \vec{\mathbf{M}}_{\mathrm{GA}} + \vec{\mathbf{p}}_{\mathrm{A}} \times \vec{\mathbf{T}}(0,t) \tag{3.52}$$

where $\vec{\mathbf{I}}_{\mathrm{A}}$ is the centroidal moment of inertia tensor of $\mathcal{A}$, $\vec{\boldsymbol{\omega}}_{\mathrm{A/N}}$ is the angular velocity of $\mathcal{F}_A$ relative to $\mathcal{F}_N$,

$$\vec{\boldsymbol{\omega}}_{\mathrm{A/N}} = \vec{\boldsymbol{\omega}}_{\mathrm{A/O}} + \vec{\boldsymbol{\omega}}_{\mathrm{O/N}} \tag{3.53}$$

and $\vec{\mathbf{M}}_{\mathrm{GA}}$ is the gravity-gradient torque acting on $\mathcal{A}$ about G_A. Because the size of $\mathcal{A}$ is small relative to its orbit radius, we use a linear approximation for the gravity-gradient torque,[23,55]

$$\vec{\mathbf{M}}_{\mathrm{GA}} = \frac{3\mu}{r_A^5} \vec{\mathbf{r}}_{\mathrm{A}} \times \vec{\mathbf{I}}_{\mathrm{A}} \cdot \vec{\mathbf{r}}_{\mathrm{A}} \tag{3.54}$$

Using Eq. (3.54) in Eq. (3.52), the rotational equations of motion of $\mathcal{A}$ are written as

$$\vec{\mathbf{I}}_{\mathrm{A}} \cdot \dot{\vec{\boldsymbol{\omega}}}_{\mathrm{A/N}} + \vec{\boldsymbol{\omega}}_{\mathrm{A/N}} \times \vec{\mathbf{I}}_{\mathrm{A}} \cdot \vec{\boldsymbol{\omega}}_{\mathrm{A/N}} = \frac{3\mu}{r_A^5} \vec{\mathbf{r}}_{\mathrm{A}} \times \vec{\mathbf{I}}_{\mathrm{A}} \cdot \vec{\mathbf{r}}_{\mathrm{A}} + \vec{\mathbf{p}}_{\mathrm{A}} \times \vec{\mathbf{T}}(0,t) \tag{3.55}$$

When expressed relative to $\mathcal{F}_A$ and combined with the kinematic relationship defined by Eq. (3.17), the rotational equations of motion govern the evolution of the quaternion $\bar{\mathbf{q}}_{\mathrm{A}}$, and thus the orientation of $\mathcal{F}_A$ relative to $\mathcal{F}_O$. Because $\mathcal{F}_A$ is a body-fixed coordinate frame for the rigid body $\mathcal{F}_A$, the orientation of $\mathcal{F}_A$ relative to $\mathcal{F}_O$ defines the attitude of $\mathcal{A}$ relative to the orbital frame.

3.2.5 Equations of Motion of the Tether

The motion of the tether can be decomposed into two separate modes. The first mode is represented by the motion of the coordinate axis $\hat{\mathbf{e}}_3$ relative to $\mathcal{F}_O$. Recall that $\hat{\mathbf{e}}_3$ points from P_A to P_B, and the undeformed tether lies entirely along $\hat{\mathbf{e}}_3$. The motion of $\hat{\mathbf{e}}_3$ relative to $\mathcal{F}_O$ therefore defines the pendular mode of the tether motion relative to the orbital frame. The second mode of the tether motion is the elastic vibrations of the tether. These vibrations define the deformation of the tether away from its undeformed alignment with $\hat{\mathbf{e}}_3$. Each of these two separate modes of motion have a different set of governing equations of motion. The equations of motion for the pendular mode govern the evolution of the tether attitude angles α and β, and the equations of motion for the elastic vibration mode govern the evolution of the tether displacements U, V, and W.

The equations of motion for the pendular mode of the tether motion are derived by first applying Newton's Second Law to $\mathcal{B}$,

$$m_B \ddot{\vec{\mathbf{r}}}_{\mathrm{B}} = \vec{\mathbf{F}}_{\mathrm{GB}} - \vec{\mathbf{T}}(L,t) \tag{3.56}$$

where $\vec{\mathbf{r}}_{\mathrm{B}}$ is the position of G_B relative to O, m_B is the mass of $\mathcal{B}$, $\vec{\mathbf{F}}_{\mathrm{GB}}$ is the gravitational force of the central body acting on $\mathcal{B}$, and $\vec{\mathbf{T}}(L,t)$ is the tether tension acting on $\mathcal{B}$ at the attachment point P_B. As done with $\mathcal{A}$, the gravitational force acting on $\mathcal{B}$ is modeled using Newton's Law of Universal Gravitation,

$$\vec{\mathbf{F}}_{\mathrm{GB}} = -\frac{m_B \mu}{r_B^3}\vec{\mathbf{r}}_{\mathrm{B}} \tag{3.57}$$

where r_B is the magnitude of $\vec{\mathbf{r}}_{\mathrm{B}}$. Using Eq. (3.57) in Eq. (3.56), the translational equation of motion of $\mathcal{B}$ is written as

$$\ddot{\vec{\mathbf{r}}}_{\mathrm{B}} = \frac{\vec{\mathbf{F}}_{\mathrm{B}}}{m_B} \tag{3.58}$$

where $\vec{\mathbf{F}}_{\mathrm{B}}$ is the total external force vector acting on $\mathcal{B}$,

$$\vec{\mathbf{F}}_{\mathrm{B}} = -\frac{m_B \mu}{r_B^3}\vec{\mathbf{r}}_{\mathrm{B}} - \vec{\mathbf{T}}(L,t) \tag{3.59}$$

Noting that $\vec{\mathbf{r}}_{\mathrm{B}}$ can be written as

$$\vec{\mathbf{r}}_{\mathrm{B}} = \vec{\mathbf{r}}_{\mathrm{A}} + \vec{\mathbf{p}}_{\mathrm{A}} + \vec{\mathbf{r}}(L,t) - \vec{\mathbf{p}}_{\mathrm{B}} \tag{3.60}$$

Eq.(3.58) is written as

$$\ddot{\vec{\mathbf{r}}}(L,t) = \vec{\mathbf{a}}_{\mathrm{L}} \tag{3.61}$$

where we have defined the acceleration quantity

$$\vec{\mathbf{a}}_{\mathrm{L}} = \frac{\vec{\mathbf{F}}_{\mathrm{B}}}{m_B} - \ddot{\vec{\mathbf{r}}}_{\mathrm{A}} - \ddot{\vec{\mathbf{p}}}_{\mathrm{A}} + \ddot{\vec{\mathbf{p}}}_{\mathrm{B}} \tag{3.62}$$

Noting that there cannot be any transverse displacement of the tether at either of its ends, we can express $\vec{\mathbf{r}}(L,t)$ as

$$\vec{\mathbf{r}}(L,t) = [L + W(L,t)]\hat{\mathbf{e}}_3 \tag{3.63}$$

and the inertial derivative on the left-hand-side of Eq. (3.61) is written as

$$\ddot{\vec{\mathbf{r}}}(L,t) = \ddot{r}_{L1}\hat{\mathbf{e}}_1 + \ddot{r}_{L2}\hat{\mathbf{e}}_2 + \ddot{r}_{L3}\hat{\mathbf{e}}_3 \tag{3.64}$$

where

$$\ddot{r}_{L1} = 2\dot{W}(L,t)(\dot{\alpha}+\dot{\theta})\cos\beta + [L+W(L,t)][(\ddot{\alpha}+\ddot{\theta})\cos\beta - 2(\dot{\alpha}+\dot{\theta})\dot{\beta}\sin\beta] \tag{3.65}$$

$$\ddot{r}_{L2} = 2\dot{W}(L,t)\dot{\beta} + [L+W(L,t)][\ddot{\beta} + (\dot{\alpha}+\dot{\theta})^2\sin\beta\cos\beta] \tag{3.66}$$

$$\ddot{r}_{L3} = \ddot{W}(L,t) - [L+W(L,t)][(\dot{\alpha}+\dot{\theta})^2\cos^2\beta + \dot{\beta}^2] \tag{3.67}$$

Note that the quantities $\dot{\theta}$ and $\ddot{\theta}$ are defined in Eqs. (3.3) and (3.4). Expressing $\vec{\mathbf{a}}_{\mathrm{L}}$ relative to $\mathcal{F}_E$ as

$$\vec{\mathbf{a}}_{\mathrm{L}} = a_{L1}\hat{\mathbf{e}}_1 + a_{L2}\hat{\mathbf{e}}_2 + a_{L3}\hat{\mathbf{e}}_3 \tag{3.68}$$

and considering the components of Eq. (3.61) in the $\hat{\mathbf{e}}_1$ and $\hat{\mathbf{e}}_2$ directions, the equations of motion for the tether attitude angles α and β are

$$(\ddot{\alpha}+\ddot{\theta})\cos\beta - 2(\dot{\alpha}+\dot{\theta})\dot{\beta}\sin\beta = \frac{a_{L1} - 2\dot{W}(L,t)(\dot{\alpha}+\dot{\theta})\cos\beta}{L+W(L,t)} \tag{3.69}$$

$$\ddot{\beta} + (\dot{\alpha}+\dot{\theta})^2\sin\beta\cos\beta = \frac{a_{L2} - 2\dot{W}(L,t)\dot{\beta}}{L+W(L,t)} \tag{3.70}$$

Note that the pendular mode of the tether motion is affected by the elastic vibrations of the tether, as evidenced by the longitudinal displacement terms $W(L,t)$ and $\dot{W}(L,t)$ in Eqs. (3.69) and (3.70). There are also terms related to the transverse vibrations of the tether in Eqs. (3.69) and (3.70), which appear in the equations through the tension term in $\vec{\mathbf{a}}_{\mathrm{L}}$.

The equations of motion governing the elastic vibrations of the tether are derived by considering the motion of a stretched differential element of the tether. Figure 3.5 shows a free-body diagram of a stretched differential length element, ds. The forces acting on ds are the gravitational force of the central body, $\vec{\mathbf{F}}_{\mathrm{GT}}$, the electrodynamic force, $\vec{\mathbf{F}}_{\mathrm{ED}}$, and the tension at each end of the element. Applying Newton's Second Law to ds, we have

$$\rho\, ds\ddot{\vec{\mathbf{r}}}_{\mathrm{T}} = \vec{\mathbf{F}}_{\mathrm{GT}} + \vec{\mathbf{T}}(s+ds,t) - \vec{\mathbf{T}}(s,t) + \vec{\mathbf{F}}_{\mathrm{ED}} \tag{3.71}$$

where $\vec{\mathbf{r}}_{\mathrm{T}}$ is the position of ds relative to O, and ρ is the linear mass density of the tether such that the mass of the differential tether element is $\rho\, ds$. Note that ρ is time-varying because the length of the tether changes with time while the mass of the tether remains constant. As done with $\mathcal{A}$ and $\mathcal{B}$, the gravitational force of the central body acting on ds is given by Newton's Law of Universal Gravitation,

$$\vec{\mathbf{F}}_{\mathrm{GT}} = -\frac{\rho\, ds\mu}{r_T^3}\vec{\mathbf{r}}_{\mathrm{T}} \tag{3.72}$$

where r_T is the magnitude of $\vec{\mathbf{r}}_{\mathrm{T}}$. The electrodynamic force acting on ds is given by Eq. (3.37). Using these expressions for $\vec{\mathbf{F}}_{\mathrm{GT}}$ and $\vec{\mathbf{F}}_{\mathrm{ED}}$ in Eq. (3.71) and dividing both sides of the equation by $\rho\, ds$, the equation of motion of ds becomes

$$\ddot{\vec{\mathbf{r}}}_{\mathrm{T}} = -\frac{\mu}{r_T^3}\vec{\mathbf{r}}_{\mathrm{T}} + \frac{1}{\rho}\frac{\partial\vec{\mathbf{T}}}{\partial s} + \frac{i}{\rho}\frac{\partial\vec{\mathbf{r}}}{\partial s}\times\vec{\mathbf{B}} \tag{3.73}$$

where we have used the fact that

$$\frac{\partial\vec{\mathbf{T}}(s,t)}{\partial s} = \frac{\vec{\mathbf{T}}(s+ds,t) - \vec{\mathbf{T}}(s,t)}{ds} \tag{3.74}$$

Equation (3.73) is in terms of the time-varying spatial coordinate s, so we would like to transform it into a form that is in terms of the time-independent spatial coordinate $\bar{s}$. Changing

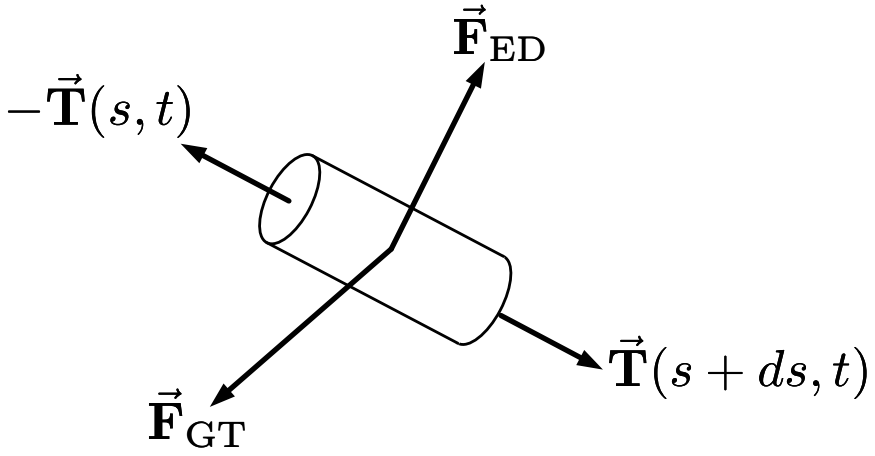

Figure 3.5: Free-body diagram of a stretched differential tether length element ds

variables to $\bar{s}$ in Eq. (3.73), we obtain

$$\ddot{\vec{\mathbf{r}}}_{\mathrm{T}} = -\frac{\mu}{r_T^3}\vec{\mathbf{r}}_{\mathrm{T}} + \frac{1}{\rho}\frac{\partial \vec{\mathbf{T}}}{\partial \bar{s}}\frac{\partial \bar{s}}{\partial s} + \frac{i}{\rho}\frac{\partial \vec{\mathbf{r}}}{\partial \bar{s}}\frac{\partial \bar{s}}{\partial s} \times \vec{\mathbf{B}} \tag{3.75}$$

Noting that a differential tether element must have the same mass in its stretched and unstretched state, it must be true that

$$\rho ds = \bar{\rho} d\bar{s} \tag{3.76}$$

where $\bar{\rho}$ is the unstretched linear mass density of the tether. From Eq. (3.76), ρ and $\bar{\rho}$ are related by

$$\bar{\rho} = \rho\frac{\partial s}{\partial \bar{s}} \tag{3.77}$$

Unlike ρ, $\bar{\rho}$ does not change as the tether deforms, making it a preferable choice as a system parameter. Using Eq. (3.77) in Eq. (3.75), the equation of motion of the tether is written as

$$\ddot{\vec{\mathbf{r}}}_{\mathrm{T}} = -\frac{\mu}{r_T^3}\vec{\mathbf{r}}_{\mathrm{T}} + \frac{1}{\bar{\rho}}\frac{\partial \vec{\mathbf{T}}}{\partial \bar{s}} + \frac{i}{\bar{\rho}}\frac{\partial \vec{\mathbf{r}}}{\partial \bar{s}} \times \vec{\mathbf{B}} \tag{3.78}$$

which is in terms of the time-independent spatial coordinate $\bar{s}$ and the constant parameter $\bar{\rho}$.

Noting that the position of the tether relative to O can be written as

$$\vec{\mathbf{r}}_{\mathrm{T}} = \vec{\mathbf{r}}_{\mathrm{A}} + \vec{\mathbf{p}}_{\mathrm{A}} + \vec{\mathbf{r}} \tag{3.79}$$

the tether equation of motion can be further rewritten as

$$\ddot{\vec{\mathbf{r}}} = -\frac{\mu}{r_T^3}\vec{\mathbf{r}}_{\mathrm{T}} + \frac{1}{\bar{\rho}}\frac{\partial \vec{\mathbf{T}}}{\partial \bar{s}} + \frac{i}{\bar{\rho}}\frac{\partial \vec{\mathbf{r}}}{\partial \bar{s}} \times \vec{\mathbf{B}} - \ddot{\vec{\mathbf{r}}}_{\mathrm{A}} - \ddot{\vec{\mathbf{p}}}_{\mathrm{A}} \tag{3.80}$$

Equation (3.80) is a partial differential equation that governs the evolution of the shape of the tether relative to P_A. The boundary condition of Eq. (3.80) at P_A is

$$\vec{\mathbf{r}}(0,t) = \vec{\mathbf{0}} \tag{3.81}$$

and the boundary condition of Eq. (3.80) at P_B is given by Eq. (3.61).

Using the expression for $\vec{\mathbf{r}}(\bar{s},t)$ given by Eq. (3.23) and expressing Eq. (3.80) relative to $\mathcal{F}_E$ yields partial differential equations for the tether vibration coordinates U, V, and W. Because there can be no transverse displacement at the ends of the tether, the boundary conditions for U and V are

$$U(0,t) = U(L,t) = 0 \tag{3.82}$$

$$V(0,t) = V(L,t) = 0 \tag{3.83}$$

From Eq. (3.81), the boundary condition of the longitudinal displacement at P_A is

$$W(0,t) = 0 \tag{3.84}$$

The boundary condition of the longitudinal displacement at P_B is determined by taking the component of Eq. (3.61) in the $\hat{\mathbf{e}}_3$ direction,

$$\ddot{W}(L,t) = a_{L3} + [L + W(L,t)][(\dot{\alpha} + \dot{\theta})^2 \cos^2\beta + \dot{\beta}^2] \tag{3.85}$$

The complete set of equations of motion of the tether is given by Eqs. (3.69), (3.70), and (3.80), combined with the boundary conditions defined in Eqs. (3.81) and (3.61). The pendular motion of the tether is governed by Eqs. (3.69) and (3.70), and the elastic vibrations are governed by Eq. (3.80). Note that the pendular and vibration modes of the tether motion are not independent, in that the elastic vibrations affect the pendular motion and visa versa.

3.2.6 Equations of Motion of $\mathcal{B}$

Given the orbital motion of G_A, the attitude motion of $\mathcal{A}$, and the motion of the tether, we can determine the motion of the tether attachment point P_B on $\mathcal{B}$. The motion of P_B defines the translational motion of $\mathcal{B}$, so we do not need to derive equations of motion for the translational motion of $\mathcal{B}$. The only equations of motion we must determine are those that govern the attitude motion of $\mathcal{B}$ relative to $\mathcal{F}_O$.

As done with $\mathcal{A}$, the attitude equations of motion of $\mathcal{B}$ are derived using Euler's rotational equations,

$$\vec{\mathbf{I}}_{\mathrm{B}} \cdot \dot{\vec{\boldsymbol{\omega}}}_{\mathrm{B/N}} + \vec{\boldsymbol{\omega}}_{\mathrm{B/N}} \times \vec{\mathbf{I}}_{\mathrm{B}} \cdot \vec{\boldsymbol{\omega}}_{\mathrm{B/N}} = \vec{\mathbf{M}}_{\mathrm{GB}} - \vec{\mathbf{p}}_{\mathrm{B}} \times \vec{\mathbf{T}}(L,t) \tag{3.86}$$

where $\vec{\mathbf{I}}_{\mathrm{B}}$ is the centroidal moment of inertia tensor of $\mathcal{B}$, $\vec{\boldsymbol{\omega}}_{\mathrm{B/N}}$ is the angular velocity of $\mathcal{F}_B$ relative to $\mathcal{F}_N$,

$$\vec{\boldsymbol{\omega}}_{\mathrm{B/N}} = \vec{\boldsymbol{\omega}}_{\mathrm{B/O}} + \vec{\boldsymbol{\omega}}_{\mathrm{O/N}} \tag{3.87}$$

and $\vec{\mathbf{M}}_{\mathrm{GB}}$ is the gravity-gradient torque acting on $\mathcal{B}$ about G_B. We once again use a linear approximation for the gravity-gradient torque,

$$\vec{\mathbf{M}}_{\mathrm{GB}} = \frac{3\mu}{r_B^5} \vec{\mathbf{r}}_{\mathrm{B}} \times \vec{\mathbf{I}}_{\mathrm{B}} \cdot \vec{\mathbf{r}}_{\mathrm{B}} \tag{3.88}$$

Using Eq. (3.88) in Eq. (3.86), the rotational equations of motion of $\mathcal{B}$ are

$$\vec{\mathbf{I}}_{\mathrm{B}} \cdot \dot{\vec{\boldsymbol{\omega}}}_{\mathrm{B/N}} + \vec{\boldsymbol{\omega}}_{\mathrm{B/N}} \times \vec{\mathbf{I}}_{\mathrm{B}} \cdot \vec{\boldsymbol{\omega}}_{\mathrm{B/N}} = \frac{3\mu}{r_B^5} \vec{\mathbf{r}}_{\mathrm{B}} \times \vec{\mathbf{I}}_{\mathrm{B}} \cdot \vec{\mathbf{r}}_{\mathrm{B}} - \vec{\mathbf{p}}_{\mathrm{B}} \times \vec{\mathbf{T}}(L,t) \tag{3.89}$$

When expressed relative to $\mathcal{F}_B$ and combined with the kinematic relationship defined by Eq. (3.17), the rotational equations of motion of $\mathcal{B}$ govern the evolution of the quaternion $\bar{\mathbf{q}}_{\mathrm{B}}$, and thus the attitude motion of $\mathcal{B}$ relative to $\mathcal{F}_O$.

3.2.7 Summary of the Mathematical Model

The mathematical model presented in this section defines the equations of motion governing the various aspects of the system dynamics. These aspects are the orbital motion of the system, the attitude motion of the end bodies, and the motion of the tether. Equations (3.46–3.51) govern the evolution of the osculating orbit elements of G_A, and thus the orbital motion of the system. The equations of motion for the attitude of $\mathcal{A}$ are given by Eq. (3.55). The pendular motion of the tether is governed by Eqs. (3.69) and (3.70), and the elastic vibrations of the tether are governed by Eq. (3.80). The boundary conditions for the tether elastic vibrations are defined by Eqs. (3.81) and (3.61). Equation (3.89) governs the attitude motion of $\mathcal{B}$.

The complete set of equations of motion that comprise the mathematical model is a mix of ordinary and partial differential equations. These equations are coupled and highly nonlinear, making a direct analytical treatment of them completely intractable. This is not unexpected, however, because the top-level model is intended to be the model that is the most complicated possible, yet still practical from a computational standpoint. Any computational model for the mathematical model must therefore consist entirely of numerical solutions of the mathematical model. In the next section, we present two such computational models.

3.3 Computational Models

The computational models for the mathematical model presented in the previous section consist entirely of the tools required to produce numerical solutions to the system equations of motion. To determine these numerical solutions, the equations of motion must be discretized and a computer program must be written to numerically solve the discretized equations of motion. Because the equations of motion governing the elastic vibrations of the tether are partial differential equations, they must be discretized in both time and space. The equations of motion governing the system orbital motion, end body attitude motion, and the pendular motion of the tether are ordinary differential equations that must only be discretized in time.

In this section, we present two different computational models based on two different methods of spatially discretizing the equations of motion for the tether elastic vibrations. The first method is the assumed modes method (AMM), and the second method is the finite element method (FEM). In both of these methods, the partial differential equations governing the tether elastic vibrations are transformed into a finite set of ordinary differential equations. This set of ordinary differential equations is then temporally discretized, and the full set of discretized equations of motion can be used to determine numerical solutions for the system motion.

3.3.1 Assumed Modes Method

The assumed modes method is one of the more common methods of spatially discretizing the partial differential equations governing the elastic vibrations of the tether. Several studies that have applied the AMM to non-electrodynamic TSS are those by Beletsky and Levin,[5] Ruiz et al.,[53] and Pradhan et al.[50] The discretization procedure presented below is similar to those used in these studies, with the exception that the electrodynamic force acting along the tether is taken into account.

To spatially discretize the tether vibration equations of motion using the AMM, we begin with Eq. (3.80) and rewrite the inertial derivative on the left-hand side of the equation as

$$\ddot{\vec{\mathbf{r}}} = \mathring{\mathring{\vec{\mathbf{r}}}} + \dot{\vec{\boldsymbol{\omega}}}_{\mathrm{E/N}} \times \vec{\mathbf{r}} + \vec{\boldsymbol{\omega}}_{\mathrm{E/N}} \times (\vec{\boldsymbol{\omega}}_{\mathrm{E/N}} \times \vec{\mathbf{r}}) + 2\vec{\boldsymbol{\omega}}_{\mathrm{E/N}} \times \mathring{\vec{\mathbf{r}}} \tag{3.90}$$

where $\mathring{(\,)}$ denotes a time-derivative as seen by $\mathcal{F}_E$. Using Eq. (3.90) in Eq. (3.80) and defining the acceleration quantity

$$\begin{aligned} \vec{\mathbf{a}}_{\mathrm{T}} = &- \frac{\mu}{r_T^3}\vec{\mathbf{r}}_{\mathrm{T}} + \frac{1}{\bar{\rho}}\frac{\partial \vec{\mathbf{T}}}{\partial \bar{s}} + \frac{i}{\bar{\rho}}\frac{\partial \vec{\mathbf{r}}}{\partial \bar{s}} \times \vec{\mathbf{B}} - \ddot{\vec{\mathbf{r}}}_{\mathrm{A}} - \ddot{\vec{\mathbf{p}}}_{\mathrm{A}} \\ &- \dot{\vec{\boldsymbol{\omega}}}_{\mathrm{E/N}} \times \vec{\mathbf{r}} - \vec{\boldsymbol{\omega}}_{\mathrm{E/N}} \times (\vec{\boldsymbol{\omega}}_{\mathrm{E/N}} \times \vec{\mathbf{r}}) - 2\vec{\boldsymbol{\omega}}_{\mathrm{E/N}} \times \mathring{\vec{\mathbf{r}}} \end{aligned} \tag{3.91}$$

the equation of motion for the tether elastic vibrations is written as

$$\mathring{\mathring{\vec{\mathbf{r}}}} = \vec{\mathbf{a}}_{\mathrm{T}} \tag{3.92}$$

From Eq. (3.23), the left-hand side of Eq. (3.92) is

$$\overset{\circ\circ}{\vec{\mathbf{r}}} = \ddot{U}\hat{\mathbf{e}}_1 + \ddot{V}\hat{\mathbf{e}}_2 + \ddot{W}\hat{\mathbf{e}}_3 \tag{3.93}$$

Expressing $\vec{\mathbf{a}}_{\mathrm{T}}$ relative to $\mathcal{F}_E$ as

$$\vec{\mathbf{a}}_{\mathrm{T}} = a_{T1}\hat{\mathbf{e}}_1 + a_{T2}\hat{\mathbf{e}}_2 + a_{T3}\hat{\mathbf{e}}_3 \tag{3.94}$$

and using Eq. (3.93) and (3.94) in Eq.(3.92), the vibration equations of motion are written in terms of the tether displacements as

$$\ddot{U} = a_{T1} \tag{3.95}$$
$$\ddot{V} = a_{T2} \tag{3.96}$$
$$\ddot{W} = a_{T3} \tag{3.97}$$

The boundary conditions of Eq. (3.95–3.97) are given by Eqs. (3.82–3.85).

Next, we assume that each tether displacement can be expressed as a finite sum of products of time-dependent generalized coordinates, $C_{ij}(t)$, and spatially-dependent assumed mode functions, $N_{ij}(\bar{s})$,

$$U(\bar{s},t) = \sum_{j=1}^{N_T} C_{1j}(t)N_{1j}(\bar{s}) \tag{3.98}$$

$$V(\bar{s},t) = \sum_{j=1}^{N_T} C_{2j}(t)N_{2j}(\bar{s}) \tag{3.99}$$

$$W(\bar{s},t) = \sum_{j=1}^{N_L} C_{3j}(t)N_{1j}(\bar{s}) \tag{3.100}$$

where N_T is the number of transverse assumed modes and N_L is the number of longitudinal assumed modes. Note that the numbers of transverse and longitudinal assumed modes can be different. The only constraints on the assumed mode functions are that they form a linearly independent, complete set, and that they satisfy the geometric boundary conditions of the tether. Recall that the geometric boundary conditions of the tether are given by Eqs. (3.82–3.84). Substituting the assumed solution forms defined by Eqs. (3.98–3.100) into Eqs. (3.95–3.97), we obtain

$$\sum_{j=1}^{N_T} \ddot{C}_{1j}N_{1j} = a_{T1} \tag{3.101}$$

$$\sum_{j=1}^{N_T} \ddot{C}_{2j}N_{2j} = a_{T2} \tag{3.102}$$

$$\sum_{j=1}^{N_L} \ddot{C}_{3j}N_{3j} = a_{T3} \tag{3.103}$$

The final step in the AMM discretization is to apply the Galerkin method[38] to Eqs. (3.101–3.103); however, we must consider the transverse and longitudinal vibrations separately because of the form of their respective boundary conditions.

For $i = 1, \ldots, N_T$, multiply Eq. (3.101) by N_{1i} and multiply Eq. (3.102) by N_{2i}, then integrate over the length of the tether to obtain

$$\sum_{j=1}^{N_T} m_{1ij}\ddot{C}_{1j} = a_{T1i} \quad , \quad i = 1, \ldots, N_T \tag{3.104}$$

$$\sum_{j=1}^{N_T} m_{2ij}\ddot{C}_{2j} = a_{T2i} \quad , \quad i = 1, \ldots, N_T \tag{3.105}$$

where we have defined

$$m_{kij} = \int_0^L N_{ki} N_{kj}\, d\bar{s} \tag{3.106}$$

$$a_{Tki} = \int_0^L a_{Tk} N_{ki}\, d\bar{s} \tag{3.107}$$

Equations (3.104) and (3.105) each define a set of N_T ordinary differential equations for the N_T generalized coordinates C_{ij}. Defining the matrices

$$\mathbf{M}_k = [m_{kij}] \tag{3.108}$$

$$\mathbf{a}_{\mathrm{T}k} = [a_{Tki}] \tag{3.109}$$

$$\mathbf{C}_k = [C_{ki}] \tag{3.110}$$

we can express each of Eqs. (3.104) and (3.105) in matrix form as

$$\mathbf{M}_k \ddot{\mathbf{C}}_k = \mathbf{a}_{\mathrm{T}k} \tag{3.111}$$

Equation (3.111) defines the spatially discretized equations of motion for the transverse vibrations of the tether. In this work, the assumed mode functions for the transverse vibrations are taken as

$$N_{ij} = \sqrt{2} \sin\left(\frac{j\pi}{L}\bar{s}\right) \tag{3.112}$$

Note that these assumed mode functions satisfy the geometric boundary conditions for the transverse vibrations defined in Eqs. (3.82) and (3.83). These functions are also orthonormal, such that the mass matrices simplify to

$$\mathbf{M}_k = \mathbf{1} \tag{3.113}$$

where $\mathbf{1}$ is the identity matrix.

Considering now the equations for the longitudinal vibrations, multiplying Eq. (3.103) by N_{3i} for $i = 1, \ldots, N_L - 1$ and integrating over the length of the tether, we obtain

$$\sum_{j=1}^{N_L} m_{3ij} \ddot{C}_{3j} = a_{T3i} \quad , \quad i = 1, \ldots, N_L - 1 \tag{3.114}$$

where m_{3ij} and a_{T3i} are defined as in Eqs. (3.106) and (3.107). We do not multiply by the assumed mode function and integrate over the tether for $i = 1, \ldots, N_L$ in this case because we want to include an equation that accounts for the dynamic boundary condition of the longitudinal vibrations, which is defined by Eq. (3.85). Using Eq. (3.100) in Eq. (3.85), we have

$$\sum_{j=1}^{N_L} \ddot{C}_{3j} N_{3j}(L) = a_{L3} + \left[L + \sum_{j=1}^{N_L} C_{3j} N_{3j}(L) \right] [(\dot{\alpha} + \dot{\theta})^2 \cos^2 \beta + \dot{\beta}^2] \tag{3.115}$$

Equations (3.114) and (3.115) define a set of N_L ordinary differential equations for the N_L generalized coordinates C_{3j}. Defining the matrices

$$\mathbf{M}_3 = \begin{bmatrix} m_{311} & \ldots & m_{31N_L} \\ \vdots & \ddots & \vdots \\ N_{31}(L) & \ldots & N_{3N_L}(L) \end{bmatrix} \tag{3.116}$$

$$\mathbf{a}_{\mathrm{T3}} = \begin{pmatrix} a_{T31} \\ \vdots \\ a_{L3} + \left[L + \sum_{j=1}^{N_L} C_{3j} N_{3j}(L) \right] [(\dot{\alpha} + \dot{\theta})^2 \cos^2 \beta + \dot{\beta}^2] \end{pmatrix} \tag{3.117}$$

and using Eq. (3.110), we can express Eqs. (3.114) and (3.115) in matrix form as

$$\mathbf{M}_3 \ddot{\mathbf{C}}_3 = \mathbf{a}_{\mathrm{T3}} \tag{3.118}$$

Equation (3.118) defines the spatially discretized equations of motion for the longitudinal vibrations of the tether. The shape functions for the longitudinal vibration are taken as

$$N_{3j}(\bar{s}) = \left(\frac{\bar{s}}{L} \right)^j \tag{3.119}$$

Note that these assumed mode functions satisfy the geometric boundary condition given by Eq. (3.84). Unlike the transverse assumed mode functions, however, the longitudinal assumed mode functions are not orthogonal. This means that the mass matrix $\mathbf{M}_3$ is fully populated, and taking its inverse in Eq. (3.118) will become increasingly computationally intensive as N_L increases.

The complete set of spatially discretized equations of motion for the tether elastic vibrations is given by Eqs. (3.111) and (3.118). Combining these equations with the equations of motion

for the system orbital motion, end body attitude motion, and pendular tether motion forms a set of ordinary differential equations for the entire motion of the system. This set of ordinary differential equations is temporally discretized and solved numerically using the built-in MATLAB function `ode15s`, which uses a variable-order method based on numerical differentiation formulas to solve stiff systems of ordinary differential equations and differential algebraic equations. Note that these numerical solutions are approximate solutions for the system equations of motion, and they should approach the solution of the equations of motion as both the temporal and spatial discretizations are refined.

3.3.2 Finite Element Method

The finite element method is a far less commonly used spatial discretization method for TSS dynamics than is the AMM. One application of the FEM to a TSS is that of Steiner et al.,[61] in which the dynamics of a system consisting of two rigid end bodies connected by a flexible, variable length tether are numerically simulated. Another study that applied the FEM to a similar problem is that by Kuhn et al.;[29] however, the system considered in this study is a simple string pendulum, and not a TSS. In what is presented below, we use a similar procedure to that used in these works to apply the FEM to a TSS that includes electrodynamic forcing.

In the FEM discretization, we begin by writing Eq. (3.80) in the weak form. Let $N_i(\bar{s})$ be a shape function defined over the length of the tether. Multiplying Eq. (3.80) by N_i and integrating over the tether, we obtain

$$\int_0^L \ddot{\vec{\mathbf{r}}} N_i d\bar{s} = \int_0^L \left(-\frac{\mu}{r_T^3}\vec{\mathbf{r}}_{\mathrm{T}} + \frac{1}{\bar{\rho}}\frac{\partial \vec{\mathbf{T}}}{\partial \bar{s}} + \frac{i}{\bar{\rho}}\frac{\partial \vec{\mathbf{r}}}{\partial \bar{s}} \times \vec{\mathbf{B}} - \ddot{\vec{\mathbf{r}}}_{\mathrm{A}} - \ddot{\vec{\mathbf{p}}}_{\mathrm{A}} \right) N_i d\bar{s} \tag{3.120}$$

Integrating the tension term in Eq. (3.120) by parts, we have

$$\int_0^L \frac{1}{\bar{\rho}}\frac{\partial \vec{\mathbf{T}}}{\partial \bar{s}} d\bar{s} = \frac{1}{\bar{\rho}} \left[\vec{\mathbf{T}}(L,t) N_i(L) - \vec{\mathbf{T}}(0,t) N_i(0) - \int_0^L \vec{\mathbf{T}} \frac{dN_i}{d\bar{s}} d\bar{s} \right] \tag{3.121}$$

From Eqs. (3.40) and (3.58), the tension at the ends of the tether can be written as

$$\vec{\mathbf{T}}(0,t) = m_A \left(\ddot{\vec{\mathbf{r}}}_{\mathrm{A}} + \frac{\mu}{r_A^3}\vec{\mathbf{r}}_{\mathrm{A}} \right) \tag{3.122}$$

$$\vec{\mathbf{T}}(L,t) = -m_B \left(\ddot{\vec{\mathbf{r}}}_{\mathrm{B}} + \frac{\mu}{r_B^3}\vec{\mathbf{r}}_{\mathrm{B}} \right) \tag{3.123}$$

Using Eqs. (3.122) and (3.123) in Eq. (3.121), and using the resulting expression in Eq. (3.120), we obtain

$$\begin{aligned} \int_0^L \ddot{\vec{\mathbf{r}}} N_i d\bar{s} = \int_0^L \left(-\frac{\mu}{r_T^3}\vec{\mathbf{r}}_{\mathrm{T}} + \frac{i}{\bar{\rho}}\frac{\partial \vec{\mathbf{r}}}{\partial \bar{s}} \times \vec{\mathbf{B}} - \ddot{\vec{\mathbf{r}}}_{\mathrm{A}} - \ddot{\vec{\mathbf{p}}}_{\mathrm{A}} \right) N_i d\bar{s} - \int_0^L \frac{1}{\bar{\rho}} \vec{\mathbf{T}} \frac{dN_i}{d\bar{s}} d\bar{s} \\ - \frac{m_A}{\bar{\rho}} \left(\ddot{\vec{\mathbf{r}}}_{\mathrm{A}} + \frac{\mu}{r_A^3}\vec{\mathbf{r}}_{\mathrm{A}} \right) N_i(0) - \frac{m_B}{\bar{\rho}} \left(\ddot{\vec{\mathbf{r}}}_{\mathrm{B}} + \frac{\mu}{r_B^3}\vec{\mathbf{r}}_{\mathrm{B}} \right) N_i(L) \end{aligned} \tag{3.124}$$

Recalling that $\vec{\mathbf{r}}_{\mathrm{T}} = \vec{\mathbf{r}}_{\mathrm{A}} + \vec{\mathbf{p}}_{\mathrm{A}} + \vec{\mathbf{r}}$ and $\vec{\mathbf{r}}_{\mathrm{B}} = \vec{\mathbf{r}}_{\mathrm{A}} + \vec{\mathbf{p}}_{\mathrm{A}} + \vec{\mathbf{r}}(L,t) - \vec{\mathbf{p}}_{\mathrm{B}}$, and defining the quantities

$$\gamma_{1i} = \int_0^L N_i d\bar{s} + \frac{m_B}{\bar{\rho}} N_i(L) + \frac{m_A}{\bar{\rho}} N_i(0) \tag{3.125}$$

$$\gamma_{2i} = \int_0^L N_i d\bar{s} + \frac{m_B}{\bar{\rho}} N_i(L) \tag{3.126}$$

$$\gamma_{3i} = \frac{m_B}{\bar{\rho}} N_i(L) \tag{3.127}$$

$$\vec{\mathbf{g}}_i = -\mu \left[\int_0^L \frac{\vec{\mathbf{r}}_{\mathrm{T}}}{r_T^3} N_i d\bar{s} + \frac{m_B}{\bar{\rho}} \frac{\vec{\mathbf{r}}_{\mathrm{B}}}{r_B^3} N_i(L) + \frac{m_A}{\bar{\rho}} \frac{\vec{\mathbf{r}}_{\mathrm{A}}}{r_A^3} N_i(0) \right] \tag{3.128}$$

$$\vec{\mathbf{f}}_i = -\frac{1}{\bar{\rho}} \int_0^L \vec{\mathbf{T}} \frac{dN_i}{d\bar{s}} d\bar{s} + \frac{i}{\bar{\rho}} \int_0^L \frac{\partial \vec{\mathbf{r}}}{\partial \bar{s}} \times \vec{\mathbf{B}} N_i d\bar{s} \tag{3.129}$$

Eq. (3.124) is rewritten as

$$\int_0^L \ddot{\vec{\mathbf{r}}} N_i d\bar{s} + \frac{m_B}{\bar{\rho}} \ddot{\vec{\mathbf{r}}}(L,t) N_i(L) = -\gamma_{1i} \ddot{\vec{\mathbf{r}}}_{\mathrm{A}} - \gamma_{2i} \ddot{\vec{\mathbf{p}}}_{\mathrm{A}} + \gamma_{3i} \ddot{\vec{\mathbf{p}}}_{\mathrm{B}} + \vec{\mathbf{g}}_i + \vec{\mathbf{f}}_i \tag{3.130}$$

Equation (3.130) is the desired weak form of the equation of motion of the tether elastic vibrations.

As done in the AMM discretization, in the FEM discretization we assume that the tether displacements can be written as finite sums of products of time-dependent generalized coordinates, $C_{ij}(t)$, and spatially-dependent shape functions, $N_j(\bar{s})$,

$$U(\bar{s},t) = \sum_{j=1}^{n} C_{1j}(t) N_j(\bar{s}) \tag{3.131}$$

$$V(\bar{s},t) = \sum_{j=1}^{n} C_{2j}(t) N_j(\bar{s}) \tag{3.132}$$

$$W(\bar{s},t) = \sum_{j=1}^{n} C_{3j}(t) N_j(\bar{s}) \tag{3.133}$$

where n is the number of assumed degrees of freedom for the tether displacements. At this point we must note that there are two fundamental differences between the AMM and FEM discretizations. First, in the FEM the assumed solution form for all three displacements use the same shape function, whereas in the AMM different functions are used for the transverse and longitudinal displacements. The second difference between the discretization methods is related to the generalized coordinates used in the assumed solution forms for the tether displacements. In the AMM, the generalized coordinates are simply coefficients in series representations of the tether displacements. In the FEM, however, physical significance is

attached to the generalized coordinates by taking them as values of displacements, slopes, or curvatures at various points along the tether. These points are called nodes, and the length of tether between two nodes is called a finite element. Because the generalized coordinates represent actual physical quantities, the shape functions in the FEM are interpolation functions for those physical quantities. This last point underscores the second fundamental difference between the AMM and FEM discretizations: the assumed solution in the AMM takes the form of a series representation, whereas the assumed solution in the FEM takes the form of an interpolation function.

Using the assumed solution forms defined by Eqs. (3.131–3.132) along with Eq. (3.90), the equations of motion for the tether elastic vibrations become

$$\begin{aligned}
&\sum_{j=1}^{n} m_{ij} \Big[\ddot{C}_{1j} - 2(\dot{C}_{2j}\sin\beta - \dot{C}_{3j}\cos\beta)(\dot{\alpha}+\dot{\theta}) - C_{1j}(\dot{\alpha}+\dot{\theta})^2 - (C_{2j}\sin\beta - C_{3j}\cos\beta)(\ddot{\alpha}+\ddot{\theta}) \\
&\qquad -2(C_{2j}\cos\beta + C_{3j}\sin\beta)(\dot{\alpha}+\dot{\theta})\dot{\beta}\sin\beta\Big] \\
&= -\gamma_{1i}\ddot{r}_{A1} - \gamma_{2i}\ddot{p}_{A1} + \gamma_{3i}\ddot{p}_{B1} - \gamma_{4i}\Big[(\ddot{\alpha}+\ddot{\theta})\sin\beta + 2(\dot{\alpha}+\dot{\theta})\dot{\beta}\cos\beta\Big] + g_{i1} + f_{i1}
\end{aligned} \tag{3.134}$$

$$\begin{aligned}
&\sum_{j=1}^{n} m_{ij} \Big[\ddot{C}_{2j} + 2\dot{C}_{1j}(\dot{\alpha}+\dot{\theta})\sin\beta + 2\dot{C}_{3j}\dot{\beta} + C_{1j}(\ddot{\alpha}+\ddot{\theta})\sin\beta + C_{1j}(\dot{\alpha}+\dot{\theta})\dot{\beta}\cos\beta \\
&\qquad -(C_{2j}\sin\beta - C_{3j}\cos\beta)(\dot{\alpha}+\dot{\theta})^2\sin\beta - C_{2j}\dot{\beta}^2 + C_{3j}\ddot{\beta}\Big] \\
&= -\gamma_{1i}\ddot{r}_{A2} - \gamma_{2i}\ddot{p}_{A2} + \gamma_{3i}\ddot{p}_{B2} - \gamma_{4i}\Big[\ddot{\beta} + (\dot{\alpha}+\dot{\theta})^2\sin\beta\cos\beta\Big] + g_{i2} + f_{i2}
\end{aligned} \tag{3.135}$$

$$\begin{aligned}
&\sum_{j=1}^{n} m_{ij} \Big[\ddot{C}_{3j} - 2\dot{C}_{1j}(\dot{\alpha}+\dot{\theta})\dot{\beta}\cos\beta - 2\dot{C}_{2j}\dot{\beta} - C_{1j}(\ddot{\alpha}+\ddot{\theta})\cos\beta - C_{2j}\ddot{\beta} \\
&\qquad -C_{2j}(\dot{\alpha}+\dot{\theta})^2\sin\beta\cos\beta - C_{3j}(\dot{\alpha}+\dot{\theta})^2\cos^2\beta - C_{3j}\dot{\beta}^2\Big] \\
&= -\gamma_{1i}\ddot{r}_{A3} - \gamma_{2i}\ddot{p}_{A3} + \gamma_{3i}\ddot{p}_{B3} - \gamma_{4i}\Big[(\dot{\alpha}+\dot{\theta})^2\cos^2\beta + \dot{\beta}^2\Big] + g_{i3} + f_{i3}
\end{aligned} \tag{3.136}$$

where we have defined the quantities

$$m_{ij} = \int_0^L N_i N_j d\bar{s} \tag{3.137}$$

$$\gamma_{4i} = \int_0^L \bar{s} N_i d\bar{s} \tag{3.138}$$

In Eqs. (3.134–3.136), the quantities $\ddot{r}_{Aj}$, $\ddot{p}_{Aj}$, $\ddot{p}_{Bj}$, g_{ij}, and f_{ij} represent the components of the vectors $\ddot{\vec{\mathbf{r}}}_{\mathrm{A}}$, $\ddot{\vec{\mathbf{p}}}_{\mathrm{A}}$, $\ddot{\vec{\mathbf{p}}}_{\mathrm{B}}$, $\vec{\mathbf{g}}_i$, and $\vec{\mathbf{f}}_i$ in the $\hat{\mathbf{e}}_j$ direction.

Equations (3.134–3.136) apply for $i = 1, \ldots, n$, so they form a set of $3n$ ordinary differential equations for the $3n$ nodal coordinates, C_{ij}. Note, however, that several of the C_{ij} are fixed

because they must satisfy the boundary conditions of the tether. At this point, Eqs. (3.134–3.136) are in a general form that applies to any choice of finite element and global shape functions. We now specialize these equations so that they apply to the particular system we are considering.

Let the tether be partitioned into N_e uniform finite elements, each with a length of

$$\ell_e = \frac{L}{N_e} \tag{3.139}$$

Each element contains two nodes, with each node located at one of the ends of the element. We want the solution for each displacement to have continuity of displacement and slope so that there are no physically unrealistic kinks in the shape of the tether. We therefore use the displacement and displacement derivative (slope) at each node as the nodal degrees of freedom. Each element therefore contains four degrees of freedom: a displacement and slope at each end of the element.

Define the element natural coordinate ξ as

$$\begin{aligned} \xi &= \frac{\bar{s} - \bar{s}_0}{\bar{s}_f - \bar{s}_0} \\ &= \frac{\bar{s} - \bar{s}_0}{\ell_e} \end{aligned} \tag{3.140}$$

where $\bar{s}_0$ and $\bar{s}_f$ are the values of $\bar{s}$ at the beginning and end of a particular element, respectively. Note that the element natural coordinate is defined in the range $\xi \in [0, 1]$. Because each element contains four degrees of freedom, we can interpolate each displacement (we consider U from here on, put what is presented applies to V and W as well) using a third-order polynomial as

$$U^e(\xi, t) = c_0 + c_1\xi + c_2\xi^2 + c_3\xi^3 \tag{3.141}$$

where c_i are constant coefficients. Note that U^e is the displacement for a particular element, and not the displacement for the entire tether. The global displacement profile is determined by piecing together all of the element displacement profiles, such as the one in Eq. (3.141). The degrees of freedom of the element serve as boundary conditions for Eq. (3.141), so the element displacement profile must satisfy

$$U^e(0, t) = c_0 \tag{3.142}$$

$$\frac{dU^e(0, t)}{d\xi} = c_1 \tag{3.143}$$

$$U^e(1, t) = c_0 + c_1 + c_2 + c_3 \tag{3.144}$$

$$\frac{dU^e(1, t)}{d\xi} = c_1 + 2c_2 + 3c_3 \tag{3.145}$$

Solving Eqs. (3.142–3.145) for the constants c_i, we obtain

$$c_0 = U^e(0,t) \tag{3.146}$$
$$c_1 = \frac{dU^e(0,t)}{d\xi} \tag{3.147}$$
$$c_2 = -3U^e(0,t) - 2\frac{dU^e(0,t)}{d\xi} + 3U^e(1,t) - \frac{dU^e(1,t)}{d\xi} \tag{3.148}$$
$$c_3 = 2U^e(0,t) + \frac{dU^e(0,t)}{d\xi} - 2U^e(1,t) + \frac{dU^e(1,t)}{d\xi} \tag{3.149}$$

Substituting Eqs. (3.146–3.149) into Eq. (3.141), the displacement over each element can be written as

$$U^e(\xi,t) = C^e_{11}(t)N^e_1(\xi) + C^e_{12}(t)N^e_2(\xi) + C^e_{13}(t)N^e_3(\xi) + C^e_{14}(t)N^e_4(\xi) \tag{3.150}$$

where we have defined the element nodal coordinates

$$C^e_{11}(t) = U^e(0,t) \tag{3.151}$$
$$C^e_{12}(t) = \frac{dU^e(0,t)}{d\xi} \tag{3.152}$$
$$C^e_{13}(t) = U^e(1,t) \tag{3.153}$$
$$C^e_{14}(t) = \frac{dU^e(1,t)}{d\xi} \tag{3.154}$$

and the element shape functions

$$N^e_1(\xi) = 1 - 3\xi^2 + 2\xi^3 \tag{3.155}$$
$$N^e_2(\xi) = \xi - 2\xi^2 + \xi^3 \tag{3.156}$$
$$N^e_3(\xi) = 3\xi^2 - 2\xi^3 \tag{3.157}$$
$$N^e_4(\xi) = -\xi^2 + \xi^3 \tag{3.158}$$

A plot of the element shape functions is shown in Fig. 3.6. Note that these functions are the cubic Hermite interpolation polynomials, which interpolate the nodal degrees of freedom for each element.

The element shape functions are locally defined for each particular finite element; however, we can use them to define the global shape functions. Because there are N_e finite elements and 2 degrees of freedom per element, there are $n = 2(N_e + 1)$ total degrees of freedom for each displacement, and there are $2(N_e + 1)$ global shape functions. From the definitions of the element nodal coordinates, a global coordinate C_{ij} is a nodal displacement for odd j, and a nodal slope for even j. Using the element shape functions, define the global shape functions as

$$N_{2j-1}(\bar{s}) = \begin{cases} 0, & 0 \le \bar{s} < (j-2)\ell_e \\ N^e_3, & (j-2)\ell_e \le \bar{s} \le (j-1)\ell_e \\ N^e_1, & (j-1)\ell_e \le \bar{s} \le j\ell_e \\ 0, & j < \bar{s} \le L \end{cases} \tag{3.159}$$

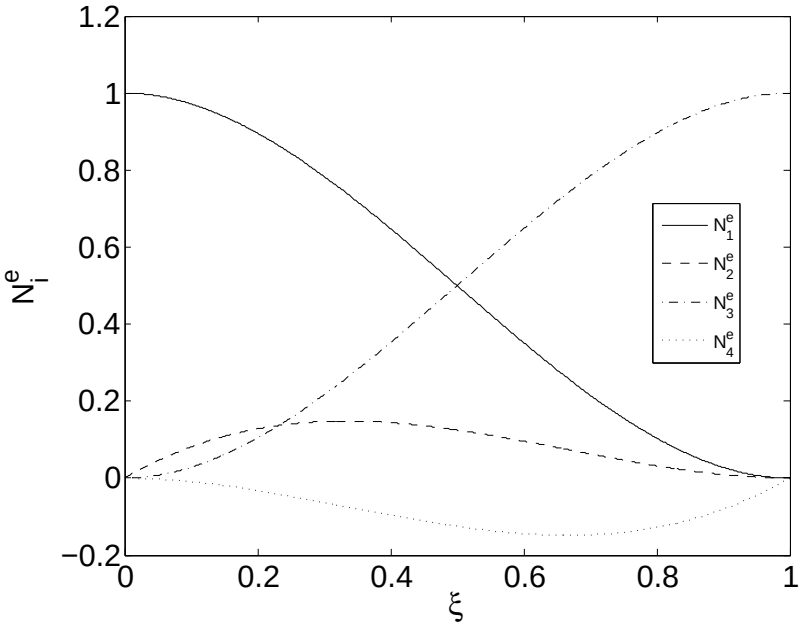

Figure 3.6: Plot of element shape functions N_i^e

$$N_{2j}(\bar{s}) = \begin{cases} 0, & 0 \le \bar{s} < (j-2)\ell_e \\ N_4^e, & (j-2)\ell_e \le \bar{s} \le (j-1)\ell_e \\ N_2^e, & (j-1)\ell_e \le \bar{s} \le j\ell_e \\ 0, & j < \bar{s} \le L \end{cases} \tag{3.160}$$

for $j = 1, \ldots, N_e + 1$. An example of the global shape functions for $N_e = 3$ and $L = 1$ is shown in Figs. 3.7 and 3.8. When used in Eqs. (3.131–3.133), the global shape functions serve to interpolate the global nodal degrees of freedom, C_{ij}. Because of the form of the global shape functions, we are actually forming the global displacement profiles using a type of cubic spline interpolation.

Using the global shape functions in Eqs. (3.134–3.136) yields the desired set of $3n$ ordinary differential equations for the nodal degrees of freedom. Using Eqs. (3.131–3.133) in Eqs. (3.82–3.85), we find that several of the nodal degrees of freedom must satisfy the relations

$$C_{11}(t) = C_{1,n-1}(t) = 0 \tag{3.161}$$

$$C_{21}(t) = C_{2,n-1}(t) = 0 \tag{3.162}$$

$$C_{31} = 0 \tag{3.163}$$

$$\ddot{C}_{3,n-1} = a_{L3} + (L + C_{3,n-1})[(\dot{\alpha} + \dot{\theta})^2 \cos^2\beta + \dot{\beta}^2] \tag{3.164}$$

for all time in order to ensure that the boundary conditions are satisfied. Enforcing Eqs. (3.161–3.164) in Eqs. (3.134–3.136) removes 6 of the equations from the set, resulting in $3(n-2)$ ordinary differential equations for the remaining unconstrained nodal degrees of freedom.

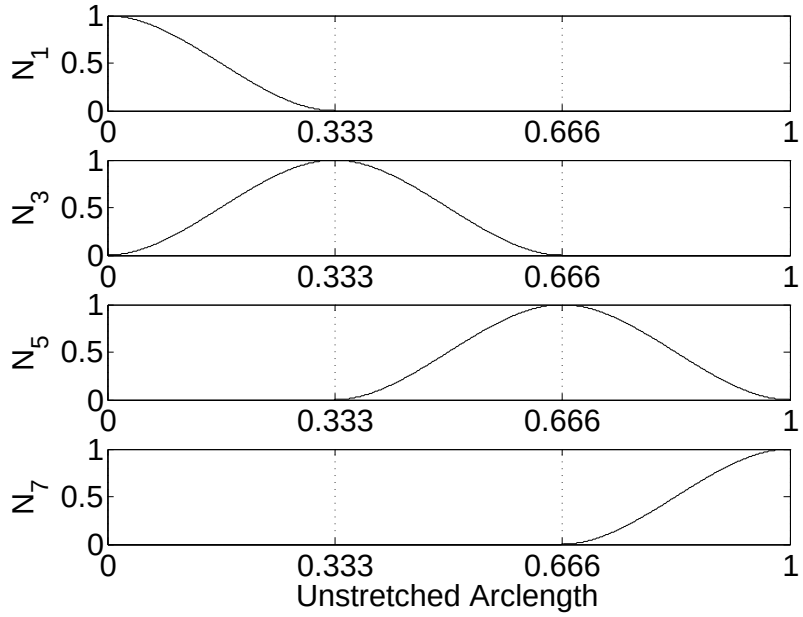

Figure 3.7: Plot of global shape functions N_j for odd j

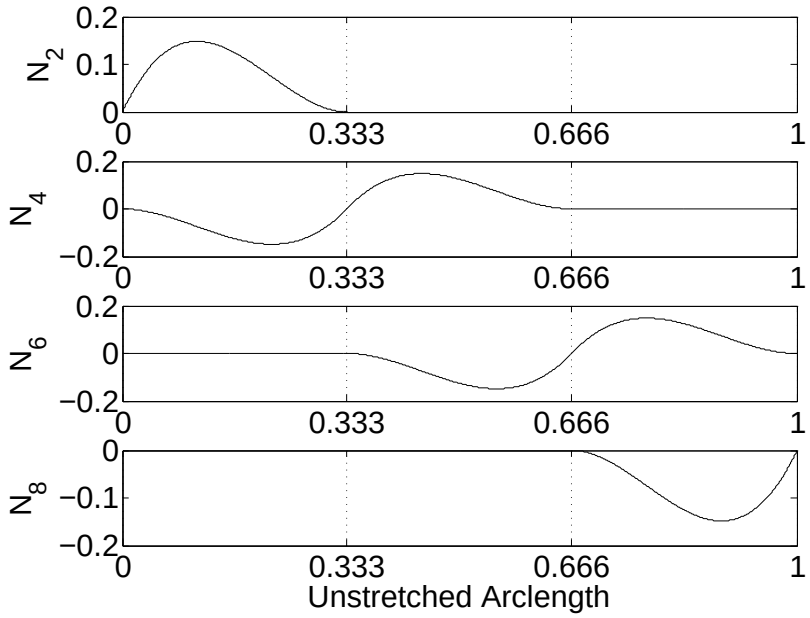

Figure 3.8: Plot of global shape functions N_j for even j

Combining Eqs. (3.134–3.136) with the equations of motion for the system orbital motion, end body attitude motion, and pendular tether motion defines the complete set of spatially discretized equations of motion for the system. As done with the computational model employing the AMM, the spatially discretized equations are temporally discretized and solved numerically using the built-in MATLAB function `ode15s`. Note that these numerical solutions are approximations of the solution of the system equations of motion that increase in accuracy as the spatial and temporal discretizations are refined.

3.4 Verification of Computational Models

The computational models employing the AMM and FEM presented in the previous section rely on discretized forms of the system equations of motion defined in the mathematical model. The discretized equations of motion are coded in MATLAB and solved numerically using the function `ode15s`. These numerical solutions can then be used to make predictions about the various aspects of the system dynamics. The coding of the discretized equations of motion is not a trivial task, however, and any number of errors can be made in the coding process. Some of these errors can be significant, and their effect is to cause the numerical solutions to display obviously incorrect behavior. Other coding mistakes can be much more subtle, and their effects can be practically undetectable in many numerical solutions. Any type of coding mistake, no matter how insignificant its effect on the numerical solution, must be identified and eliminated from the code, and we would like a method of identifying when coding mistakes are present. This process of ensuring that the code is mistake-free is known as code verification, or verification of the computational model.

One possible method of identifying coding mistakes for the TSS is to use work-energy relations to monitor the total energy of the system predicted by the numerical solution. Expressions governing the change of the total energy of the system can be derived and numerically integrated along with the discretized equations of motion for the system dynamics. The energy predicted by this numerical integration should match to a high degree of accuracy the system energy calculated in post-processing of the predicted system dynamics. This type of energy-check method of code verification was used by Pradhan[49] on a planar TSS consisting of two rigid end bodies connected by a flexible tether. The system configuration considered was conservative, so the system dynamics predicted by the computational model were expected to be energy-conserving. Several cases were considered, and the variations of the total system energy away from a constant value were found to be small.

In this work, we use a more rigorous method to verify the computational models known as the method of manufactured solutions (MMS). The MMS is more commonly used in the field of computational fluid dynamics, but it can be applied to any system with a mathematical model containing partial differential equations. One of the main advantages of the MMS over other methods of code verification is that it is extremely sensitive to coding mistakes, making it ideal for identifying even the most trivial coding errors. To the author's knowledge,

this work is the first instance of the application of the MMS to the computational model of a TSS. Two excellent resources on the MMS are the book by Roache[51] and the paper by Roy.[52] The presentation presented below is adapted from these two sources.

3.4.1 The Method of Manufactured Solutions

For most physical systems like the TSS considered in this work, the mathematical model used to model the behavior of the system does not admit an analytical solution. Because there is no such analytical solution, there is nothing to compare the numerical solutions of the computational model against to verify the computational model. In fact, there would be no need for numerical solutions if an analytical solution existed for the mathematical model. The MMS provides a means of verifying computational models in the above described situation by considering a modified mathematical model for which an analytical solution is known.

To demonstrate the fundamental principles of the MSS we consider an illustrative example. This example is relatively simple, but the basic ideas presented below are applicable to much more complicated equations and sets of equations. Let $u = u(x,t)$ be some quantity of interest defined on the spatial and temporal domains $x \in [0,1]$ and $t \in [0,\infty)$, and let the governing equation for u be

$$\frac{\partial u}{\partial t} = u^2 \frac{\partial u}{\partial x} \tag{3.165}$$

Now, introduce an arbitrary term f into the right-hand side of Eq. (3.165) to obtain the modified governing equation

$$\frac{\partial u}{\partial t} = u^2 \frac{\partial u}{\partial x} + f \tag{3.166}$$

At this point it may seem like the addition of f into the governing equation has merely complicated the situation, but we must remember that f is an arbitrary term that we can choose to be whatever we like. We can therefore choose f such that the exact analytical solution to Eq. (3.166) is any function we desire. In this manner, we choose f to manufacture a solution to the modified governing equation.

For the simple problem that we are considering, let the manufactured solution be

$$u^*(x,t) = \cos(t)\sin(\pi x) \tag{3.167}$$

where we use a superscript "*" to indicate a manufactured solution. Note that the manufactured solution does not have to be physically meaningful or realistic in any way. It is often advantageous to choose an unrealistic manufactured solution that contains lower frequency content than the actual solution, because much coarser spatial and temporal discretizations can be used to produce accurate numerical solutions to the modified governing equation (which are needed later on in the method). The only constraints on the manufactured solution are that it should be smooth with smooth derivatives. Because of these constraints,

trigonometric and exponential functions are generally the best choices for manufactured solutions. Substituting Eq. (3.167) into Eq. (3.166), we can solve for f as

$$f = -\sin(t)\sin(\pi x) - \pi\cos^3(t)\sin(\pi x)\cos(\pi x) \tag{3.168}$$

which is the value of f required to manufacture the desired exact solution. Using Eq. (3.168) in Eq. (3.166) yields an equation with the exact solution given by Eq. (3.167).

The boundary conditions of the governing equation can be dealt with in one of three ways in the MMS. The first method of dealing with the boundary conditions is to enforce that the boundary conditions behave according to the desired manufactured solution. For the example we are considering, this means that we use Eq. (3.167) to define conditions at the boundaries, so we could set

$$u(0,t) = u(1,t) = 0 \tag{3.169}$$

Note that we can also use the manufactured solution to set values of derivatives of u at the boundaries. The only requirement is that the boundary conditions behave according to the manufactured solution.

The second method of dealing with boundary conditions in the MMS is to include additional terms in the original boundary conditions that force them to agree with the manufactured solution. For the example we are considering, suppose that the boundary conditions of Eq. (3.165) are

$$u(0,t) = 1 \tag{3.170}$$

$$\frac{\partial u(1,t)}{\partial x} = \sin(t) \tag{3.171}$$

Adding the terms f_0 and f_1 into these boundary conditions, we create a modified set of boundary condition to go along with the modified governing equation,

$$u(0,t) = 1 + f_0 \tag{3.172}$$

$$\frac{\partial u(1,t)}{\partial x} = \sin(t) + f_1 \tag{3.173}$$

If the desired manufactured solution is given by Eq. (3.167), then f_0 and f_1 are chosen as

$$f_0 = -1 \tag{3.174}$$

$$f_1 = \pi\cos(t) - \sin(t) \tag{3.175}$$

These choices of f_0 and f_1 guarantee that the boundary conditions agree with the manufactured solution for all time.

The third method of dealing with boundary conditions in the MMS is to simply select the manufactured solution such that it agrees with the actual physical boundary conditions for all time. In many cases, however, this method is impractical due to the complicated nature

of the actual boundary conditions. It may be trivial to form a manufactured solution that conforms to relatively simple geometric boundary conditions, but it can be quite difficult to find a manufactured solution that fits to other types of boundary conditions, such as dynamic conditions. For this reason, the first two methods discussed above are almost always used in practice in place of this third method.

Another point that must be noted is that the manufactured solution defines the required initial conditions of the modified governing equation. For the example we are considering, from Eq. (3.167) the initial profile for u must be

$$u(x, 0) = \sin(\pi x) \tag{3.176}$$

This basic principle also applies to systems containing higher-order time derivatives, in that the manufactured solution must be used to determine any initial velocity or acceleration profiles that are required to solve the modified equation and boundary conditions.

Once the modified governing equation is formed and a method of handling the boundary conditions is selected, the modified equation and boundary conditions are discretized using the method used for the original governing equation and boundary conditions. Numerical solutions are computed using increasing levels of discretization refinement, and the numerical solutions are compared to the manufactured solution. Because the manufactured solution is the exact solution to the modified equation and boundary conditions, the numerical solutions should converge to the manufactured solution as the discretization is refined. For some discretization methods, such as the FEM, we also know the rate at which the numerical solutions should converge to the manufactured solution.

If the numerical solutions of the modified equation and boundary conditions do not converge to the manufactured solution as expected, then there must be mistakes in the code used to solve the discretized equations. These mistakes can then be identified and eliminated from the code, and new numerical solutions to the modified equation and boundary conditions can be determined. Once the numerical solutions converge to the manufactured solution as expected, the code used to solve the modified equation has been verified, and the terms introduced to form the modified equation and boundary conditions can simply be removed from the code. The end result of this process is a code that solves the discretized form of the original governing equation and boundary conditions that is free of any coding mistakes that result in solution errors. The numerical solutions will therefore converge to the actual solution of the original governing equation and boundary conditions as the discretization is refined.

In the remainder of this section the MMS is applied to the computational models for the TSS employing both the AMM and FEM spatial discretizations. The equations of motion for the

tether are modified by introducing a term $\vec{\mathbf{f}}_{\mathrm{T}}$ into Eq. (3.80), and a term $\vec{\mathbf{f}}_{\mathrm{L}}$ into Eq. (3.58),

$$\ddot{\vec{\mathbf{r}}} = -\frac{\mu}{r_T^3}\vec{\mathbf{r}}_{\mathrm{T}} + \frac{1}{\bar{\rho}}\frac{\partial \vec{\mathbf{T}}}{\partial \bar{s}} + \frac{i}{\bar{\rho}}\frac{\partial \vec{\mathbf{r}}}{\partial \bar{s}} \times \vec{\mathbf{B}} - \ddot{\vec{\mathbf{r}}}_{\mathrm{A}} - \ddot{\vec{\boldsymbol{\rho}}}_{\mathrm{A}} + \vec{\mathbf{f}}_{\mathrm{T}} \tag{3.177}$$

$$m_B \ddot{\vec{\mathbf{r}}}_{\mathrm{B}} = \vec{\mathbf{F}}_{\mathrm{B}} + \vec{\mathbf{f}}_{\mathrm{L}} \tag{3.178}$$

The term $\vec{\mathbf{f}}_{\mathrm{T}}$ serves to modify the equations governing the tether elastic vibrations, and the term $\vec{\mathbf{f}}_{\mathrm{L}}$ serves to modify the boundary conditions of the tether elastic vibrations and the equations governing the pendular motion of the tether. Equations (3.177) and (3.178) apply to both the AMM and FEM discretizations; however, there are some differences in the manner in which the MMS is applied to the computational models employing the two methods. For this reason, we consider the FEM and AMM computational models separately, and highlight the differences in the application of the MMS to the two computational models as we procede.

3.4.2 Finite Element Method

The first step in applying the MMS to the FEM computational model is to spatially discretize Eqs. (3.177) and (3.178) using the procedure detailed in §3.3.2. Writing Eqs. (3.177) and (3.178) in the weak form, we obtain

$$\int_0^L \ddot{\vec{\mathbf{r}}} N_i d\bar{s} + \frac{m_B}{\bar{\rho}} \ddot{\vec{\mathbf{r}}}(L,t) N_i(L) = -\gamma_{1i} \ddot{\vec{\mathbf{r}}}_{\mathrm{A}} - \gamma_{2i} \ddot{\vec{\boldsymbol{\rho}}}_{\mathrm{A}} + \gamma_{3i} \ddot{\vec{\boldsymbol{\rho}}}_{\mathrm{B}} + \vec{\mathbf{g}}_i + \vec{\mathbf{f}}_i + \vec{\mathbf{h}}_i \tag{3.179}$$

where we have defined the term

$$\vec{\mathbf{h}}_i = \int_0^L \vec{\mathbf{f}}_{\mathrm{T}} N_i d\bar{s} + \frac{1}{\bar{\rho}} \vec{\mathbf{f}}_{\mathrm{L}} N_i(L) \tag{3.180}$$

Note that $\vec{\mathbf{h}}_i$ contains the terms that serve to modify the original governing equations and boundary conditions. Using Eq. (3.179) and proceeding as outlined in §3.3.2, we obtain a spatially discretized set of ordinary differential equations for the modified governing equations. These equations are once again temporally discretized and solved numerically using the MATLAB function `ode15s`.

Let F represent the exact solution to the modified equations and f represent the numerical solution determined for a certain level of discretization refinement. The solutions F and f correspond to one of the tether displacements U, V, or W. Note that F is known because we have "manufactured" an exact solution to the modified equations and boundary conditions. For the FEM, the discretization error of the numerical solution is calculated using the discrete l^2-norm,

$$\epsilon = \sqrt{\frac{1}{N}\sum_{j=1}^{N}(f_j - F_j)^2} \tag{3.181}$$

where the summation is over all points in space and time in the solution domain, and a subscript j indicates a value evaluated at the j^{th} point in the solution domain. As the discretization is refined, the discretization error should approach zero as the numerical solution approaches the manufactured solution. The discretization error can be expressed as

$$\epsilon = C_{\Delta h}\Delta h^P + C_{\Delta t}\Delta t^Q + \text{H.O.T} \tag{3.182}$$

where Δh is a measure of the spatial discretization, Δt is a measure of the temporal discretization, $C_{\Delta h}$ and $C_{\Delta t}$ are constants, and H.O.T represents higher-order terms in Δh and Δt. The terms P and Q are the formal orders of accuracy of the spatial and temporal discretizations, and define the rate at which the numerical solution approaches the manufactured solution. For the FEM, Δh is proportional to $1/N_e$, and Δt is proportional to the average time step used in the temporal discretization. If the numerical solution is in the asymptotic solution range (meaning that it is sufficiently close to the manufactured solution), then the higher-order terms are negligible, and the discretization error becomes

$$\epsilon = C_{\Delta h}\Delta h^P + C_{\Delta t}\Delta t^Q \tag{3.183}$$

Further, if we know that the error due to the temporal discretization is insignificant relative to the spatial discretization error, then we can simply write the discretization error as

$$\epsilon = C_{\Delta h}\Delta h^P \tag{3.184}$$

The temporal discretization error will be negligible for situations in which highly-accurate time integrators are used with tight integration tolerances. This is the case for most of the built-in MATLAB ODE solvers, including `ode15s`, which use variable-length time steps and allow for very tight tolerances to minimize temporal discretization error. Given two numerical solutions with discretization errors ϵ_1 and ϵ_2, an observed order of accuracy can be calculated using Eq. (3.184) as

$$P = \frac{\ln(\epsilon_1/\epsilon_2)}{\ln(r)} \tag{3.185}$$

where the refinement factor $r = N_{e2}/N_{e1}$ provides a measure of the relative level of refinement between the two numerical solutions. If the FEM discretization computer code accurately solves the discretized equations of motion, then P determined from Eq. (3.185) will converge to the formal order of accuracy of the method as the number of finite elements in increased. The FEM discretization used in this work employs cubic shape functions, so the formal order of accuracy of the method is 4.[1] As the number of finite elements is increased, the observed order of accuracy determined using Eq. (3.185) should therefore approach 4 if there are no mistakes in the code.

The manufactured solution used for the FEM in this work is

$$U^*(\bar{s},t) = 50\sin(2t)\sin\left(\frac{\pi}{L}\right) \tag{3.186}$$

$$V^*(\bar{s},t) = 25\sin(t)\sin\left(\frac{\pi}{L}\right) \tag{3.187}$$

$$W^*(\bar{s},t) = 10\cos(t)\left(\frac{\bar{s}}{L}\right)^3 \tag{3.188}$$

$$\alpha^*(\bar{s},t) = \frac{2\pi}{180}\cos\left(\frac{\sqrt{\mu p}}{r_A^2}t\right) \tag{3.189}$$

$$\beta^*(\bar{s},t) = \frac{\pi}{180}\cos\left(2\frac{\sqrt{\mu p}}{r_A^2}t\right) \tag{3.190}$$

where r_A and p are the instantaneous values of the orbit radius of G_A and the orbital parameter of the osculating orbit of G_A, respectively. Note that the initial conditions of all numerical solutions of the modified equations are determined using Eqs. (3.186–3.190). It is vital that the initial conditions are determined using these equations, because if they are not then the numerical solutions will not approach the manufactured solution as the discretization is refined, even if there are no coding mistakes. The MMS terms $\vec{\mathbf{f}}_{\mathrm{T}}$ and $\vec{\mathbf{f}}_{\mathrm{L}}$ are calculated numerically, and the integral terms containing $\vec{\mathbf{g}}_{\mathrm{i}}$, $\vec{\mathbf{f}}_{\mathrm{i}}$, $\vec{\mathbf{f}}_{\mathrm{T}}$, and $\vec{\mathbf{f}}_{\mathrm{L}}$ are evaluated numerically using Simpson's Rule with 101 evaluation points per finite element. This number of points was determined to be sufficient to render the error due to the numerical integration using Simpson's rule negligible relative to the discretization error. The absolute and relative time integration tolerances used by `ode15s` are both set to 10^{-12} for all numerical solutions. These tight tolerances ensure that round-off errors and iterative convergence errors that accumulate during numerical integration do not have a significant impact on the discretization error, and thus the observed order of accuracy. The system parameters used to determine all of the numerical solutions are listed in Table 3.1, and all numerical solutions are determined over the time interval $t \in [0, 2\pi]$ s. The time span of 2π s may seem like a short simulation time for a TSS, but the periods of the manufactured tether displacements are all on the order of 2π s. Thus, while the integration time would be short for a simulation of the actual motion of a TSS, it is sufficient to determine discretization errors and observed orders of accuracy for the manufactured solution used in this study. Simulations are performed using 2 to 32 finite elements with a refinement factor of $r = 2$.

Figures 3.9 and 3.10 show the discretization errors and observed orders of accuracy for the tether displacements calculated from the numerical solutions. Numerical values are listed in Table 3.2. The discretization errors for each displacement decrease at roughly equal rates as the number of finite elements is increased, indicating that they all have the same order of accuracy. The observed orders of accuracy confirm this observation, as the orders of accuracy converge to a value of 4 for all three displacements. As mentioned previously, because the FEM discretization we have used employs cubic shape functions, it has a formal order of accuracy of 4. Thus, the observed order of accuracy of the numerical solutions matches the formal order of accuracy, and we can be confident that there are no coding

Table 3.1: System parameters used to determine numerical solutions for the MMS applied to the FEM

System Parameter	
Unstretched Length L, m	20,000
Unstretched Linear Mass Density $\bar{\rho}$, kg/m	0.0025
Longitudinal Stiffness EA, N	54,978
Structural Damping Constant c, s	0.06
$\mathcal{A}$ Mass m_A, kg	500
$\mathcal{B}$ Mass m_B, kg	50
$\mathcal{A}$ Inertias $\boldsymbol{I}_A$, kg-m^2	diag[300 400 200]
$\mathcal{B}$ Inertias $\boldsymbol{I}_B$, kg-m^2	diag[30 40 20]
$\mathcal{A}$ Attachment Vector $\mathbf{p}_A$, m	[0 0 1]
$\mathcal{B}$ Attachment Vector $\mathbf{p}_B$, m	[0 0 -0.1]
Current i, A	1

mistakes in the code used to solve the modified FEM discretized equations of motion. The terms introduced to create the modified equations and boundary conditions can simply be removed from this code, resulting in an error-free code that generates numerical solutions of the original equations. The accuracy of these numerical solutions increases as the number of finite elements used in the spatial discretization is increased.

3.4.3 Assumed Modes Method

The first step in applying the MMS to the AMM computational model is to spatially discretize Eqs. (3.177) and (3.178) using the procedure detailed in §3.3.1. Doing so results in a set of modified spatially discretized equations for the motion of the tether, which are temporally discretized and solved numerically using the MATLAB function `ode15s`. Note that the integral terms on the right-hand sides of the discretized equations of motion, defined by Eq. (3.107) are evaluated numerically when determining the numerical solutions.

A different approach to determining the accuracy of the numerical solutions of the modified equations is used for the AMM computational model than was used for the FEM computational model. With the FEM, we were able to perform an element refinement study and determine observed orders of accuracy. These orders of accuracy converged to the formal order of accuracy of the FEM discretization as the number of finite elements was increased, thus verifying that the computer code implementing the FEM discretization is mistake-free. With the AMM, we take advantage of the structure of the assumed solution form for the tether displacements to create a scenario in which the solution to the discretized equations of motion is *exactly* the manufactured solution. The numerical solution should then match the

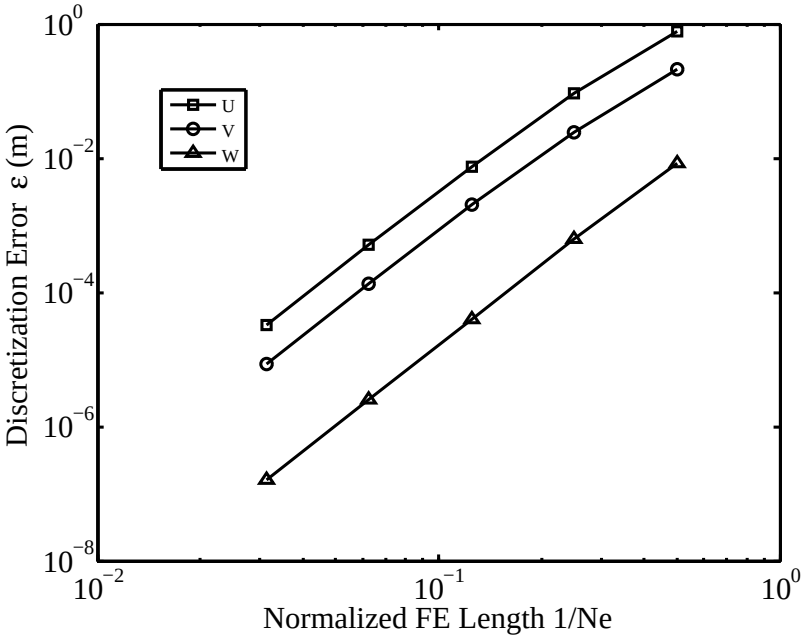

Figure 3.9: Discretization error as a function of normalized finite element length

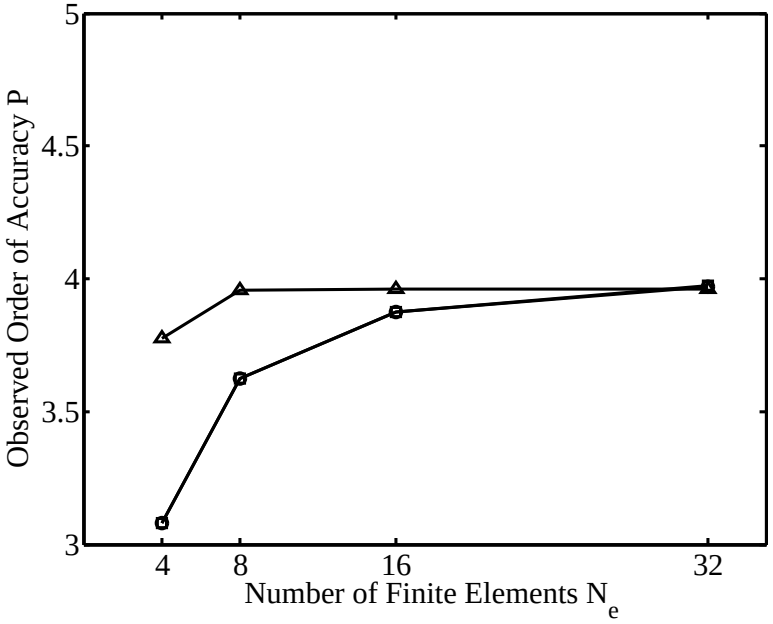

Figure 3.10: Observed order of accuracy as a function of number of finite elements

Table 3.2: Finite element discretization refinement results

Elements	Discretization Error	Error Ratio	Observed Accuracy
	U Displacement		
2	0.66076950		
4	0.07812766	8.45756182	3.08024182
8	0.00633334	12.33592802	3.62479435
16	0.00043225	14.65220335	3.87304572
32	0.00002758	15.67135128	3.97005768
	V Displacement		
2	0.16512387		
4	0.01953099	8.45445561	3.07971186
8	0.00158330	12.33562141	3.62475849
16	0.00010808	14.64985584	3.87281456
32	0.00000690	15.65400028	3.96845947
	W Displacement		
2	0.00612407		
4	0.00046950	13.04385461	3.70529836
8	0.00003027	15.50906066	3.95503940
16	0.00000194	15.58361089	3.96195766
32	0.00000012	15.67354582	3.97025969

manufactured solution with a high degree of accuracy, and the agreement should improve as the integral terms in the right-hand sides of the discretized equations of motion are evaluated more accurately.

Recall that in the AMM the tether displacements are assumed to be of the form:

$$U(\bar{s},t) = \sum_{j=1}^{N_T} C_{1j}\sqrt{2}\sin\left(\frac{j\pi}{L}\bar{s}\right) \tag{3.191}$$

$$V(\bar{s},t) = \sum_{j=1}^{N_T} C_{2j}\sqrt{2}\sin\left(\frac{j\pi}{L}\bar{s}\right) \tag{3.192}$$

$$W(\bar{s},t) = \sum_{j=1}^{N_T} C_{3j}\left(\frac{\bar{s}}{L}\right)^j \tag{3.193}$$

Now, let the manufactured solution for the tether displacements be

$$U^*(\bar{s},t) = A_1\sin(2t)\left[\sin\left(\frac{\pi}{L}\bar{s}\right)+\sin\left(\frac{3\pi}{L}\bar{s}\right)\right] \tag{3.194}$$

$$V^*(\bar{s},t) = A_2\sin(t)\left[\sin\left(\frac{\pi}{L}\bar{s}\right)+\sin\left(\frac{2\pi}{L}\bar{s}\right)\right] \tag{3.195}$$

$$W^*(\bar{s},t) = A_3\cos(t)\left[\left(\frac{\bar{s}}{L}\right)-\left(\frac{\bar{s}}{L}\right)^2+\left(\frac{\bar{s}}{L}\right)^3\right] \tag{3.196}$$

The manufactured solution for the pendular motion of the tether is the same as that used in the application of the MMS to the FEM. Comparing Eqs. (3.191-3.193) with Eqs. (3.194-3.196), we see that for $N_T, N_L \geq 3$ the solution to the discretized equations of motion should match the manufactured solution with

$$C_{11}(t) = C_{13}(t) = \frac{A_1\sin(2t)}{\sqrt{2}} \tag{3.197}$$

$$C_{12}(t) = 0 \tag{3.198}$$

$$C_{21}(t) = C_{22}(t) = \frac{A_2\sin(t)}{\sqrt{2}} \tag{3.199}$$

$$C_{23}(t) = 0 \tag{3.200}$$

$$C_{31}(t) = C_{33}(t) = A_3\cos(t) \tag{3.201}$$

$$C_{32}(t) = -A_3\cos(t) \tag{3.202}$$

There will be some error due to round-off and the fact that the integral terms in the discretized equations of motion are evaluated numerically, but these errors should decrease as the integral terms are evaluated more accurately. The integral terms are evaluated numerically using Simpson's rule with with various numbers of evaluation points. The system

parameters used in all of the numerical solutions are the same as those used in the application of the MMS to the FEM, and are listed in Table 3.1. The time span for all numerical solutions is 2π s.

The errors between the numerical solutions and the manufactured solution are plotted in Figs. 3.11–3.13. For all three of the tether displacements the difference between the numerically calculated coefficients and the exact solution values decrease as the number of right-hand side evaluation points is increased before leveling off around steady values. This convergence is most likely due to round-off errors and iterative convergence errors that arise during the numerical integration of the discretized equations. The steady values reached by all three displacements are on the order of 10^{-9}, which is equivalent to an error of approximately $10^{-9}\%$ between the numerical and exact solutions. Because of these low errors between the numerical and manufactured solutions, we conclude that the computer code that implements the AMM discretization of the modified equations is mistake-free. The terms introduced to modify the original governing equations can simply be removed to produce a mistake-free computer code that produces numerical solutions of the original governing equations. The accuracy of these numerical solutions increases as the number of assumed modes is used in the spatial discretization.

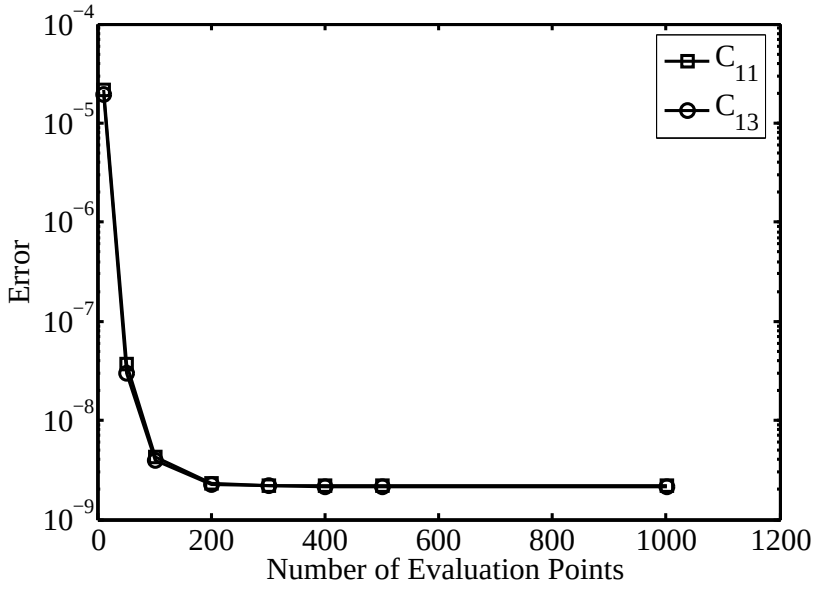

Figure 3.11: Error between numerical and manufactured solutions for the generalized coordinates of the tether displacement U

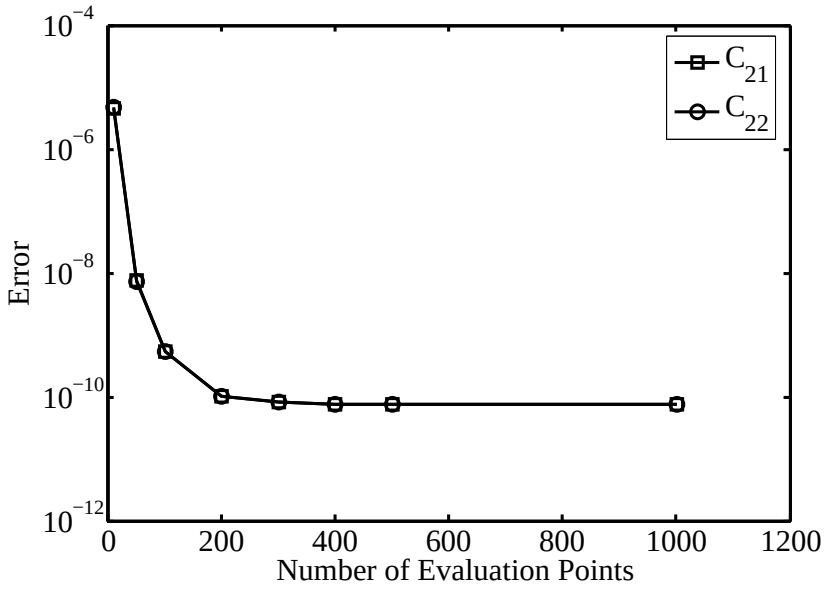

Figure 3.12: Error between numerical and manufactured solutions for the generalized coordinates of the tether displacement V

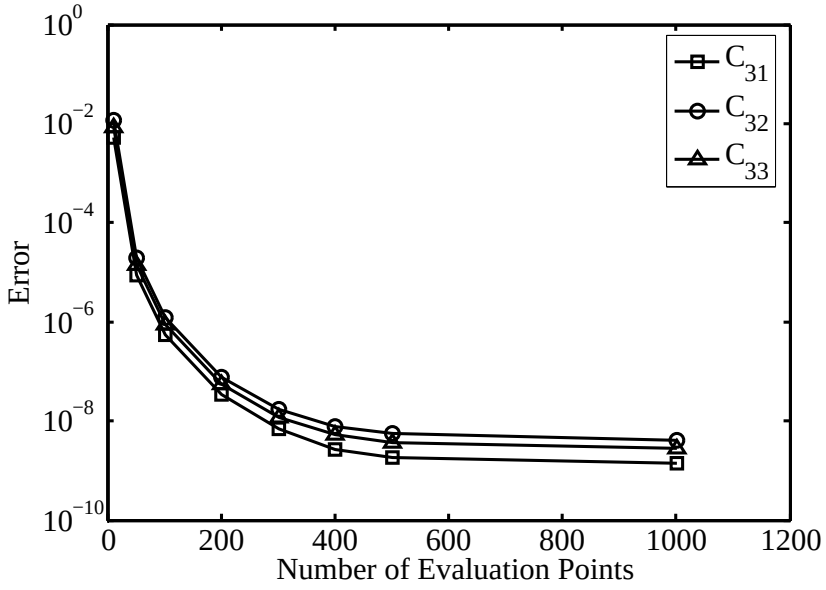

Figure 3.13: Error between numerical and manufactured solutions for the generalized coordinates of the tether displacement W

3.5 Comparison of Computational Models

In the previous section we used the MMS to verify that the numerical solutions produced by the computational models employing the AMM and FEM spatial discretizations are accurate solutions of the mathematical model. From this analysis, we know that the numerical solutions produced by both computational models approach the solution of the mathematical model as the spatial and temporal discretizations are refined. In this section, we present a qualitative comparison of the two computational models, with the objective of determining which model is better suited for application to a TSS.

The most significant difference between the AMM and FEM computational models relates to the computational time required for the models to produce numerical solutions. Numerical experiments have shown that both computational models work well for low numbers of assumed modes or finite elements, in that both produce numerical solutions in a relatively short computational time. However, as the number of assumed modes used in the AMM computational model to approximate the longitudinal vibrations increases, the computational time increases rapidly, rendering the model practically useless. To see why this happens, consider the mass matrix of the discretized equations for the longitudinal vibrations, which is defined by Eq. (3.116). As N_L increases, the columns of the longitudinal mass matrix become increasingly similar, causing the mass matrix to become nearly singular. This nearly-singular behavior introduces significant numerical errors into the calculation of the accelerations of the longitudinal degrees of freedom because the inverse of the mass matrix is used in their calculations, and these errors in the accelerations can actually cause the longitudinal vibrations to diverge when they should not. As the time integrator attempts to compensate for this divergent behavior, the time steps become very small and the total integration time becomes prohibitively large. The FEM does not have this same problem because the diagonal structure of the system mass matrices ensures that their columns are always linearly independent, so there are no problems in taking their inverses due to ill-conditioning.

Nearly singular behavior of the system mass matrix for simple polynomial shape functions in the AMM has been reported previously,[57] and the simplest method of eliminating the problem is to use a different set of assumed mode functions for the longitudinal vibrations. The best possible set is an orthogonal set that makes the mass matrix diagonal and trivially invertible. Another possibility is to use the mode shapes for the longitudinal vibrations of a similar, but much simpler, problem as the longitudinal assumed mode functions. For example, one could use the longitudinal mode shapes for a simple string pendulum as the longitudinal modes shapes for the TSS. The mode shapes of the simpler problem would be orthogonal or nearly orthogonal, and the resulting mass matrix would always have a well-defined inverse. Other possible sets of longitudinal assumed mode functions exist, but their analysis and implementation is left for future work.

Another advantage of the FEM over the AMM not specific to the shape functions used in the AMM is that initial conditions are much easier to set in the FEM. Since the degrees

of freedom in the FEM are simply displacements and slopes at points along the tether, any arbitrary initial tether shape can be trivially converted to a set of initial coordinates for numerical integration. This is not the case with the AMM, in which determining a set of coordinates from an arbitrary tether shape requires a process similar to calculating the coefficients of a Fourier series. While this is not necessarily a difficult task, it is more involved than the process required in the FEM.

For the reasons discussed above, we conclude that the FEM computational model is better suited for application to the TSS than is the AMM computational model. All applications of the top-level computational model presented later in this dissertation use the FEM computational model, so from this point forward the phrase "top-level computational model" refers to the FEM computational model presented in this chapter. In the next section, we present the outputs of the top-level computational model for two different applications of a TSS, along with a discussion of the various aspects of the system dynamics.

3.6 Examples of Computational Model Output

In this section we present examples of the output of the top-level computational model for two different TSS. The first system is a spinning, non-electrodynamic TSS, and the second system is a local-vertically aligned electrodynamic TSS. The top-level computational model is used to produce numerical solutions for both examples, and we present and discuss the numerical solutions for both systems.

3.6.1 Example 1: Spinning Tethered Satellite System

The first example that we consider is for a spinning, non-electrodynamic TSS. The system parameters used in this example are listed in Table 3.3, and the initial conditions used to produce the numerical solution are listed in Table 3.4. Note that 4 finite elements are used in the spatial discretization, and the time span of the numerical solution is approximately 5 orbits of the system. The initial conditions correspond to the system being on a nearly circular orbit with an altitude of roughly 400 km. The entire system is nominally spinning in the orbit plane at roughly 5 times per orbit, but there is a small initial out-of-plane tether attitude angle of 1°. The tether initially has sinusoidal transverse displacements (both U and V) with maximum displacement of 20 m, and the initial longitudinal displacement profile is cubic. Note that this cubic displacement profile is determined using a quadratic expression for the tension in the tether, as in Ref. [5].

The time history of the osculating orbit elements predicted by the top-level computational model is shown in Fig. 3.14. Note that the osculating orbit elements (and all of the other quantities presented for the examples considered in this section) are plotted against a nondimensional time, which is defined as the dimensional time divided by the orbital period of the

Table 3.3: System parameters used to determine numerical solution for Example 1

Primary End Body $\mathcal{A}$	
m_A (kg)	500
$\mathbf{I}_\mathrm{A}$ (kg-m^2)	diag(300 400 500)
$\mathbf{p}_\mathrm{A}$ (m)	$(0\ 0\ 1)^\mathrm{T}$
Secondary End Body $\mathcal{B}$	
m_B (kg)	50
$\mathbf{I}_\mathrm{B}$ (kg-m^2)	diag(30 40 50)
$\mathbf{p}_\mathrm{B}$ (m)	$(0\ 0\ -0.1)^\mathrm{T}$
Tether	
L (km)	20
$\bar{\rho}$ (kg/km)	2.5
EA (N)	55,000
c (s)	0.5
N_e	4
Central Body	
μ (km^3/s^2)	3.986×10^5

initial orbit of $\mathcal{A}$, P_O. For this example, the only orbital perturbation acting on the system is the gravitational perturbation due to the distributed mass of the system. This perturbation results in small, quasi-periodic oscillations of the orbit elements over the solution time span, as shown by Fig. 3.14. The semimajor axis varies by approximately 70 km, which is about 1% of the initial value of 6,770 km. The frequency of the oscillations of a is roughly 5 cylces per orbit, and the oscillations are about an average value of approximately 6,805 km. The eccentricity varies in the range 0.001-0.01, with oscillations occurring about an approximate average value of 0.005. Note that this average value is 5 times larger than the initial eccentricity of 0.001, but is still a relatively low value for orbital eccentricity. The variation of Ω over the solution time span is quite small, being on the order of 0.001% of the initial value of 300°. The variation in the inclination is equally small, also being on the order of 0.001% of the initial inclination. The reason for such small variations in Ω and I is that the motion takes place predominantly in the orbital plane, so the disturbance acceleration normal to the orbit plane is small. From Eqs. (3.48) and (3.49), small out-of-plane disturbance accelerations result in small changes in Ω and I, which is indeed the case for this example. The variation in ω is much larger than the variations in the other orbit elements considered thus far, with the maximum variation from the initial value of 45° begin roughly 55°. The large variations are seen because the eccentricity of the system orbit is small, and, according to Eq. (3.50), the variations in ω are proportional to $1/e$. The variation in ν is also proportional to $1/e$, resulting in the large variations seen in Fig. 3.14(f). Because the orbit of the system is nearly circular, the true anomaly nominally behaves in a nearly-linear fasion; however, the

Table 3.4: Initial conditions used to determine numerical solution for Example 1

System Orbital Motion	
a (km)	6,770
e	0.001
Ω (deg)	300
I (deg)	50
ω (deg)	45
ν (deg)	0
$\mathcal{A}$ Attitude Motion	
$\bar{\mathbf{q}}_{\mathrm{A}}$	$(1\ 0\ 0\ 0)^{\mathrm{T}}$
$\boldsymbol{\omega}_{\mathrm{A/O}}$ (deg/s)	$(0\ 0.3247\ 0)^{\mathrm{T}}$
$\mathcal{B}$ Attitude Motion	
$\bar{\mathbf{q}}_{\mathrm{B}}$	$(1\ 0\ 0\ 0)^{\mathrm{T}}$
$\boldsymbol{\omega}_{\mathrm{B/O}}$ (deg/s)	$(0\ 0.3247\ 0)^{\mathrm{T}}$
Pendular Tether Motion	
α (deg)	0
β (deg)	1
$\dot{\alpha}$ (deg/s)	0.3247
$\dot{\beta}$ (deg/s)	0
Tether Elastic Vibrations	
$U(\bar{s},0)$ (m)	$20\sin\left(\frac{\pi\bar{s}}{L}\right)$
$\dot{U}(\bar{s},0)$ (m)	0
$V(\bar{s},0)$ (m)	$20\sin\left(\frac{\pi\bar{s}}{L}\right)$
$\dot{V}(\bar{s},0)$ (m)	0
$W(\bar{s},0)$ (m)	$26.6181\left[\frac{\bar{s}}{L}-\frac{1}{9}\left(\frac{\bar{s}}{L}\right)^3\right]$
$\dot{W}(\bar{s},0)$ (m)	$0.0011\left[\frac{\bar{s}}{L}-\frac{1}{9}\left(\frac{\bar{s}}{L}\right)^3\right]$

large variations in ω result in large deviations from this nominal behavior.

The attitude motion of $\mathcal{A}$ predicted by the top-level computational model is shown in Fig. 3.15. Because the entire system is nominally spinning in the orbit plane, $\mathcal{A}$ has a spinning attitude motion as well. The spinning attitude motion of $\mathcal{A}$ is illustrated by the behavior of q_{A2} and q_{A4}, which vary between -1 and 1. Recalling the definition of a quaternion in Eqs. (3.9–3.11), this variation means that $\mathcal{A}$ is undergoing a continuous rotation about the $\hat{\mathbf{a}}_2$ axis, which remains roughly normal to the orbit plane. There is also some small attitude motion about the $\hat{\mathbf{a}}_1$ and $\hat{\mathbf{a}}_3$ axes, as illustrated by the small amplitude oscillations of q_{A1} and q_{A3}, but the attitude motion of $\mathcal{A}$ is dominated by the planar spin.

The attitude motion of $\mathcal{B}$ predicted by the top-level computational model is similar to that for $\mathcal{A}$, as shown by Fig. 3.16. The motion is dominated by a continuous spin about an axis that is approximately normal to the orbit plane, but there is also small attitude oscillations about the $\hat{\mathbf{b}}_1$ and $\hat{\mathbf{b}}_3$ axes as well.

The time-history of the pendular motion of the tether predicted by the top-level computational model is shown in Fig. 3.17. Because the tether is nominally spinning in the orbit plane, the in-plane tether attitude angle α undergoes a continuous growth as the tether spins. Note that we have shown the time-history of α modulo 360° so that the number of rotations performed by the tether can be more easily distinguished. As shown by Fig. 3.17(a), the tether performs just under 5 complete rotations per orbit, and the rotation rate is relatively constant. This latter fact can be seen by examining Fig. 3.17(c), which shows that $\dot{\alpha}$ undergoes small-amplitude oscillations about an average value of approximately 0.315°/s. The initial out-of-plane deviation of the tether is 1°, resulting in the out-of-plane pendular attitude oscillations shown in Fig. 3.17(b). These oscillations are quasi-periodic with an amplitude that is approximately the same as the initial out-of-plane deviation of 1°.

The elastic vibrations of the tether predicted by the top-level computational model are shown in Figs. 3.18(a)–3.18(c). Note that these plots show the tether displacements at the points $\bar{s} = L/4$, $L/2$, and $3L/4$. The plot for the longitudinal displacement also shows the displacement at $\bar{s} = L$. As Figs. 3.18(a)–3.18(c) show, the transverse vibrations are quasi-periodic, with the tether midpoint undergoing oscillations at an amplitude of roughly 20 m. Note that these displacements are on the order of 0.1% of the unstretched tether length. The longitudinal displacements are also quasi-periodic, and the displacement at $\bar{s} = L$ oscillates near 20 m over the entire solution time span. Also note that the amplitude of the oscillations of the longitudinal displacement becomes larger as $\bar{s}$ increases.

Figures 3.18(d) and 3.18(e) show the stretched length of the tether and the tension at the tether attachment points predicted by the top-level computational model. The stretched length of the tether oscillates near 20.02 km for the entire solution time span, meaning that the tether is stretched by approximately 0.1%. Note that the plot of the stretched tether length is quite similar to the plot of $W(L,t)$. This similarity is due to the fact that the stretched tether length is predominantly affected by the longitudinal displacement, such that the two quantities behave in a similar manner. The tension at P_A oscillates about

an approximate average value of 55 N, and the tension at P_B oscillates at an approximate average value of 40 N. The amplitudes of the tension oscillations at P_A and P_B are both rough 5 N, although the amplitude of the oscillations at P_A is slightly larger. Note that the tension at P_A is higher than the tension at P_B, illustrating that the tension decreases along the tether from the primary end body toward the secondary end body.

To summarize the system dynamics predicted by the top-level computational model for this example, the variation of the system orbit is quite small, with the exception of the argument of periapsis. The tether undergoes a predominantly spinning motion in the orbit plane at roughly 5 rotations per orbit, and the out-of-plane attitude motion remains on the order of the initial deviation of 1°. Both end bodies also undergo a predominantly spinning attitude motion in the orbit plane that follows the spinning motion of the tether. The transverse vibrations of the tether are quasi-periodic and oscillate with an amplitude that is roughly equal to the initial displacement amplitude. The longitudinal vibrations are also quasi-periodic and result in a roughly 0.1% stretching of the tether.

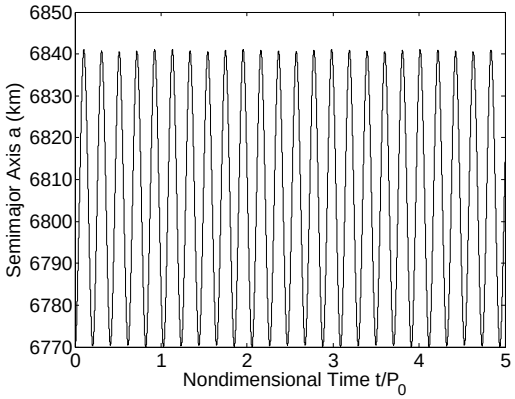

(a) Semimajor axis a

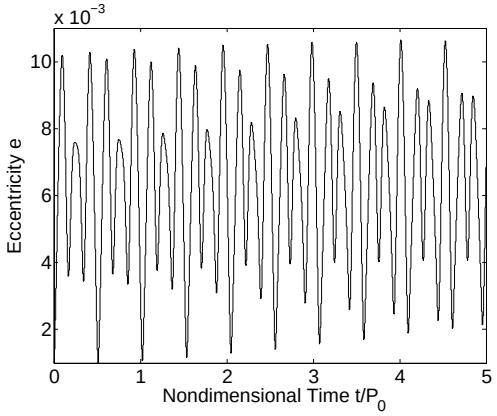

(b) Eccentricity e

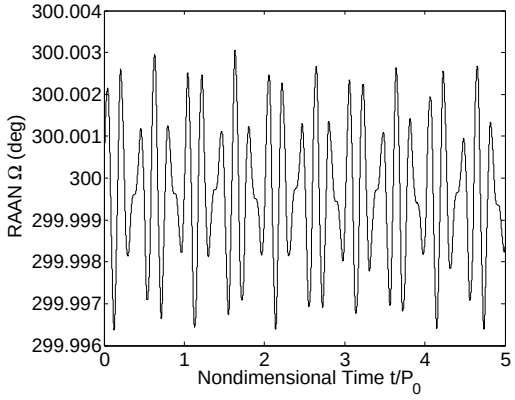

(c) RAAN Ω

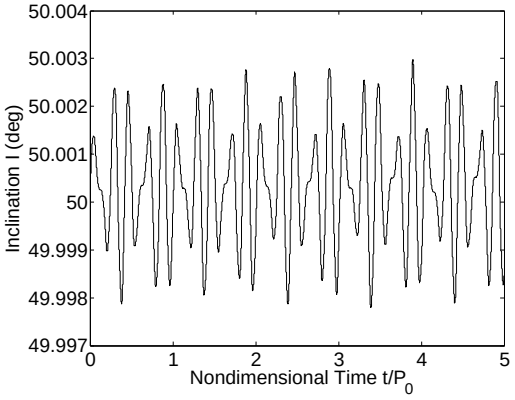

(d) Inclination I

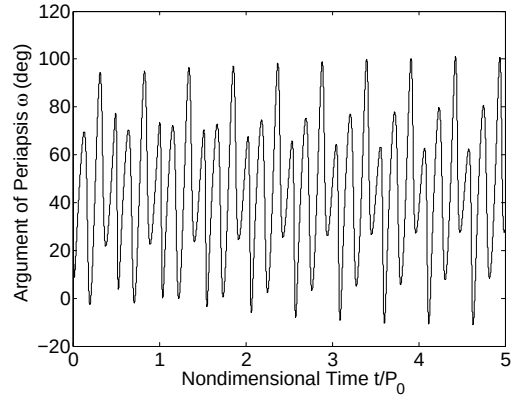

(e) Argument of Periapsis ω

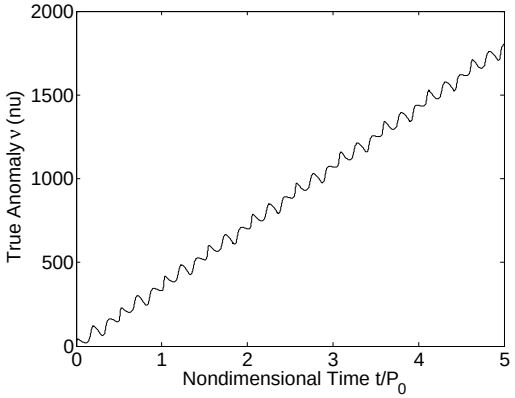

(f) True Anomaly ν

Figure 3.14: Time history of the osculating orbit elements predicted by the top-level computational model for Example 1

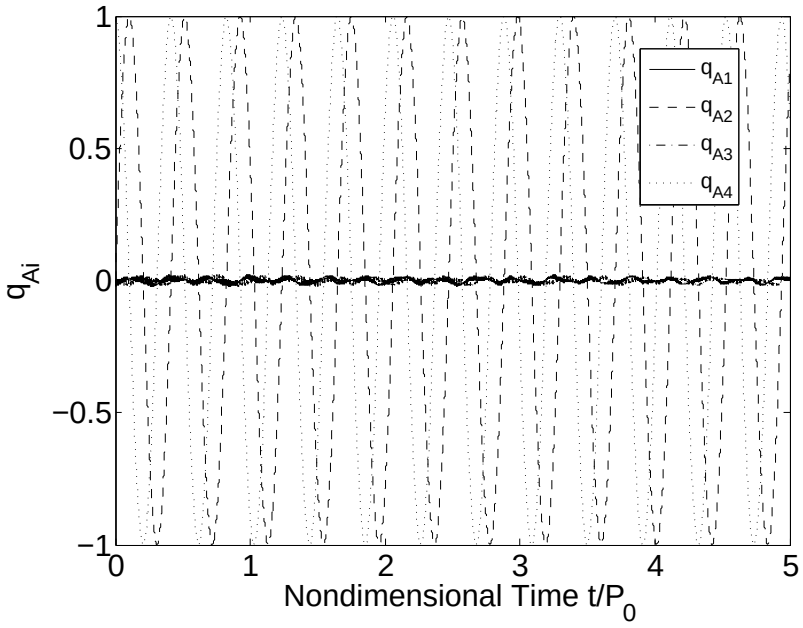

(a) Quaternion for attitude of $\mathcal{A}$ relative to $\mathcal{F}_O$, $\bar{\mathbf{q}}_{\mathrm{A}}$

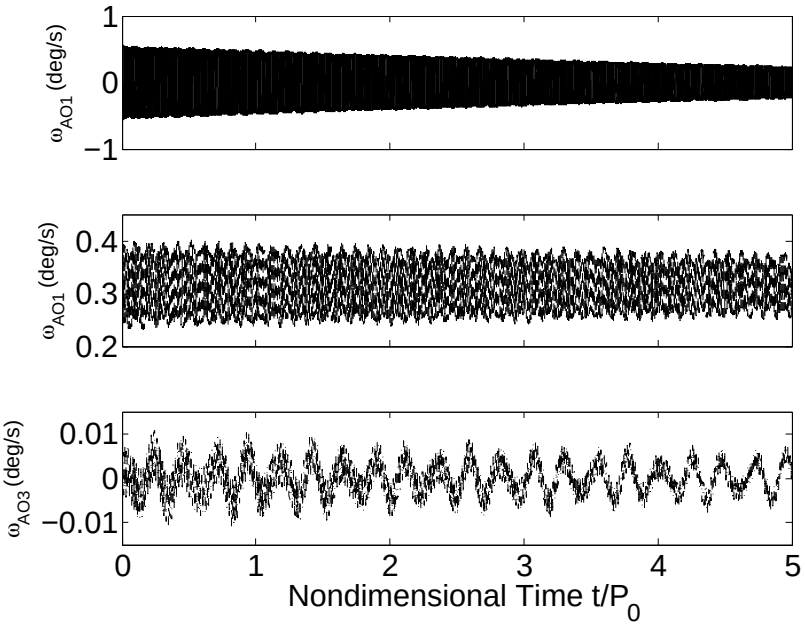

(b) Components of $\vec{\boldsymbol{\omega}}_{\mathrm{A/O}}$ expressed relative to $\mathcal{F}_A$

Figure 3.15: Time history of the attitude motion of $\mathcal{A}$ predicted by the top-level computational model for Example 1

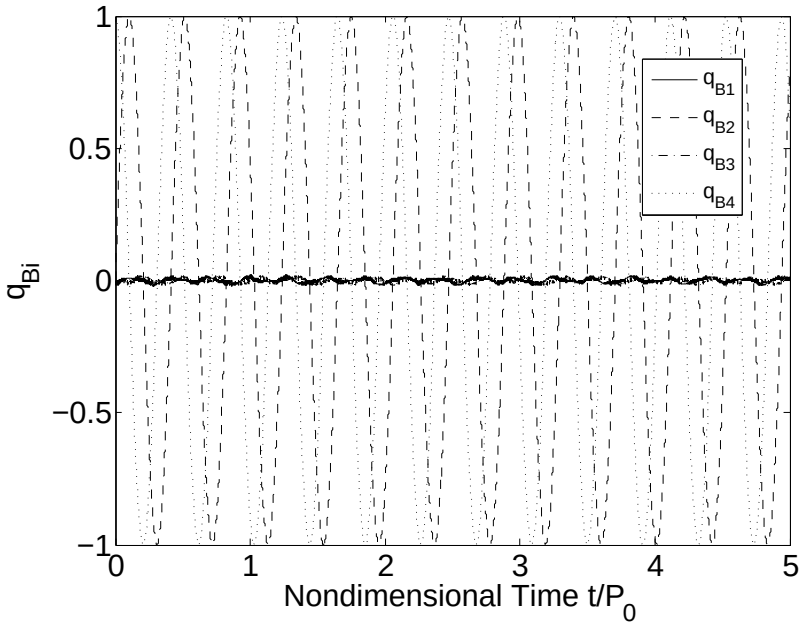

(a) Quaternion for attitude of $\mathcal{B}$ relative to $\mathcal{F}_O$, $\bar{\mathbf{q}}_{\mathrm{B}}$

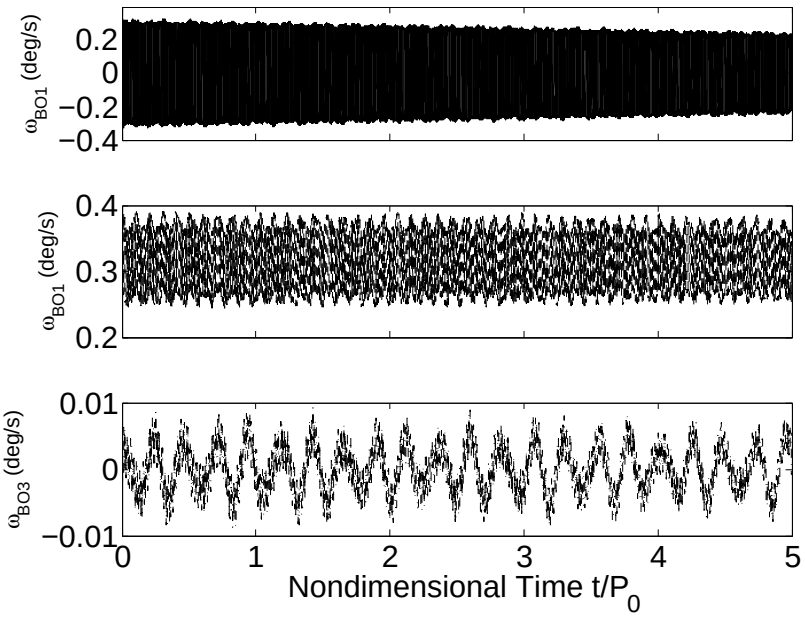

(b) Components of $\vec{\boldsymbol{\omega}}_{\mathrm{B/O}}$ expressed relative to $\mathcal{F}_B$

Figure 3.16: Time history of the attitude motion of $\mathcal{B}$ predicted by the top-level computational model for Example 1

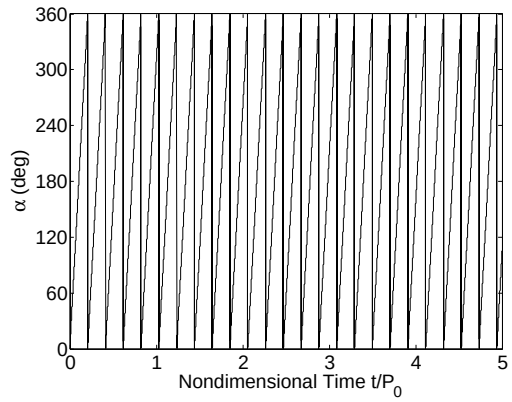

(a) In-plane angle α

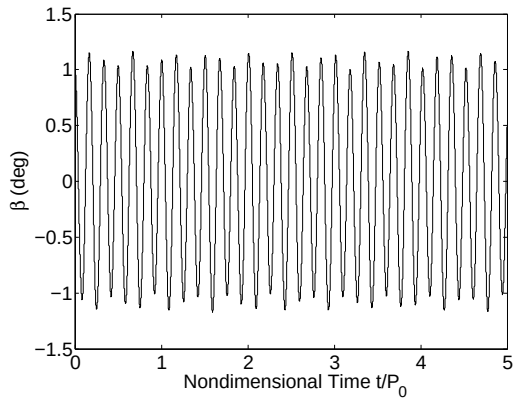

(b) Out-of-plane angle β

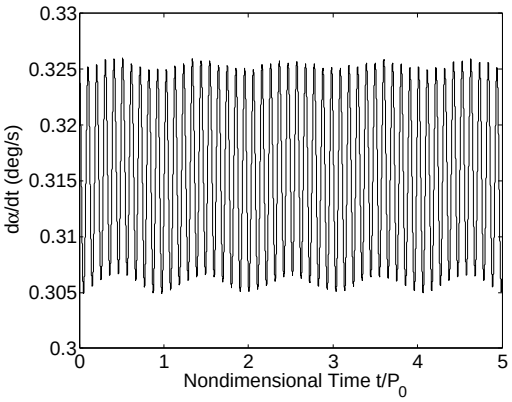

(c) In-plane angular velocity $\dot{\alpha}$

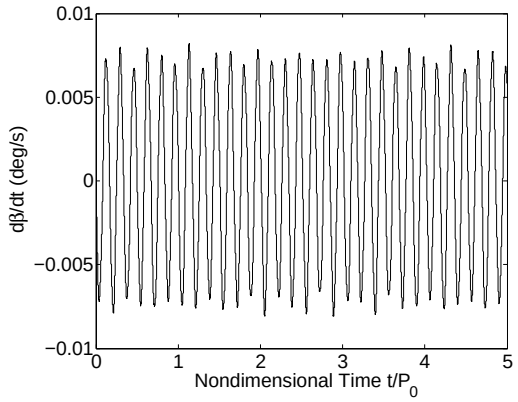

(d) Out-of-plane angular velocity $\dot{\beta}$

Figure 3.17: Time history of the pendular motion of the tether predicted by the top-level computational model for Example 1

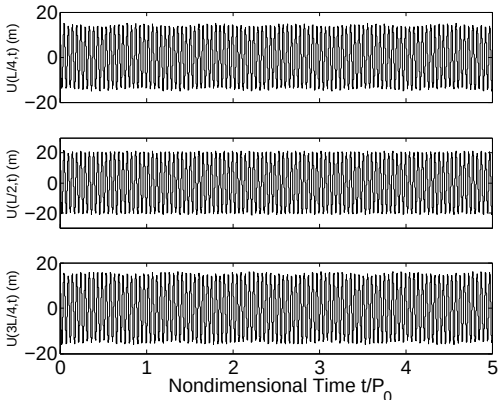

(a) Transverse displacement U

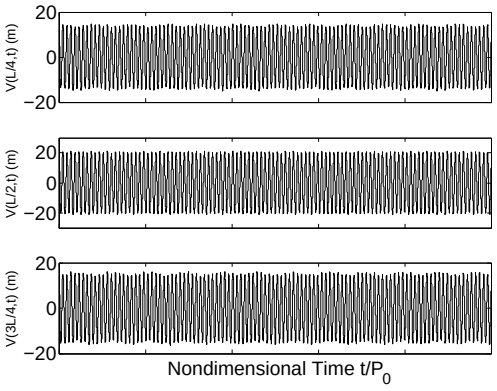

(b) Transverse displacement V

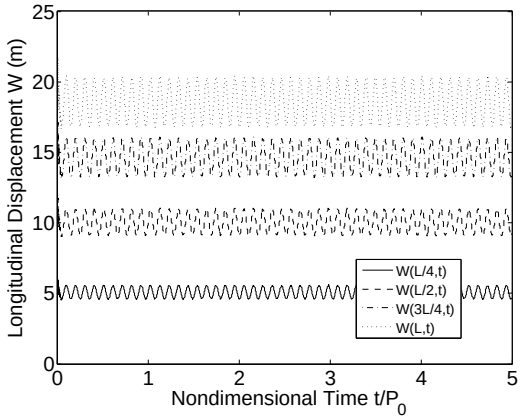

(c) Longitudinal displacement W

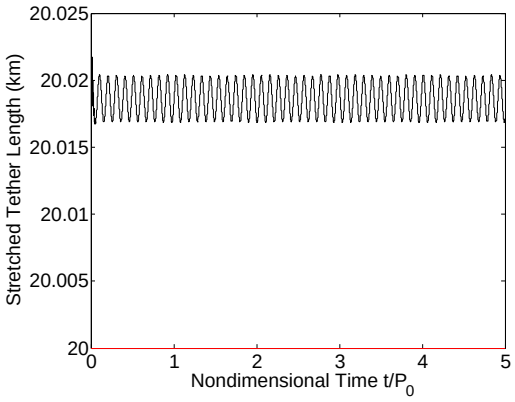

(d) Stretched tether length

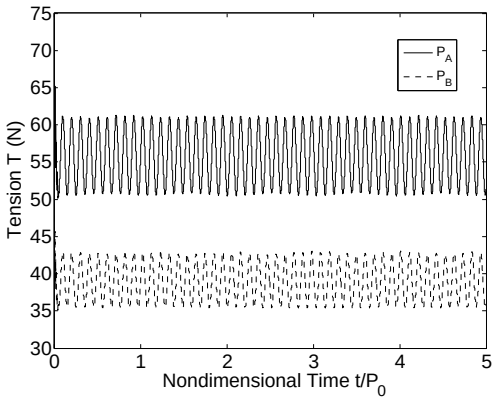

(e) Tension at the tether attachment points

Figure 3.18: Time history of the elastic vibrations of the tether predicted by the top-level computational model for Example 1

3.6.2 Example 2: Electrodynamic Tethered Satellite System

In this example we consider a local-vertically aligned electrodynamic TSS. The system parameters used in this example are listed in Table 3.5. Note that 4 finite elements are used for the spatial discretization, and the central body is Earth. We assume that the electrical current in the tether is held at a constant value of -1 A. The initial conditions used to determine the numerical solution are listed in Table 3.6. These initial conditions correspond to the system being on a nearly-circular orbit with an altitude of roughly 400 km, and the entire system is aligned along the local vertical direction. The tether has no initial transverse displacement, but once again has an initial cubic longitudinal displacement profile that is determined by assuming a quadratic tension profile.

Table 3.5: System parameters used to determine numerical solution for Example 2

Primary End Body $\mathcal{A}$	
m_A (kg)	5,000
$\mathbf{I}_{\mathrm{A}}$ (kg-m^2)	diag(3,000 4,000 5,000)
$\mathbf{p}_{\mathrm{A}}$ (m)	$(0\ 0\ 1)^{\mathrm{T}}$
Secondary End Body $\mathcal{B}$	
m_B (kg)	500
$\mathbf{I}_{\mathrm{B}}$ (kg-m^2)	diag(300 400 500)
$\mathbf{p}_{\mathrm{B}}$ (m)	$(0\ 0\ -1)^{\mathrm{T}}$
Tether	
L (km)	20
$\bar{\rho}$ (kg/km)	2.5
EA (N)	55,000
c (s)	0.5
i (A)	-1
N_e	4
Central Body	
μ (km^3/s^2)	3.986×10^5
μ_M (T-km^3)	8×10^6
Θ_0 (deg)	0
Γ (deg)	11.5

The time history of the osculating orbit elements predicted by the top-level computational model is shown in Fig. 3.19. In this example, the disturbance acceleration affecting the system orbit is a combination of a gravitational perturbation due to the distributed mass of the system and a perturbation due to the electrodynamic force, with the electrodynamic force being the dominant component. The electrodynamic force causes a secular increase in the semimajor axis of approximately 2.3 km. The RAAN and inclination also experience secular

Table 3.6: Initial conditions used to determine numerical solution for Example 2

System Orbital Motion	
a (km)	6,770
e	0.001
Ω (deg)	300
I (deg)	50
ω (deg)	45
ν (deg)	0
$\mathcal{A}$ Attitude Motion	
$\bar{\mathbf{q}}_{\mathrm{A}}$	$(1\ 0\ 0\ 0)^{\mathrm{T}}$
$\boldsymbol{\omega}_{\mathrm{A/O}}$ (deg/s)	$(0\ 0\ 0)^{\mathrm{T}}$
$\mathcal{B}$ Attitude Motion	
$\bar{\mathbf{q}}_{\mathrm{B}}$	$(1\ 0\ 0\ 0)^{\mathrm{T}}$
$\boldsymbol{\omega}_{\mathrm{B/O}}$ (deg/s)	$(0\ 0\ 0)^{\mathrm{T}}$
Pendular Tether Motion	
α (deg)	0
β (deg)	0
$\dot{\alpha}$ (deg/s)	0
$\dot{\beta}$ (deg/s)	0
Tether Elastic Vibrations	
$U(\bar{s},0)$ (m)	0
$\dot{U}(\bar{s},0)$ (m)	0
$V(\bar{s},0)$ (m)	0
$\dot{V}(\bar{s},0)$ (m)	0
$W(\bar{s},0)$ (m)	$14.7146\left[\frac{\bar{s}}{L}-\frac{1}{63}\left(\frac{\bar{s}}{L}\right)^3\right]$
$\dot{W}(\bar{s},0)$ (m)	0

drifts due to the electrodynamic force, with both quantities decreasing over the solution time span. Note, however, that the decrease in both quantities is quite small compared to their initial values. The eccentricity and argument of periapsis do not appear to exhibit any secular drift, and instead undergo quasi-periodic oscillations about an average value. For the eccentricity, the average value is roughly 0.00175, and the amplitude of the oscillations is about 0.00075. The average value of ω is approximately the initial value of 45°, and the amplitude of the oscillations is about 25°. Both e and ω oscillate at approximately 5 cycles per orbit. The true anomaly increases continuously as expected, with some variations due to the variation in the argument of periapsis.

Figure 3.20 shows the time history of the attitude motion of $\mathcal{A}$. The principal axes of $\mathcal{A}$ are initially aligned with $\mathcal{F}_O$, and, as the figure shows, undergoes small amplitude oscillations about this initial orientation. This behavior is illustrated by the fact that q_{A4} is approximately 1 over the entire solution time span, while the other q_{Ai} remain near zero. The attitude motion of $\mathcal{B}$ is similar to that of $\mathcal{A}$, as shown by Fig. 3.21. The principal axes of $\mathcal{B}$ are initially aligned with $\mathcal{F}_O$, and the body undergoes small amplitude oscillations about the initial orientation over the solution time span.

The time history of the pendular tether motion predicted by the top-level computational model is shown in Fig. 3.22. The tether is initially aligned with the local vertical direction, and the electrodynamic force drives small amplitude in- and out-of-plane tether attitude motion. The maximum magnitude of both the in- and out-of-plane tether attitude angles is 0.45°. Note that the out-of-plane attitude angle behaves in a much more periodic manner than does the in-plane angle, which appears to be oscillating in a somewhat chaotic manner.

The tether elastic vibrations predicted by the top-level computational model are shown in Figs. 3.23(a)–3.23(c). As with the first example we considered, the elastic vibrations are illustrated by displaying the tether displacements at several points along the tether. The tether is initially aligned with the local vertical with some longitudinal stretching, and the electrodynamic force drives transverse vibrations of the tether. As Fig. 3.23(a) shows, the displacement u undergoes quasi-periodic oscillations. Note that U at all of the points shown is positive because the component of the electrodynamic force in the $\hat{\mathbf{e}}_1$ direction is always positive for this example, thus driving the positive oscillations seen in Fig. 3.23(a). The same cannot be said for the displacement V, however, as seen by Fig. 3.23(b). The behavior of V appears to be a combination of oscillations at a high frequency and oscillations at a low frequency. The high frequency is simply the natural oscillation frequency of the tether, and the low frequency is due to the fact that the component of the electrodynamic force in the $\hat{\mathbf{e}}_2$ direction slowly changes as the system moves in its inclined orbit. This force component slowly oscillates back and forth between positive and negative quantities at a frequency slightly lower that the orbital frequency (due to the rotation of the magnetic field), resulting in the alternately positive and negative character of V seen in Fig. 3.23(b). The combination of the behaviors of U and V results is a sort of slowly-varying "skip-rope" motion of the tether as seen by the frame $\mathcal{F}_E$. The tether longitudinal vibrations behave much in the same manner as seen in the first example we considered. As illustrated by Fig. 3.23(c),

the longitudinal stretching of the tether remains relatively constant, with a longitudinal displacement at $\bar{s} = L$ of approximately 13 m. Another point to note about Fig. 3.23(c) is that the longitudinal displacement undergoes a period of high-frequency oscillation at the beginning of the motion that damps out within a fraction of an orbit. This behavior illustrates the primary affect of the structural damping in the tether, which is to damp out high-frequency longitudinal vibrations.

The stretched tether length and tension at the tether attachment points predicted by the top-level computational model are shown in Figs. 3.23(d)–3.23(e). The stretched length of the tether undergoes a short period of high-frequency oscillations that damp out around a value of roughly 20.013 km, meaning that the tether is stretched by 0.065%. As discussed in the previous example, the behavior of the stretched tether length closely resembles the behavior of the longitudinal vibrations. The tension at P_A oscillates about an average value slightly larger than 36 N, and the tension at P_B oscillates about an average value near 35 N. As seen in the first example we considered, the tension in the tether decreases as $\bar{s}$ increases from P_A to P_B.

To summarize the system dynamics predicted by the top-level computational model for this example, the electrodynamic force causes secular changes in the semimajor axis, RAAN, and inclination of the system orbit. The change in the semimajor axis is relatively significant, while the changes in the RAAN and inclination are practically negligible. The principal axes of both end bodies are initially aligned with the orbital frame and undergo small amplitude attitude oscillations about this initial configuration. The electrodynamic force drives small amplitude in- and out-of-plane pendular tether motion, with the maximum magnitude of both in- and out-of-plane motion being roughly 0.45°. The transverse vibrations induced by the electrodynamic force are relatively complex, exhibiting a "skip-rope" type of motion. The longitudinal vibrations are similar to those seen in the first example we considered, in that they remain at relatively constant values over the solution time span.

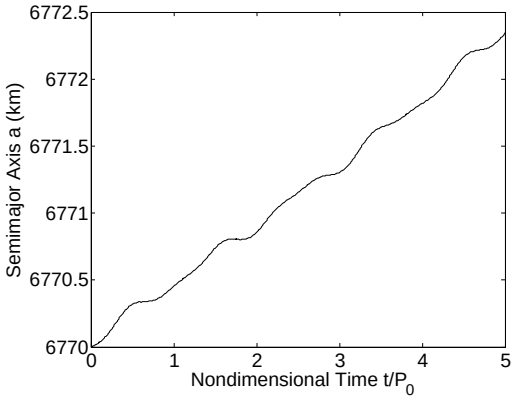

(a) Semimajor axis a

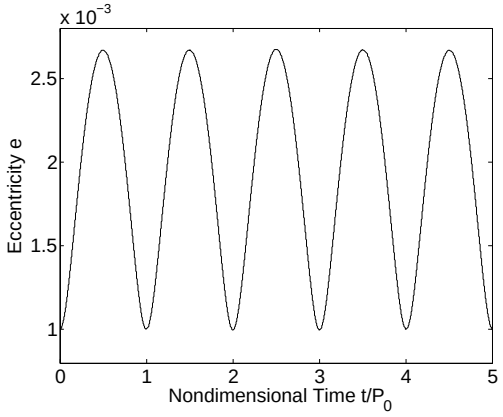

(b) Eccentricity e

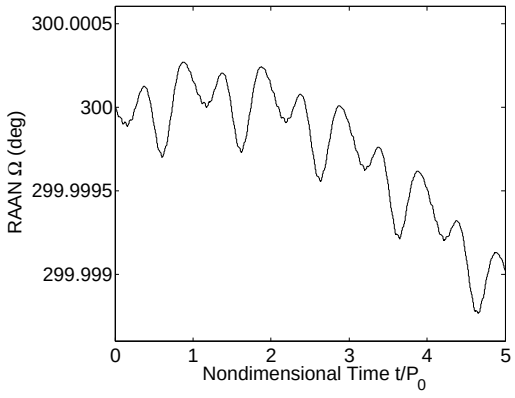

(c) RAAN Ω

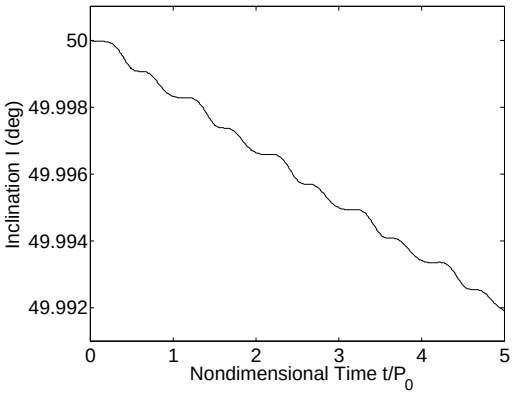

(d) Inclination I

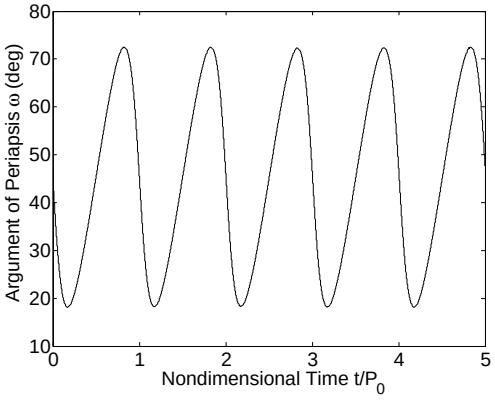

(e) Argument of Periapsis ω

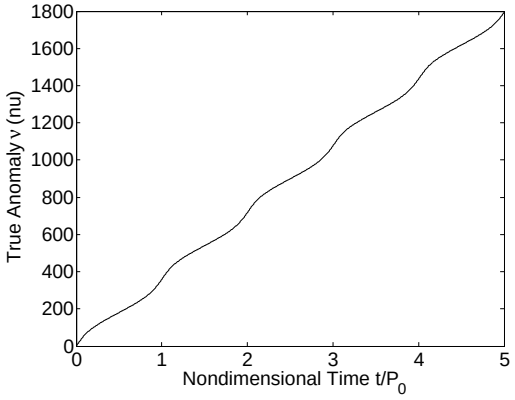

(f) True Anomaly ν

Figure 3.19: Time history of the osculating orbit elements predicted by the top-level computational model for Example 2

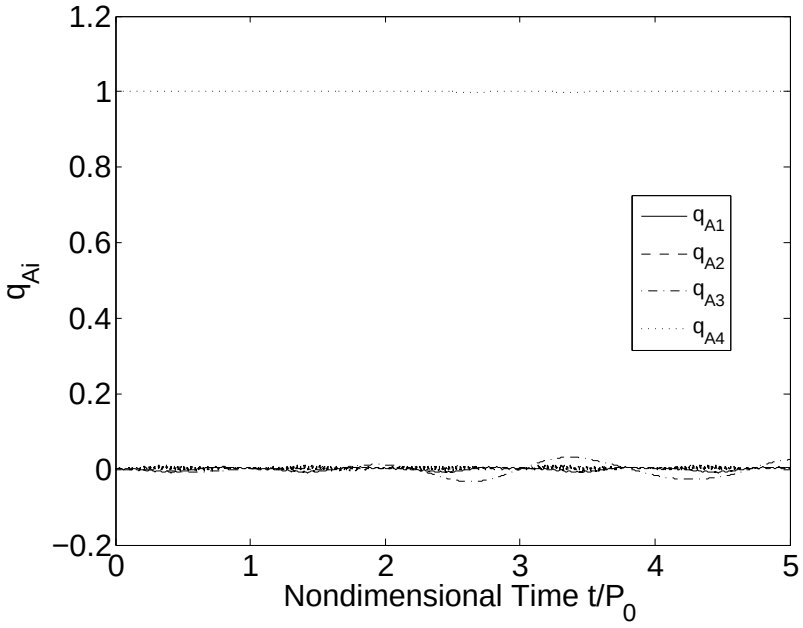

(a) Quaternion for attitude of $\mathcal{A}$ relative to $\mathcal{F}_O$, $\bar{\mathbf{q}}_{\mathrm{A}}$

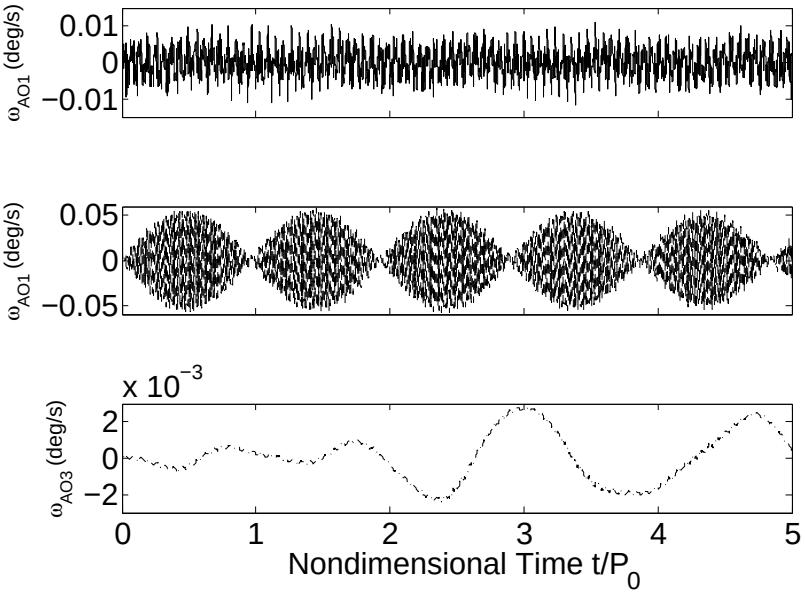

(b) Components of $\vec{\boldsymbol{\omega}}_{\mathrm{A/O}}$ expressed relative to $\mathcal{F}_A$

Figure 3.20: Time history of the attitude motion of $\mathcal{A}$ predicted by the top-level computational model for Example 2

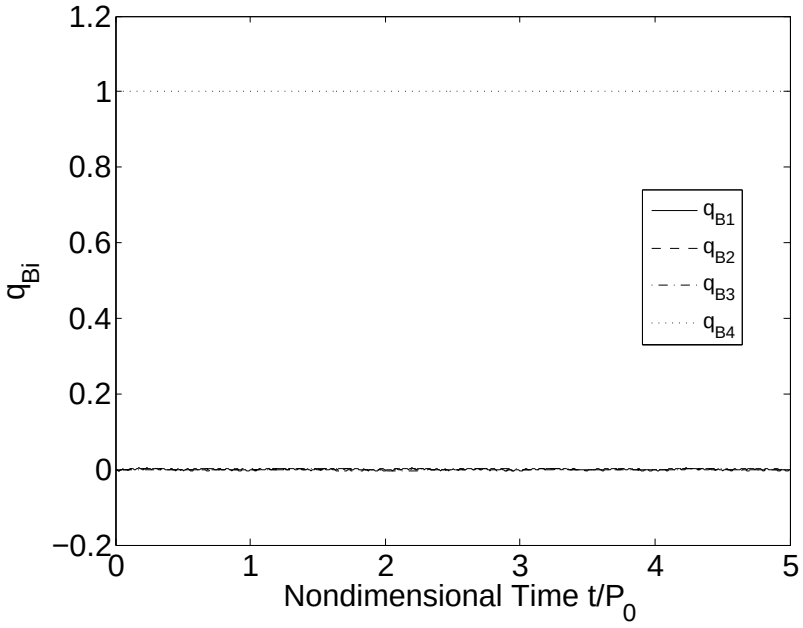

(a) Quaternion for attitude of $\mathcal{B}$ relative to $\mathcal{F}_O$, $\bar{\mathbf{q}}_{\mathrm{B}}$

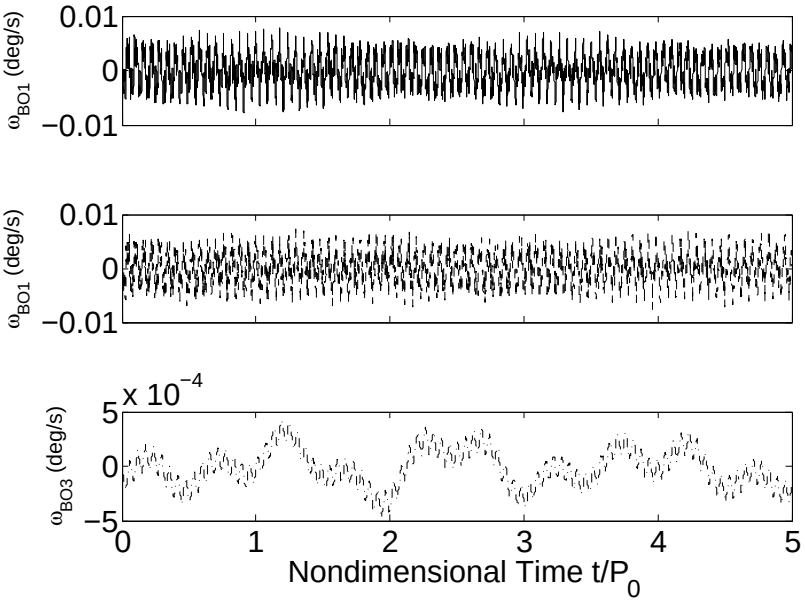

(b) Components of $\vec{\boldsymbol{\omega}}_{\mathrm{B/O}}$ expressed relative to $\mathcal{F}_B$

Figure 3.21: Time history of the attitude motion of $\mathcal{B}$ predicted by the top-level computational model for Example 2

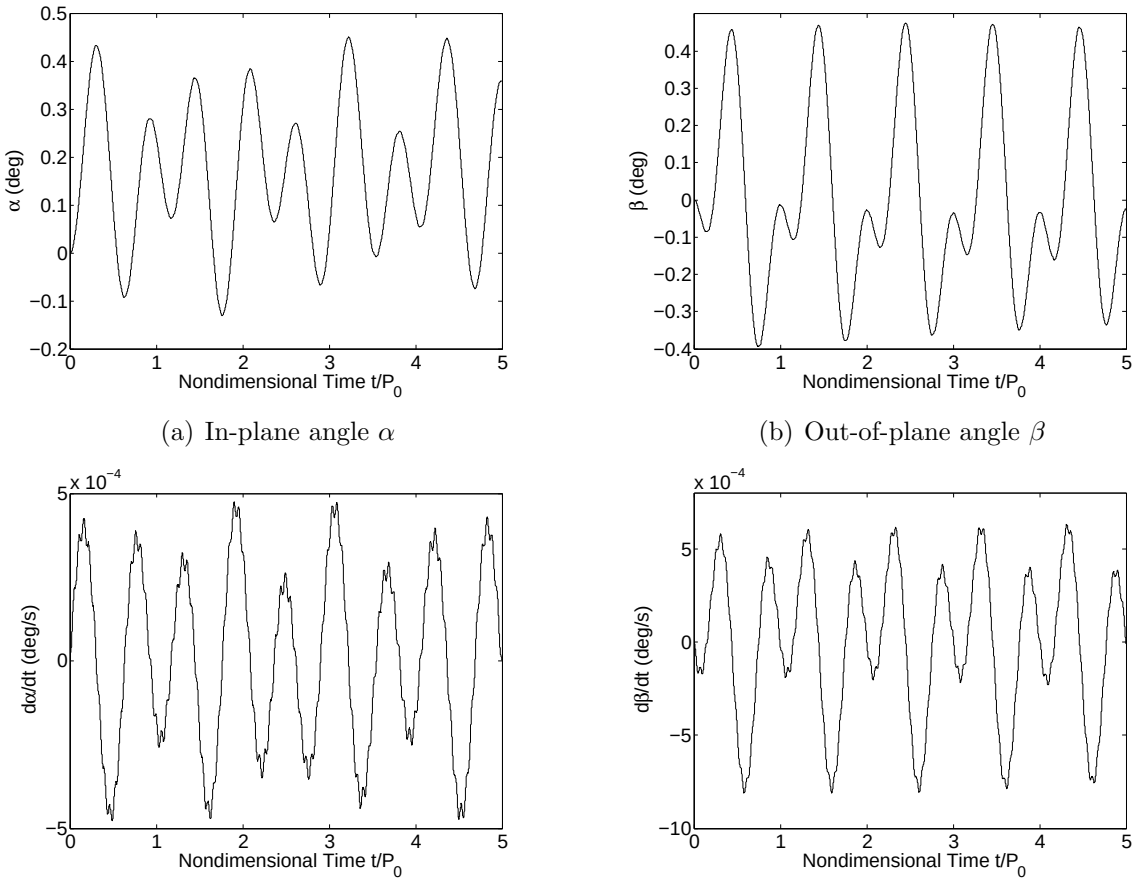

(a) In-plane angle α

(b) Out-of-plane angle β

(c) In-plane angular velocity $\dot{\alpha}$

(d) Out-of-plane angular velocity $\dot{\beta}$

Figure 3.22: Time history of the pendular motion of the tether predicted by the top-level computational model for Example 2

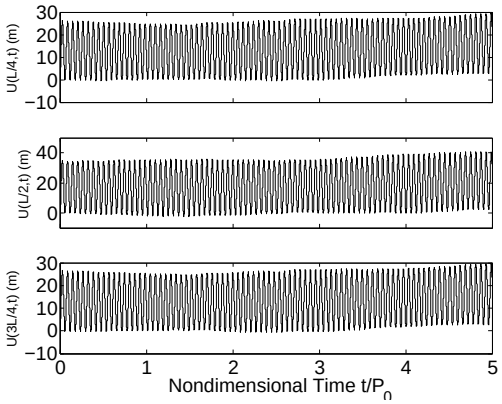

(a) Transverse displacement U

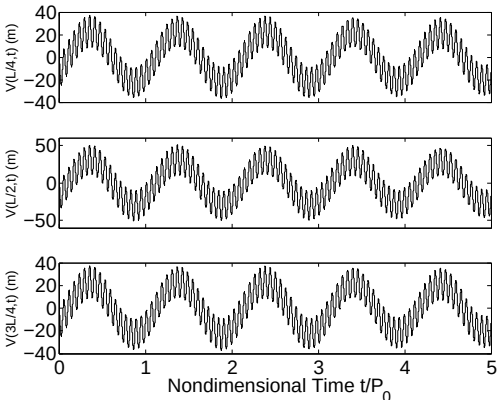

(b) Transverse displacement V

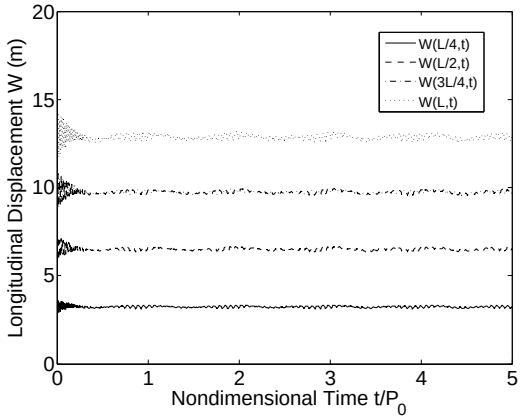

(c) Longitudinal displacement W

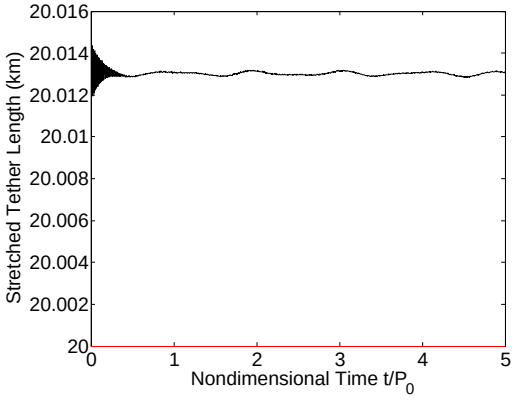

(d) Stretched tether length

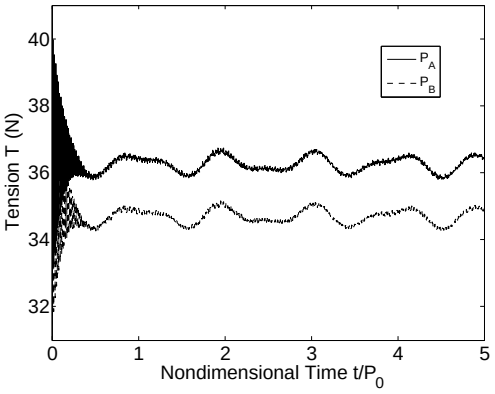

(e) Tension at the tether attachment points

Figure 3.23: Time history of the elastic vibrations of the tether predicted by the top-level computational model for Example 2

3.7 Summary of the Top-Level System Model

In this chapter we presented the top-level system model used in this work to study the dynamics and control of spinning and electrodynamic TSS. The system is modeled as two finite rigid bodies connected by a tether that is modeled as an elastic string. The magnetic field of the central body is modeled as a tilted dipole that rotates with the central body. A mathematical model for the system dynamics was developed that consists of equations of motion governing the orbital motion of the system, the attitude motion of the end bodies, and the motion of the tether. Two different computational models for the mathematical model were developed, each employing a different method of spatially discretizing the partial differential equations governing the elastic vibrations of the tether. The first computational model uses the assumed modes method, and the second computational model uses the finite element method. The computer codes used to solve the discretized equations of motion for each computational model were verified using the method of manufactured solutions, which provides a means of showing that the computer codes are error-free. A qualitative analysis of the two computational models was conducted in which we concluded that the FEM computational model is better suited to the study of TSS dynamics and control than the AMM computational model presented in this work. This conclusion was based on the fact that the AMM computational model produces bad results for large numbers of longitudinal assumed modes. In the final section of this chapter we presented two examples of numerical solutions produced by the FEM computational model, which we termed the top-level computational model.

In the remainder of this dissertation, the top-level computational model is used to validate various results and predictions obtained using lower-level system models and their associated computational models. Because adequate experimental data on TSS dynamics and control is not available, no predictions related to TSS dynamics and control can truly be validated. However, the top-level system model is intended to be a sufficiently accurate representation of the actual physical system, so numerical solutions produced by the top-level computational model are used in the place of experimental data. If a result obtained from a lower-level computational model compares favorably to numerical solutions determined from the top-level computational model, then the result will be considered validated.

Chapter 4

Dynamics of Spinning Tethered Satellite Systems

The proposal of TSS such as MXER has brought about a renewed interest in the study of spinning TSS. As mentioned in §1.3.1, a great deal of research has already been conducted on spinning TSS dynamics; however, there remain several areas of the subject that must be addressed. In particular, a complete picture of the dynamics of the tether in spinning TSS has yet to be completed, and virtually no effort has been made to validate results obtained using simplified models. The objective of this chapter is to address these two unresolved issues.

In this chapter we present a detailed analysis of the dynamics of the tether in spinning TSS. The analysis is performed using a lower-level system model that is a simplification of the top-level system model presented in Ch. 3. The mathematical model is derived, and various elements of the computational model are presented. Specifically, we derive analytical results pertaining to the out-of-plane pendular motion and transverse vibrations of the tether. All of the results obtained from the lower-level system model are compared to numerical simulations determined using the top-level computational model for the purposes of validation. In the cases for which the lower-level results are not validated we present an analysis of the modeling assumptions affecting the results, and recommend appropriate changes to the lower-level system model.

4.1 Physical System and Conceptual Model

The physical system under consideration is a spinning TSS in orbit around an arbitrary central body. The system consists of two end bodies connected by a single tether. In this particular study we are not considering any effects due to electrodynamic forcing, so the tether does not carry any electrical current.

The conceptual model for the lower-level system model used in this study is formulated by starting with the top-level conceptual model and making several additional simplifying assumptions. We are primarily interested in the dynamics of the tether, so these assumptions are intended to isolate the tether dynamics from the other aspects of the system dynamics. First, we assume that the end body attitude motion has a negligible influence on the tether and model the end bodies as point masses. Second, we assume that the primary end body is much more massive than the secondary end body and the tether such that the primary end body orbits the central body on an unperturbed circular orbit. Further, we assume that any effects on the tether dynamics due to the eccentricity of the system orbit are negligible, meaning that we can take the primary end body as constrained to an unperturbed circular orbit. These assumptions have the effect of eliminating or prescribing all aspects of the system dynamics except the motion of the tether.

Recall that the motion of the tether can be decomposed into a pendular mode and an elastic vibration mode. Because the elastic vibrations are expected to remain small relative to the length of the tether in a typical spinning TSS, we assume that the pendular motion of the tether is unaffected by the elastic vibrations. We also assume that the longitudinal vibrations are negligible, such that the transverse vibrations are the only relevant aspects of the elastic vibrations. Because the transverse vibrations are assumed to be small, we further assume that they do not have any effect on the tension in the tether, such that the tension is the same as that of an equivalent rigid tether. Under these assumptions, the motion of the tether can be viewed as transverse vibrations superimposed upon the motion of a rigid tether. Note that similar conceptual models for spinning TSS dynamics to the one used in this chapter were considered in Refs. [5] and [8].

4.2 Mathematical Model

A diagram of the system under the modeling assumptions discussed above is shown in Fig. 4.1. The primary end body is denoted $\mathcal{A}$, and the secondary end body is denoted $\mathcal{B}$. The center of the central body is the point O, and the position of $\mathcal{A}$ relative to O is $\vec{\mathbf{r}}_{\mathrm{A}}$. Note that $\vec{\mathbf{r}}_{\mathrm{A}}$ is prescribed for all time because $\mathcal{A}$ is constrained to an unperturbed circular orbit. Let ds be a differential tether length element located at an arclength s along the tether from $\mathcal{A}$, and let the position of ds relative to $\mathcal{A}$ be $\vec{\mathbf{r}}$.

4.2.1 Coordinate Frames and Kinematics

Three coordinate frames are used in the development of the mathematical model. Let $\mathcal{F}_N$ be the inertial frame with coordinate axes $\hat{\mathbf{n}}_i$. The inertial frame is centered at O with $\hat{\mathbf{n}}_3$ aligned with the spin axis of the central body, and the $\hat{\mathbf{n}}_1 - \hat{\mathbf{n}}_2$ plane defining the equatorial plane of the central body.

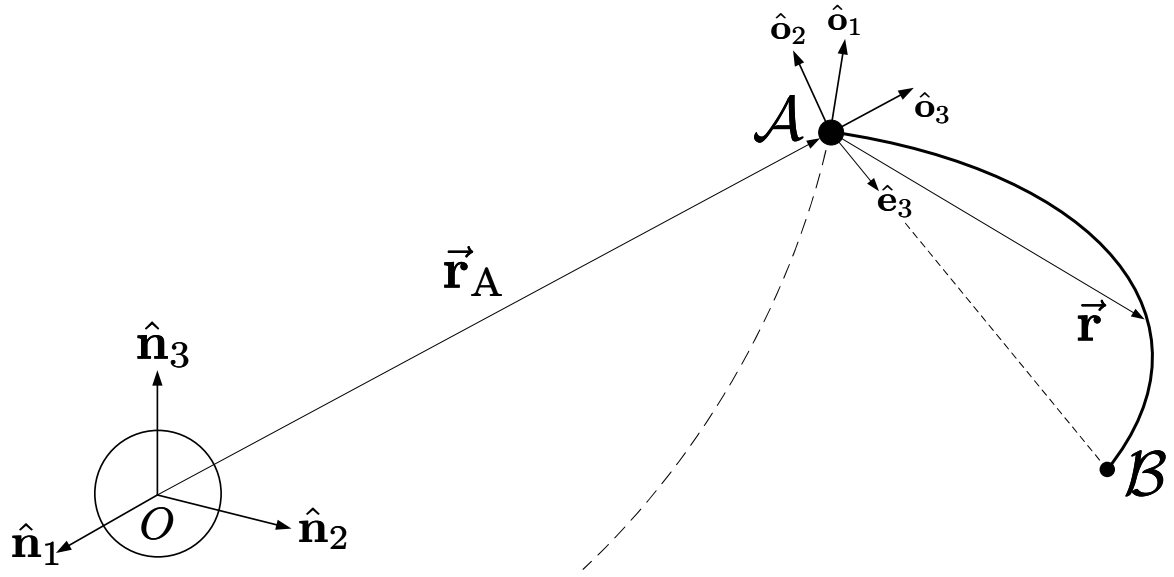

Figure 4.1: Diagram of lower-level spinning TSS model

The orbital frame $\mathcal{F}_O$, with coordinate axes $\hat{\mathbf{o}}_i$, is defined in a similar manner as in Sec. 3.2.1 for the top-level mathematical model. The axis $\hat{\mathbf{o}}_3$ points from O to $\mathcal{A}$, the axis $\hat{\mathbf{o}}_2$ points in the direction of the angular momentum of the $\mathcal{A}$ orbit, and $\hat{\mathbf{o}}_1$ completes the right-handed triad. Because $\mathcal{A}$ is constrained to an unperturbed circular orbit, the angular velocity of $\mathcal{F}_O$ relative to $\mathcal{F}_N$ is

$$\vec{\boldsymbol{\omega}}_{\mathrm{O/N}} = \Omega_A \hat{\mathbf{o}}_2 \tag{4.1}$$

where Ω_A is the constant angular rate of the $\mathcal{A}$ orbit. Defining r_A as the constant orbit radius of $\mathcal{A}$, Ω_A and r_A are related by

$$r_A^3 \Omega_A^2 = \mu \tag{4.2}$$

where μ is the gravitational parameter of the central body. The angular acceleration of $\mathcal{F}_O$ relative to $\mathcal{F}_N$ is zero because $\vec{\boldsymbol{\omega}}_{\mathrm{O/N}}$ is constant.

The tether-fixed frame $\mathcal{F}_E$, with coordinate axes $\hat{\mathbf{e}}_i$, is defined in the same manner as in §3.2.1 for the top-level mathematical model. The orbital frame is transformed to $\mathcal{F}_E$ by performing a 2-1 Euler rotation sequence through the angles α and $-\beta$ such that $\hat{\mathbf{e}}_3$ points from $\mathcal{A}$ to $\mathcal{B}$. The DCM that maps $\mathcal{F}_O$ to $\mathcal{F}_E$ is given by Eq. (3.19), and the angular velocity of $\mathcal{F}_E$ relative to $\mathcal{F}_O$ is given by Eq. (3.20).

4.2.2 Tether Geometry

As discussed in §3.2.2 for the top-level mathematical model, the position of a differential tether element relative to $\mathcal{A}$ can be expressed as

$$\vec{\mathbf{r}}(\bar{s},t) = \bar{s}\hat{\mathbf{e}}_3 + \vec{\mathbf{u}}(\bar{s},t) \tag{4.3}$$

where $\bar{s}$ is the unstretched arclength and $\vec{\mathbf{u}}$ is the displacement of the tether away from its unstretched state. Because we assume that the longitudinal displacement is negligible,

$$\vec{\mathbf{u}} = U(\bar{s},t)\hat{\mathbf{e}}_1 + V(\bar{s},t)\hat{\mathbf{e}}_2 \tag{4.4}$$

where U and V are transverse displacements, and Eq. (4.3) becomes

$$\vec{\mathbf{r}}(\bar{s},t) = U(\bar{s},t)\hat{\mathbf{e}}_1 + V(\bar{s},t)\hat{\mathbf{e}}_2 + \bar{s}\hat{\mathbf{e}}_3 \tag{4.5}$$

Recall that the unit tangent vector of the tether is defined by Eq. (3.24). Using Eq. (4.5) in Eq. (3.24), we have

$$\hat{\boldsymbol{\tau}}(\bar{s},t) = \frac{\partial U}{\partial \bar{s}}\frac{\partial \bar{s}}{\partial s}\hat{\mathbf{e}}_1 + \frac{\partial V}{\partial \bar{s}}\frac{\partial \bar{s}}{\partial s}\hat{\mathbf{e}}_2 + \frac{\partial \bar{s}}{\partial s}\hat{\mathbf{e}}_3 \tag{4.6}$$

Because the transverse displacements are assumed to remain small, we make the approximation

$$\frac{\partial \bar{s}}{\partial s} \approx 1 \tag{4.7}$$

such that the unit tangent vector is written as

$$\hat{\boldsymbol{\tau}}(\bar{s},t) = \frac{\partial U}{\partial \bar{s}}\hat{\mathbf{e}}_1 + \frac{\partial V}{\partial \bar{s}}\hat{\mathbf{e}}_2 + \hat{\mathbf{e}}_3 \tag{4.8}$$

Using Eq. (4.8), the tension in the tether is expressed as

$$\begin{aligned}\vec{\mathbf{T}}(\bar{s},t) &= T(\bar{s},t)\hat{\boldsymbol{\tau}}(\bar{s},t) \\ &= T\left(\frac{\partial U}{\partial \bar{s}}\hat{\mathbf{e}}_1 + \frac{\partial V}{\partial \bar{s}}\hat{\mathbf{e}}_2 + \hat{\mathbf{e}}_3\right)\end{aligned} \tag{4.9}$$

where T is the scalar tension in the tether. In this mathematical model we do not relate T to the geometry of the tether, as done in the top-level mathematical model. Instead, we use an approximate expression for the tension that is derived by assuming that the transverse displacements do not affect the tension, which is in accordance with the assumptions used in the model. This derivation is presented later in this section.

4.2.3 Pendular Equations of Motion

Because we assume that the elastic vibrations of the tether do not affect the pendular motion of the tether, we derive the equations governing the pendular motion by assuming that the tether remains undeformed and aligned with $\hat{\mathbf{e}}_3$. In this case, the entire system acts as a rigid body, and the equations governing its motion are derived by treating it as a rigid body.

Applying Euler's rotational equation to the undeformed system, we have

$$\vec{\mathbf{I}}_{\mathrm{C}} \cdot \dot{\vec{\boldsymbol{\omega}}}_{\mathrm{E/N}} + \vec{\boldsymbol{\omega}}_{\mathrm{E/N}} \times \vec{\mathbf{I}}_{\mathrm{C}} \cdot \vec{\boldsymbol{\omega}}_{\mathrm{E/N}} = \vec{\mathbf{M}}_{\mathrm{C}} \tag{4.10}$$

where $\vec{\mathbf{I}}_{\mathrm{C}}$ is the centroidal moment of inertia tensor of the system and $\vec{\mathbf{M}}_{\mathrm{C}}$ is the total external moment acting about the system mass center. Note that $\vec{\boldsymbol{\omega}}_{\mathrm{E/N}}$ is used as the body angular velocity in Eq. (4.10) because the undeformed system remains aligned with $\hat{\mathbf{e}}_3$, so $\mathcal{F}_E$ is a body-fixed frame for the undeformed system. Recall that one of the assumptions made in formulating the conceptual model is that $\mathcal{A}$ is much more massive than $\mathcal{B}$ and the tether, such that $\mathcal{A}$ remains on an unperturbed circular orbit. Another consequence of this assumption is that the system mass center and $\mathcal{A}$ are essentially the same point, and we can approximate Eq. (4.10) as

$$\vec{\mathbf{I}}_{\mathrm{A}} \cdot \dot{\vec{\boldsymbol{\omega}}}_{\mathrm{E/N}} + \vec{\boldsymbol{\omega}}_{\mathrm{E/N}} \times \vec{\mathbf{I}}_{\mathrm{A}} \cdot \vec{\boldsymbol{\omega}}_{\mathrm{E/N}} = \vec{\mathbf{M}}_{\mathrm{A}} \tag{4.11}$$

where $\vec{\mathbf{I}}_{\mathrm{A}}$ is the moment of inertia tensor of the system about $\mathcal{A}$ and $\vec{\mathbf{M}}_{\mathrm{A}}$ is the total external moment acting on the system about $\mathcal{A}$. Because all of the system mass in the undeformed system lies entirely along the $\hat{\mathbf{e}}_3$ axis, $\vec{\mathbf{I}}_{\mathrm{A}}$ is defined as

$$\vec{\mathbf{I}}_{\mathrm{A}} = I_A(\mathbf{1} - \hat{\mathbf{e}}_3\hat{\mathbf{e}}_3) \tag{4.12}$$

where I_A is the scalar moment of inertia of the system about O and $\mathbf{1}$ is the identity tensor. Combining Eqs. (3.20) and (4.1), the angular velocity and acceleration of $\mathcal{F}_E$ relative to $\mathcal{F}_N$ are

$$\vec{\boldsymbol{\omega}}_{\mathrm{E/N}} = -\dot{\beta}\hat{\mathbf{e}}_1 + (\dot{\alpha} + \Omega_A)\cos\beta\hat{\mathbf{e}}_2 + (\dot{\alpha} + \Omega_A)\sin\beta\hat{\mathbf{e}}_3 \tag{4.13}$$

$$\dot{\vec{\boldsymbol{\omega}}}_{\mathrm{E/N}} = -\ddot{\beta}\hat{\mathbf{e}}_1 + [\ddot{\alpha}\cos\beta - (\dot{\alpha} + \Omega_A)\dot{\beta}\sin\beta]\hat{\mathbf{e}}_2 + [\ddot{\alpha}\sin\beta + (\dot{\alpha} + \Omega_A)\dot{\beta}\cos\beta]\hat{\mathbf{e}}_3 \tag{4.14}$$

The external moment acting on the system about $\mathcal{A}$ is due entirely to the gravity-gradient acting over the length of the system. Because the length of the system is small relative to the orbit radius of the system, we use a linear approximation for the gravity-gradient torque[23]

$$\vec{\mathbf{M}}_{\mathrm{A}} = 3\Omega_A^2\hat{\mathbf{o}}_3 \times \vec{\mathbf{I}}_{\mathrm{A}} \cdot \hat{\mathbf{o}}_3 \tag{4.15}$$

Combining Eqs. (4.11–4.15) and expressing the result relative to $\mathcal{F}_E$, we find that the equations governing the pendular motion of the tether are

$$\ddot{\alpha}\cos\beta - 2(\dot{\alpha} + \Omega_A)\dot{\beta}\sin\beta + 3\Omega_A^2\sin\alpha\cos\alpha\cos\beta = 0 \tag{4.16}$$

$$\ddot{\beta} + [(\dot{\alpha} + \Omega_A)^2 + 3\Omega_A^2\cos^2\alpha]\sin\beta\cos\beta = 0 \tag{4.17}$$

Note that these equations are identical to the equations governing the motion of a dumbbell satellite constrained to a circular orbit.[11] This makes sense, of course, because the undeformed system is in fact a dumbbell satellite constrained to a circular orbit. This fact will be utilized when analyzing Eqs. (4.16) and (4.17) later in this chapter.

4.2.4 Transverse Vibration Equations of Motion

The equations of motion for the transverse vibrations of the tether are derived in a similar manner as the elastic vibration equations of motion for the top-level mathematical model. Following the steps outlined in §3.2.5 and omitting the electrodynamic force, the equation of motion of the tether is

$$\ddot{\vec{\mathbf{r}}}_{\mathrm{T}} = -\frac{\mu}{r_T^3}\vec{\mathbf{r}}_{\mathrm{T}} + \frac{1}{\bar{\rho}}\frac{\partial \vec{\mathbf{T}}}{\partial \bar{s}} \tag{4.18}$$

where $\vec{\mathbf{r}}_{\mathrm{T}}$ is the position of a differential tether element relative to O, r_T is the magnitude of $\vec{\mathbf{r}}_{\mathrm{T}}$, and $\bar{\rho}$ is the linear mass density of the undeformed tether. Noting that

$$\vec{\mathbf{r}}_{\mathrm{T}} = \vec{\mathbf{r}}_{\mathrm{A}} + \vec{\mathbf{r}} \tag{4.19}$$

Eq. (4.18) is rewritten as

$$\ddot{\vec{\mathbf{r}}} = -\frac{\mu}{r_T^3}\vec{\mathbf{r}}_{\mathrm{T}} + \frac{1}{\bar{\rho}}\frac{\partial \vec{\mathbf{T}}}{\partial \bar{s}} - \ddot{\vec{\mathbf{r}}}_{\mathrm{A}} \tag{4.20}$$

Using Eq. (4.9), the tension partial derivative term in Eq. (4.20) is

$$\frac{\partial \vec{\mathbf{T}}}{\partial \bar{s}} = \left(T\frac{\partial^2 U}{\partial \bar{s}^2} + \frac{\partial T}{\partial \bar{s}}\frac{\partial U}{\partial \bar{s}}\right)\hat{\mathbf{e}}_1 + \left(T\frac{\partial^2 V}{\partial \bar{s}^2} + \frac{\partial T}{\partial \bar{s}}\frac{\partial V}{\partial \bar{s}}\right)\hat{\mathbf{e}}_2 + \frac{\partial T}{\partial \bar{s}}\hat{\mathbf{e}}_3 \tag{4.21}$$

Because $\mathcal{A}$ is constrained to a circular orbit,

$$\begin{aligned}\ddot{\vec{\mathbf{r}}}_{\mathrm{A}} &= -r_A\Omega_A^2\hat{\mathbf{o}}_3 \\ &= r_A\Omega_A^2(\sin\alpha\hat{\mathbf{e}}_1 + \cos\alpha\sin\beta\hat{\mathbf{e}}_2 - \cos\alpha\cos\beta\hat{\mathbf{e}}_3)\end{aligned} \tag{4.22}$$

As done in the derivation of the pendular equations of motion, because the length of the tether is small relative to the orbit radius of the system the gravitational acceleration term is approximated by linearizing about the position of $\mathcal{A}$, such that

$$-\frac{\mu}{r_T^3}\vec{\mathbf{r}}_{\mathrm{T}} = g_1\hat{\mathbf{e}}_1 + g_2\hat{\mathbf{e}}_2 + g_3\hat{\mathbf{e}}_3 \tag{4.23}$$

where

$$g_1 = \Omega_A^2[r_A\sin\alpha + U(3\sin^2\alpha - 1) + 3V\sin\alpha\cos\alpha\sin\beta - 3\bar{s}\sin\alpha\cos\alpha\cos\beta] \tag{4.24}$$

$$g_2 = \Omega_A^2[\, r_A \cos\alpha \sin\beta + 3U \sin\alpha \cos\alpha \sin\beta + V(3\cos^2\alpha \sin^2\beta - 1) - 3\bar{s}\cos^2\alpha \sin\beta \cos\beta] \tag{4.25}$$

$$g_3 = -\Omega_A^2[\, r_A \cos\alpha \cos\beta + 3U \sin\alpha \cos\alpha \cos\beta + 3V \cos^2\alpha \sin\beta \cos\beta + \bar{s}(1 - 3\cos^2\alpha \cos^2\beta)] \tag{4.26}$$

Using the expression for $\vec{\mathbf{r}}$ defined in Eq. (4.5), the left-hand side of Eq. (4.20) is written as

$$\ddot{\vec{\mathbf{r}}} = \ddot{r}_1\hat{\mathbf{e}}_1 + \ddot{r}_2\hat{\mathbf{e}}_2 + \ddot{r}_3\hat{\mathbf{e}}_3 \tag{4.27}$$

where

$$\ddot{r}_1 = \ddot{U} - 2\dot{V}(\dot{\alpha} + \Omega_A^2)\sin\beta - U(\dot{\alpha} + \Omega_A^2)^2 - V[\ddot{\alpha}\sin\beta + 2(\dot{\alpha} + \Omega_A)\dot{\beta}\cos\beta] + \bar{s}[\ddot{\alpha}\cos\beta - 2(\dot{\alpha} + \Omega_A)\dot{\beta}\sin\beta] \tag{4.28}$$

$$\ddot{r}_2 = \ddot{V} + 2\dot{U}(\dot{\alpha} + \Omega_A)\sin\beta + U\ddot{\alpha}\sin\beta - V[(\dot{\alpha} + \Omega_A)^2\sin^2\beta + \dot{\beta}^2] + \bar{s}[\ddot{\beta} + (\dot{\alpha} + \Omega_A)^2\sin\beta\cos\beta] \tag{4.29}$$

$$\ddot{r}_3 = -2\dot{U}(\dot{\alpha} + \Omega_A)\cos\beta - 2\dot{V}\dot{\beta} - U\ddot{\alpha}\cos\beta - V[\ddot{\beta} - (\dot{\alpha} + \Omega_A)^2\sin\beta\cos\beta] - \bar{s}[(\dot{\alpha} + \Omega_A)^2\cos^2\beta + \dot{\beta}^2] \tag{4.30}$$

Combining Eqs. (4.20–4.30) and taking the components in the $\hat{\mathbf{e}}_1$ and $\hat{\mathbf{e}}_2$ directions, the equations of motion for the transverse vibrations of the tether are

$$\begin{aligned} &\ddot{U} - 2\dot{V}(\dot{\alpha} + \Omega_A^2)\sin\beta - U[(\dot{\alpha} + \Omega_A^2)^2 + \Omega_A^2(3\sin^2\alpha - 1)] \\ &- V[\ddot{\alpha}\sin\beta + 2(\dot{\alpha} + \Omega_A)\dot{\beta}\cos\beta + 3\Omega_A^2\sin\alpha\cos\alpha\sin\beta] \\ &+ \bar{s}[\ddot{\alpha}\cos\beta - 2(\dot{\alpha} + \Omega_A)\dot{\beta}\sin\beta + 3\Omega_A^2\sin\alpha\cos\alpha\cos\beta] \\ &= \frac{1}{\bar{\rho}}\left(T\frac{\partial^2 U}{\partial\bar{s}^2} + \frac{\partial T}{\partial\bar{s}}\frac{\partial U}{\partial\bar{s}}\right) \end{aligned} \tag{4.31}$$

$$\begin{aligned} &\ddot{V} + 2\dot{U}(\dot{\alpha} + \Omega_A)\sin\beta + U(\ddot{\alpha}\sin\beta - 3\Omega_A^2\sin\alpha\cos\alpha\sin\beta) \\ &- V[(\dot{\alpha} + \Omega_A)^2\sin^2\beta + \dot{\beta}^2] \\ &+ \bar{s}[\ddot{\beta} + (\dot{\alpha} + \Omega_A)^2\sin\beta\cos\beta + 3\Omega_A^2\cos^2\alpha\sin\beta\cos\beta] \\ &= \frac{1}{\bar{\rho}}\left(T\frac{\partial^2 V}{\partial\bar{s}^2} + \frac{\partial T}{\partial\bar{s}}\frac{\partial V}{\partial\bar{s}}\right) \end{aligned} \tag{4.32}$$

Using the pendular equations of motion defined in Eqs. (4.16) and (4.17), the transverse vibrations equations of motion reduce to

$$\begin{aligned} &\ddot{U} - 2\dot{V}(\dot{\alpha} + \Omega_A^2)\sin\beta - U[(\dot{\alpha} + \Omega_A^2)^2 + \Omega_A^2(3\sin^2\alpha - 1)] - 2V(\dot{\alpha} + \Omega_A)\dot{\beta}\sec\beta \\ &= \frac{1}{\bar{\rho}}\left(T\frac{\partial^2 U}{\partial\bar{s}^2} + \frac{\partial T}{\partial\bar{s}}\frac{\partial U}{\partial\bar{s}}\right) \end{aligned} \tag{4.33}$$

$$\begin{aligned}
&\ddot{V} + 2\dot{U}(\dot{\alpha}+\Omega_A)\sin\beta + 2U[(\dot{\alpha}+\Omega_A)\dot{\beta}\tan\beta - 3\Omega_A^2\sin\alpha\cos\alpha]\sin\beta \\
&- V[(\dot{\alpha}+\Omega_A)^2\sin^2\beta + \dot{\beta}^2 + \Omega_A^2(3\cos^2\alpha\sin^2\beta - 1)] \\
&= \frac{1}{\bar{\rho}}\left(T\frac{\partial^2 V}{\partial \bar{s}^2} + \frac{\partial T}{\partial \bar{s}}\frac{\partial V}{\partial \bar{s}}\right)
\end{aligned} \tag{4.34}$$

To complete the equations of motion for the transverse vibrations we need an expression for the tension in the tether. Taking the component of Eq. (4.20) in the $\hat{\mathbf{e}}_3$ direction, we have

$$\begin{aligned}
&- 2\dot{U}(\dot{\alpha}+\Omega_A)\cos\beta - 2\dot{V}\dot{\beta} - U(\ddot{\alpha}\cos\beta - 3\Omega_A^2\sin\alpha\cos\alpha\cos\beta) \\
&- V[\ddot{\beta} - (\dot{\alpha}+\Omega_A)^2\sin\beta\cos\beta - 3\Omega_A^2\cos^2\alpha\sin\beta\cos\beta] \\
&- \bar{s}[(\dot{\alpha}+\Omega_A)^2\cos^2\beta + \dot{\beta}^2 + \Omega_A^2(3\cos^2\alpha\cos^2\beta - 1)] \\
&= \frac{1}{\bar{\rho}}\frac{\partial T}{\partial \bar{s}}
\end{aligned} \tag{4.35}$$

Now, recall that one of the assumptions made in the formulation of the conceptual model is that the transverse vibrations do no affect the tension in the tether. Neglecting the transverse vibration terms in Eq. (4.35), we find that the variation of the tension over the tether is

$$\frac{\partial T}{\partial \bar{s}} = -\bar{\rho}\bar{s}[(\dot{\alpha}+\Omega_A)^2\cos^2\beta + \dot{\beta}^2 + \Omega_A^2(3\cos^2\alpha\cos^2\beta - 1)] \tag{4.36}$$

Integrating Eq. (4.36) with respect to $\bar{s}$, we obtain

$$T(\bar{s},t) = -\frac{1}{2}\bar{\rho}\bar{s}^2[(\dot{\alpha}+\Omega_A)^2\cos^2\beta + \dot{\beta}^2 + \Omega_A^2(3\cos^2\alpha\cos^2\beta - 1)] + C \tag{4.37}$$

where C is an integration constant. To determine C, we consider the motion of $\mathcal{B}$, which defines the conditions of the tether at $\bar{s} = L$. Applying Newton's Second Law to $\mathcal{B}$, the equation of motion of $\mathcal{B}$ is

$$m_B\ddot{\vec{\mathbf{r}}}_{\mathrm{B}} = -\frac{m_B\mu}{r_B^3}\vec{\mathbf{r}}_{\mathrm{B}} - \vec{\mathbf{T}}(L,t) \tag{4.38}$$

where $\vec{\mathbf{r}}_{\mathrm{B}} = \vec{\mathbf{r}}_{\mathrm{A}} + \vec{\mathbf{r}}(L,t)$ is the position of $\mathcal{B}$ relative to O and m_B is the mass of $\mathcal{B}$. Using the linear approximation for the gravitational acceleration term evaluated at $\bar{s} = L$ and taking the component of Eq. (4.38) in the $\hat{\mathbf{e}}_3$ direction, we find that the tension at $\mathcal{B}$ is

$$T(L,t) = m_B L[(\dot{\alpha}+\Omega_A)^2\cos^2\beta + \dot{\beta}^2 + \Omega_A^2(3\cos^2\alpha\cos^2\beta - 1)] \tag{4.39}$$

Setting $\bar{s} = L$ in Eq. (4.37), we must also have

$$T(L,t) = -\frac{1}{2}\bar{\rho}L^2[(\dot{\alpha}+\Omega_A)^2\cos^2\beta + \dot{\beta}^2 + \Omega_A^2(3\cos^2\alpha\cos^2\beta - 1)] + C \tag{4.40}$$

Equating Eqs. (4.39) and (4.40), we find that the integration constant must be

$$C = c_A[(\dot{\alpha}+\Omega_A)^2\cos^2\beta + \dot{\beta}^2 + \Omega_A^2(3\cos^2\alpha\cos^2\beta - 1)] \tag{4.41}$$

where we have defined the quantity

$$c_A = m_B L + \frac{1}{2}\bar{\rho} L^2 \tag{4.42}$$

Note that c_A is the first moment of inertia of the undeformed system about $\mathcal{A}$. Using Eq. (4.41) in Eq. (4.37), the tension in the tether is expressed as

$$T(\bar{s},t) = [(\dot{\alpha}+\Omega_A)^2\cos^2\beta + \dot{\beta}^2 + \Omega_A^2(3\cos^2\alpha\cos^2\beta - 1)]\left(c_A - \frac{1}{2}\bar{\rho}\bar{s}^2\right) \tag{4.43}$$

Using Eq. (4.43) in Eqs. (4.33) and (4.34), we obtain

$$\begin{aligned}
&\ddot{U} - 2\dot{V}(\dot{\alpha}+\Omega_A^2)\sin\beta - U[(\dot{\alpha}+\Omega_A^2)^2 + \Omega_A^2(3\sin^2\alpha - 1)] - 2V(\dot{\alpha}+\Omega_A)\dot{\beta}\sec\beta \\
&= [(\dot{\alpha}+\Omega_A)^2\cos^2\beta + \dot{\beta}^2 + \Omega_A^2(3\cos^2\alpha\cos^2\beta - 1)]\left[\left(\frac{c_A}{\bar{\rho}} - \frac{\bar{s}^2}{2}\right)\frac{\partial^2 U}{\partial \bar{s}^2} - \bar{s}\frac{\partial U}{\partial \bar{s}}\right]
\end{aligned} \tag{4.44}$$

$$\begin{aligned}
&\ddot{V} + 2\dot{U}(\dot{\alpha}+\Omega_A)\sin\beta + 2U[(\dot{\alpha}+\Omega_A)\dot{\beta}\tan\beta - 3\Omega_A^2\sin\alpha\cos\alpha]\sin\beta \\
&- V[(\dot{\alpha}+\Omega_A)^2\sin^2\beta + \dot{\beta}^2 + \Omega_A^2(3\cos^2\alpha\sin^2\beta - 1)] \\
&= [(\dot{\alpha}+\Omega_A)^2\cos^2\beta + \dot{\beta}^2 + \Omega_A^2(3\cos^2\alpha\cos^2\beta - 1)]\left[\left(\frac{c_A}{\bar{\rho}} - \frac{\bar{s}^2}{2}\right)\frac{\partial^2 V}{\partial \bar{s}^2} - \bar{s}\frac{\partial V}{\partial \bar{s}}\right]
\end{aligned} \tag{4.45}$$

Equations (4.44) and (4.45) are a set of coupled, second-order partial differential equations that govern the transverse vibrations of the tether. Because there can be no transverse displacement at either end of the tether, the boundary conditions of Eqs. (4.44) and (4.45) are

$$U(0,t) = U(L,t) = 0 \tag{4.46}$$

$$V(0,t) = V(L,t) = 0 \tag{4.47}$$

4.2.5 Nondimensional Equations of Motion

The complete set of equations of motion governing the motion of the tether is given by Eqs. (4.16), (4.17), and (4.44–4.47). These equations are cast in a nondimensional form by first defining the nondimensional time

$$\tau = \Omega_A t \tag{4.48}$$

and denoting derivatives with respect to τ as $\mathring{(\,)}$. Note that τ is the angle through which $\mathcal{A}$ moves in its circular orbit over a time t. Using the nondimensional time, the pendular equations of motion are written in nondimensional form as

$$\mathring{\dot{\alpha}}\cos\beta - 2(\mathring{\alpha}+1)\mathring{\beta}\sin\beta + 3\sin\alpha\cos\alpha\cos\beta = 0 \tag{4.49}$$

$$\mathring{\dot{\beta}} + [(\mathring{\alpha}+1)^2 + 3\cos^2\alpha]\sin\beta\cos\beta = 0 \tag{4.50}$$

To cast the transverse vibration equations of motion in nondimensional form we also define the nondimensional spatial coordinate

$$x = \frac{\bar{s}}{L} \tag{4.51}$$

and denote derivatives with respect to x as $(\,)'$. Let the nondimensional transverse displacements be defined as

$$u = \frac{U}{L} \tag{4.52}$$

$$v = \frac{V}{L} \tag{4.53}$$

and define the nondimensional parameter

$$\gamma = \frac{\bar{\rho} L^2}{c_A} \tag{4.54}$$

Note that, using Eq. (4.42), we can also express γ as

$$\gamma = \frac{\bar{\rho} L}{m_B + \frac{1}{2}\bar{\rho} L} \tag{4.55}$$

From Eq. (4.55), we can see that $\gamma \in [0, 2]$, with $\gamma = 0$ corresponding to a massless tether and $\gamma = 2$ corresponding to $m_B = 0$. Using Eqs. (4.48) and (4.51–4.55), the transverse vibration equations of motion and boundary conditions are written in nondimensional form as

$$\begin{aligned} &\mathring{\mathring{u}} - 2\mathring{v}(\mathring{\alpha}+1)\sin\beta - u[(\mathring{\alpha}+1)^2 + 3\sin^2\alpha - 1] - 2v(\mathring{\alpha}+1)\mathring{\beta}\sec\beta \\ &= [(\mathring{\alpha}+1)^2\cos^2\beta + \mathring{\beta}^2 + 3\cos^2\alpha\cos^2\beta - 1]\left[\left(\frac{2-\gamma x^2}{2\gamma}\right)u'' - xu'\right] \end{aligned} \tag{4.56}$$

$$\begin{aligned} &\mathring{\mathring{v}} + 2\mathring{u}(\mathring{\alpha}+1)\sin\beta + 2u[(\mathring{\alpha}+1)\mathring{\beta}\tan\beta - 3\sin\alpha\cos\alpha]\sin\beta \\ &- v[(\mathring{\alpha}+1)^2\sin^2\beta + \mathring{\beta}^2 + 3\cos^2\alpha\sin^2\beta - 1] \\ &= [(\mathring{\alpha}+1)^2\cos^2\beta + \mathring{\beta}^2 + 3\cos^2\alpha\cos^2\beta - 1]\left[\left(\frac{2-\gamma x^2}{2\gamma}\right)v'' - xv'\right] \end{aligned} \tag{4.57}$$

$$u(0,\tau) = u(1,\tau) = 0 \tag{4.58}$$

$$v(0,\tau) = v(1,\tau) = 0 \tag{4.59}$$

Equations (4.49), (4.50), and (4.56–4.57) define the complete set of nondimensional equations of motion for the system. In the next two sections, several aspects of the computational model for the lower-level system model considered in this chapter are developed using these equations.

4.3 Computational Model: Pendular Motion of the Tether

In this section we develop several aspects of the lower-level computational model for the spinning TSS. Specifically, in this section we focus on the pendular motion of the tether. Recall that the equations governing the pendular motion of the tether, Eqs. (4.49) and (4.50), are the same as the attitude equations of motion for a dumbbell satellite constrained to a circular orbit acted upon only by gravity-gradient torque. A dumbbell satellite is a special type of rigid satellite model, so the analysis of the tether pendular motion is the same as the analysis of a spinning rigid body on a circular orbit acted upon only by gravity-gradient torque. Kane and Shippy[27] studied such a system by assuming that the deviations away from the nominal spinning trajectory were small and linearizing the equations of motion about the nominal spin. For small out-of-plane motion, the in-plane motion is not affected by the out-of-plane motion, and an exact solution for the in-plane motion was determined. This solution was used in the linearized equations for the out-of-plane motion, resulting in a system of homogeneous linear equations with periodic, time-varying coefficients. Floquet theory was applied to determine the stability properties of the out-of-plane motion for various combinations of satellite inertia parameters and average in-plane spin rate. Because of limitations in computing power at the time, only a few specific cases were considered; however, it was demonstrated that the out-of-plane motion is unstable for certain combinations of inertia parameters and average in-plane spin rate. Meirovitch and Wallace[40] used purely analytical methods to extend the analysis of Kane and Shippy by assuming that the satellite is nearly symmetric about the spin axis. This assumption cannot be applied to a spinning TSS, so the extended results of Meirvitch and Wallace do not apply to the present study of spinning TSS pendular motion. Kane[26] applied the same analysis methods used by Kane and Shippy to a nominally Earth-pointing satellite and showed that the out-of-plane motion is unstable for certain combinations of satellite inertia parameters and in-plane libration amplitude. Once again, limitations in computing power limited the analysis to a few specific cases. Breakwell and Pringle[9] later showed that the instability in the out-of-plane motion discovered by Kane is due to a nonlinear internal resonance within the system equations of motion.

The results outlined in the previous paragraph clearly indicate that the system model used in this chapter will predict unstable out-of-plane pendular motion for certain system configurations. The description of these instabilities is not complete, however, because previous research has only considered a handful of specific cases, or made assumptions about the system geometry that do not apply to a spinning TSS. Modern computing power allows us to make a complete description of the out-of-plane motion and any associated instabilities. In addition, the analysis of a spinning TSS requires the variation of only a single parameter because the inertia ratios are set values for any TSS. Because of this fact, the analysis presented in this section can be viewed as an application of the results of Refs. [27] and [26] to a specific type of spinning satellite (a TSS); however, the analysis presented in this section

provides a much more detailed and complete analysis for that specific case.

Following the analysis methods used in Refs. [27] and [26], we use the fact that the nominal pendular motion of the tether is a planar spin and linearize Eqs. (4.49) and (4.50) about $\beta = \mathring{\beta} = 0$ to obtain

$$\mathring{\mathring{\alpha}} + 3\sin\alpha\cos\alpha = 0 \tag{4.60}$$

$$\mathring{\mathring{\beta}} + [(\mathring{\alpha}+1)^2 + 3\cos^2\alpha]\beta = 0 \tag{4.61}$$

Note that in this approximation the in-plane pendular motion–the "spin" of the tether–is not affected by the small out-of-plane deviation. We can therefore solve Eq. (4.60) for α and use the solution in Eq. (4.61) to analyze the small out-of-plane deviations, thus providing a complete picture of the pendular motion of the tether in the viscinity of a nominal planar spinning trajectory[1].

4.3.1 Solution for In-Plane Motion

To determine the solution for the in-plane motion we first integrate Eq. (4.60) to obtain

$$\mathring{\alpha} = \pm\sqrt{h - 3\sin^2\alpha} \tag{4.62}$$

where the "+" is for systems with a positive angular rate and the "-" is for systems with a negative angular rate. The constant h serves as a measure of the energy of the in-plane pendular motion. In fact, h is actually a simplified version of the Hamiltonian of the pendular equations of motion,[5]

$$\mathcal{H} = (\mathring{\alpha}^2 + 3\sin^2\alpha)\cos^2\beta + \mathring{\beta}^2 + 4\sin^2\beta \tag{4.63}$$

Linearizing Eq. (4.63) for small β we arrive at the same expression given by Eq. (4.16), so h is a measure of the energy of the pendular motion assuming small out-of-plane motion. Plotting Eq. (4.62) in the $\alpha - \mathring{\alpha}$ plane for various values of h, we obtain the phase portrait shown in Fig. 4.2. No motion is possible for $h < 0$, and the in-plane motion is in equilibrium at $\alpha = \pm n\pi$ for $h = 0$. For $0 < h < 3$, the in-plane motion undergoes periodic oscillations about one of the equilibrium states, and for $h > 3$ the in-plane motion is a continuous rotation with the direction of the rotation determined by the sign of the initial rotation rate. The value $h = 3$ corresponds to separatrices that separate the regions of libration and rotation. The ovals in Fig. 4.2 correspond to regions of negative tension in the tether. Assuming small out-of-plane motion in Eq. (4.43) and changing to nondimensional variables, the tension in the tether is expressed as

$$T(x,\tau) = c_A\Omega_A^2[(\mathring{\alpha}+1)^2 + 3\cos^2\alpha - 1]\left(1 - \frac{1}{2}\gamma x^2\right) \tag{4.64}$$

[1]The analysis presented in this section is also presented in Ref. [19]

and we see that the tension in the tether becomes negative when

$$(\mathring{\alpha}+1)^2+3\cos^2\alpha-1<0 \tag{4.65}$$

The ovals in Fig. 4.2 enclose the regions in the $\alpha-\mathring{\alpha}$ plane that satisfy Eq. (4.65).

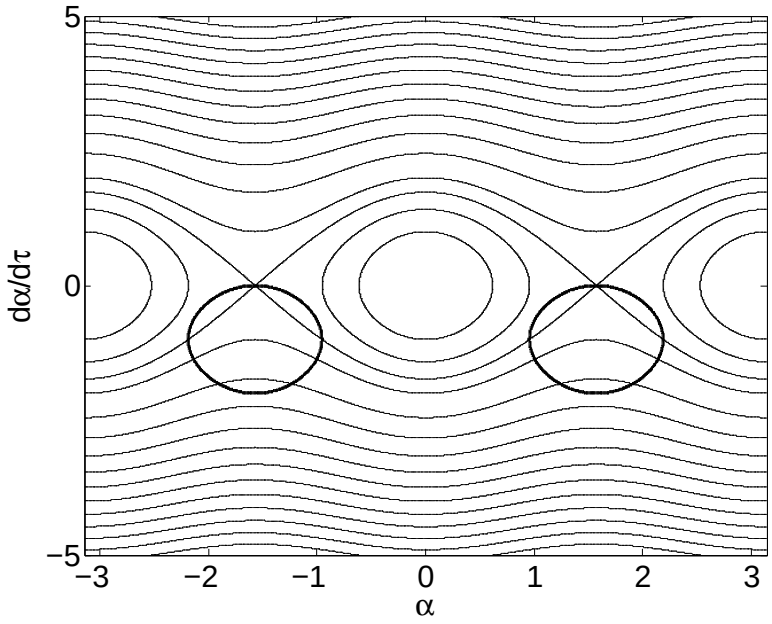

Figure 4.2: Phase portrait for in-plane motion assuming small out-of-plane motion

Returning to Eq. (4.62), define the quantity $\kappa^2=3/h$ such that

$$\frac{d\alpha}{\sqrt{1-\kappa^2\sin^2\alpha}}=\pm\sqrt{h}\,d\tau \tag{4.66}$$

Integrating Eq. (4.66), the in-plane angle must satisfy

$$\pm\sqrt{h}\,\tau+\psi=F(\alpha,\kappa) \tag{4.67}$$

where ψ is a constant and $F=F(\phi,k)$ is the incomplete elliptic integral of the first kind.[32] Solving Eq. (4.67) for α, the solution for the in-plane libration angle is

$$\alpha(\tau)=\begin{cases}\sin^{-1}\left(\frac{1}{\kappa}\mathrm{sn}\left(\sqrt{3}\,\tau+\psi,\frac{1}{\kappa}\right)\right), & h<3\\ \mathrm{am}(\pm\sqrt{h}\,\tau+\psi,\kappa), & h>3\end{cases} \tag{4.68}$$

where $\mathrm{am}(u,k)$ is the Jacobi amplitude, and $\mathrm{sn}(u,k)$ is a Jacobi elliptic function. See Lawden[32] for a complete theoretical treatment of the Jacobi elliptic functions. We have not

included the $h = 3$ case in Eq. (4.68) because it would most likely never be encountered in a real system, and is mostly of academic interest. Also, note that the "$\pm$" has been discarded in the oscillatory solution because there is no need to distinguish between solutions with positive and negative rotation rates when the motion is oscillatory. The constant ψ serves as a type of phase-angle in both of the solutions in Eq. (4.68), so the qualitative behavior of the motion is completely determined by the value of h. Without loss of generality, we can assume that $\psi = 0$, such that

$$\alpha(\tau) = \begin{cases} \sin^{-1}\left(\frac{1}{\kappa}\mathrm{sn}\left(\sqrt{3}\,\tau, \frac{1}{\kappa}\right)\right), & h < 3 \\ \\ \mathrm{am}(\pm\sqrt{h}\,\tau, \kappa), & h > 3 \end{cases} \tag{4.69}$$

This assumption has the effect of shifting the nondimensional time such that $\alpha(0) = 0$. Taking the derivative of Eq. (4.69), the in-plane angular rate can be expressed as

$$\mathring{\alpha} = \begin{cases} \sqrt{h}\,\mathrm{cn}\left(\sqrt{3}\,\tau, \frac{1}{\kappa}\right), & h < 3 \\ \\ \pm\sqrt{h}\,\mathrm{dn}(\sqrt{h}\,\tau, \kappa), & h > 3 \end{cases} \tag{4.70}$$

where $\mathrm{cn}(u, k)$ and $\mathrm{dn}(u, k)$ are Jacobi elliptic functions.[32] Note once again that for $h > 3$, the "+" sign corresponds to solutions with a positive rotation rate, and the "-" sign corresponds to solutions with a negative rotation rate.

For $h < 3$, the in-plane motion is oscillatory with a period of

$$T_\alpha = \frac{4K(\frac{1}{\kappa})}{\sqrt{3}} \tag{4.71}$$

where $K = K(k)$ is the complete elliptic integral of the first kind.[32] Figure 4.3 shows the number of in-plane oscillations per orbit as a function of h. As h approaches zero, the number of oscillations approaches $\sqrt{3}$, which is in agreement with the frequency of the in-plane oscillations obtained by assuming that α remains small.[5] As h approaches 3, the number of oscillations per orbit approaches zero as the motion approaches the separatrix separating oscillation and rotation. For $h > 3$, the in-plane motion becomes a rotation relative to the orbital frame, and is no longer periodic in the sense that trajectories in the phase space are closed. However, the motion is periodic in the sense that the in-plane motion completes one rotation relative to the orbital frame in a fixed amount of time. The rotational period is

$$T_\alpha = \frac{4K(\kappa)}{\sqrt{h}} \tag{4.72}$$

and the number of rotations per orbit is plotted in Fig. 4.4. As h decreases toward 3, the number of rotations per orbit approaches zero as the motion approaches the separatrix. As h increases away from 3, the number of rotations per orbit steadily increases and approaches $\sqrt{h}$ as h approaches infinity.

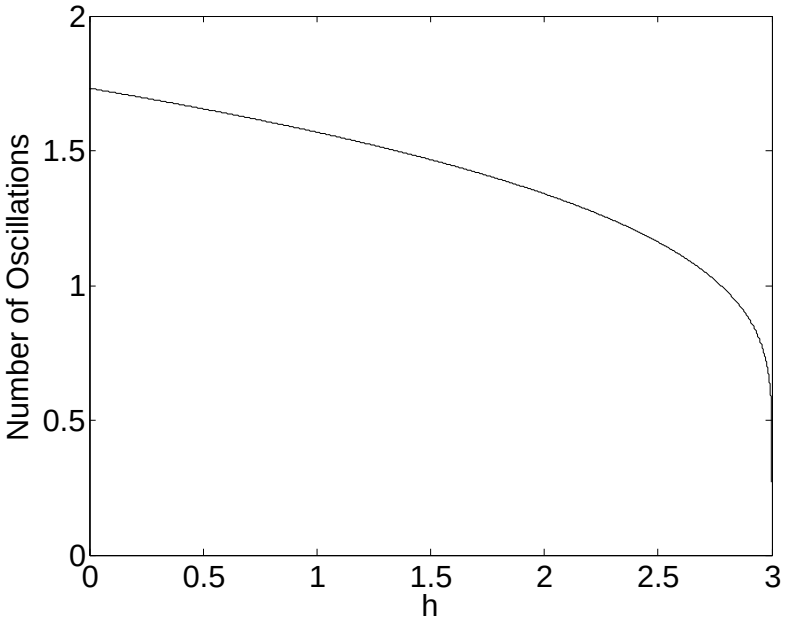

Figure 4.3: Number of oscillations per orbit for oscillatory systems

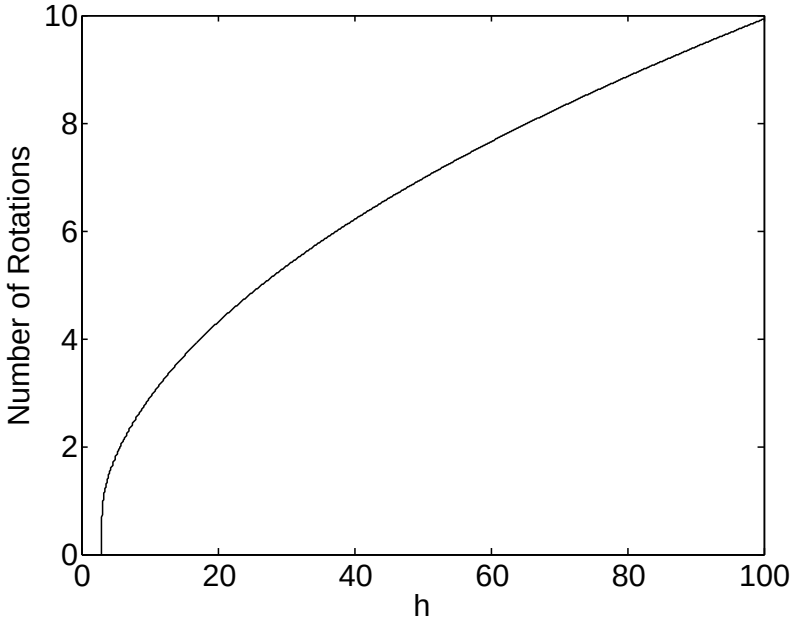

Figure 4.4: Number of rotations per orbit for rotating system

4.3.2 Floquet Analysis of Out-of-Plane Motion

Following the methods of Refs. [27] and [26], we use the solution for the in-plane motion to study the behavior of the out-of-plane motion. Substituting Eqs. (4.69) and (4.70) into Eq. (4.61), the equation of motion for the out-of-plane motion has the form

$$\overset{\circ\circ}{\beta} + p(\tau)\beta = 0 \tag{4.73}$$

where $p(\tau)$ is a periodic function. Equation (4.73) is a Hill's equation, so the stability properties of the out-of-plane motion can be determined using Floquet theory.[39] Since the form of $p(\tau)$ is different for oscillatory and rotational in-plane motion, we consider each case separately.

Oscillatory In-Plane Motion

We are primarily concerned with spinning TSS, however we include the analysis of oscillatory systems here for the sake of providing a complete analysis of small out-of-plane pendular motion. When the in-plane motion is oscillatory, the function $p(\tau)$ is

$$p(\tau) = \left[1 + \sqrt{h}\,\mathrm{cn}\left(\sqrt{3}\,\tau, \frac{1}{\kappa}\right)\right]^2 + 3\,\mathrm{dn}^2\left(\sqrt{3}\,\tau, \frac{1}{\kappa}\right) \tag{4.74}$$

which has the period

$$T_p = \frac{4K(\frac{1}{\kappa})}{\sqrt{3}} \tag{4.75}$$

The magnitudes of the eigenvalues of the monodromy matrix for Eqs. (4.73) and (4.74) are shown in Fig. 4.5. For $0 < h < 2.16$, both eigenvalues have a magnitude of 1, indicating that the out-of-plane motion is purely oscillatory and remains bounded. At $h = 2.16$, the magnitude of λ_1 becomes greater than 1, and the out-of-plane motion becomes unstable. This instability continues up to $h = 2.82$, at which point the motion again becomes purely oscillatory. At $h = 2.95$, the magnitude of λ_1 again becomes greater than 1, and the motion is unstable. As h approaches 3, the magnitudes of both of the eigenvalues approach 1. The stability properties of the out-of-plane motion for the case of oscillatory in-plane motion are summarized in Table 4.1. All of the cases considered by Kane[26] were for systems with $h < 0.1$, and the out-of-plane motion was found to be stable in all of those cases. Therefore, the results obtained above agree with previous results. In addition, the regions of unstable out-of-plane motion discovered above were not reported in Refs. [26] or [9] because both of those studies considered only relatively small amplitude in-plane oscillations, and the unstable regions correspond to relatively large amplitude in-plane motion.

To better understand the behavior of the out-of-plane motion as h is varied we consider the behavior of the eigenvalues of the monodromy matrix in the complex plane. Figure 4.6

Table 4.1: Stability properties of the out-of-plane pendular motion for oscillatory in-plane pendular motion

Region	**Stability Properties**
$0 < h < 2.16$	bounded oscillatory motion
$2.16 \leq h \leq 2.82$	unstable
$2.82 < h < 2.95$	bounded oscillatory motion
$2.95 \leq h < 3$	unstable

illustrates the motion of the eigenvalues of the monodromy matrix. Because the out-of-plane motion is governed by a second-order equation, the product of the two eigenvalues is 1, and the eigenvalues must be either on the real axis or on the unit circle in the complex plane.[39] For a value of h just greater than 0, the eigenvalues are at a point on the unit circle (points A), and the motion is bounded and non-periodic. As h increases, the eigenvalues move to the left along the unit circle until they both become -1 at $h = 2.16$. At this point, the out-of-plane motion is either periodic with a period of $T_\beta = 2T_p = 9.72696$ or unstable, depending on initial conditions. As h increases past 2.16, the eigenvalues split along the negative real axis such that $\lambda_1\lambda_2 = 1$ (points B) and the motion is unstable because the magnitude of one of the eigenvalues is greater than one. The eigenvalues then reverse direction and approach -1, and both become -1 at $h = 2.82$. At this point, the out-of-plane motion is again either periodic with period $T_\beta = 2T_p = 13.0285$ or unstable. As h increases past 2.82, the eigenvalues move to the right along the unit circle, and the motion is bounded and non-periodic. At $h = 2.95$, the eigenvalues are both 1 and the out-of-plane motion is periodic with period $T_\beta = T_p = 7.95287$ or unstable. As h increases past 2.95, the eigenvalues split along the real axis such that $\lambda_1\lambda_2 = 1$ (points C), and the motion is unstable. Both eigenvalues approach 1 as h approaches 3. Summarizing the analysis of Fig. 4.6, the out-of-plane motion is bounded and non-periodic for most values of h between 0 and 3. At the specific values h =2.16, 2.88, 2.95 the out-of-plane motion can be periodic with a period of T_p or $2T_p$, and the out-of-plane motion is unstable in the ranges $2.16 \leq h \leq 2.82$ and $2.95 \leq h < 3$.

Positive Rotational In-Plane Motion

When the in-plane motion is rotational with a positive rotation rate, the function $p(\tau)$ is

$$p(\tau) = \left[1 + \sqrt{h}\,\mathrm{dn}\left(\sqrt{h}\,\tau, \kappa\right)\right]^2 + 3\,\mathrm{cn}^2\left(\sqrt{h}\,\tau, \kappa\right) \tag{4.76}$$

which has the period

$$T_p = \frac{2K(\kappa)}{\sqrt{h}} \tag{4.77}$$

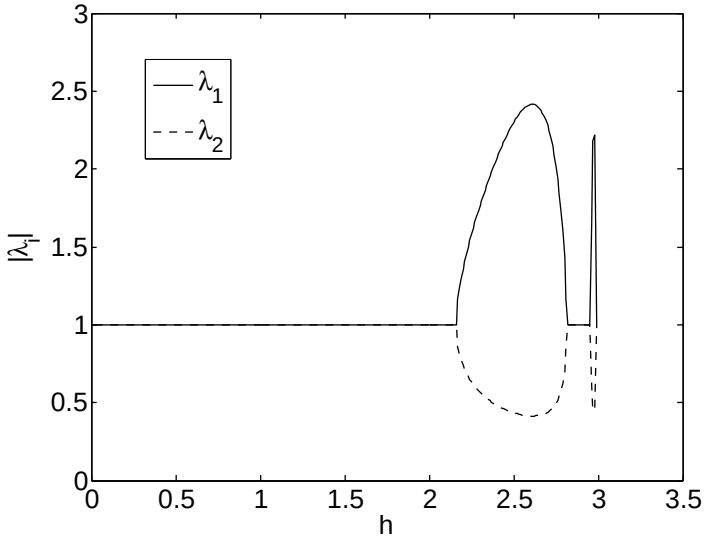

Figure 4.5: Magnitudes of the eigenvalues of the monodromy matrix of the out-of-plane motion for oscillatory in-plane motion

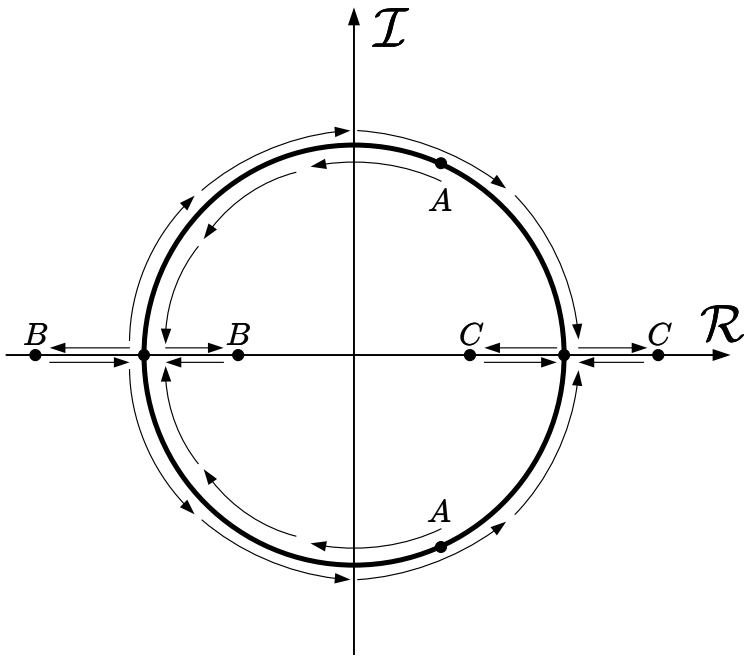

Figure 4.6: Motion in the complex plane of the eigenvalues of the monodromy matrix of the out-of-plane motion for oscillatory in-plane motion

The magnitudes of the eigenvalues of the monodromy matrix for Eqs. (4.73) and (4.76) are shown in Fig. 4.7. For $3 < h < 3.36$, both eigenvalues have a magnitude of 1 and the out-of-plane motion is bounded and oscillatory. At $h = 3.36$, the magnitude of λ_1 becomes greater than 1 and the out-of-plane motion becomes unstable. This instability continues through $h = 3.55$, at which point the magnitudes of both of the eigenvalues become 1 again. For $h > 3.55$, the magnitudes of both of the eigenvalues are 1, and the out-of-plane motion is bounded and oscillatory. The stability properties of the out-of-plane motion for the case of positive rotational in-plane motion are summarized in Table 4.2. Two cases of positive in-plane rotation were considered by Kane and Shippy,[27] corresponding to $h = 3.20$ and $h = 26.5$. The out-of-plane motion was found to be stable in these specific cases, so the results obtained above agree with previous results.

Table 4.2: Stability properties of the out-of-plane pendular motion for positive rotational in-plane pendular motion

Region	**Stability Properties**
$3 < h < 3.36$	bounded oscillatory motion
$3.36 \leq h \leq 3.55$	unstable
$h > 3.55$	bounded oscillatory motion

The motion of the eigenvalues of the monodromy matrix in the complex plane is illustrated in Fig. 4.8. For a value of h just greater than 3, the eigenvalues are on the unit circle (points A), and the motion is bounded and non-periodic. As h increases, the eigenvalues move to the right along the unit circle until they are both 1 at $h = 3.36$. At this point, the out-of-plane motion is either periodic with a period of $T_\beta = T_p = 2.77756$ or unstable, depending on initial conditions. As h increases past 3.36, the eigenvalues split along the positive real axis such that $\lambda_1\lambda_2 = 1$ (points B), and the out-of-plane motion is unstable. The eigenvalues then reverse direction and approach 1 along the positive real axis until they are both 1 at $h = 3.55$. At this point the out-of-plane motion is either periodic with a period of $T_\beta = T_p = 2.52008$ or unstable. As h increases past 3.55, the eigenvalues move to the left along the unit circle, and the motion is oscillatory and non-periodic. As h approaches infinity, the eigenvalues asymptotically approach -1, meaning that there are no additional regions of unstable out-of-plane motion, and the out-of-plane motion is bounded and non-periodic for $h > 3.55$. However, because the eigenvalues approach -1 as h approaches infinity, the out-of-plane motion approaches a periodic motion with period $2T_p$ as h approaches infinity. Summarizing the analysis of Fig. 4.8, the out-of-plane motion is bounded and non-periodic for most values of h greater than 3 and a positive in-plane rotation rate. At the specific values $h = 3.36$ and $h = 3.55$ the out-of-plane motion can be periodic with period T_p, and the out-of-plane motion is unstable in the range $3.36 \leq h \leq 3.55$.

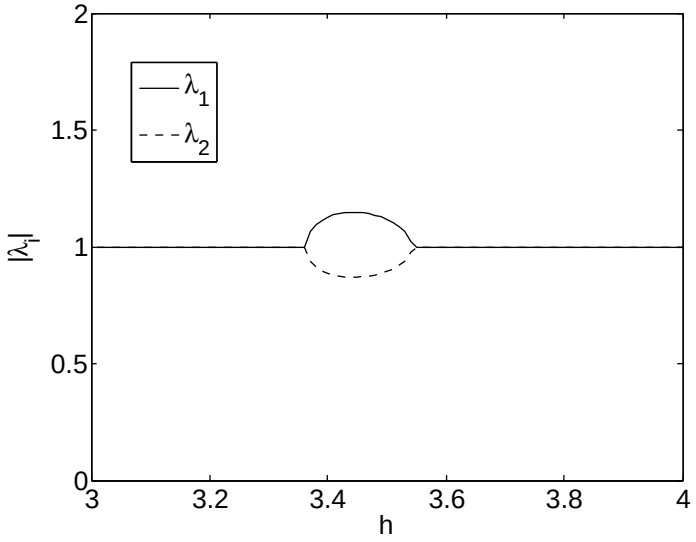

Figure 4.7: Magnitudes of the eigenvalues of the monodromy matrix of the out-of-plane motion for positive rotational in-plane motion

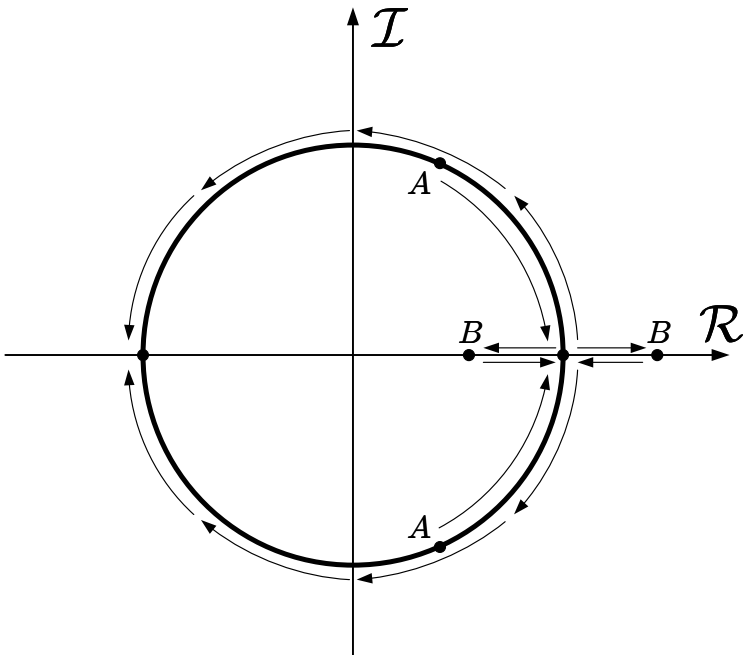

Figure 4.8: Motion in the complex plane of the eigenvalues of the monodromy matrix of the out-of-plane motion for positive rotational in-plane motion

Negative Rotational In-Plane Motion

When the in-plane motion is rotational with a negative rotation rate, the function $p(\tau)$ is

$$p(\tau) = \left[1 - \sqrt{h}\,\mathrm{dn}\left(\sqrt{h}\,\tau, \kappa\right)\right]^2 + 3\,\mathrm{cn}^2\left(\sqrt{h}\tau, \kappa\right) \tag{4.78}$$

which has the same period as systems with a positive in-plane rotation rate, Eq. (4.77). The magnitudes of the eigenvalues of the monodromy matrix for Eqs. (4.73) and (4.78) are shown in Fig. 4.9. For $3 < h < 3.04$, the magnitudes of both of the eigenvalues are 1, and the out-of-plane motion is bounded and oscillatory. At $h = 3.04$, the magnitude of λ_1 becomes greater than 1 and the out-of-plane motion becomes unstable. This instability persists until $h = 4.89$, at which point the magnitudes of both of the eigenvalues are once again equal to 1. For $h > 4.89$, the magnitudes of both of the eigenvalues are equal to 1, and the out-of-plane motion is bounded and oscillatory. The stability properties of the out-of-plane motion for the case of negative rotational in-plane motion are summarized in Table 4.3. The only case of negative in-plane rotation considered by Kane and Shippy[27] corresponds to $h = 3.20$, and the out-of-plane motion was found to be unstable. Therefore, the results obtained above agree with previous results.

Table 4.3: Stability properties of the out-of-plane pendular motion for negative rotational in-plane pendular motion

Region	**Stability Properties**
$3 < h < 3.04$	bounded oscillatory motion
$3.04 \leq h \leq 4.89$	unstable
$h > 4.89$	bounded oscillatory motion

The motion of the eigenvalues of the monodromy matrix in the complex plane is illustrated in Fig. 4.10. For a value of h just greater than 3, the eigenvalues are on the unit circle (points A), and the out-of-plane motion is bounded and non-periodic. As h increases, the eigenvalues move to the left along the unit circle until they are both -1 at $h = 3.04$. At this point, the out-of-plane motion is either periodic with a period of $T_\beta = 2T_p = 8.16746$ or unstable, depending on initial conditions. As h increases past 3.04, the eigenvalues split along the negative real axis such that $\lambda_1\lambda_2 = 1$ (points B), and the out-of-plane motion is unstable. The eigenvalues then approach -1 along the negative real axis until they are once again both -1 at $h = 4.89$, and the out-of-plane motion is periodic with period $T_\beta = 2T_p = 3.55337$ or unstable. As h increases past 4.89, the eigenvalues move to the right along the unit circle until they reach the points C, at which point they reverse direction and approach -1 along the unit circle. As h approaches infinity, the eigenvalues asymptotically approach -1 and there are no additional regions of unstable out-of-plane motion. The out-of-plane motion is bounded and non-periodic for all $h > 4.89$. As with systems with a positive in-plane

rotation rate, the out-of-plane motion does approach a periodic trajectory with period $2T_p$ as h approaches infinity because the eigenvalues asymptotically approach -1. Summarizing the analysis of Fig. 4.10, the out-of-plane motion is bounded and non-periodic for most values of h greater than 3 and a negative in-plane rotation rate. For the specific values $h = 3.04$ and $h = 4.89$ the out-of-plane motion can be periodic with period $2T_p$, and the out-of-plane motion is unstable in the range $3.04 \leq h \leq 4.89$.

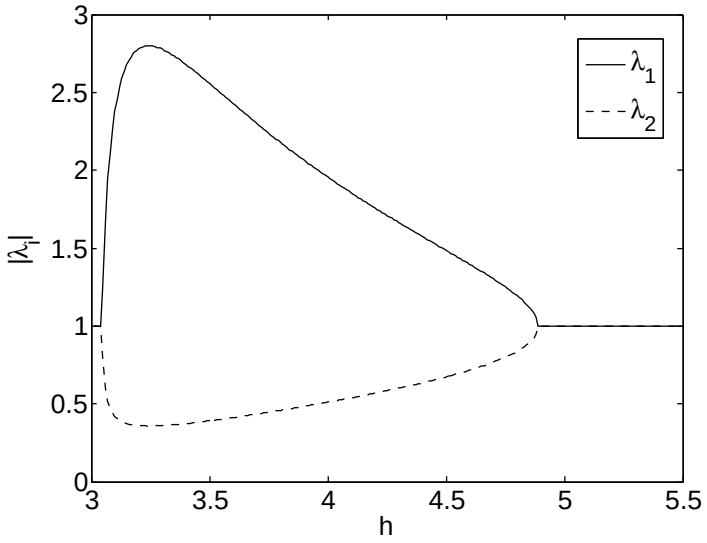

Figure 4.9: Magnitudes of the eigenvalues of the monodromy matrix of the out-of-plane motion for negative rotational in-plane motion

Summary of Out-of-Plane Instabilities

The stability properties of small out-of-plane motion are summarized in Fig. 4.11. The shaded regions correspond to in-plane trajectories that result in unstable out-of-plane motion, and the unshaded regions correspond to in-plane trajectories that result in bounded, oscillatory out-of-plane motion. The oval regions are the regions of negative tension discussed previously. Note that a significant portion of the unstable oscillatory regions and the entire unstable negative rotational region pass through regions of negative tension, so these types of motions should be avoided regardless of the instability in the out-of-plane pendular motion. The unstable regions for positive in-plane rotation corresponds to systems that perform between 1.13 and 1.25 rotations per orbit.

We must also note that some previous research has indicated that an infinite alternation of stable and unstable regions may exist in a small strip around the separatrices in Fig. 4.11. Such a prediction is made in Ref. [56], in which first-order series expansions of the system

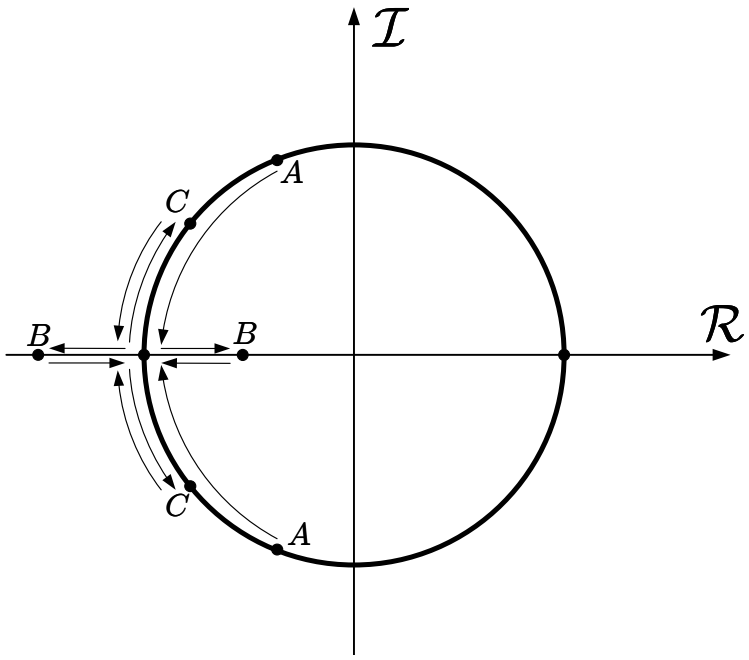

Figure 4.10: Motion in the complex plane of the eigenvalues of the monodromy matrix of the out-of-plane motion for negative rotational in-plane motion

Hamiltonian are used to derive the predictions of infinite stability alternation near the separatrices. If this type of stability behavior does indeed exist, it could be included in the analysis presented in this section by using a very small increment of h when numerically calculating the monodromy matrix required by Floquet theory. Small increments of h could capture some, but not all of the stability alternations as the separatrix is approached. However, it should be pointed out that the behavior of the system in a region so near the separatrices is of little practical interest, most notably because the tether will always become slack, or very near slack, at some point in these regions. For this reason, we do no consider a more detailed study of the motion of the system near the separatrices.

4.3.3 Approximate Solution for Out-of-Plane Motion for Large h

From the results of the Floquet analysis presented previously in this section, the lower-level computational model predicts that small out-of-plane pendular motion of the tether remains bounded for systems with rotational in-plane motion and relatively large values of h. The out-of-plane motion is oscillatory and non-periodic, but approaches a periodic trajectory as h approaches infinity. In light of these results, we would like to determine solutions for the out-of-plane motion for large values of h. Such solutions will provide a great deal more information about the characteristics of the out-of-plane motion, and can also be

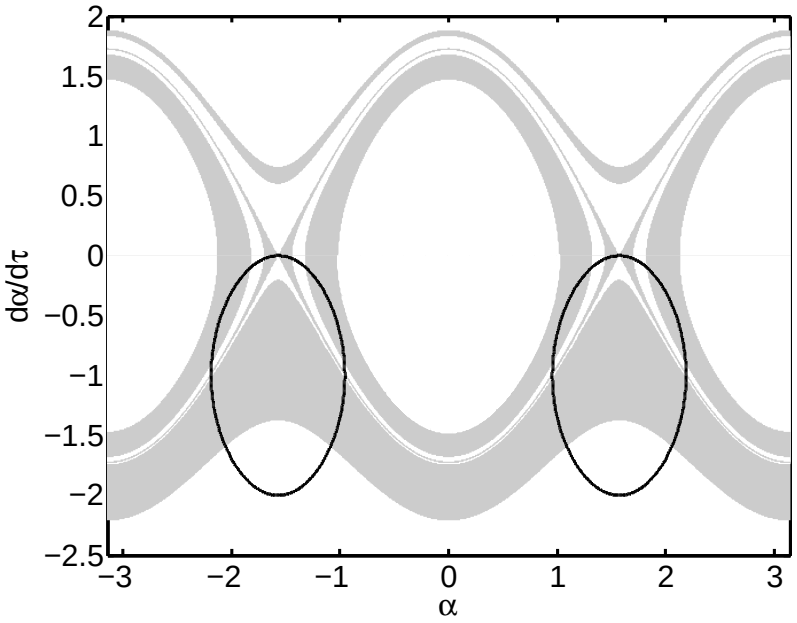

Figure 4.11: Regions of unstable out-of-plane motion

used as generating solutions for perturbation analysis of spinning TSS experiencing small external perturbations. Since the equation of small out-of-plane motion is non-autonomous, the determination of an exact general solution is a nontrivial task. However, solutions that approximate the exact solution for small out-of-plane motion can be determined with negligible error when h is relatively large.

Recall that the equation of small out-of-plane motion is given by Eq. (4.73), where the periodic function $p(\tau)$ is given by Eq. (4.76) for positive rotating systems and Eq. (4.78) for negative rotating systems. Using several identities for the elliptic functions,[32] we can rewrite $p(\tau)$ as

$$p(\tau) = h - 2 \pm 2\sqrt{h}\,\mathrm{dn}(\sqrt{h}\,\tau, \kappa) + 6\,\mathrm{cn}^2(\sqrt{h}\,\tau, \kappa) \tag{4.79}$$

where the "+" sign is for positive rotating systems and the "-" sign is for negative rotating systems. The Fourier series for the elliptic functions $\mathrm{cn}(u,k)$ and $\mathrm{dn}(u,k)$ are[10]

$$\mathrm{cn}(u,k) = \frac{2\pi}{kK}\sum_{m=0}^{\infty}\frac{q^{m+\frac{1}{2}}}{1+q^{2m+1}}\cos\left(\frac{(2m+1)\pi}{2K}u\right) \tag{4.80}$$

$$\mathrm{dn}(u,k) = \frac{\pi}{2K} + \frac{2\pi}{K}\sum_{m=0}^{\infty}\frac{q^{m+1}}{1+q^{2m+1}}\cos\left(\frac{(m+1)\pi}{K}u\right) \tag{4.81}$$

where the nome, q, is defined as

$$q = e^{-\frac{\pi K'}{K}} \tag{4.82}$$

$$K'(k) = K(\sqrt{1-k^2}) \tag{4.83}$$

Plots of the Fourier coefficients for $\mathrm{cn}(u,k)$ and $\mathrm{dn}(u,k)$ are shown in Figs. 4.12(a) and 4.12(b). In these plots A_m is the coefficient on the cosine terms inside the summations in Eqs. (4.80) and (4.81). For $h > 25$, the first coefficient in the Fourier series for both $\mathrm{cn}(u,k)$ and $\mathrm{dn}(u,k)$ is roughly two orders of magnitude greater than all of the other Fourier coefficients. Therefore, for these values of h, we can approximate $\mathrm{cn}(u,k)$ and $\mathrm{dn}(u,k)$ by retaining only the first terms in the series in Eqs. (4.80) and (4.81),

$$\mathrm{cn}(u,k) \approx \frac{2\pi}{kK}\left(\frac{\sqrt{q}}{1+q}\right)\cos\left(\frac{\pi}{2K}u\right) \tag{4.84}$$

$$\mathrm{dn}(u,k) \approx \frac{\pi}{2K} + \frac{2\pi}{K}\left(\frac{q}{1+q}\right)\cos\left(\frac{\pi}{K}u\right) \tag{4.85}$$

Using Eqs. (4.84) and (4.85), we can approximate $p(\tau)$ as

$$p(\tau) \approx \bar{a} + 2\bar{b}\cos(2\nu) \tag{4.86}$$

where we have defined

$$\bar{a} = \left[1 + \frac{4\pi^2 q}{K^2(1+q)^2}\right] h \pm \frac{\pi\sqrt{h}}{K} - 2 \tag{4.87}$$

$$\bar{b} = \frac{2\pi\sqrt{h}q}{K(1+q)}\left[\frac{\pi\sqrt{h}}{K(1+q)} \pm 1\right] \tag{4.88}$$

$$\nu = \frac{\pi\sqrt{h}}{2K}\tau \tag{4.89}$$

Figures 4.13(a) and 4.13(b) show the error in the approximation of $p(\tau)$ over one period for various values of h. For positive rotating systems, the error in $p(\tau)$ is less than 0.25% for $h > 25$, and for negative rotating systems the percent error is less than 0.5% for $h > 25$. As h increases, the error becomes progressively smaller, indicating that the approximation given by Eq. (4.86) is quite accurate for $h > 25$. Using Eq. (4.86) and changing independent variables to ν, the equation of small out-of-plane motion can be written as

$$\frac{d^2\beta}{d\nu^2} + [a + 2b\cos(2\nu)]\beta = 0 \tag{4.90}$$

where

$$a = \frac{4K^2}{\pi^2}\left[1 + \frac{4\pi^2 q}{K^2(1+q)^2}\right] \pm \frac{4K}{\pi\sqrt{h}} - \frac{8K^2}{\pi^2 h} \tag{4.91}$$

$$b = \frac{8K}{\pi\sqrt{h}}\left(\frac{q}{1+q}\right)\left[\frac{\pi\sqrt{h}}{K(1+q)} \pm 1\right] \tag{4.92}$$

Equation (4.90) is recognized as Mathieu's equation,[37] for which we can use Floquet's theorem to determine an approximate analytical solution.

Floquet's theorem states that a solution to Eq. (4.90) can be written as[39]

$$\beta(\nu) = e^{\rho\nu}\phi(\nu) \tag{4.93}$$

where ρ is the characteristic exponent and $\phi(\nu)$ is a periodic function of ν with period π. Note that, in general, both ρ and ϕ are complex. Because $\phi(\nu)$ is periodic, we can expand it in a Fourier series such that

$$\beta(\nu) = e^{\rho\nu}\sum_{n=-\infty}^{\infty} c_n e^{2in\nu} \tag{4.94}$$

where c_n are the coefficients of the series. Rewriting $p(\nu)$ as

$$p(\nu) = a + b(e^{2i\nu} + e^{-2i\nu}) \tag{4.95}$$

and using Eq. (4.94), we can rewrite Eq. (4.90) as

$$\sum_{n=-\infty}^{\infty} (\rho + 2in)^2 c_n e^{(\rho+2in)\nu} + [a + b(e^{2i\nu} + e^{-2i\nu})]\sum_{n=-\infty}^{\infty} c_n e^{(\rho+2in)\nu} = 0 \tag{4.96}$$

Collecting powers of $e^{2in\nu}$, we obtain the following infinite set of linear algebraic equations for the Fourier coefficients,

$$bc_{n-1} + [a + (\rho + 2in)^2]c_n + bc_{n+1} = 0, \qquad n = -\infty, ..., \infty \tag{4.97}$$

The system of equations given by Eq. (4.97) can be written in matrix form as

$$\mathbf{Ac} = \mathbf{0} \tag{4.98}$$

where $\mathbf{A}$ is an infinite tri-diagonal matrix, $\mathbf{c}$ is a column matrix containing all of the Fourier coefficients, and $\mathbf{0}$ is the infinite zero column matrix. For Eq. (4.98) to have a non-trivial solution, the determinant of $\mathbf{A}$, Δ, must be zero. It can be shown that[37,39]

$$\Delta(i\rho) = \Delta(0) - \sin^2\left(\frac{1}{2}\pi i\rho\right)\csc^2\left(\frac{1}{2}\pi\sqrt{a}\right) \tag{4.99}$$

so the characteristic exponent must satisfy the transcendental equation

$$\sin^2\left(\frac{1}{2}\pi i\rho\right) = \Delta(0)\sin^2\left(\frac{1}{2}\pi\sqrt{a}\right) \tag{4.100}$$

If $b^2 \ll 1$, then we can approximate $\Delta(0)$ as[37]

$$\Delta(0) \approx 1 - \frac{\pi b^2 \cot\left(\frac{1}{2}\pi\sqrt{a}\right)}{4\sqrt{a}(a-1)} \tag{4.101}$$

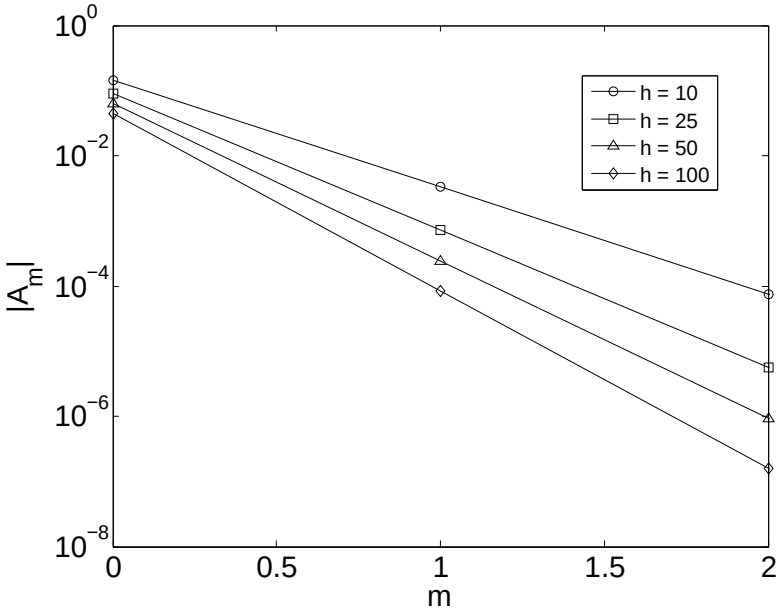

(a) $\mathrm{cn}(u, k)$

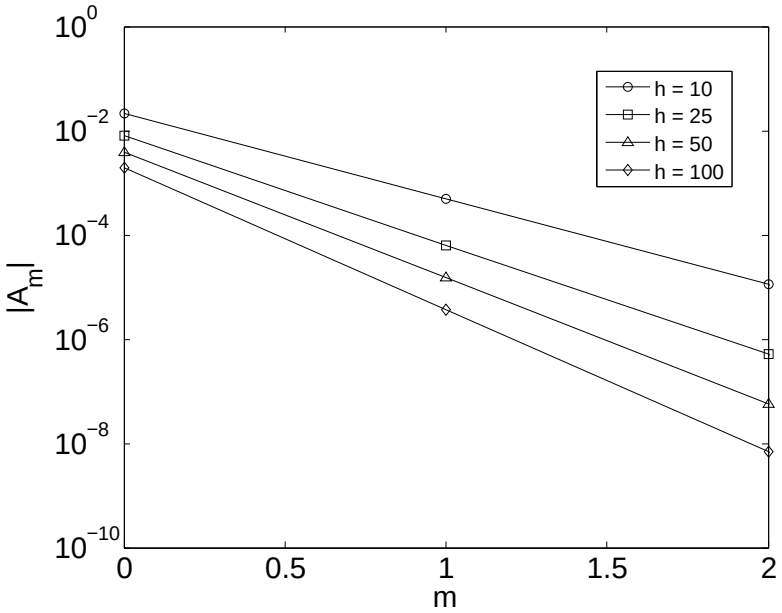

(b) $\mathrm{dn}(u, k)$

Figure 4.12: Magnitude of Fourier coefficients for the elliptic functions $\mathrm{cn}(u, k)$ and $\mathrm{dn}(u, k)$

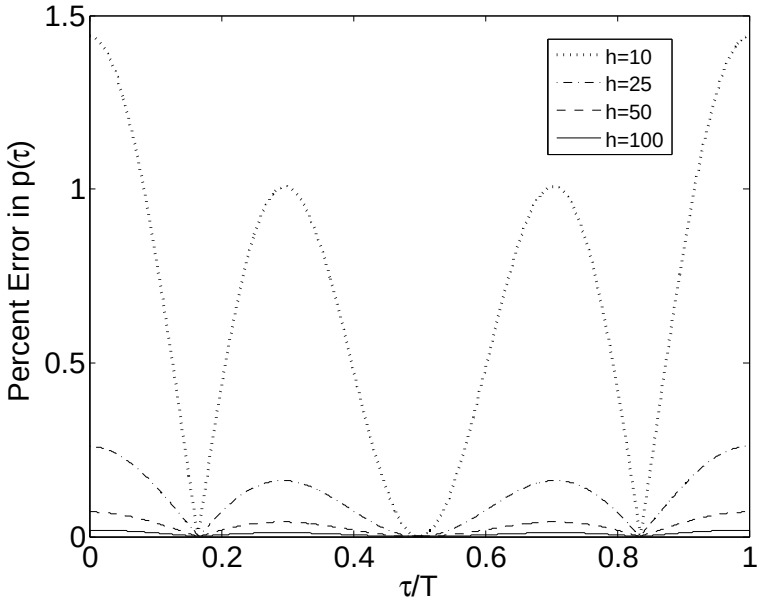

(a) Positive in-plane rotation

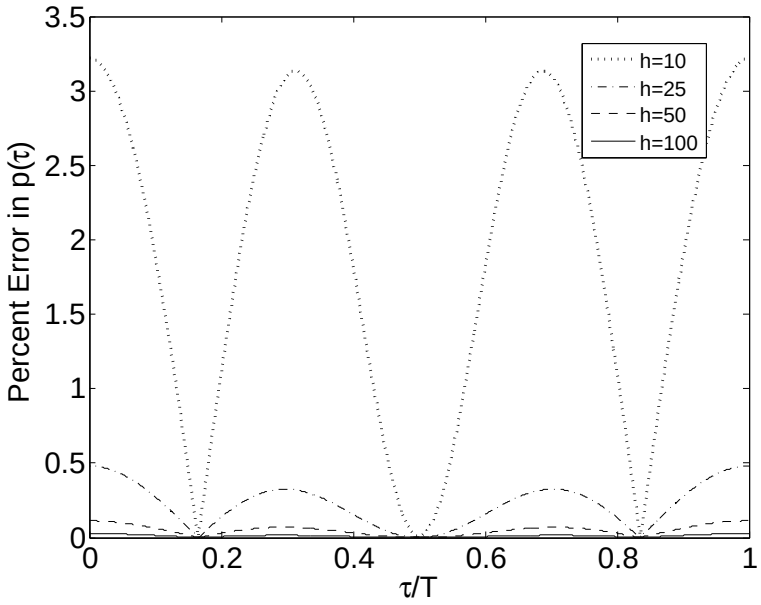

(b) Negative in-plane rotation

Figure 4.13: Error in the approximation of $p(\tau)$ for various values of h

and Eq. (4.100) can be approximated as

$$\cos(i\pi\rho) = \cos(\pi\sqrt{a}) + \frac{\pi b^2 \sin(\pi\sqrt{a})}{4\sqrt{a}(a-1)} \tag{4.102}$$

Figure 4.14 shows b^2 as a function of h for both positive and negative rotating systems. Note that b^2 is roughly 100 times smaller than 1 for $h > 25$, so the approximations given above are valid for relatively large values of h. Given values of a and b, the characteristic exponent can be determined from Eq. (4.102), which can then be used in Eq. (4.97) to determine the Fourier coefficients for $\phi(\nu)$. This procedure is valid for general out-of-plane motion; however, we are considering the motion for large values of h for which we know that the motion remains bounded and oscillatory, so we can simplify the solution further.

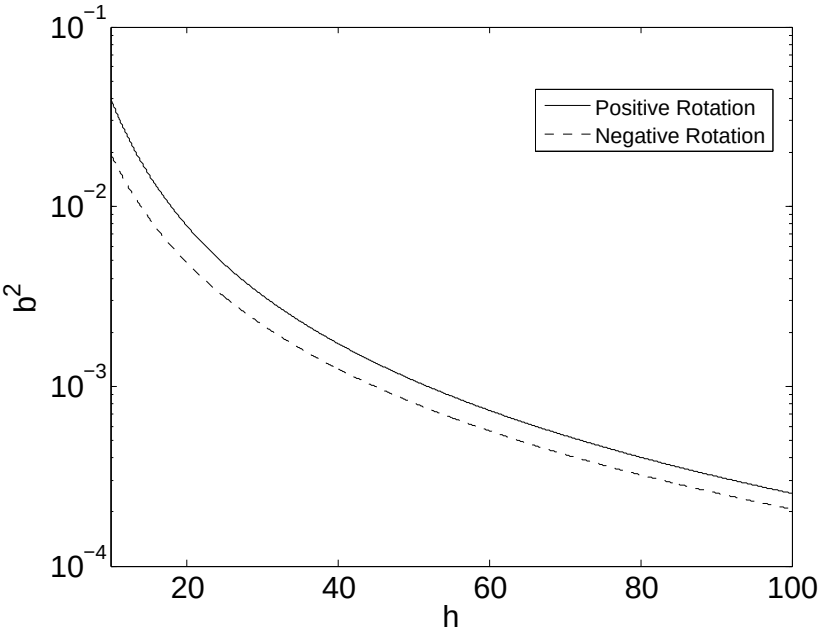

Figure 4.14: b^2 as a function of h for positive and negative rotating systems

According to Floquet theory, the characteristic exponents of Eq. (4.90) can be written as[37]

$$\rho_n = \frac{\ln(|\lambda_n|) + i\arg(\lambda_n)}{\pi}, \qquad n = 1, 2 \tag{4.103}$$

where λ_n are the characteristic multipliers of the system, which are also the eigenvalues of the monodromy matrix. Note that there are two characteristic exponents because there are two distinct, linearly independent solutions to Eq. (4.90) that can be written in the form of Eq. (4.93). Since we are considering bounded motion, the magnitude of the characteristic

multipliers is 1, $|\lambda_n| = 1$, and the characteristic exponents must be purely imaginary. Also, since there are only two characteristic exponents, they must form a complex conjugate pair, and they can be written as

$$\rho = \pm i\mu \tag{4.104}$$

where $\mu > 0$ is a real number. Using Eq. (4.104) in Eq. (4.102), we can solve for μ as

$$\mu = \frac{1}{\pi}\cos^{-1}\left(\cos(\pi\sqrt{a}) + \frac{\pi b^2 \sin(\pi\sqrt{a})}{4\sqrt{a}(a-1)}\right) \tag{4.105}$$

The percent error in the approximate solution for μ as a function of h is shown in Fig. 4.15. The error was determined by calculating μ numerically and comparing the approximate value determined from Eq. (4.105) with the numerical value. For both positive and negative rotating systems, the percent error is less than 10^{-4} for $h > 25$, indicating that the approximation given by Eq. (4.105) works quite well for relatively large values of h.

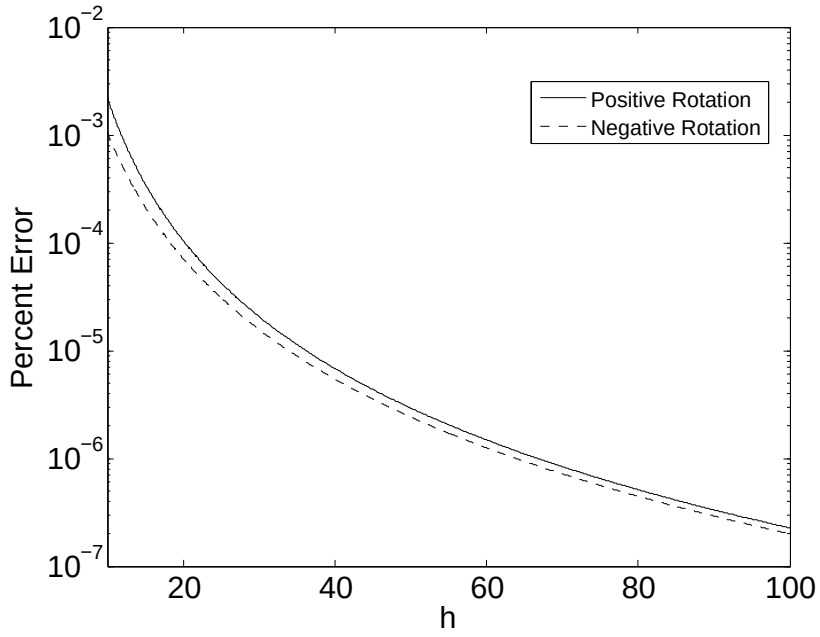

Figure 4.15: Percent Error in μ as a function of h for positive and negative rotating systems

Now that we have approximate expressions for the characteristic exponents, we return our attention to Eq. (4.97) and the solution for the Fourier coefficients of $\phi(\nu)$ and the general solution for β. Dividing Eq. (4.97) by $a + (\rho + 2i\,n)^2$, we obtain

$$\xi_n^{\pm} c_{n-1}^{\pm} + c_n^{\pm} + \xi_n^{\pm} c_{n+1}^{\pm} = 0, \qquad n = -\infty, ..., \infty \tag{4.106}$$

where we have defined

$$\xi_n^{\pm} = \frac{b}{a - (2n \pm \mu)^2} \tag{4.107}$$

The "+" sign in Eqs. (4.106) and (4.107) corresponds to $\rho = i\mu$, and the "-" sign corresponds to $\rho = -i\mu$. Noting that $\xi_n^+ = \xi_{-n}^-$, from Eq. (4.106) it must also be true that $c_n^+ = c_{-n}^-$. The solutions for β are therefore

$$\beta^{\pm}(\nu) = e^{\pm i\mu\nu} \sum_{n=-\infty}^{\infty} c_n^+ e^{\pm 2in\nu} \tag{4.108}$$

Letting $c_n = c_n^+$ and making use of Euler's identity, Eq. (4.108) is rewritten as

$$\beta^{\pm}(\nu) = \sum_{n=-\infty}^{\infty} c_n[\cos((2n+\mu)\nu) \pm i\sin((2n+\mu)\nu)] \tag{4.109}$$

and the general solution for β can be written

$$\begin{aligned} \beta(\nu) &= C_1\beta^+(\nu) + C_2\beta^-(\nu) \\ &= B_1 \sum_{n=-\infty}^{\infty} c_n \cos((2n+\mu)\nu) + iB_2 \sum_{n=-\infty}^{\infty} c_n \sin((2n+\mu)\nu) \\ &= B_1\,\mathrm{cm}(a,b,\nu) + iB_2\,\mathrm{sm}(a,b,\nu) \end{aligned} \tag{4.110}$$

where B_i are constants and we have defined the functions

$$\mathrm{cm}(a,b,\nu) = \sum_{n=-\infty}^{\infty} c_n \cos((2n+\mu)\nu) \tag{4.111}$$

$$\mathrm{sm}(a,b,\nu) = \sum_{n=-\infty}^{\infty} c_n \sin((2n+\mu)\nu) \tag{4.112}$$

Note that c_n and μ are functions of a and b. Because Eq. (4.90) is linear and homogeneous, we can use Eqs. (4.110-4.112) to express any real solution for β as

$$\beta(\nu) = B_1\,\mathrm{cm}(a,b,\nu) + B_2\,\mathrm{sm}(a,b,\nu) \tag{4.113}$$

Numerical experiments show that the dominant values of c_n are for $-2 \le n \le 1$, so we set all other values of c_n equal to zero and determine approximate values of the most dominant coefficients. Also, because Eq. (4.90) is homogeneous, the amplitude of the solution is arbitrary, and we can set $c_0 = 1$. This leaves us with the linear system

$$\begin{bmatrix} 1 & 0 & 0 & 0 & 0 & 0 \\ \xi_{-2} & 1 & \xi_{-2} & 0 & 0 & 0 \\ 0 & \xi_{-1} & 1 & \xi_{-1} & 0 & 0 \\ 0 & 0 & 0 & 1 & 0 & 0 \\ 0 & 0 & 0 & \xi_1 & 1 & \xi_1 \\ 0 & 0 & 0 & 0 & 0 & 1 \end{bmatrix} \begin{pmatrix} c_{-3} \\ c_{-2} \\ c_{-1} \\ c_0 \\ c_1 \\ c_2 \end{pmatrix} = \begin{pmatrix} 0 \\ 0 \\ 0 \\ 1 \\ 0 \\ 0 \end{pmatrix} \tag{4.114}$$

from which we obtain

$$c_{-2} = \frac{\xi_{-2}\xi_{-1}}{1-\xi_{-2}\xi_{-1}} \tag{4.115}$$

$$c_{-1} = -\frac{\xi_{-1}}{1-\xi_{-2}\xi_{-1}} \tag{4.116}$$

$$c_1 = -\xi_1 \tag{4.117}$$

Using Eqs. (4.115-4.117), we can approximate the functions $\mathrm{cm}(a,b,\nu)$ and $\mathrm{sm}(a,b,\nu)$ as

$$\begin{aligned}\mathrm{cm}(a,b,\nu) = &\left(\frac{\xi_{-2}\xi_{-1}}{1-\xi_{-2}\xi_{-1}}\right)\cos((\mu-4)\nu) - \left(\frac{\xi_{-1}}{1-\xi_{-2}\xi_{-1}}\right)\cos((\mu-2)\nu) \\ &+ \cos(\mu\nu) - \xi_1\cos((\mu+2)\nu)\end{aligned} \tag{4.118}$$

$$\begin{aligned}\mathrm{sm}(a,b,\nu) = &\left(\frac{\xi_{-2}\xi_{-1}}{1-\xi_{-2}\xi_{-1}}\right)\sin((\mu-4)\nu) - \left(\frac{\xi_{-1}}{1-\xi_{-2}\xi_{-1}}\right)\sin((\mu-2)\nu) \\ &+ \sin(\mu\nu) - \xi_1\sin((\mu+2)\nu)\end{aligned} \tag{4.119}$$

We normalize $\mathrm{cm}(a,b,\nu)$ and $\mathrm{sm}(a,b,\nu)$ such that $\mathrm{cm}(a,b,0)=1$ and $\mathrm{sm}'(a,b,0)=1$, where the prime denotes differentiation with respect to ν. Defining the normalization factors

$$f_c = 1-\xi_{-1}-\xi_1(1-\xi_{-2}\xi_{-1}) \tag{4.120}$$

$$f_s = \mu[1-\xi_1-\xi_{-1}(1-\xi_{-2}\xi_1)] + 2[\xi_{-1}(1+\xi_{-2}(-2+\xi_1)) - \xi_1] \tag{4.121}$$

the normalized forms of $\mathrm{cm}(a,b,\nu)$ and $\mathrm{sm}(a,b,\nu)$ are

$$\begin{aligned}\mathrm{cm}(a,b,\nu) = &\frac{\xi_{-2}\xi_{-1}\cos((\mu-4)\nu) - \xi_{-1}\cos((\mu-2)\nu)}{f_c} \\ &+ \frac{(1-\xi_{-2}\xi_{-1})[\cos(\mu\nu) - \xi_1\cos((\mu+2)\nu)]}{f_c}\end{aligned} \tag{4.122}$$

$$\begin{aligned}\mathrm{sm}(a,b,\nu) = &\frac{\xi_{-2}\xi_{-1}\sin((\mu-4)\nu) - \xi_{-1}\sin((\mu-2)\nu)}{f_s} \\ &+ \frac{(1-\xi_{-2}\xi_{-1})[\sin(\mu\nu) - \xi_1\sin((\mu+2)\nu)]}{f_s}\end{aligned} \tag{4.123}$$

Using the normalized forms of Eqs. (4.122) and (4.123), the constants B_i are determined as

$$B_1 = \beta(0) \tag{4.124}$$

$$B_2 = \frac{2K\beta'(0)}{\pi\sqrt{h}} \tag{4.125}$$

The approximate solution for β can be interpreted as a linear combination of four simple harmonic oscillators,

$$\beta(\tau) = A\sum_{n=1}^{4} C_n\cos(\omega_n\tau+\delta) \tag{4.126}$$

where A and δ are constants that depend on the initial conditions, and

$$\omega_n = \frac{\pi\sqrt{h}[\mu - (6-2n)]}{2K} \tag{4.127}$$

$$C_1 = \xi_{-2}\xi_{-1} \tag{4.128}$$

$$C_2 = -\xi_{-1} \tag{4.129}$$

$$C_3 = 1 - \xi_{-2}\xi_{-1} \tag{4.130}$$

$$C_4 = -\xi_1(1 - \xi_{-2}\xi_{-1}) \tag{4.131}$$

The magnitudes of the approximate solution coefficients and the approximate solution frequencies are plotted as functions of h in Figs. 4.16(a) and 4.16(b) for positive rotating systems, and in Figs. 4.17(a) and 4.17(b) for negative rotating systems.

For systems with a positive in-plane rotation, the dominant term in the approximate solution for β is the $n = 2$ term, followed by the $n = 3$, $n = 1$, and $n = 4$ terms. The dominance of the $n = 2$ term becomes more pronounced as h increases, and all of the frequencies increase as h increases. Note that there are two distinct "high" frequencies ($n = 1, 4$) and two distinct "low" frequencies, and that the two most dominant terms in the approximate solution correspond to the low frequencies. The higher frequency terms are relatively minor contributions to the out-of-plane motion for all higher values of h.

For systems with a negative in-plane rotation, the dominant term in the approximate solution for β is the $n = 3$ term, followed by the $n = 2$, $n = 4$, and $n = 1$ terms. The dominance of the $n = 3$ term increases as h increases. As with systems with a positive in-plane rotation, all of the approximate solution frequencies increase as h increases, and they can be divided into two high frequencies ($n = 1, 4$) and two low frequencies ($n = 2, 3$). The low frequency terms provide the most significant contribution to the out-of-plane motion, and the high frequency terms provide relatively minor contributions.

4.3.4 Bounds on Out-of-Plane Motion

The Floquet analysis of the linearized equations of motion for the pendular motion of the tether predicts that the out-of-plane motion grows unbounded for certain values of h. This is not necessarily the case for the nonlinear system, however, as the fact that the quantity $\mathcal{H}$ defined in Eq. (4.63) is conserved can place bounds on the possible out-of-plane motion.

Define the quantities

$$\mathcal{T} = \mathring{\alpha}^2 \cos^2\beta + \mathring{\beta}^2 \tag{4.132}$$

$$\mathcal{V} = 3\sin^2\alpha\cos^2\beta + 4\sin^2\beta \tag{4.133}$$

such that $\mathcal{H}$ can be expressed as

$$\mathcal{H} = \mathcal{T} + \mathcal{V} \tag{4.134}$$

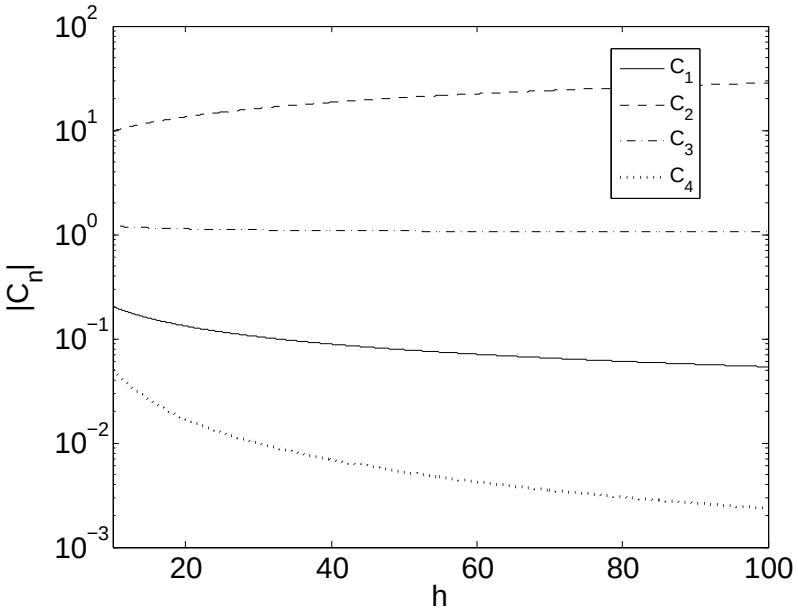

(a) Approximate solution coefficient magnitudes

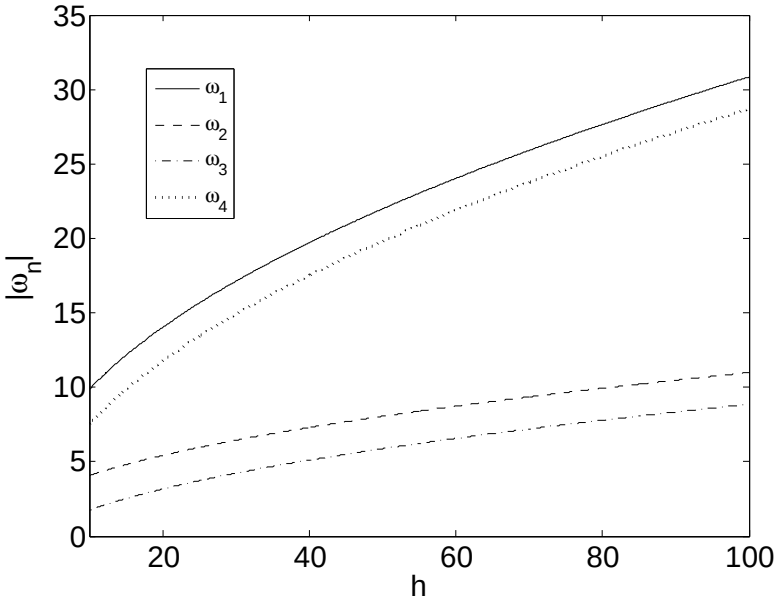

(b) Approximate solution frequencies

Figure 4.16: Out-of-plane approximate solution properties for systems with positive in-plane rotation

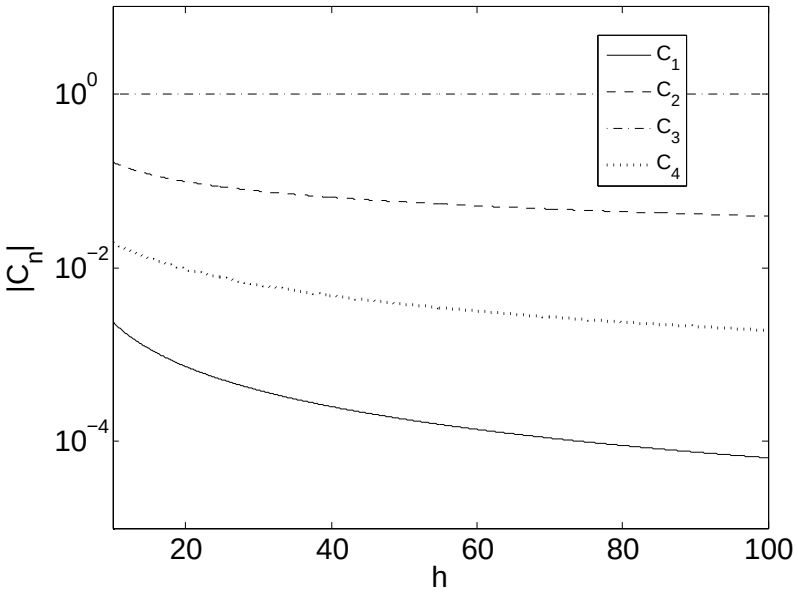

(a) Approximate solution coefficient magnitudes

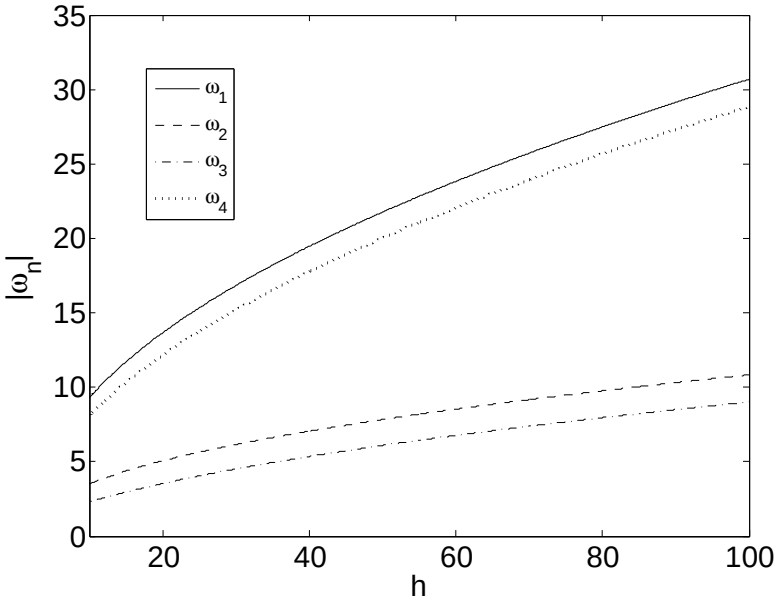

(b) Approximate solution frequencies

Figure 4.17: Out-of-plane approximate solution properties for systems with negative in-plane rotation

Note that $\mathcal{T}$ and $\mathcal{V}$ are the kinetic and potential energies of the pendular motion of the tether relative to the orbital frame. For a given value of $\mathcal{H}$, the maximum possible values of α and β occur when $\mathcal{T} = 0$, such that $\mathcal{V} = \mathcal{H}$. This fact is analagous to the fact that the maximum amplitude of a simple pendulum occurs when the pendulum is stationary, and all of its energy is potential energy. The contours of $\mathcal{V} = \mathcal{H}$ in the $\alpha - \beta$ plane define the admissable regions for α and β for particular values of $\mathcal{H}$, and can therefore be used to analyze the boundedness of the system attitude motion.

Contours of $\mathcal{V} = \mathcal{H}$ are shown in Fig. 4.18. For $\mathcal{H} < 3$, the admissable regions of α and β are closed, and both α and β must be bounded for all time. For $3 < \mathcal{H} < 4$, the admissable regions are open in the α-direction, but closed in the β-direction. This means that α may grow unbounded for $3 < \mathcal{H} < 4$, but β must remain bounded for all time. For $\mathcal{H} > 4$, it is not possible to have $\mathcal{V} = \mathcal{H}$ and $\mathcal{T}$ must always be some positive value. This means that for $\mathcal{H} > 4$ the tether can never be stationary relative to the orbital frame and must therefore be rotating in some sense.

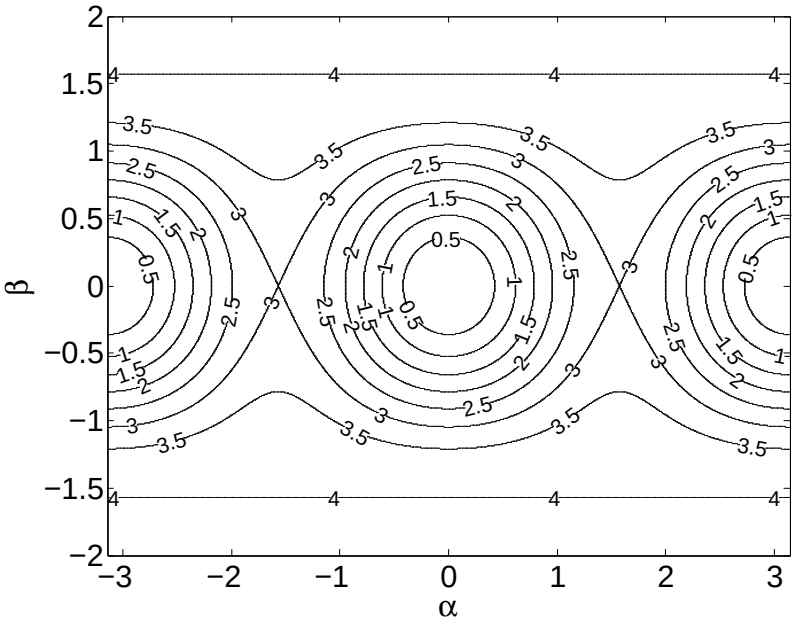

Figure 4.18: Contours of $\mathcal{H}$ for $\mathcal{T} = 0$

Now, consider the situation in which the system is nominally oscillating or spinning in the orbit plane with some small initial out-of-plane deviations. In this case, $\mathcal{H}$ is

$$\mathcal{H} = h\cos^2\beta(0) + \mathring{\beta}(0)^2 + 4\sin^2\beta(0) \tag{4.135}$$

where we have used the definition

$$h = \mathring{\alpha}(0)^2 + 3\sin^2\alpha(0) \tag{4.136}$$

because the pendular motion is ideally planar with energy level h, but there are small initial out-of-plane deviations. The out-of-plane motion must remain bounded if $\mathcal{H} < 4$, in which case the maximum possible value of β is

$$\beta_{max} = \sin^{-1}\left(\frac{\sqrt{h\cos^2\beta(0) + \mathring{\beta}(0)^2 + 4\sin^2\beta(0)}}{2}\right) \tag{4.137}$$

Since we are assuming that the initial out-of-plane deviations are small, we can approximate β_{max} as

$$\beta_{max} \approx \sin^{-1}\left(\frac{\sqrt{h}}{2}\right) \tag{4.138}$$

So, for $h > 4$ it is possible for small initial out-of-plane deviations to grow unbounded, but for $h < 4$ the out-of-plane motion must remain bounded. As indicated by the Floquet analysis, the out-of-plane motion can grow quite large, but it must remain bounded for $h < 4$. This means that the out-of-plane motion will not grow unbounded in the unstable regions discovered previously in this section for systems with a positive in-plane rotation.

4.3.5 Summary of Computational Predictions

In this section we presented aspects of the lower-level computational model pertaining to the pendular motion of the tether. Because the nominal pendular motion of the tether is a planar spin, the equations governing the pendular motion were linearized about $\beta = \mathring{\beta} = 0$ and the solution for the in-plane motion was determined analytically. This solution was then used in the equation governing the out-of-plane motion, resulting in a Hill's equation. Floquet theory was used to show that this equation is unstable for certain in plane spin rates, meaning that the lower-level computational model predicts unstable out-of-plane motion for some cases. The out-of-plane motion does not grow unbounded, however, due to the fact that the equations governing the pendular motion are conservative. This fact was used to determine approximate bounds on the out-of-plane motion for unstable cases. For relatively high in-plane spin rates the Hill's equation governing the small out-of-plane motion is accurately approximated by a Mathieu's equation for which approximate solutions were determined. These approximate solutions take the form of linear combinations of four simple harmonic oscillators, each with a different oscillation frequency and relative magnitude. Later in this chapter, many of the results derived in this section using the lower-level system model are compared to numerical solutions determined using the top-level computational model for the purposes of validation.

4.4 Computational Model: Transverse Vibrations of the Tether

In this section we develop several aspects of the lower-level computational model related to the transverse vibrations of the tether. The analysis of the transverse vibrations makes use of some of the results related to the tether pendular motion presented in the previous section, and many of the analysis methods that we apply to the transverse vibrations are similar to those applied to the pendular motion. Unlike the results presented in the previous section, the analytical results related to the tether transverse vibrations presented in this section are not original contributions, in that they duplicate the results presented in Refs. [5] and [8]. The original contribution related to the tether transverse vibrations is provided in the next section in which the top-level computational model is used to perform validation tests on the results presented in this section.

4.4.1 Analysis Using Separation of Variables

As done in the analysis of the pendular motion of the tether, we assume that the out-of-plane pendular motion is small. In addition, we assume that the transverse vibrations of the tether are small relative to the length of the tether, such that u and v are small quantities. Combining these assumptions, the equations of motion of the tether transverse vibrations simplify to

$$\mathring{\mathring{u}} - [(\mathring{\alpha}+1)^2 + 3\sin^2\alpha - 1]u = [(\mathring{\alpha}+1)^2 + 3\cos^2\alpha - 1]\left[\left(\frac{2-\gamma x^2}{2\gamma}\right)u'' - xu'\right] \tag{4.139}$$

$$\mathring{\mathring{v}} + v = [(\mathring{\alpha}+1)^2 + 3\cos^2\alpha - 1]\left[\left(\frac{2-\gamma x^2}{2\gamma}\right)v'' - xv'\right] \tag{4.140}$$

Note that because we assume that β is small, the solution for α is given by Eqs. (4.69) and (4.70).

To analyze Eqs. (4.139) and (4.140) we apply the principle of separation of variables.[7] Assume solutions for u and v of the form

$$u(x,\tau) = X_u(x)F_u(\tau) \tag{4.141}$$

$$v(x,\tau) = X_v(x)F_v(\tau) \tag{4.142}$$

where X_u and X_v are spatially-dependent mode shapes, and F_u and F_v are time-dependent functions. Using Eq. (4.141) in Eq. (4.140), we find that X_u and F_u must satisfy

$$\frac{\mathring{\mathring{F}}_u - [(\mathring{\alpha}+1)^2 + 3\sin^2\alpha - 1]F_u}{[(\mathring{\alpha}+1)^2 + 3\cos^2\alpha - 1]F_u} = \frac{1}{X_u}\left[\left(\frac{2-\gamma x^2}{2\gamma}\right)X_u'' - xX_u'\right] \tag{4.143}$$

The left-hand side of Eq. (4.143) is a function of τ only, and the right-hand side is a function of x only. Because Eq. (4.143) must hold for all τ and x, both sides of the expression must be equal to the same constant, which we denote $-\lambda_u$,

$$\frac{\mathring{\mathring{F}}_u - [(\mathring{\alpha}+1)^2 + 3\sin^2\alpha - 1]F_u}{[(\mathring{\alpha}+1)^2 + 3\cos^2\alpha - 1]F_u} = \frac{1}{X_u}\left[\left(\frac{2-\gamma x^2}{2\gamma}\right)X_u'' - xX_u'\right] = -\lambda_u \tag{4.144}$$

From this point forward we refer to the constant λ_u as an eigenvalue of Eq. (4.139). Using Eq. (4.141) in the boundary conditions for u, we obtain

$$X_u(0)F_u(\tau) = X_u(1)F_u(\tau) = 0 \tag{4.145}$$

which must hold for all τ. From Eqs. (4.144) and (4.145), the mode shape X_u must satisfy the boundary value problem

$$(2-\gamma x^2)X_u'' - 2\gamma x X_u' + 2\gamma\lambda_u X_u = 0 \tag{4.146}$$

$$X_u(0) = X_u(1) = 0 \tag{4.147}$$

Note that Eq. (4.146) is a nonstandard form of the Legendre differential equation.[7] From Eq. (4.144), the function F_u must satisfy the differential equation

$$\mathring{\mathring{F}}_u + [(\lambda_u - 1)(\mathring{\alpha}+1)^2 + (\lambda_u+1)(3\cos^2\alpha - 1) - 1]F_u = 0 \tag{4.148}$$

Using Eq. (4.142) in Eq. (4.140) and following the procedure illustrated above, we find that the mode shape X_v must satisfy the boundary value problem

$$(2-\gamma x^2)X_v'' - 2\gamma x X_v' + 2\gamma\lambda_v X_v = 0 \tag{4.149}$$

$$X_v(0) = X_v(1) = 0 \tag{4.150}$$

and the function F_v must satisfy the differential equation

$$\mathring{\mathring{F}}_v + [\lambda_v(\mathring{\alpha}+1)^2 + \lambda_v(3\cos^2\alpha - 1) + 1]F_v = 0 \tag{4.151}$$

Note that the constant λ_v in Eqs. (4.149) and (4.151) is an eigenvalue of Eq. (4.140).

Comparing Eqs. (4.146) and (4.147) with Eqs. (4.149) and (4.150) we see that the mode shapes for u and v are governed by the same boundary value problem. Without loss of generality, we can therefore define $X(x) = X_u(x) = X_v(x)$ and $\lambda = \lambda_u = \lambda_v$, such that the mode shapes for the transverse vibrations are governed by

$$(2-\gamma x^2)X'' - 2\gamma x X' + 2\gamma\lambda X = 0 \tag{4.152}$$

$$X(0) = X(1) = 0 \tag{4.153}$$

and the solutions for u and v are written as

$$u(x,\tau) = X(x)F_u(\tau) \tag{4.154}$$
$$v(x,\tau) = X(x)F_v(\tau) \tag{4.155}$$

Using the assumed solution forms of Eqs. (4.154) and (4.155) we have separated the solutions for the transverse vibrations into independent components. The spatially-dependent mode shapes are governed by Eqs. (4.152) and (4.153), and the time-dependent functions are governed by Eqs. (4.148) and (4.151). Recalling that we have an exact solution for α because β is assumed to be small, we can see that Eqs. (4.148) and (4.151) take the form of Hill's equations. Given an appropriate value of λ, we can use Floquet theory to analyze the stability properties of Eqs. (4.148) and (4.151), and thus the stability properties of the tether transverse vibrations. To determine appropriate values of λ, we must analyze the boundary value problem defined in Eqs. (4.152) and (4.153).

4.4.2 Solution for the Mode Shapes

To determine an expression for the mode shapes of the transverse vibrations we assume a solution in the form of a power series,

$$X(x) = \sum_{n=1}^{\infty} a_n x^n \tag{4.156}$$

Note that the summation in Eq. (4.156) begins at $n = 1$ because the assumed solution form for X must satisfy the boundary condition $X(0) = 0$. Using Eq. (4.156) in Eq. (4.152) and collecting powers of x, we find that all a_n for even n must be zero and a_1 can be any nonzero real number. Setting $a_1 = 1$, we find that a_n with odd n must satisfy

$$a_{2n+1} = \frac{\gamma^n}{(2n+1)!} \prod_{m=1}^{n} \left[\frac{1}{2}(2m)(2m-1) - \lambda \right], \qquad n = 1, \ldots, \infty \tag{4.157}$$

Using Eq. (4.157) in Eq. (4.156), the solution for X becomes

$$X(x) = x \, {}_2F_1\left(\sigma_1, \sigma_2; \frac{3}{2}; \frac{1}{2}\gamma x^2\right) \tag{4.158}$$

where ${}_2F_1\left(a, b; c; z\right)$ is a hypergeometric function and

$$\sigma_1 = \frac{3 - \sqrt{1 + 8\lambda}}{4} \tag{4.159}$$
$$\sigma_2 = \frac{3 + \sqrt{1 + 8\lambda}}{4} \tag{4.160}$$

See Ref. [4] for an excellent discussion of hypergeometric functions. Applying the boundary condition $X(1) = 0$ to Eq. (4.158), we obtain

$$ {}_2F_1\left(\sigma_1, \sigma_2; \frac{3}{2}; \frac{1}{2}\gamma\right) = 0 \tag{4.161} $$

For any given value of γ there exists an infinite number of positive values of λ that satisfy Eq. (4.161). Let these values of λ be ordered in ascending order, and denote the n^{th} value as λ_n. For each λ_n, there exists a corresponding mode shape, $X_n(x)$, that satisfies Eqs. (4.152) and (4.153).

Figure 4.19 shows a plot of the hypergeometric function in Eq. (4.161) for $\gamma = 1$. By determining the roots of this function, we find that the first four eigenvalues are $\lambda_1 = 7.72$, $\lambda_2 = 31.72$, $\lambda_3 = 71.72$, and $\lambda_4 = 127.72$. The mode shapes corresponding to the first four eigenvalues are plotted in Fig. 4.20. Note that the mode shapes are similar in quality to sine waves.

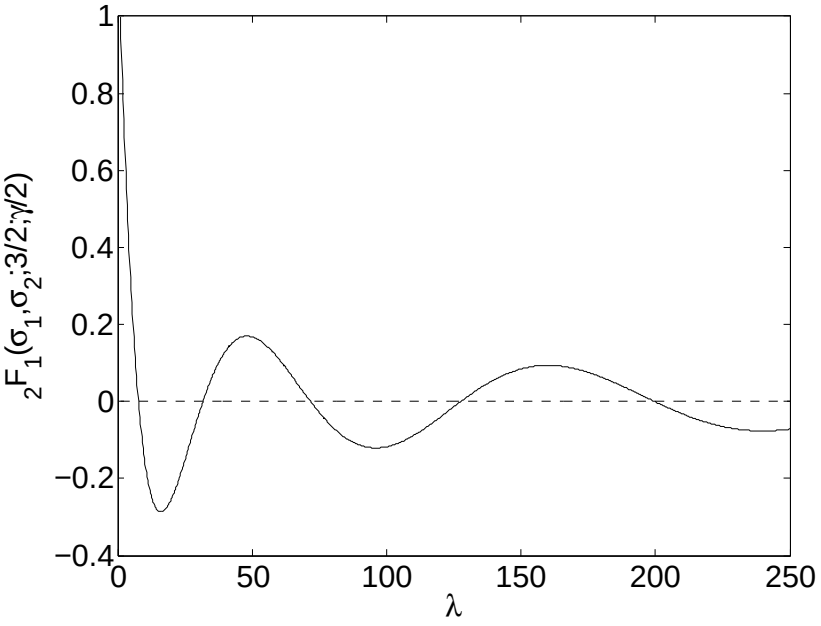

Figure 4.19: Plot of ${}_2F_1\left(\sigma_1, \sigma_2; \frac{3}{2}; \frac{1}{2}\gamma\right)$ for $\gamma = 1$

As γ approaches 0, all of the eigenvalues approach infinity, and the mode shapes become more like sine waves. This fact is illustrated by Fig. 4.21, which shows plots of the first four mode shapes for $\gamma = 0.1$. Note that the first four eigenvalues for this case are $\lambda_1 = 96.78$, $\lambda_2 = 387.89$, $\lambda_3 = 873.06$, $\lambda_4 = 1552.3$. As γ approaches 2, the smallest eigenvalue, λ_1, approaches 1, and the mode shapes become less like sine waves. The first four mode shapes

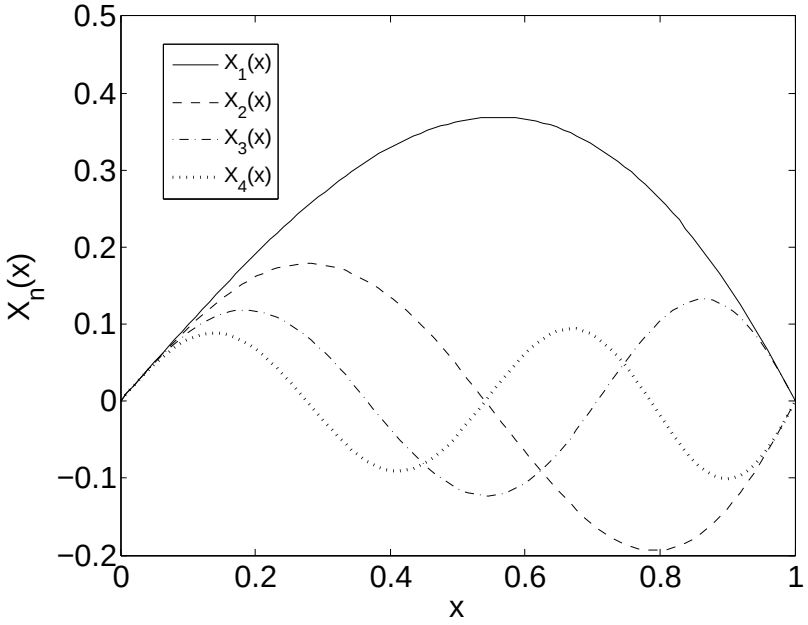

Figure 4.20: First four mode shapes of the tether transverse vibrations for $\gamma = 1$

for $\gamma = 1.9$ are plotted in Fig. 4.22. The eigenvalues corresponding to these mode shapes are $\lambda_1 = 2.34$, $\lambda_2 = 10.45$, $\lambda_3 = 24.06$, and $\lambda_4 = 43.13$. As Fig. 4.22 shows, the mode shapes become skewed toward $x = 1$ as γ approaches 2.

4.4.3 Floquet Analysis

Now that we have a means of determining the values of λ for a given value of γ, we return our attention to Eqs. (4.148) and (4.151). Using the solution for α defined in Eq. (4.69), Eqs. (4.148) and (4.151) are written as

$$\overset{\circ\circ}{F}_u + p_u(\tau)F_u = 0 \tag{4.162}$$

$$\overset{\circ\circ}{F}_v + p_v(\tau)F_v = 0 \tag{4.163}$$

where the periodic functions p_u and p_v are

$$p_u(\tau) = (\lambda - 1)[\pm\sqrt{h}\,\mathrm{dn}(\sqrt{h}\,\tau, \kappa) + 1]^2 + (\lambda + 1)[3\,\mathrm{cn}^2(\sqrt{h}\,\tau, \kappa) - 1] - 1 \tag{4.164}$$

$$p_v(\tau) = \lambda[\pm\sqrt{h}\,\mathrm{dn}(\sqrt{h}\,\tau, \kappa) + 1]^2 + \lambda[3\,\mathrm{cn}^2(\sqrt{h}\,\tau, \kappa) - 1] + 1 \tag{4.165}$$

Note that the "+" is for systems with a positive in-plane rotational rate, and the "-" is for systems with a negative in-plane rotation rate. As mentioned previously, Eqs. (4.162) and

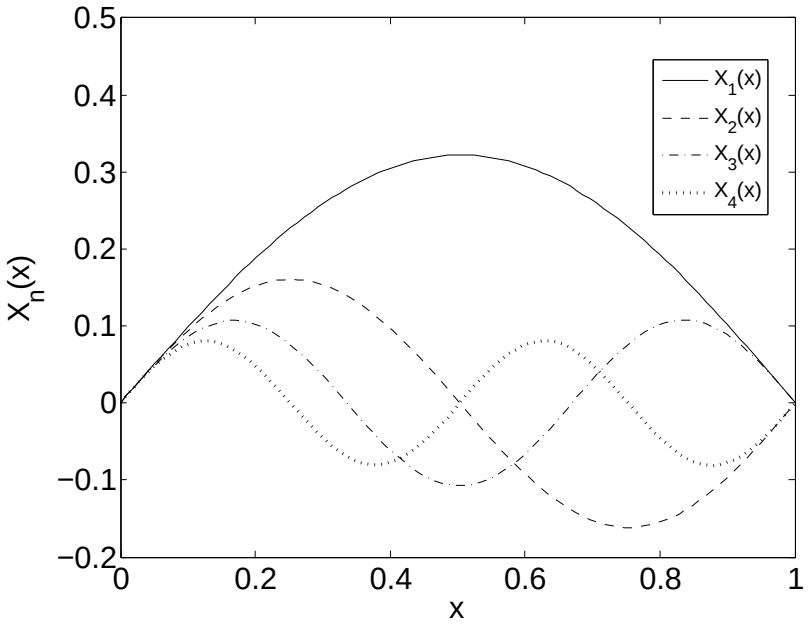

Figure 4.21: First four mode shapes of the tether transverse vibrations for $\gamma = 0.1$

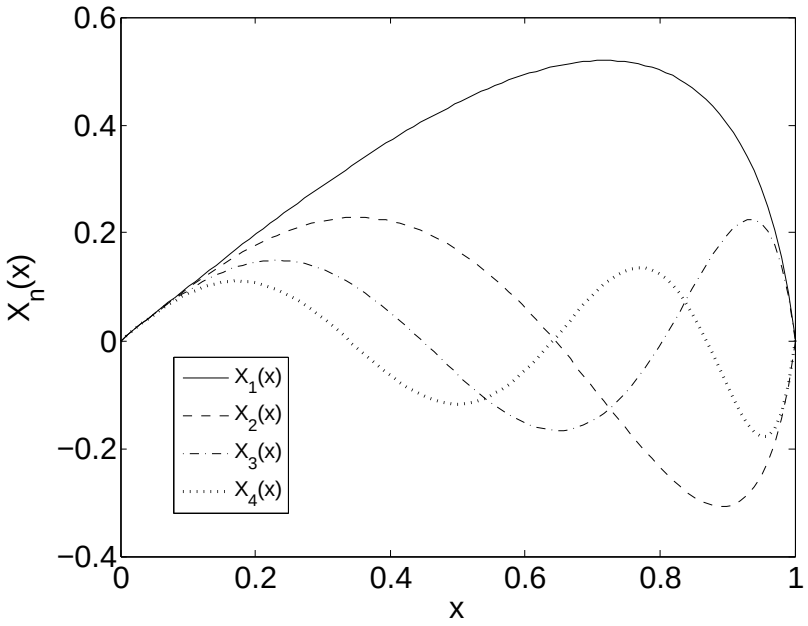

Figure 4.22: First four mode shapes of the tether transverse vibrations for $\gamma = 1.9$

(4.163) are Hill's equations, and their stability properties can be determined using Floquet theory. These properties are dependent on the two free parameters in the equations: 1) the eigenvalue λ; and 2) the in-plane pendular motion energy constant h.

The stability properties of $F_u(\tau)$ and $F_v(\tau)$ for systems with a positive in-plane rotation rate are illustrated by the plots in Fig. 4.23. In this study of the tether transverse vibrations we do not consider systems with a negative in-plane rotation rate, or systems undergoing oscillatory in-plane pendular motion. In the plots in Fig. 4.23, the shaded regions correspond to unstable behavior, and the unshaded regions correspond to bounded, oscillatory behavior. Note that the abscissa for both plots is $1/\lambda$, and the ordinate is $1/h$. The plots are shown in this manner so that the entire admissable region of λ and h can be shown on a single plot. As the plots show, there are distinct regions of instability in both F_u and F_v for relatively low values of λ and h. Recalling that λ approaches 1 as γ approaches 2, these larger instability regions correspond to slowly spinning systems in which the mass of the tether is much larger than the mass of $\mathcal{B}$. As both λ and h increase–corresponding to increases in the mass of $\mathcal{B}$ and the in-plane spin rate, respectively–the instability regions decrease in size to the point that they practically vanish.

To better understand how the stability of the transverse vibrations is related to the plots in Fig. 4.23, consider the plots in Fig. 4.24. These plots are the same as those in Fig. 4.23, except that the first four eigenvalues for a system with $\gamma = 1.99$ and $h = 5$ are each plotted with an "$\times$". For any particular value of γ, there is a minimum eigenvalue, λ_1, corresponding to the first mode of the transverse vibrations. The minimum eigenvalue in Fig. 4.24 is the "$\times$" farthest to the right because the abscissa of the plots is $1/\lambda$. For each higher-order mode, there is a corresponding $\lambda_n > \lambda_1$, and the location of the "$\times$" corresponding to each higher-order mode moves horizontally to the left on the plot as the mode number increases. If any "$\times$" lies in an unstable region for either F_u or F_v, then one of the modes of the transverse vibrations is unstable. Because the transverse vibrations are a linear combination of all of the modes, if one of the modes is unstable then the transverse vibrations on the whole are unstable. Note that the case illustrated in Fig. 4.24 represents stable transverse vibrations because none of the modes of the transverse vibrations lie in unstable regions for F_u or F_v.

4.4.4 Summary of Computational Predictions

In this section we presented aspects of the lower-level computational model pertaining to the transverse vibrations of the tether. The equations governing the transverse vibrations were simplified by assuming small out-of-plane pendular motion of the tether, and that the transverse vibrations are small relative to the length of the tether. The resulting simplified equations were analyzed using separation of variables, and the mode shapes for the transverse vibrations were determined. Using the solution for the in-plane pendular motion derived in the previous section and the solution for the mode shapes, the stability properties of the

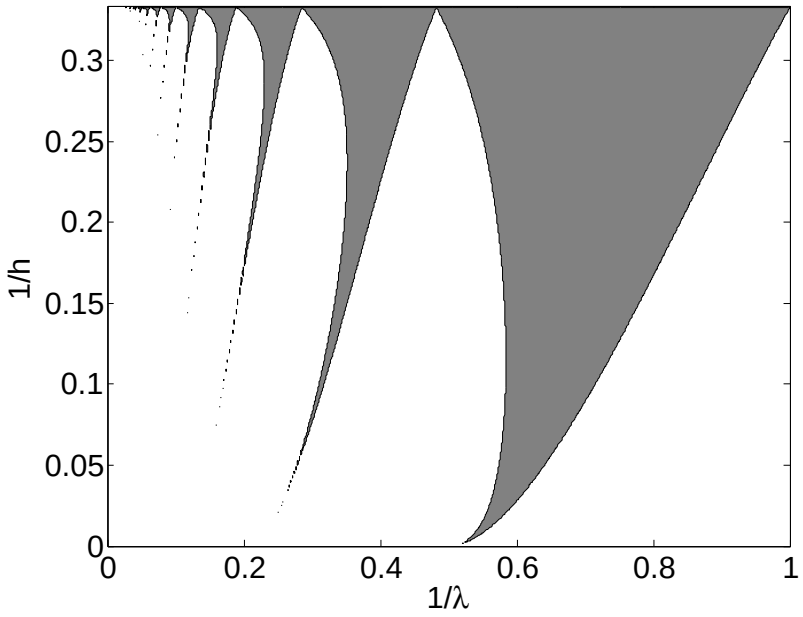

(a) $F_u(\tau)$

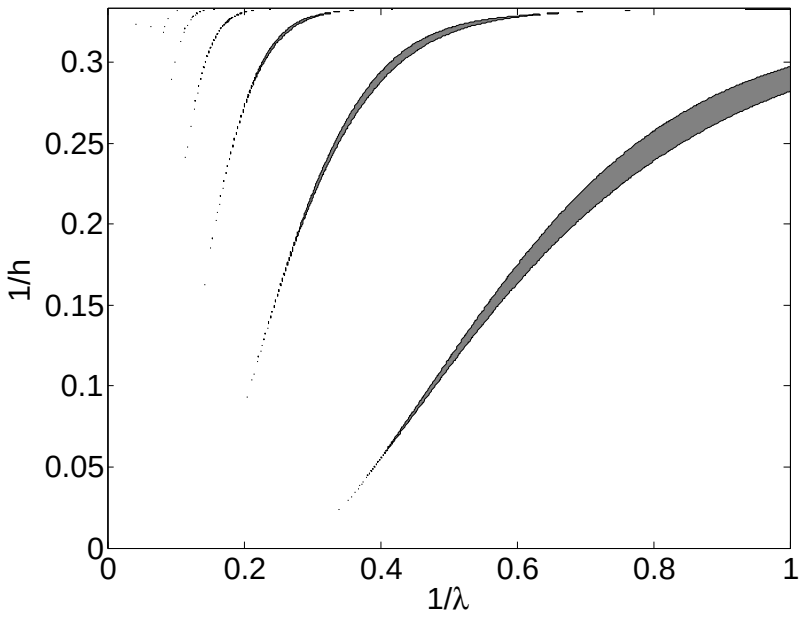

(b) $F_v(\tau)$

Figure 4.23: Stability regions for the functions $F_u(\tau)$ and $F_v(\tau)$

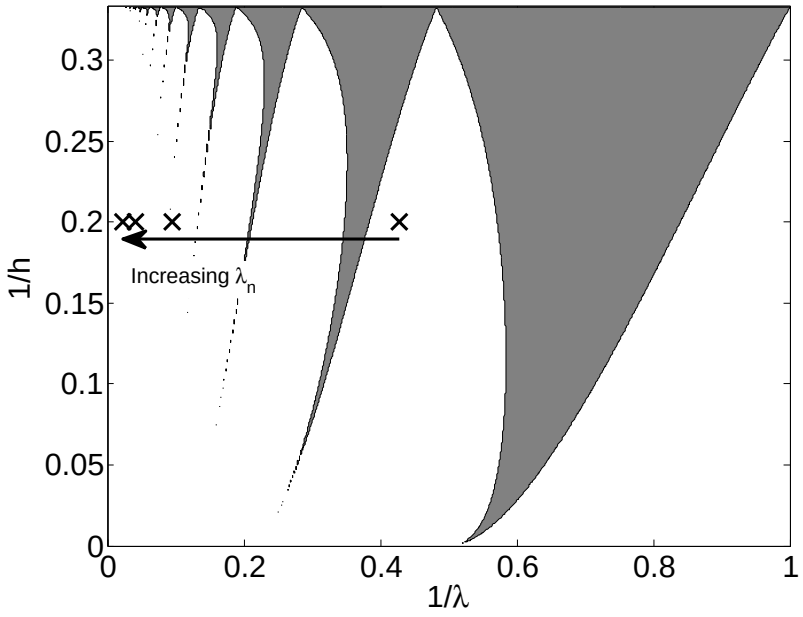

(a) $F_u(\tau)$

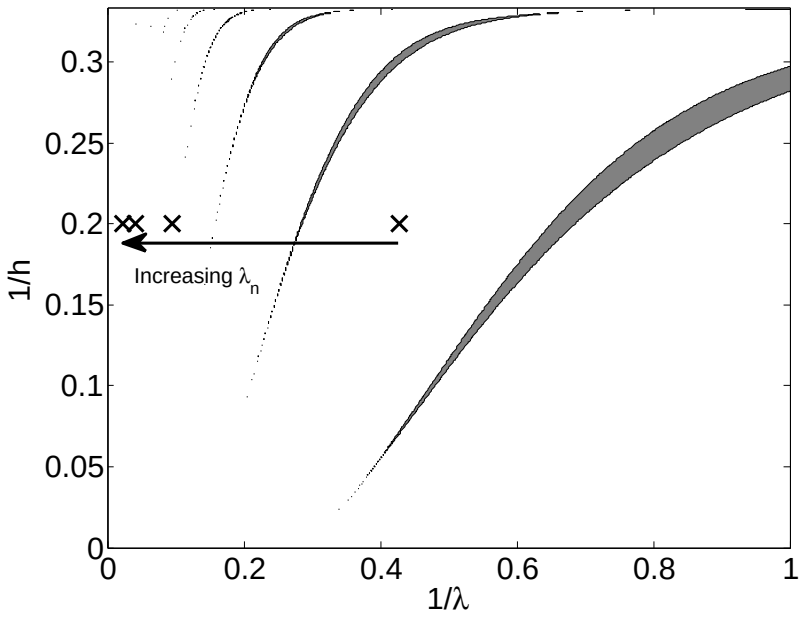

(b) $F_v(\tau)$

Figure 4.24: Relationship between eigenvalues and stability regions for the functions $F_u(\tau)$ and $F_v(\tau)$ for $\gamma = 1.99$ and $h = 5$

transverse vibrations were analyzed using Floquet theory.

The lower-level computational model predicts distinct regions of transverse vibration instability for certain types of systems. The largest regions of instability correspond to systems with relatively low values of λ and h. A low value of h means that the in-plane spin rate is relatively low, which could apply to any type of spinning TSS. Low values of λ correspond to systems with values of γ near 2 because λ_1 approaches 1 as γ approaches 2, and λ_1 is the minumum eigenvalue for a given value of γ. As mentioned previously, a γ near 2 means that the mass of the tether is much greater than the mass of $\mathcal{B}$, so the lower-level computational model predicts that these types of systems have the largest range of configurations that experience unstable transverse vibrations. As both λ and h increase, the instability regions decrease in size and become virtually nonexistent. This means that the lower-level computational model predicts that systems with a relatively high in-plane spin rate and large secondary end body mass will practically never experience unstable transverse vibrations. In the next section, we use numerical solutions determined using the top-level computational model to perform validation tests on these results related to the stability of the transverse vibrations of the tether.

4.5 Validation of the Computational Model

In §4.3 and §4.4 we developed several elements of the lower-level computational model related to the dynamics of the tether in a spinning TSS. Specifically, we showed that the lower-level model predicts that both the pendular motion and elastic vibrations of the tether are unstable for certain system configurations, and we also determined approximate solutions for the out-of-plane pendular motion for systems with a relatively high in-plane spin rate. In this section we apply the model validation procedure outlined in Ch. 2 to these computational predictions. For any results that are not validated through the application of this procedure, we perform an analysis of the modeling assumptions used in the lower-level model to determine how the model should be altered to produce better agreement with the top-level computational model.

4.5.1 Pendular Motion of the Tether

The lower-level computational model predicts that the out-of-plane pendular motion of the tether is unstable for certain ranges of the the parameter h, which is a measure of the energy of the in-plane pendular motion. For relatively large values of h, the out-of-plane pendular motion is predicted to be stable and oscillatory, and approximate solutions for the out-of-plane motion can be expressed as finite sums of simple harmonic oscillators. These computational predictions are now compared to the top-level computational model for the purposes of validation; however, validation tests are only performed on the results that are

applicable to spinning systems with a positive spin rate. These types of systems are the most likely to be used in an actual application, so we confine our attention to them.

Out-of-Plane Instabilities

Figure 4.25 shows the out-of-plane pendular motion predicted by the top-level computational model for a system with initial conditions corresponding to $h = 3.5$. The system parameters and initial conditions used to generate this numerical solution are listed in Tables 4.4 and 4.5, respectively. Note that the values of m_B, $\bar{\rho}$, and L used correspond to $\gamma = 0.4$, and that the quantities Ω_{A0} and $f(0)$ are defined as

$$\Omega_{A0} = \sqrt{\frac{\mu}{a(0)^3}} \tag{4.166}$$

$$f(0) = [\dot{\alpha}(0) + \Omega_{A0}]^2 \cos^2\beta(0) + \dot{\beta}(0)^2 + \Omega_{A0}^2[3\cos^2\alpha(0)\cos^2\beta(0) - 1] \tag{4.167}$$

The lower-level computational model predicts that the out-of-plane pendular motion for this system is unstable, and the top-level computational model makes a similar prediction. As mentioned in §4.3, the out-of-plane motion is not "unstable" in the strictest sense of the word; however, a small initial value of β does grow quite large in a relatively small number of orbits of the system. This result indicates that the predictions made by the lower-level computational model apply to the top-level model, and are therefore validated. Before we make this conclusion, however, we must perform several more validations test for systems with different values of h and different system parameters.

Table 4.6 displays the results of a number of additional validation tests. As shown by the table, these tests were performed at a number of points inside the range of h predicted by the lower-level computational model to result in instability. For each value of h tested, the value of γ for the system was also varied across the feasible range. The value of γ was varied by varying m_B while holding $\bar{\rho}$ and L constant. The system parameters and initial conditions used in all of these additional tests are listed in Tables 4.4 and 4.5. For all of the additional tests performed, the out-of-plane instability predicted by the lower-level computational model is also predicted by the top-level computational model. We must note, however, that the growth of β becomes less significant as the boundaries of the instability region are approached. This fact is particularly true as h approaches the lower boundary of 3.36. In any case, the agreement between the lower- and top-level computational models over the entire predicted instability region for a wide range of system parameters means that the lower-level predictions are validated. A spinning TSS with a positive in-plane spin rate corresponding to h between 3.36 and 3.55 is expected to experience large growth in the out-of-plane pendular motion.

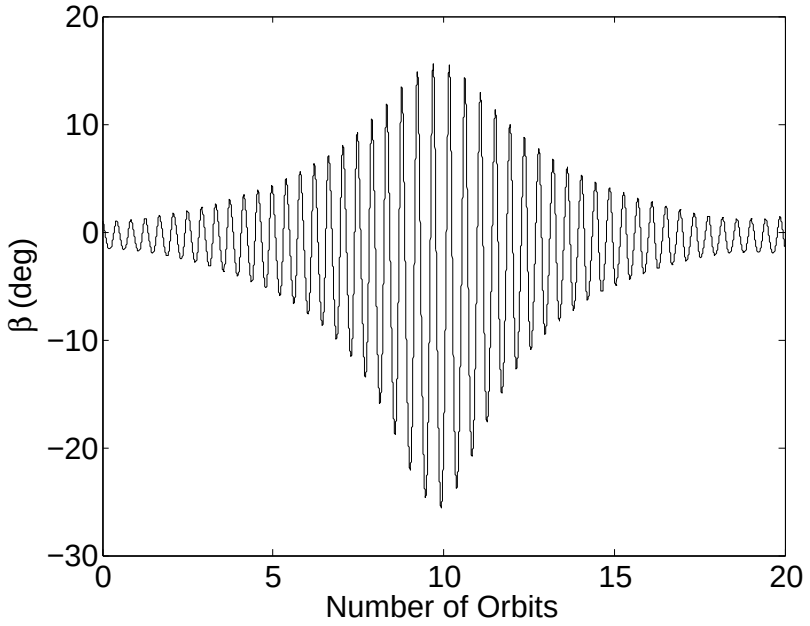

Figure 4.25: Out-of-plane pendular motion of the tether predicted by the top-level computational model for $h = 3.5$ and $\gamma = 0.4$

Table 4.4: System parameters used in validation tests for the instabilities in the out-of-plane pendular motion of the tether

Primary End Body $\mathcal{A}$	
m_A (kg)	50,000
$\mathbf{I}_{\mathrm{A}}$ (kg-m^2)	diag(30,000 40,000 50,000)
$\mathbf{p}_{\mathrm{A}}$ (m)	$(0\ 0\ 1)^{\mathrm{T}}$
Secondary End Body $\mathcal{B}$	
m_B (kg)	$\left(\frac{2-\gamma}{2\gamma}\right)\bar{\rho}L$
$\mathbf{I}_{\mathrm{B}}$ (kg-m^2)	diag(300 400 500)
$\mathbf{p}_{\mathrm{B}}$ (m)	$(0\ 0\ 0)^{\mathrm{T}}$
Tether	
L (km)	20
$\bar{\rho}$ (kg/km)	2.5
EA (N)	55,000
c (s)	0.5
N_e	4
Central Body	
μ (km^3/s^2)	3.986×10^5

Table 4.5: Initial conditions used in validation tests for the instabilities in the out-of-plane pendular motion of the tether

System Orbital Motion	
a (km)	6,770
e	0.001
Ω (deg)	300
I (deg)	50
ω (deg)	45
ν (deg)	0
$\mathcal{A}$ Attitude Motion	
$\bar{\mathbf{q}}_{\mathrm{A}}$	$(1\ 0\ 0\ 0)^{\mathrm{T}}$
$\boldsymbol{\omega}_{\mathrm{A/O}}$ (deg/s)	$(0\ \sqrt{h}\,\Omega_{A0}\ 0)^{\mathrm{T}}$
$\mathcal{B}$ Attitude Motion	
$\bar{\mathbf{q}}_{\mathrm{B}}$	$(1\ 0\ 0\ 0)^{\mathrm{T}}$
$\boldsymbol{\omega}_{\mathrm{B/O}}$ (deg/s)	$(0\ \sqrt{h}\,\Omega_{A0}\ 0)^{\mathrm{T}}$
Pendular Tether Motion	
α (deg)	0
β (deg)	1°
$\dot{\alpha}$ (deg/s)	$\sqrt{h}\,\Omega_{A0}$
$\dot{\beta}$ (deg/s)	0
Tether Elastic Vibrations	
$u(\bar{s},0)$ (m)	$20\sin\left(\frac{\pi\bar{s}}{L}\right)$
$\dot{u}(\bar{s},0)$ (m)	0
$v(\bar{s},0)$ (m)	$20\sin\left(\frac{\pi\bar{s}}{L}\right)$
$\dot{v}(\bar{s},0)$ (m)	0
$w(\bar{s},0)$ (m)	$\frac{c_A L}{EA} f(0)\left[\frac{\bar{s}}{L} - \frac{\gamma}{6}\left(\frac{\bar{s}}{L}\right)^3\right]$
$\dot{w}(\bar{s},0)$ (m)	$\frac{c_A L}{EA} \dot{f}(0)\left[\frac{\bar{s}}{L} - \frac{\gamma}{6}\left(\frac{\bar{s}}{L}\right)^3\right]$

Table 4.6: Results of validation tests for the instabilities in the out-of-plane pendular motion of the tether

h	$\gamma = 0.1$	$\gamma = 0.4$	$\gamma = 1$	$\gamma = 1.6$	$\gamma = 1.9$
3.37	unstable	unstable	unstable	unstable	unstable
3.39	unstable	unstable	unstable	unstable	unstable
3.41	unstable	unstable	unstable	unstable	unstable
3.43	unstable	unstable	unstable	unstable	unstable
3.45	unstable	unstable	unstable	unstable	unstable
3.46	unstable	unstable	unstable	unstable	unstable
3.48	unstable	unstable	unstable	unstable	unstable
3.50	unstable	unstable	unstable	unstable	unstable
3.52	unstable	unstable	unstable	unstable	unstable
3.54	unstable	unstable	unstable	unstable	unstable

Approximate Solutions for the Out-of-Plane Motion

Figure 4.26 shows the predictions for the out-of-plane pendular motion made by the lower- and top-level computational models for a system with $h = 25$. The value of γ for the top-level model is 0.4, and the system parameters and initial conditions used for the top-level model are listed in Tables 4.4 and 4.5. As shown by Fig. 4.26(a), over the first orbit of the system the approximate solution determined using the lower-level computational model is virtually identical to the prediction made by the top-level computational model. However, the two predictions begin to diverge as the solution time span increases. This fact is illustrated by Fig. 4.26(b), which shows the two predictions over the tenth orbit of the system. As the figure shows, a slight phase difference has developed between the two predictions, and the phase difference grows as the solution time span increases. This result indicates that the approximate solutions for β determined using the lower-level system model provide good qualitative and short-term quantitative predictions, but cannot be used to make long-term quantitative predictions about the out-of-plane pendular motion of the tether.

To further substantiate the claim about the validity of the approximate solutions made above, several more validation tests for the approximate solutions were performed. In these tests, a Fourier analysis was used on the numerical solutions determined using the top-level computational model to determine the two most dominant frequencies of the motion. These two frequencies are then compared to the two most dominant frequencies contained in the approximate solutions. Recall that for systems with a positive in-plane spin rate, the lower-level model predicts that the two most dominant frequencies are ω_2 and ω_3 as defined by Eq. (4.127). The results of the Fourier analysis are listed in Table 4.7. Note that the frequencies listed in Table 4.7 have been nondimensionalized by the quantity Ω_{A0}. Also note that there is no variation in the frequencies predicted by the top-level computational model

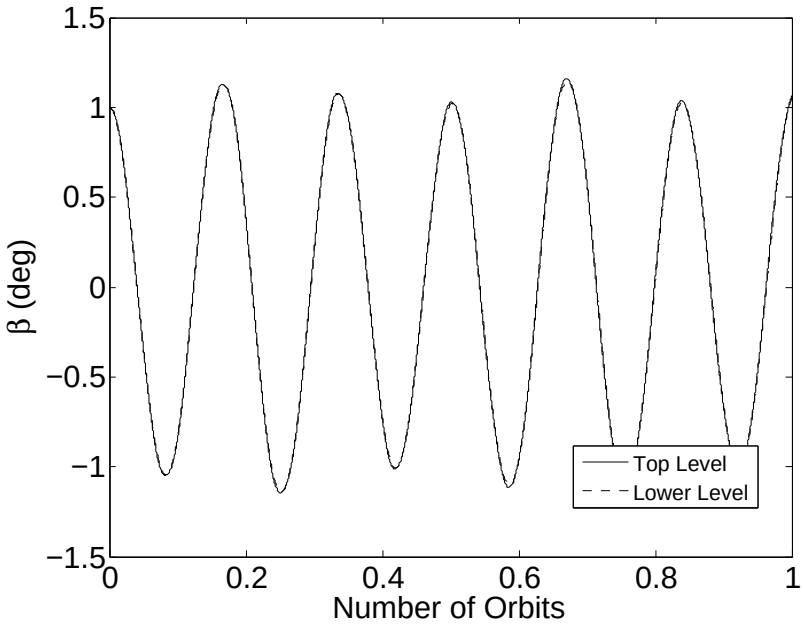

(a) Comparison over first orbit

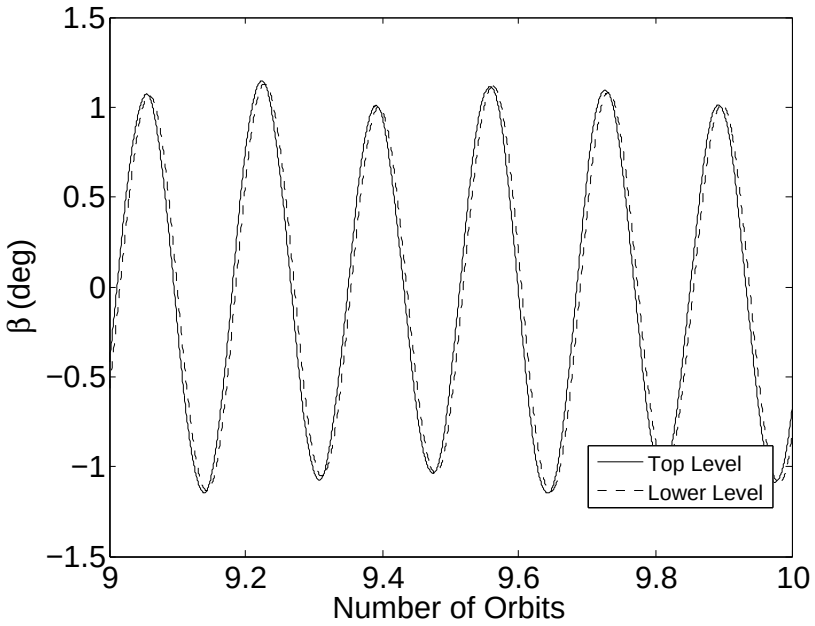

(b) Comparison over tenth orbit

Figure 4.26: Comparison of computational predictions of β made by the top- and lower-level computational models for $h = 25$ and $\gamma = 0.4$

as γ is varied. The frequencies listed in Table 4.7 are plotted against those predicted by the lower-level computational model in Fig. 4.27. As the plot shows, the frequencies predicted by the approximate solutions are close, but not exactly equal to, those predicted by the top-level computational model. These small differences explain why the two predictions are close over short time spans but diverge over large time spans. To better understand the reasoning behind this behavior, imagine a system for which the exact solution is $\sin(t)$ and the approximate solution is determined to be $\sin(0.999\,t)$. The difference between the exact and approximate solutions is only 0.1%, but the small difference will nonetheless accumulate over time and result in the type of phase difference seen in Fig. 4.27. So, while the approximate solutions for β do not provide accurate long-term qualitative predictions, they do provide accurate qualitative predictions of the out-of-plane pendular motion of the tether.

Table 4.7: Nondimensional oscillation frequencies for the out-of-plane pendular motion of the tether predicted by top-level computational model

First Frequency ω_2					
h	$\gamma = 0.1$	$\gamma = 0.4$	$\gamma = 1$	$\gamma = 1.6$	$\gamma = 1.9$
10	4.00	4.00	4.00	4.00	4.00
25	6.00	6.00	6.00	6.00	6.00
50	8.00	8.00	8.00	8.00	8.00
100	11.00	11.00	11.00	11.00	11.00
Second Frequency ω_3					
h	$\gamma = 0.1$	$\gamma = 0.4$	$\gamma = 1$	$\gamma = 1.6$	$\gamma = 1.9$
10	1.75	1.75	1.75	1.75	1.75
25	3.75	3.75	3.75	3.75	3.75
50	6.00	6.00	6.00	6.00	6.00
100	8.75	8.75	8.75	8.75	8.75

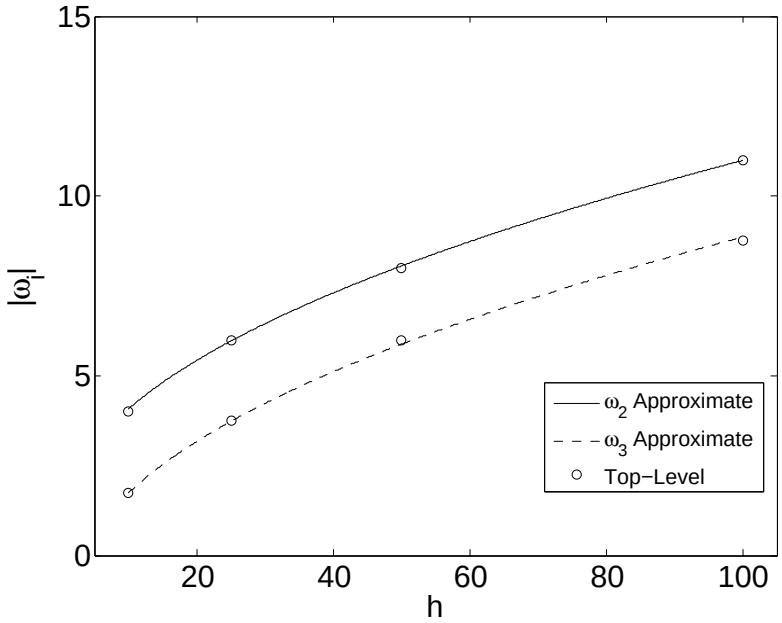

Figure 4.27: Comparison of out-of-plane pendular oscillation frequencies predicted by the top- and lower-level computational models

4.5.2 Transverse Vibrations of the Tether

The lower-level computational model predicts that the transverse vibrations of the tether are unstable for certain ranges of the parameters h and γ. For a given combination of h and γ, one or more modes of either u or v is predicted to be unstable, resulting in instability of the transverse vibrations on the whole. These computational predictions are now compared to the top-level computational model for the purposes of validation. As with the validation tests performed on the results related to the pendular motion of the tether, validation tests for the tether transverse vibrations are only performed for systems with a positive in-plane spin, as these are the types of systems that would actually be utilized in practice.

Figure 4.28 shows the transverse displacements at the tether midpoint ($\bar{s} = \frac{1}{2}L$) predicted by the top-level computational model for two cases in which the lower-level computational model predicts unstable transverse vibrations. The system parameters and initial conditions used to generate these solutions are listed in Tables 4.8 and 4.9, respectively. Figure 4.28(a) shows u at the tether midpoint predicted by the top-level computational model for a system with initial conditions and physical parameters corresponding to $h = 5$ and $\gamma = 1.3939$. For such a system, the lower-level computational model predicts that the first mode of u is unstable, meaning that u at the tether midpoint should grow over time. As Fig. 4.28(a) shows, the top-level computational model predicts quite different behavior, in that u at the tether midpoint remains bounded. Figure 4.28(b) shows v at the tether midpoint predicted by the top-level computational model for a system with initial conditions and physical paramters corresponding to $h = 5$ and $\gamma = 1.64138$. The lower-level computational model predicts that the first mode of v is unstable for such a system, meaning that v at the tether midpoint should grow over time. As shown by Fig. 4.28(b), we once again find that the top-level computational model provides a clearly different prediction, in that v at the tether midpoint remains bounded. The results shown in Fig. 4.28 indicate that the predictions made by the lower-level computational model related to the stability of the tether transverse vibrations are erroneous because they do not agree with the top-level computational model. Before we can make this claim, however, we must perform more validation tests over a wider range of the instability regions predicted by the lower-level computational model.

Figure 4.29 shows the points in the $1/\gamma - 1/h$ plane for which the additional validation tests are performed. Each test point is marked with a "$\times$", and each point lies in a region of instability predicted by the lower-level computational model. The results of the additional validation tests are listed in Table 4.10. This table lists the values of h and λ_n used in the validation tests, along with the value of n for the predicted unstable mode and the corresponding value of γ. For all of the additional validation tests performed, the first mode is the predicted unstable mode. As Table 4.10 shows, the transverse vibrations predicted by the top-level computational model for all of the additional tests are stable, in direct disagreement with the predictions made by the lower-level computational model. These results confirm the previous assertion that the predictions of the lower-level computational model are erroneous, and cannot be used to make predictions about the physical system.

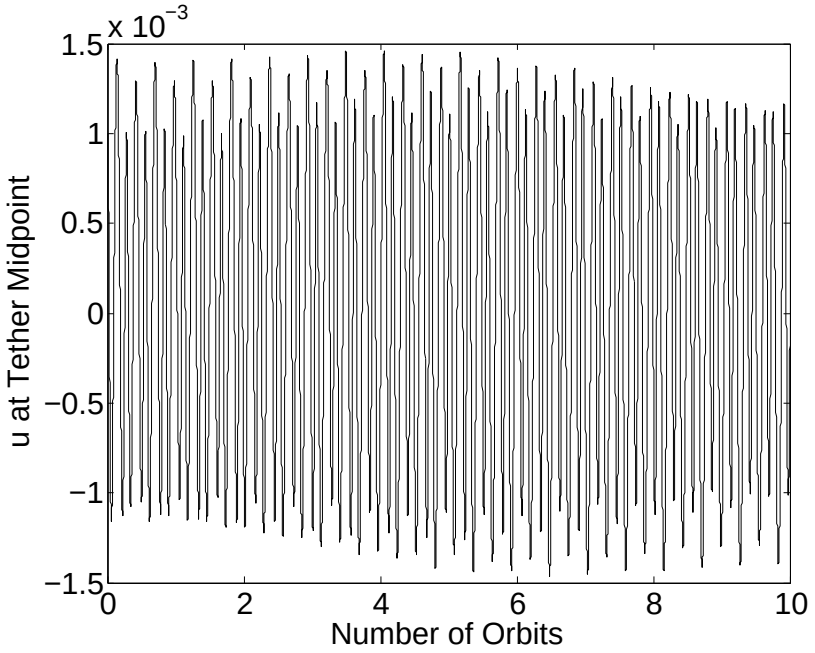

(a) u at tether midpoint for $h = 5$ and $\gamma = 1.3939$

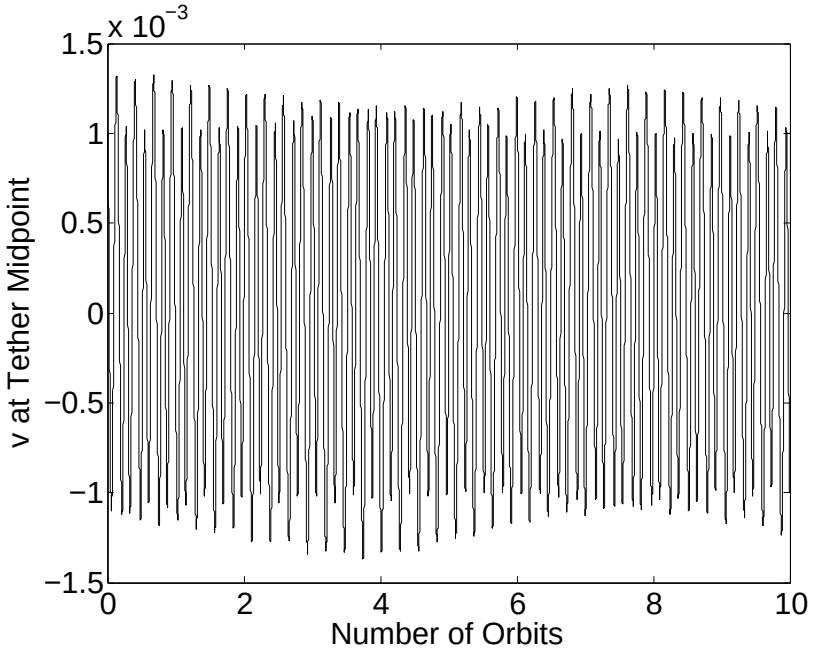

(b) v at tether midpoint for $h = 5$ and $\gamma = 1.64138$

Figure 4.28: Transverse vibrations at the tether midpoint predicted by the top-level computational model

Table 4.8: System parameters used in validation tests for the instabilities in the transverse vibrations of the tether

Primary End Body $\mathcal{A}$	
m_A (kg)	50,000
$\mathbf{I}_{\mathrm{A}}$ (kg-m^2)	diag(30,000 40,000 50,000)
$\mathbf{p}_{\mathrm{A}}$ (m)	$(0\ 0\ 1)^{\mathrm{T}}$
Secondary End Body $\mathcal{B}$	
m_B (kg)	$\left(\frac{2-\gamma}{2\gamma}\right)\bar{\rho}L$
$\mathbf{I}_{\mathrm{B}}$ (kg-m^2)	diag(300 400 500)
$\mathbf{p}_{\mathrm{B}}$ (m)	$(0\ 0\ 0)^{\mathrm{T}}$
Tether	
L (km)	20
$\bar{\rho}$ (kg/km)	2.5
EA (N)	55,000
c (s)	0.5
N_e	10
Central Body	
μ (km^3/s^2)	3.986×10^5

One important point we must address related to the validation tests for the tether transverse vibrations is that few or no tests are performed in the largest instability regions, as can be seen by studying Fig. 4.29. The reason for this lack of tests is that the largest instability regions correspond to instabilities in the first vibration mode of systems with γ approaching 2, meaning that m_B is quite small. An actual spinning TSS would not likely have small secondary end masses corresponding to such values of γ, so no tests are performed in these regions.

Because the predictions made by the lower-level computational model do not agree with those made by the top-level computational model, the lower-level model is not validated and must be altered in some way to achieve better agreement with the top-level model. In what follows, we present an analysis of the modeling assumptions used in the formulation of the lower-level model to determine exactly how the lower-level model should be changed so that it provides better predictions related to the transverse vibrations of the tether.

Table 4.9: Initial conditions used in validation tests for the instabilities in the transverse of the tether

System Orbital Motion	
a (km)	6,770
e	0.001
Ω (deg)	300
I (deg)	50
ω (deg)	45
ν (deg)	0
$\mathcal{A}$ Attitude Motion	
$\bar{\mathbf{q}}_{\mathrm{A}}$	$(1\ 0\ 0\ 0)^{\mathrm{T}}$
$\boldsymbol{\omega}_{\mathrm{A/O}}$ (deg/s)	$(0\ \sqrt{h}\,\Omega_{A0}\ 0)^{\mathrm{T}}$
$\mathcal{B}$ Attitude Motion	
$\bar{\mathbf{q}}_{\mathrm{B}}$	$(1\ 0\ 0\ 0)^{\mathrm{T}}$
$\boldsymbol{\omega}_{\mathrm{B/O}}$ (deg/s)	$(0\ \sqrt{h}\,\Omega_{A0}\ 0)^{\mathrm{T}}$
Pendular Tether Motion	
α (deg)	0
β (deg)	1°
$\dot{\alpha}$ (deg/s)	$\sqrt{h}\,\Omega_{A0}$
$\dot{\beta}$ (deg/s)	0
Tether Elastic Vibrations	
$u(\bar{s},0)$ (m)	$20\sin\left(\frac{\pi\bar{s}}{L}\right)$
$\dot{u}(\bar{s},0)$ (m)	0
$v(\bar{s},0)$ (m)	$20\sin\left(\frac{\pi\bar{s}}{L}\right)$
$\dot{v}(\bar{s},0)$ (m)	0
$w(\bar{s},0)$ (m)	$\frac{c_A L}{EA} f(0)\left[\frac{\bar{s}}{L}-\frac{\gamma}{6}\left(\frac{\bar{s}}{L}\right)^3\right]$
$\dot{w}(\bar{s},0)$ (m)	$\frac{c_A L}{EA} \dot{f}(0)\left[\frac{\bar{s}}{L}-\frac{\gamma}{6}\left(\frac{\bar{s}}{L}\right)^3\right]$

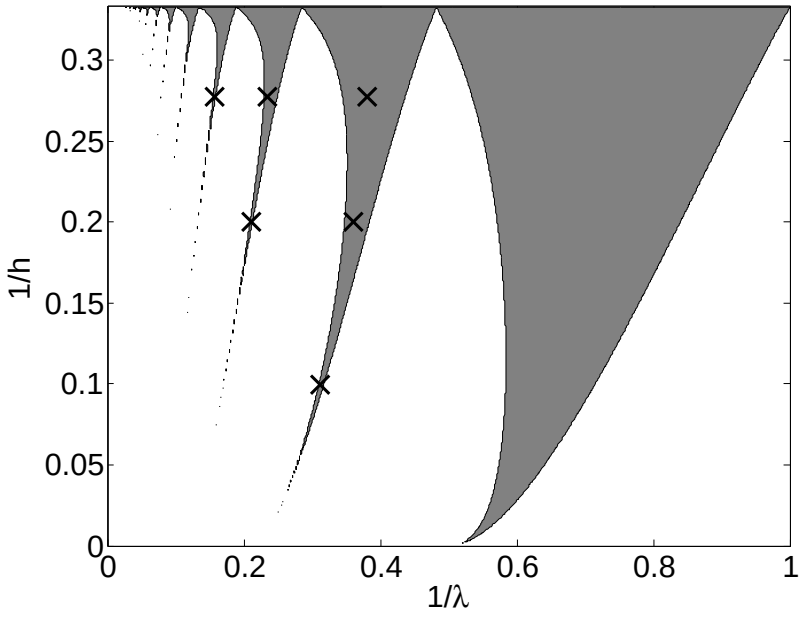

(a) Validation tests for u

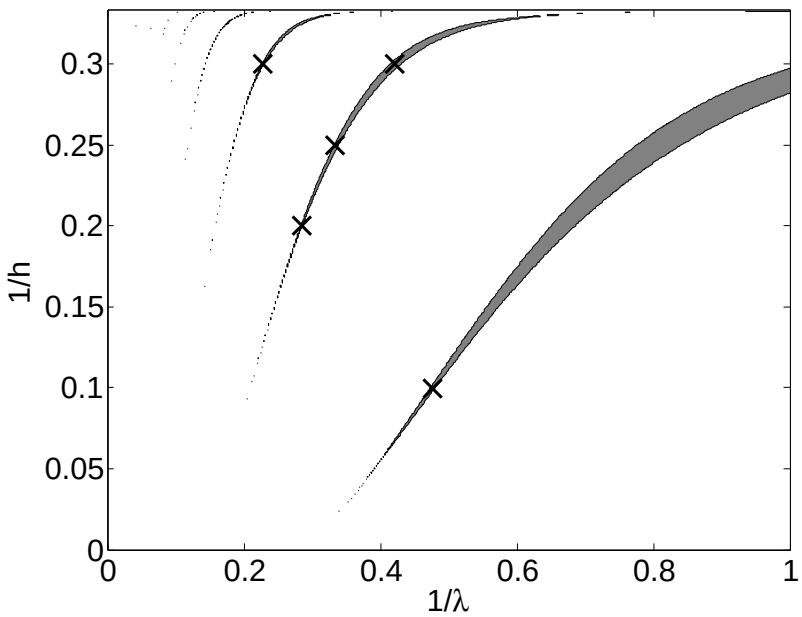

(b) Validation tests for v

Figure 4.29: Points in the $1/\gamma - 1/h$ plane used for validation tests for the transverse vibrations of the tether

Table 4.10: Parameters used in the validations tests for the transverse vibrations of the tether

u Validation Tests				
h	λ_n	n	γ	Stable/Unstable
3.6	6.37	1	1.15113	stable
3.6	4.26	1	1.48711	stable
3.6	2.63	1	1.84088	stable
5	4.76	1	1.3939	stable
5	2.78	1	1.80782	stable
10	3.2	1	1.71289	stable
v Validation Tests				
h	λ_n	n	γ	Stable/Unstable
3.33	4.38	1	1.4639	stable
3.33	2.38	1	1.89303	stable
4	2.99	1	1.7605	stable
5	3.52	1	1.64138	stable
10	2.10	1	1.94384	stable

4.5.3 Analysis of Modeling Assumptions

The modeling assumptions used to formulate the lower-level computational model used in this chapter are presented in §4.1, and their mathematical representations are presented in §4.2. One of the most important modeling assumptions is related to the tension in the tether. Recall that in the top-level model the tension in the tether is related to the geometry of the tether according to Eq. (3.32). In the lower-level model, however, we assume that the tension is independent of the tether geometry, and is given by Eq. (4.43), which is the tension in an equivalent rigid tether. The tension in the tether directly affects the frequencies of the transverse vibrations, and is a contributing factor in the parametric resonances that cause the instabilities predicted by the lower-level computational model. We therefore begin our analysis of the lower-level modeling assumptions by considering the approximation used for the tether tension.

The tension approximation given by Eq. (4.43) is analyzed as follows. Numerical solutions are determined using the top-level computational model, and the tension in the tether at any point in time is calculated using Eq. (3.32). At each point in time, the numerical solution is also used with Eq. (4.43) so calculate the approximate tension. An average percent error between the two tension predictions is then calculated as

$$\% \text{ error} = \frac{1}{\Delta t}\int_0^{\Delta t}\frac{1}{L}\int_0^{L} 100\left|\frac{T(\bar{s},t)-T_{app}(\bar{s},t)}{T_{app}(\bar{s},t)}\right| d\bar{s}\,dt \tag{4.168}$$

where Δt is the solution time span, $T(\bar{s}, t)$ is the tension predicted by the top-level computational model, and $T_{app}(\bar{s}, t)$ is the tension predicted by the approximation of Eq. 4.43.

Figure 4.30 shows comparisons made using the above described procedure for a number of different values of h and γ. The system parameters and initial conditions used to make these comparisons are the same as those listed in Tables 4.8 and 4.9, and the simulation time span is 5 orbits of the system. As the figure shows, the error between the two tension predictions is on the order of 1% for all of the comparisons made. We note, however, that there is a sharp increase in the difference between the two models for $h = 3.33$ and $\gamma = 1.9$. The relatively small differences illustrated by Fig. 4.30 indicate that the tension approximation given by Eq. (4.43) is reasonably accurate, and is most likely not the primary cause of the erroneous results predicted by the lower-level computational model. Small differences in tension will produce qualitative differences between the predictions made by the two models, such as differences in vibration frequencies, but these differences are likely not the cause of the significant qualitative differences in the predictions. We must note, however, that some of the largest differences in the tension are seen for systems wiht low h and γ near 2, which are the types of systems for which the instability regions predicted by the lower-level computational model are the largest. The tension differences for such systems may therefore play a more significant factor in the differences in the predictions made by the models, but they are still unlikely to the the primary cause of the differences.

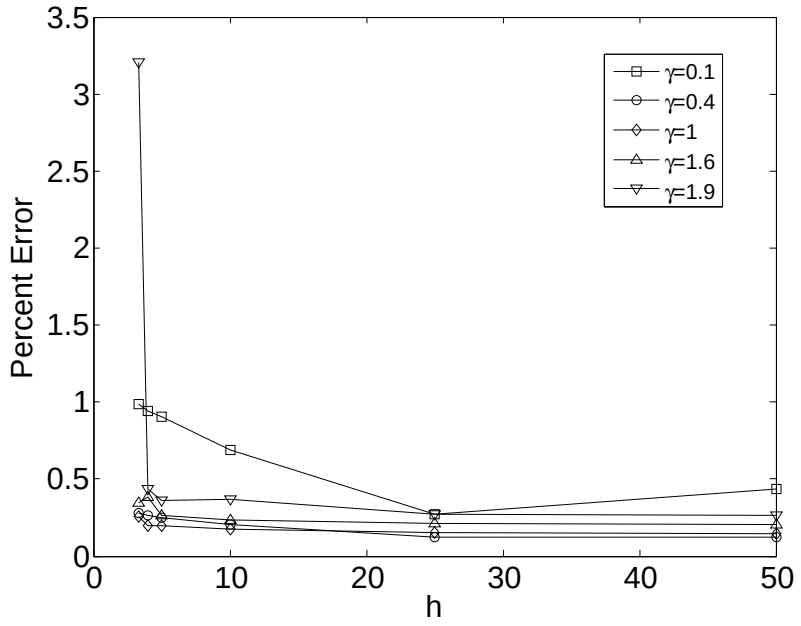

Figure 4.30: Comparison of tension in the tether predicted by the top- and lower-level computation models

The next modeling assumption that we consider is related to the pendular motion of the tether. In the top-level model, the pendular motion and elastic vibrations of the tether are coupled, such that the pendular motion affects the elastic vibrations and vice versa. In the lower-level model, however, we assumed a one-way decoupling in which the pendular motion affects the elastic vibrations, but the elastic vibrations have no affect on the pendular motion. As a result, the equations governing the pendular motion are the same as an equivalent system with a rigid tether.

This assumption related to the pendular motion of the tether is analyzed as follows. First, the top-level computational model is used to produce a numerical solution for the motion of the system. Next, a "modified" top-level computational model is used to produce a numerical solution for the same system, and the predictions made by the two models are compared. The modified top-level computational model is identical to the original top-level computational model is every way, except that Eqs. (4.16) and (4.17) are used to model the pendular motion of the tether instead of Eqs. (3.69) and (3.70). The only difference between the predictions made by the two models can therefore be directly attributed to the way in which the pendular motion of the tether is modeled.

Figure 4.31 shows two comparisons made using the procedure described above. The system parameters and initial conditions used in these comparisons are once again the same as those listed in Tables 4.8 and 4.9. Figure 4.31(a) compares the predictions made of u at the tether midpoint for systems correpsonding to $h = 5$ and $\gamma = 1.3939$. Recall that the lower-level computational model predicts that u is unstable for such a system. As the figure shows, the predictions made by the two models are drastically different–the original top-level model predicts bounded oscialltory motion (as discussed previously in this section), but the modified model predicts the type of growth predicted by the lower-level model. Note that the vibration frequencies predicted by the two models are also quite different. The same types of dramatic qualitative differences are also seen when we compare predictions for v. Figure 4.31(b) compares the predictions made of v at the tether midpoint for $h = 5$ and $\gamma = 1.644138$, which is a system for which the lower-level computational model predicts unstable v. Unlike the predictions made for u, in this case the modified top-level computational model does not predict the growth predicted by the lower-level model; however, there are still significant qualitative differences between the predictions made by the original and modified top-level models. Specifically, both the frequency and amplitude of the vibrations are different, with the most drastic difference occuring in the frequency.

A possible physical explanation for the differences in the predictions made by the lower- and top-level computational models is related to the energy of the system. In the top-level model, there is a full coupling between the two modes of the tether motion, so that energy can be freely exchanged between the pendular motion and elastic vibrations. In the lower-level model, however, the one-way decoupling means that no energy can be transferred from the pendular motion to the transverse vibrations. The energy of the pendular motion remains constant, and does not vary as the tether deforms and vibrates as happens in the top-level model. In affect, the model contains an artificial energy source that holds the

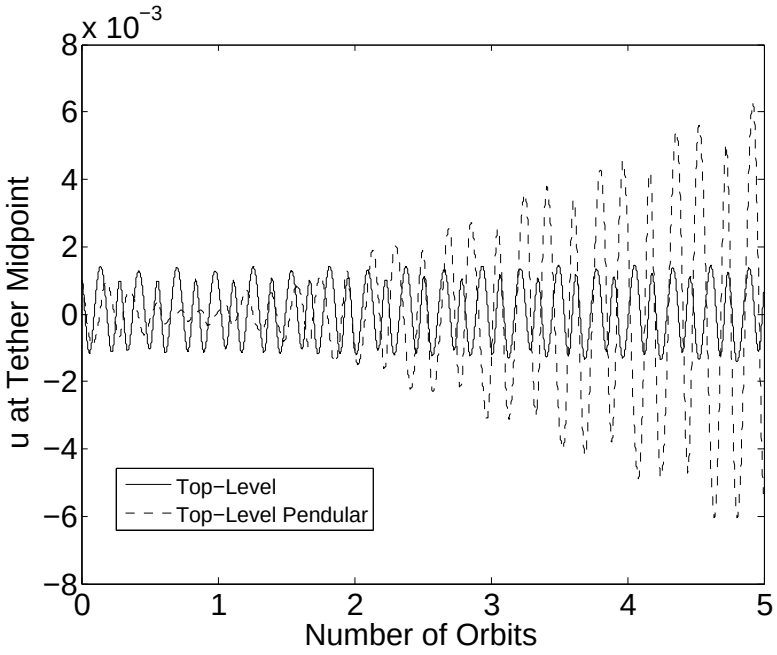

(a) u at tether midpoint for $h = 5$ and $\gamma = 1.3939$

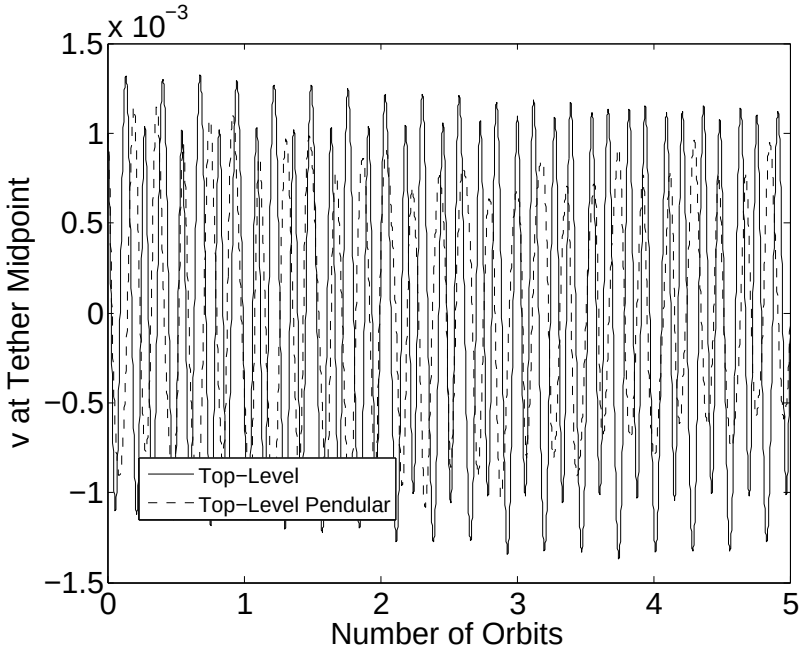

(b) v at tether midpoint for $h = 5$ and $\gamma = 1.64138$

Figure 4.31: Comparison of predictions of tether transverse displacements made by standard and modified top-level computational models

energy of the pendular motion at a constant level. Because the pendular motion drives the transverse vibrations, this artificial energy source in the pendular motion could certainly have a significant impact on the stability properties of the transverse vibrations.

Whatever their cause, the significant qualitative differences illustrated by Fig. 4.31 indicate that modeling the pendular motion of the tether using Eqs. (4.16) and (4.17) has a significant affect on the predictions of the tether transverse vibrations. It is quite unlikely that two computational models that demonstrate the qualitative differences seen in Fig. 4.31 will have the same stability properties, so we conclude that the way in which the pendular motion is modeled is one of the, if not the, most significant factors contributing to the erroneous predictions made by the lower-level computational model. Any future study of the tether transverse vibrations made using a lower-level model must take into account the full coupling between the pendular motion and transverse vibrations of the tether.

Several other modeling assumptions may also contribute to the significant differences between the predictions made by the top- and lower-level computational models. First, the effects of the longitudinal vibrations of the tether may lead to significant differences between the models–recall that the longitudinal vibrations are neglected in the lower-level model. Previous studies of axially extensible tethers have shown that the longitudinal vibrations are coupled to the in-plane pendular motion of the tether,[12,16] which in turn drives the transverse vibrations. Considering the effects of the longitudinal vibrations may therefore be necessary to accurately predict the stability properties of the transverse vibrations. Other modeling assumptions that may contribute tot he differences between the two models are constraining the system to an unperturbed circular orbit, modeling the end bodies as point masses, and assuming that gravity varies linearly over the length of the tether. For typical TSS, however, the differences in the predictions caused by these assumptions are most likely insignificant compared to the differences caused by the assumptions discussed previously.

4.6 Summary

In this chapter we used a lower-level computational model to make predictions related to the pendular motion and transverse elastic vibrations of the tether in a spinning TSS. The lower-level model is a simplification of the top-level model that is intended to isolate the dynamics of the tether, which are assumed to be the only relevant dynamics in the system.

The equations governing the pendular motion of the tether in the lower-level model are the same as those of an equivalent system in which the tether is rigid. These equations were linearized about a nominal planar spinning motion and an exact analytical solution for the in-plane motion was determined in terms of Jacobi elliptic functions. Using the solution for the in-plane motion in the linearized equation for the out-of-plane pendular motion results in a Hill's equations, the stability properties of which were analyzed using Floquet theory. For certain in-plane spin rates the out-of-plane pendular motion was found to be unstable,

in that a small initial out-of-plane deviation grows large over time. The unstable growth is not necessarily unbounded, however, and the conservative nature of the system was used to place bounds on the out-of-plane motion. For relatively high in-plane spin rates the out-of-plane pendular motion is stable, and approximate solutions were derived that are linear combinations of four simple harmonic oscillators. Note that the results related to the stability of the out-of-plane motion and the approximate solutions for high in-plane spin rates are original contributions of this work.

The equations governing the transverse elastic vibrations of the tether in the lower-level model are partial differential equations with time and arclength along the tether as independent variables. As done in the analysis of the pendular motion, these equations were linearized about a nominal planar spinning motion, resulting in decoupled, linear, partial differential equations. The method of separation of variables was applied to these equations, and the mode shapes for the transverse vibrations were determined in terms of a hypergeometric function. The eigenvalues for the vibration modes and the solution for the in-plane pendular motion were then used in the equations governing the temporal components of the solutions for the transverse vibrations, resulting in Hill's equations. Floquet theory was used to show that the transverse vibrations are unstable for certain combinations of in-plane spin rate and system mass distribution, with the largest instability regions corresponding to systems with low in-plane spin rates and low secondary end mass relative to the tether mass. Note that these results related to the stability of the transverse vibrations duplicate those presented in Refs. [5] and [8].

The computational model validation procedure presented in Ch. 2 was applied to the predictions made by the lower-level computational model related to the pendular motion and elastic vibrations of the tether. The instabilities in the out-of-plane pendular motion predicted by the lower-level model were also predicted by the top-level model for a wide range of system parameters. These results are therefore considered validated, and we can expect a spinning TSS to experience unstable out-of-plane pendular motion for certain ranges of in-plane spin rate. The approximate solution for the out-of-plane pendular motion for high in-plane spin rates also compares favorably to predictions made by the top-level computational model. The approximate solutions accurately capture the qualitative characteristics of the out-of-plane pendular motion, and also provide accurate short-term quantitative predictions. However, the approximate solutions become less quantitatively accurate over expanding time scales, and should not be used for long-term quantitative predictions.

Unlike the predictions made by the lower-level computational model related to the pendular motion of the tether, the predictions of unstable transverse vibrations were not predicted by the top-level computational model. A number of validation tests were performed for several systems predicted to experience unstable transverse vibrations, and in all cases the top-level computational model predicted that the transverse vibrations remain bounded. The lower-level computational model is therefore not validated in this case, and must be altered in some way to achieve better agreement with the top-level computational model. An analysis of the modeling assumptions used to formulate the lower-level model showed that the assumption

of a one-way coupling between the pendular motion and transverse vibrations is the most likely cause of the erroneous predictions. Any further study of the transverse vibrations of the tether must therefore relax this assumption.

The results of the validation tests on the predictions of instability in the tether transverse vibrations clearly demonstrate the necessity of performing some form of validation on results obtained from lower-level computational models. These results are undoubedtly mathematically correct, and, as mentioned several times in this dissertation, have been reported previously in the literature. The mathematical correctness of a prediction, however, does not guarantee that it can be applied to the particular physical system of interest, as demonstrated by the work presented in this chapter. The applicability of a prediction made by a lower-level computational model can only be determined by validating it against data that is believed to sufficiently represent the behavior of the actual physical system. In the absence of experimental data, we believe that the validation procedure presented in Ch. 2 and applied in this chapter is the best available option.

Chapter 5

Control of Spinning Tethered Satellite Systems

In Ch. 4 we presented a detailed analysis of the motion of the tether in a spinning TSS. A lower-level computational model was used to analyze both the pendular motion and transverse elastic vibrations of the tether, and the computational model validation procedure outlined in Ch. 2 was used to validate the predictions pertaining to the pendular motion. The dynamic analysis of the pendular motion presented in Ch. 4 is fairly complete, so the natural next step in the analysis of the pendular motion is to develop methods of controlling such motion.

In this chapter we considered numerous methods of controlling the pendular motion of the tether in a spinning TSS. Because the nominal motion of a spinning TSS is in the orbit plane, all of the control developments drive the tether to a planar pendular motion. We begin the control developments by considering the possibility of controlling the pendular motion using electrodynamic thrusting as the only control actuator. A nonlinear controllability analysis is used to show that such control is not possible, and other means of control actuation must be employed. Several different nonlinear control design techniques are then used to develop control laws that drive the system to a desired planar motion. All of these control laws are developed using a lower-level computational model, so they are also applied to the top-level computational model to assess their applicability and effectiveness.

5.1 Physical System and Conceptual Model

The physical system and conceptual model considered in the control analysis are the same as those used in the dynamic analysis presented in Ch. 4. See §4.1 for a complete description of these elements of the system model. One of the key assumptions utilized in the control developments that follow is that the elastic vibrations of the tether have no effect on the

pendular motion of the tether. This assumption allows us to use a greatly simplified mathematical model of the pendular motion to develop control laws. One final element of the conceptual model we must consider that is not discussed in §4.1 is related to the magnetic field of the central body: because we consider the possibility of controlling the pendular motion using electrodynamic thrusting, we must have a conceptual model of the magnetic field of the central body. As done for the top-level system model, we assume that the magnetic field is a tilted dipole that is fixed to the central body as it rotates.

5.2 Mathematical Model

Because the conceptual model used in the control analysis is the same as that used in Ch. 4, the mathematical model used in this chapter is virtually identical to the one derived in Sec. 4.2. However, we only need to consider the equations governing the pendular motion of the tether (which are not affected by the transverse elastic vibrations of the tether), and we must modify the pendular equations of motion to include methods of control actuation.

As shown in §4.2.3, the equations of motion governing the pendular motion of the tether can be expressed as in Eq. (4.11). In §4.2.3, the external moment acting on the system about $\mathcal{A}$, $\vec{\mathbf{M}}_{\mathrm{A}}$, is due to the gravity-gradient moment only. We must now modify $\vec{\mathbf{M}}_{\mathrm{A}}$ to include the effects of electrodynamic forcing and other methods of control actuation.

The moment about $\mathcal{A}$ due to the electrodynamic force can be expressed as

$$\vec{\mathbf{M}}_{\mathrm{EA}} = \int_0^L \vec{\mathbf{r}} \times (i\, d\vec{\mathbf{r}} \times \vec{\mathbf{B}}) \tag{5.1}$$

where i is the current in the tether and $\vec{\mathbf{B}}$ is the magnetic field vector. Assuming that the elastic vibrations of the tether have a negligible influence on the total electrodynamic moment, we make the approximations

$$\vec{\mathbf{r}} \approx \bar{s}\hat{\mathbf{e}}_3 \tag{5.2}$$

$$d\vec{\mathbf{r}} \approx d\bar{s}\hat{\mathbf{e}}_3 \tag{5.3}$$

such that Eq. (5.1) becomes

$$\vec{\mathbf{M}}_{\mathrm{EA}} = \int_0^L \bar{s}\hat{\mathbf{e}}_3 \times (i\, d\bar{s}\hat{\mathbf{e}}_3 \times \vec{\mathbf{B}}) \tag{5.4}$$

Expressing $\vec{\mathbf{B}}$ relative to $\mathcal{F}_E$ as

$$\vec{\mathbf{B}} = B_1\hat{\mathbf{e}}_1 + B_2\hat{\mathbf{e}}_2 + B_3\hat{\mathbf{e}}_3 \tag{5.5}$$

we have

$$\vec{\mathbf{M}}_{\mathrm{EA}} = -i\left(\int_0^L \bar{s}B_1\, d\bar{s}\right)\hat{\mathbf{e}}_1 - i\left(\int_0^L \bar{s}B_2\, d\bar{s}\right)\hat{\mathbf{e}}_2 \tag{5.6}$$

Note that we have assumed that i is constant along the length of the tether, as done in the top-level model.

Letting the moment about $\mathcal{A}$ due to any other external forces be

$$\vec{\mathbf{M}}_{\mathrm{AF}} = M_{AF1}\hat{\mathbf{e}}_1 + M_{AF2}\hat{\mathbf{e}}_2 \tag{5.7}$$

(there can be no moment about the $\hat{\mathbf{e}}_3$ axis because the system has no dimension about that axis) and making use of the gravity-gradient moment expression defined in Eq. (4.15), the total external moment acting on the system about $\mathcal{A}$ can be written as

$$\vec{\mathbf{M}}_{\mathrm{A}} = M_{A1}\hat{\mathbf{e}}_1 + M_{A2}\hat{\mathbf{e}}_2 \tag{5.8}$$

where

$$M_{A1} = 3I_A\Omega_A^2\cos^2\alpha\sin\beta\cos\beta - i\left(\int_0^L \bar{s}B_1\,d\bar{s}\right) + M_{AF1} \tag{5.9}$$

$$M_{A2} = -3I_A\Omega_A^2\sin\alpha\cos\alpha\cos\beta - i\left(\int_0^L \bar{s}B_2\,d\bar{s}\right) + M_{AF2} \tag{5.10}$$

Using Eqs. (5.9) and (5.10) in Eq. (4.11), the equations of motion governing the pendular motion of the tether are

$$\ddot{\alpha}\cos\beta - 2(\dot{\alpha}+\Omega_A)\dot{\beta}\sin\beta + 3\Omega_A^2\sin\alpha\cos\alpha\cos\beta = -\frac{i}{I_A}\left(\int_0^L \bar{s}B_2\,d\bar{s}\right) + \frac{M_{AF2}}{I_A} \tag{5.11}$$

$$\ddot{\beta} + [(\dot{\alpha}+\Omega_A)^2 + 3\Omega_A^2\cos^2\alpha]\sin\beta\cos\beta = \frac{i}{I_A}\left(\int_0^L \bar{s}B_2\,d\bar{s}\right) - \frac{M_{AF1}}{I_A} \tag{5.12}$$

Making use of several of the nondimensional quantities defined in §4.2.5, Eqs. (5.11) and (5.12) are cast in nondimensional form as

$$\mathring{\alpha}\cos\beta - 2(\mathring{\alpha}+1)\mathring{\beta}\sin\beta + 3\sin\alpha\cos\alpha\cos\beta = -\epsilon\int_0^1 2xb_2\,dx + u_\alpha \tag{5.13}$$

$$\mathring{\beta} + [(\mathring{\alpha}+1)^2 + 3\cos^2\alpha]\sin\beta\cos\beta = \epsilon\int_0^1 2xb_1\,dx + u_\beta \tag{5.14}$$

where we have defined the quantities

$$\epsilon = \frac{iL^2}{2I_A}\left(\frac{\mu_M}{\mu}\right) \tag{5.15}$$

$$b_i = \left(\frac{r_A^3}{\mu_M}\right)B_i \tag{5.16}$$

$$u_\alpha = \frac{M_{AF2}}{I_A\Omega_A^2} \tag{5.17}$$

$$u_\beta = -\frac{M_{AF1}}{I_A\Omega_A^2} \tag{5.18}$$

Note that μ_M is the strength of the magnetic dipole of the central body.

Equations (5.13) and (5.14) are the equations used in the remainder of this chapter to develop methods of controlling the pendular motion of the tether. The control inputs are taken to be ϵ, which is related to the electrodynamic force acting on the tether, and u_α and u_β, which are related to any non-electrodynamic moments acting on the system. Modulation of ϵ can be achieved by changing the current in the tether, possibly by means of a variable resistor or on-board voltage source. The physical source of the inputs u_α and u_β is assumed to be arbitrary at this point; however, we do note that these inputs would most likely be provided by small thrusters on the secondary end body.

5.3 Computational Model: Control of Pendular Motion

In this section we use Eqs. (5.13) and (5.14) along with various nonlinear control design techniques to develop methods of controlling the pendular motion of the tether. Because the nominal pendular motion of a spinning TSS is in the orbit plane, we desire control laws that drive β and $\mathring{\beta}$ to zero while driving the in-plane pendular motion to a desired reference trajectory. We begin the control analysis by studying the feasibility of performing such control maneuvers using the electrodynamic force as the only control actuator. This analysis serves to motivate the control law developments presented later in this section.

5.3.1 Controllability Using Electrodynamic Forcing

If the electrodynamic force is allowed to be the only control input, the equations of motion governing the pendular motion of the tether become

$$\mathring{\mathring{\alpha}}\cos\beta - 2(\mathring{\alpha}+1)\mathring{\beta}\sin\beta + 3\sin\alpha\cos\alpha\cos\beta = -\epsilon\int_0^1 2xb_2\,dx \tag{5.19}$$

$$\mathring{\mathring{\beta}} + [(\mathring{\alpha}+1)^2 + 3\cos^2\alpha]\sin\beta\cos\beta = \epsilon\int_0^1 2xb_1\,dx \tag{5.20}$$

At this point we make several assumptions related to the magnetic field of the central body designed to simplify the electrodynamic moment expressions in Eqs. (5.19) and (5.20). The objective of the current analysis is to demonstrate the inherent difficulties in controlling the pendular motion of the tether using electrodynamic forcing only, and the conclusions of this analysis are valid for general magnetic field models. We therefore use the simplest possible representation of the magnetic field: a nontilted, nonrotating dipole. We further assume that the circular orbit of $\mathcal{A}$ is constrained to the plane of the magnetic equator. Under

these assumptions, the unit dipole axis is aligned with the orbit normal direction, and the magnetic field vector at any point along the tether is

$$\begin{aligned}\vec{\mathbf{B}} &= \frac{\mu_M}{r_T^3}\hat{\mathbf{o}}_2 \\ &= \frac{\mu_M}{r_T^3}(\cos\beta\hat{\mathbf{e}}_2 + \sin\beta\hat{\mathbf{e}}_3)\end{aligned} \tag{5.21}$$

where r_T is the orbital radius of a differential tether element, $d\bar{s}$. Because the length of the tether in a typical TSS is much smaller than the orbit radius of the system, we linearize Eq. (5.21) about the position of $\mathcal{A}$ to obtain

$$\vec{\mathbf{B}} = \frac{\mu_M}{r_A^3}(1 - 3\ell x\cos\alpha\cos\beta)(\cos\beta\hat{\mathbf{e}}_2 + \sin\beta\hat{\mathbf{e}}_3) \tag{5.22}$$

where we have defined the nondimensional parameter

$$\ell = \frac{L}{r_A} \tag{5.23}$$

From Eq. (5.16), we have $b_1 = 0$ and

$$b_2 = (1 - 3\ell x\cos\alpha\cos\beta)\cos\beta \tag{5.24}$$

Using these quantities in Eqs. (5.19) and (5.20), the equations governing the pendular motion of the tether become

$$\mathring{\alpha}\cos\beta - 2(\mathring{\alpha}+1)\mathring{\beta}\sin\beta + 3\sin\alpha\cos\alpha\cos\beta = -\epsilon(1 - 2\ell\cos\alpha\cos\beta)\cos\beta \tag{5.25}$$

$$\mathring{\beta} + [(\mathring{\alpha}+1)^2 + 3\cos^2\alpha]\sin\beta\cos\beta = 0 \tag{5.26}$$

The controllability analysis of Eqs. (5.25) and (5.26) requires that they be in state-space form. Define the state vector

$$\mathbf{x} = \begin{pmatrix} \alpha & \beta & \mathring{\alpha} & \mathring{\beta} \end{pmatrix}^{\mathrm{T}} \tag{5.27}$$

the control input $u = \epsilon$, and the quantities

$$\mathbf{f}(\mathbf{x}) = \begin{pmatrix} \mathring{\alpha} \\ \mathring{\beta} \\ 2(\mathring{\alpha}+1)\mathring{\beta}\tan\beta - 3\sin\alpha\cos\alpha \\ -[(\mathring{\alpha}+1)^2 + 3\cos^2\alpha]\sin\beta\cos\beta \end{pmatrix} \tag{5.28}$$

$$\mathbf{g}(\mathbf{x}) = \begin{pmatrix} 0 \\ 0 \\ 2\ell\cos\alpha\cos\beta - 1 \\ 0 \end{pmatrix} \tag{5.29}$$

Using these definitions, Eqs. (5.25) and (5.26) are rewritten as

$$\mathring{\mathbf{x}} = \mathbf{f}(\mathbf{x}) + \mathbf{g}(\mathbf{x})u \tag{5.30}$$

Equation (5.30) is the standard form for a single-input nonlinear control system.

According the nonlinear control theory,[28,42,58] the system defined by Eqs. (5.28–5.30) is accessible in a region $D \subseteq \Re^4$ of the state-space if the matrix

$$\mathbf{C} = \left[\begin{array}{cccc} \mathbf{g} & [\mathbf{f},\mathbf{g}] & [\mathbf{f},[\mathbf{f},\mathbf{g}]] & [\mathbf{f},[\mathbf{f},[\mathbf{f},\mathbf{g}]]] \end{array} \right] \tag{5.31}$$

is full-rank at every point in D, where the Lie bracket $[\mathbf{a},\mathbf{b}]$ is defined as

$$[\mathbf{a},\mathbf{b}] = \frac{\partial \mathbf{b}}{\partial \mathbf{x}}\mathbf{a} - \frac{\partial \mathbf{a}}{\partial \mathbf{x}}\mathbf{b} \tag{5.32}$$

(See Corollary 3.11 of Ref. [42].) Another way of stating this accessibility condition is that the determinant of $\mathbf{C}$ must be nonzero at every point in D. Using Eqs. (5.28) and (5.29) in Eq. (5.31) to form $\mathbf{C}$ and taking its determinant, we obtain

$$|\mathbf{C}| = -(1 - 2\ell\cos\alpha\cos\beta)^4(\mathring{\alpha}+1)^2\left[(5+3\cos(2\alpha)+2\mathring{\alpha}(\mathring{\alpha}+2))\sin^2(2\beta)+8\mathring{\beta}^2\right]\cos^2\beta \tag{5.33}$$

From Eq. (5.33), we can see that there are a number of states that result in the determinant of $\mathbf{C}$ becoming 0, meaning that the system is not accessible. Because the system is not accessible, it is also not controllable. Most notably, any motion in the $\alpha - \mathring{\alpha}$ plane (corresponding to $\beta = \mathring{\beta} = 0$) is not accessible. This makes sense physically, because motion in the $\alpha - \mathring{\alpha}$ plane results in an electrodynamic force in the $\alpha - \mathring{\alpha}$ plane as well, and β cannot be controlled.

The above analysis illustrates the inherent difficulty of controlling the pendular motion of the tether using only the electrodynamic force: the nature of the electrodynamic force constrains it to be in a specific direction, perpindicular to both the tether and the magnetic field vector, at any point in time. The lack of control over the direction of the force is the factor that leads to the difficulty in controlling α and β simultaneously.

Upon further inspection, it may seem that there really is no difficultly in using the electrodynamic force to control the pendular motion of a spinning TSS because, for such a system, we want to control the motion to the $\alpha - \mathring{\alpha}$ plane, after which point we do not need any control authority over β. However, this appearance of controllability is simply an artifact of the simplified magnetic field model used in the analysis presented above. If a more realistic magnetic field model is used (such as the tilted, rotating dipole model used in the top-level system model), in general there is always a component of the electrodynamic force out of the orbit plane, and it is not possible to drive to motion to the orbit plane and then control the in-plane motion as desired. The subsequent control of the in-plane motion necessarily results in out-of-plane pendular motion, which would then have to be controlled back to zero somehow.

All of the above arguments illustrate the difficulty of controlling the pendular motion of the tether using the electrodynamic force. For these reasons, we do not consider the electrodynamic force as a control actuator in the developments that follow. Instead, we assume that arbitrary control inputs corresponding to u_α and u_β are available, such that the equations governing the pendular motion of the tether are

$$\mathring{\mathring{\alpha}}\cos\beta - 2(\mathring{\alpha}+1)\mathring{\beta}\sin\beta + 3\sin\alpha\cos\alpha\cos\beta = u_\alpha \tag{5.34}$$

$$\mathring{\mathring{\beta}} + [(\mathring{\alpha}+1)^2 + 3\cos^2\alpha]\sin\beta\cos\beta = u_\beta \tag{5.35}$$

which are obviously controllable. As mentioned previously, u_α and u_β could be provided by small thrusters on the secondary end body. In the remainder of this section, several nonlinear control design techniques are used to determine expressions for u_α and u_β that drive α and β to a desired planar trajectory.

5.3.2 Planar Trajectory Tracking

The first control design we consider is for controlling the pendular motion about an arbitrary planar reference trajectory. We therefore want to determine control laws that drive β and $\mathring{\beta}$ to 0, and α to an arbitrary reference trajectory $\alpha_r = \alpha_r(\tau)$. The method of feedback linearization is used to derive these control laws.

Let the in-plane error be defined as

$$e_\alpha = \alpha - \alpha_r \tag{5.36}$$

Differentiating Eq. (5.36) twice and using Eq. (5.34), the in-plane error dynamics are governed by

$$\mathring{\mathring{e}}_\alpha = 2(\mathring{\alpha}+1)\mathring{\beta}\tan\beta - 3\sin\alpha\cos\alpha + \frac{u_\alpha}{\cos\beta} - \mathring{\mathring{\alpha}}_r \tag{5.37}$$

Let the control input be given by

$$u_\alpha = \left[-k_{\alpha1}e_\alpha - k_{\alpha2}\mathring{e}_\alpha - 2(\mathring{\alpha}+1)\mathring{\beta}\tan\beta + 3\sin\alpha\cos\alpha + \mathring{\mathring{\alpha}}_r\right]\cos\beta \tag{5.38}$$

where $k_{\alpha i} > 0$ are constant control gains, such that the closed-loop in-plane error dynamics are

$$\mathring{\mathring{e}}_\alpha + k_{\alpha2}\mathring{e}_\alpha + k_{\alpha1}e_\alpha = 0 \tag{5.39}$$

Note that the control law given by Eq. (5.38) results in linear closed-loop error dynamics. Because $k_{\alpha i} > 0$, we can see from Eq. (5.39) that the control law given by Eq. (5.38) drives e_α exponentially to 0, and α exponentially approaches the reference trajectory. The control gains can be selected to tailor the properties of the convergence of α to α_r.

Because the reference trajectory for the out-of-plane motion is $\beta = \mathring{\beta} = 0$, the out-of-plane error is simply β. From Eq. (5.35), let u_β be given by

$$u_\beta = -k_{\beta1}\beta - k_{\beta2}\mathring{\beta} + [(\mathring{\alpha}+1)^2 + 3\cos^2\alpha]\sin\beta\cos\beta \tag{5.40}$$

where $k_{\beta i} > 0$ are constant control gains, such that the closed-loop dynamics for β are

$$\overset{\circ\circ}{\beta} + k_{\beta 2}\overset{\circ}{\beta} + k_{\beta 1}\beta = 0 \tag{5.41}$$

As with the control law for u_α, the control law given by Eq. (5.40) results in closed-loop dynamics for β. Because the control gains are positive, from Eq. (5.41) we see that the control law given by Eq. (5.40) drives β exponentially to 0. As with the in-plane motion, the control gains can be selected to tailor the response of the controlled out-of-plane motion.

To determine appropriate values for the control gains, we note that Eqs. (5.39) and (5.41) are both of the form

$$\overset{\circ\circ}{x} + k_2\overset{\circ}{x} + k_1 x = 0 \tag{5.42}$$

The characteristic polynomial of Eq. (5.42) is

$$\lambda^2 + k_2\lambda + k_1 = 0 \tag{5.43}$$

so the characteristic exponents of Eq. (5.42) are

$$\lambda_{1,2} = -\frac{k_2}{2} \pm i\sqrt{k_1 - \left(\frac{k_2}{2}\right)^2} \tag{5.44}$$

The real part of Eq. (5.44) determines the rate at which x (or equivalently, the errors in α and β) converges to 0, and the imaginary part of Eq. (5.44) determines the oscillation frequency of the controlled response of x. Given desired values for the rate of convergence and the oscillation frequency, Eq. (5.44) can be used to determine appropriate control gains.

If we desire a critically-damped controlled response for x, we set

$$k_1 = \left(\frac{k_2}{2}\right)^2 \tag{5.45}$$

such that both characteristic exponents have the same value. The error decreases in the exponential envelope defined by $e^{-k_2\tau/2}$, so if we want the error to be $p\%$ of its initial value after a time T, we choose k_2 as

$$k_2 = \frac{2}{T}\ln\left(\frac{100}{p}\right) \tag{5.46}$$

Using Eq. (5.46) in Eq. (5.45) to determine k_1 yields the control gains that result in a critically-damped controlled error response.

We now consider the application of the control laws defined in Eqs. (5.38) and (5.40) to two different reference trajectories. First, let the reference trajectory correspond to a constant in-plane spin rate,

$$\alpha_r(\tau) = \sqrt{h^*}\tau \tag{5.47}$$

where h^* is a constant that determines the in-plane spin rate. Figure 5.1 shows an example of the controlled system response and corresponding control inputs for the reference trajectory

defined in Eq. (5.47). The control gains and initial conditions used to generate the controlled system response are listed in Tables 5.1 and 5.2, respectively. As the plots in Fig. 5.1 show, the control laws are successful in driving the pendular motion to the desired planar reference trajectory. Note, however, that u_α does not approach 0 as the reference trajectory is approached, and instead approaches a steady-state oscillation with amplitude 1.5. To see why this behavior occurs, observe from Eq. (5.38) that u_α approaches the value

$$\begin{aligned} u_\alpha &= 3\sin\alpha\cos\alpha \\ &= \frac{3}{2}\sin\left(\sqrt{h^*}\tau\right) \end{aligned} \tag{5.48}$$

as the reference trajectory is approached. Physically speaking, Eq. (5.48) illustrates that the control input must counteract the gravity-gradient torque acting on the system in order to maintain a constant spin rate, resulting in steady-state oscillations of u_α. Controlling the pendular motion about a constant planar spin over extended periods of time therefore requires a great deal of control effort.

Table 5.1: Parameters used to generate controlled system response for control about a constant in-plane spin

Parameter	Value
h^*	25
$k_{\alpha 2}$	$\frac{\ln(100)}{2\pi}$
$k_{\alpha 1}$	$\frac{k_{\alpha 1}^2}{4}$
$k_{\beta 2}$	$\frac{\ln(100)}{2\pi}$
$k_{\beta 1}$	$\frac{k_{\beta 1}^2}{4}$

Table 5.2: Initial conditions used to generate controlled system response for control about a constant in-plane spin

State	Initial Value
α	0
$\mathring{\alpha}$	4.75
β	0.5°
$\mathring{\beta}$	0

Next, consider the case in which the reference trajectory is a natural planar spinning motion,

$$\alpha_r(\tau) = \mathrm{am}(\sqrt{h^*}\tau, \sqrt{3/h^*}) \tag{5.49}$$

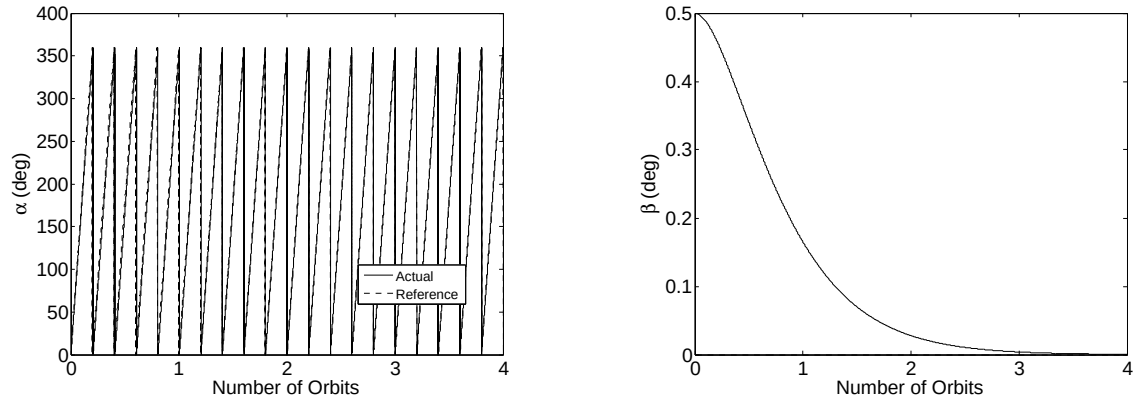

(a) In-plane angle

(b) Out-of-plane angle

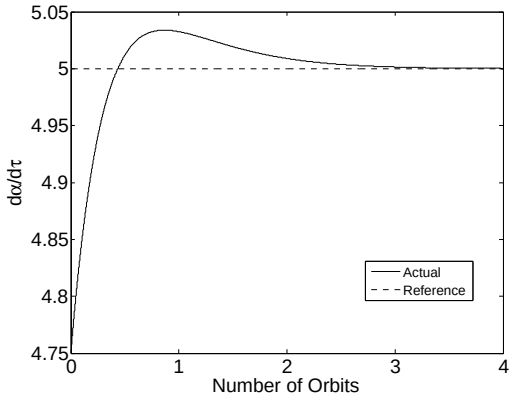

(c) In-plane angular rate

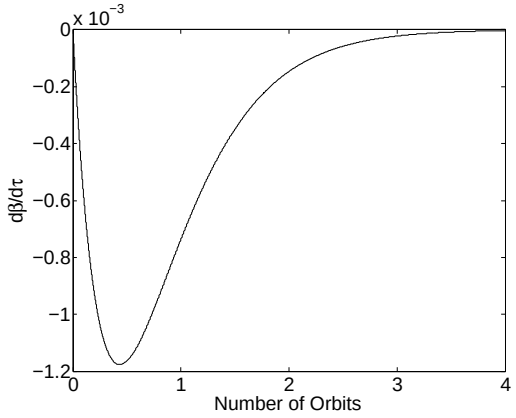

(d) Out-of-plane angular rate

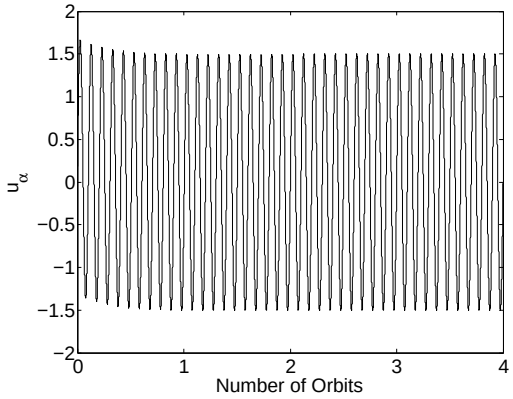

(e) In-plane control input

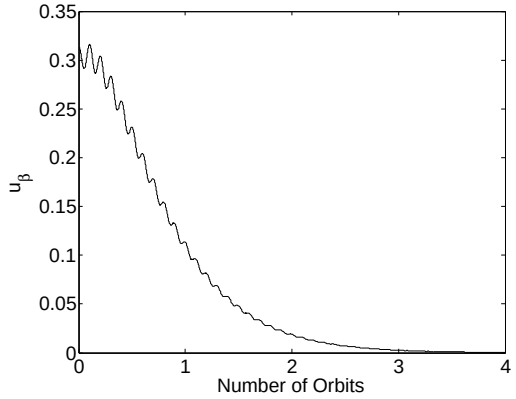

(f) Out-of-plane control input

Figure 5.1: System response and control inputs for control about a constant in-plane spin rate

Figure 5.2 shows an example of the controlled system response and corresponding control inputs for this reference trajectory. The control gains and initial conditions used to generate the solutions shown in Fig. 5.2 are once again listed in Tables 5.1 and 5.2. As with the first reference trajectory we considered, the control laws are successful in driving the pendular motion to the desired reference trajectory. We do note, however, that the in-plane control input is smaller in magnitude than for the first reference trajectory considered, and also does not experience steady-state oscillations. This behavior is due to the fact that the reference trajectory is an exact solution to the uncontrolled equations of motion, and therefore does not require any control effort to be maintained.

5.3.3 Planar $\mathcal{H}$ Tracking

In §5.3.2 we derived control laws that force the pendular motion to track a specific planar reference trajectory. We now consider the case in which the reference motion is not a specific planar motion, but is instead any natural planar motion with $h = h^*$. In this development, we are only concerned that the control drives the pendular motion to a planar trajectory with certain desired qualitative characteristics; we are not concerned with exactly matching a pre-specified time-history of α as we were previously.

Recall that the quantity $\mathcal{H}$ is defined as in Eq. (4.63). If the pendular motion is planar, then $\mathcal{H}$ is equivalent to h as defined in Eq. (4.62). The goal of the control design is therefore to drive β and $\mathring{\beta}$ to 0 while simultaneously driving $\mathcal{H}$ to a desired value of h^*. The end result will be a natural planar motion with $h = h^*$. Because we are driving the out-of-plane motion to zero, the control law for u_β is once again given by Eq. (5.40). The control gains $k_{\beta i}$ can be selected following the procedure outlined in §5.3.2.

Differentiating Eq. (4.63) and using Eqs. (5.34) and (5.35), the time rate-of-change of $\mathcal{H}$ is

$$\mathring{\mathcal{H}} = 2\left(\mathring{\alpha} u_\alpha \cos\beta + \mathring{\beta} u_\beta\right) \tag{5.50}$$

From Eq. (5.50), let u_α be given by

$$u_\alpha = -\frac{1}{\mathring{\alpha}\cos\beta}\left[\frac{k_{\mathcal{H}}(\mathcal{H} - h^*)}{2} + \mathring{\beta} u_\beta\right] \tag{5.51}$$

where $k_{\mathcal{H}} > 0$ is a constant control gain. Using Eq. (5.51) in Eq. (5.50), the closed-loop dynamics for $\mathcal{H}$ become

$$\mathring{\mathcal{H}} + k_{\mathcal{H}}\mathcal{H} = k_{\mathcal{H}} h^* \tag{5.52}$$

Analogous to the previous control law developments, we have chosen u_α to result in linear closed-loop dynamics for $\mathcal{H}$. Because $k_{\mathcal{H}}$ is positive, we see from Eq. (5.52) that the control law given by Eq. (5.51) drives $\mathcal{H}$ to h^* exponentially as τ approaches infinity. Combined with the control law given by Eq. (5.40), the control laws drive the pendular motion to a natural planar trajectory with $h = h^*$.

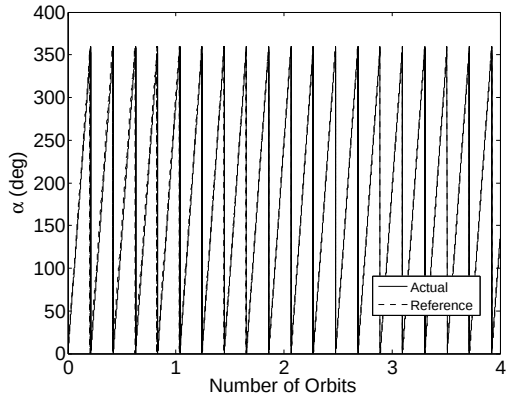

(a) In-plane angle

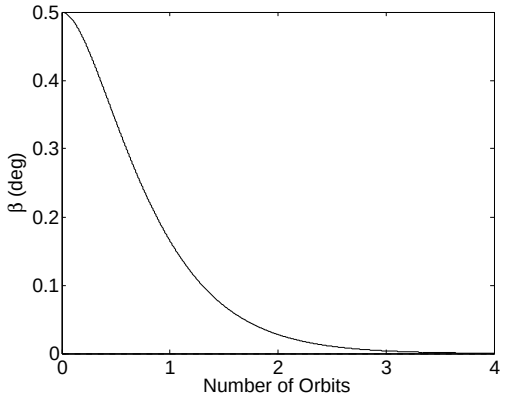

(b) Out-of-plane angle

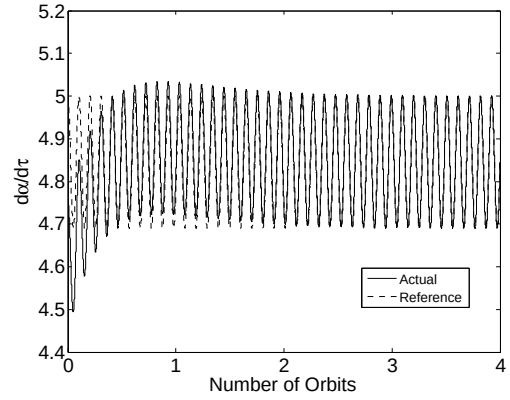

(c) In-plane angular rate

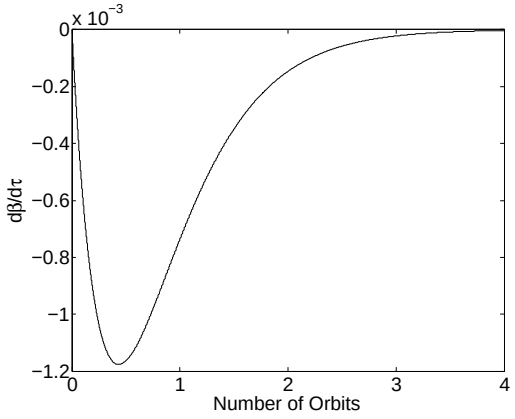

(d) Out-of-plane angular rate

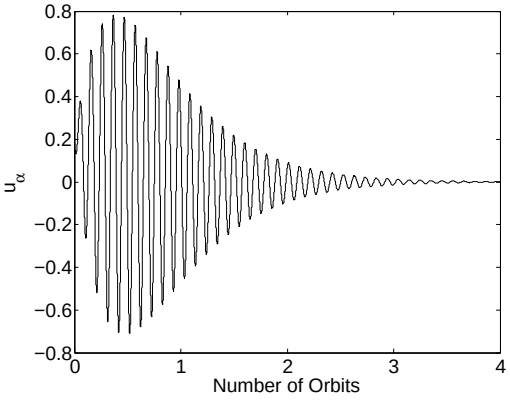

(e) In-plane control input

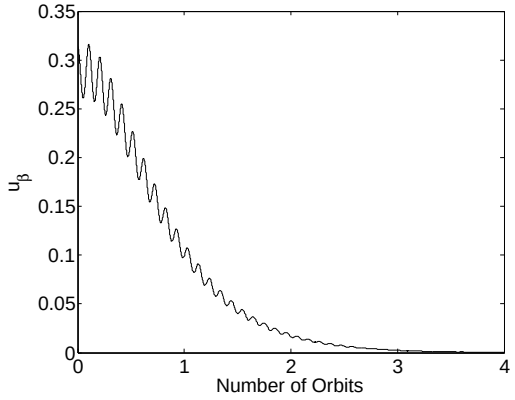

(f) Out-of-plane control input

Figure 5.2: System response and control inputs for control about a specific natural in-plane spinning trajectory

To select an appropriate value for $k_{\mathcal{H}}$, note that the solution to Eq. (5.52) is

$$\mathcal{H}(\tau) = h^* + [\mathcal{H}(0) - h^*]\, e^{-k_{\mathcal{H}}\tau} \tag{5.53}$$

which can be rewritten as

$$\frac{\mathcal{H}(\tau) - h^*}{\mathcal{H}(0) - h^*} = e^{-k_{\mathcal{H}}\tau} \tag{5.54}$$

The left-hand side of Eq. (5.54) can be viewed as an error ratio; it is the ratio of the current error in $\mathcal{H}$ to the initial error in $\mathcal{H}$. Say we want this error ratio to be a certain value, r, at a time $\tau = T$. Then from Eq. (5.54), we should select the control gain to be

$$k_{\mathcal{H}} = -\frac{\ln(r)}{T} \tag{5.55}$$

Figure 5.3 shows an example of the controlled system response for the planar $\mathcal{H}$ tracking control. The corresponding control inputs are shown in Fig. 5.4. The initial conditions used to generate the plots in Figs. 5.3 and 5.4 are listed in Table 5.2. The values of h^* and the out-of-plane control gains, $k_{\beta i}$, are the same as those listed in Table 5.1, and the value of $k_{\mathcal{H}}$ is equal to that used for both $k_\beta i$. As Fig. 5.3 shows, the control laws are successful in driving the pendular motion to a natural planar trajectory with $h = h^*$. Because the control law for u_β is the same as the one used previously, the magnitude of u_β is nearly identical to that in Figs. 5.1 and 5.2. The magnitude of u_α, however, is significantly smaller than that required by the previous control laws. This fact illustrates the primary advantage of the $\mathcal{H}$ tracking control over the control laws derived previously: the in-plane control input is significantly lower because we only require that the qualitative characteristics of the reference motion be matched. Conversely, the primary disadvantage of the $\mathcal{H}$ tracking control is that we cannot track a specific time-history for α, which could be required in certain situations.

5.3.4 Sliding Mode Control

Although the control law developments presented in this section are made using a lower-level computational model, they are intended to be applied to the top-level computational model, and ultimately an actual spinning TSS. The effect of applying control laws developed using a lower-level computational model to the top-level computational model is that the pendular motion will not be driven exactly to the desired reference trajectory, and will instead experience small amplitude oscillations about the desired planar motion. These small oscillations can be attributed to unmodeled dynamics that are not accounted for by the lower-level model. We would like to determine control laws using the lower-level computational model that can account for the effects of these unmodeled dynamics, such that they can be applied to the top-level computational model more effectively.

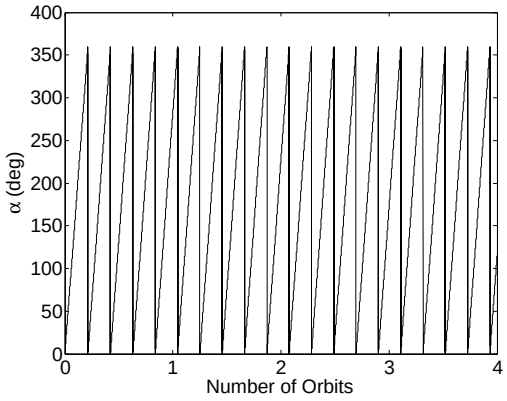

(a) In-plane angle

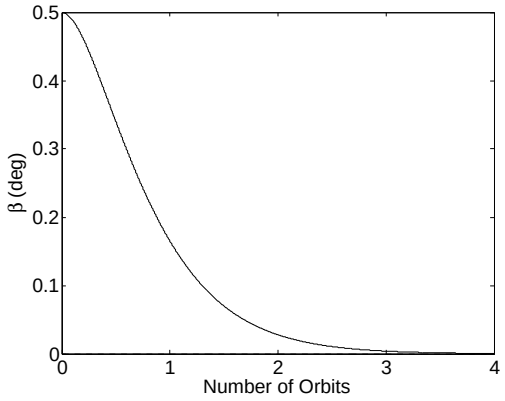

(b) Out-of-plane angle

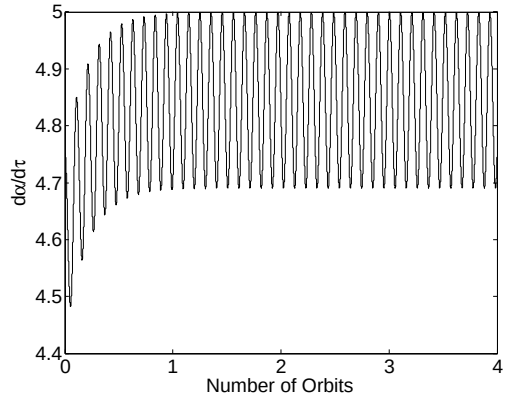

(c) In-plane angular rate

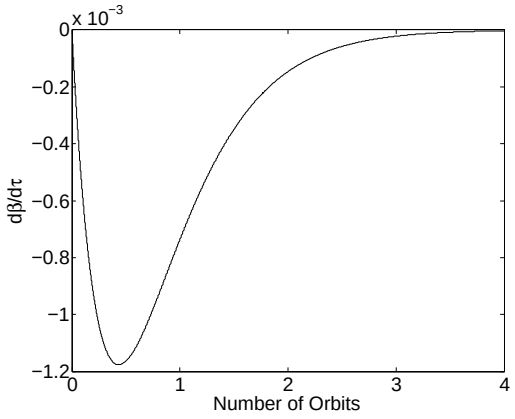

(d) Out-of-plane angular rate

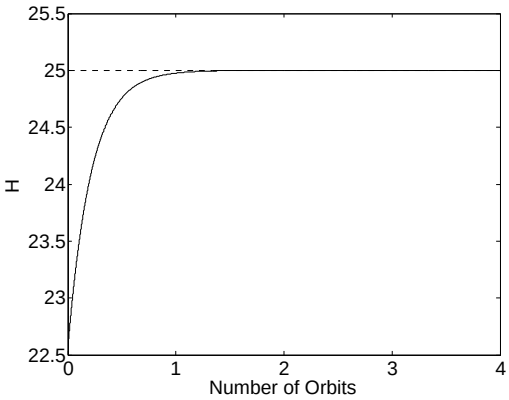

(e) $\mathcal{H}$

Figure 5.3: System response for planar $\mathcal{H}$-tracking control

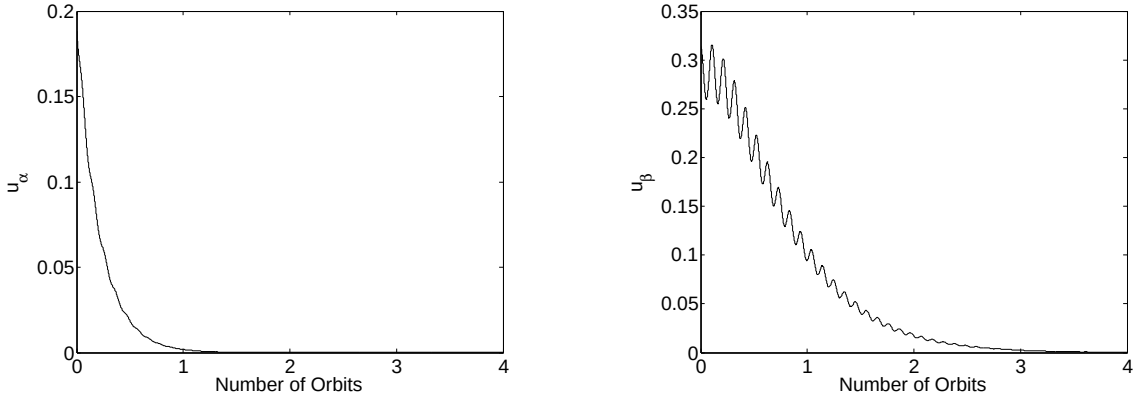

(a) In-plane control input

(b) Out-of-plane control input

Figure 5.4: Control inputs for planar $\mathcal{H}$-tracking control

To account for the effects of unmodeled dynamics in the lower-level model, we modify Eqs. (5.34) and (5.35) as follows,

$$\mathring{\alpha}\cos\beta - 2(\mathring{\alpha}+1)\mathring{\beta}\sin\beta + 3\sin\alpha\cos\alpha\cos\beta = u_\alpha + \delta_\alpha \tag{5.56}$$

$$\mathring{\beta} + [(\mathring{\alpha}+1)^2 + 3\cos^2\alpha]\sin\beta\cos\beta = u_\beta + \delta_\beta \tag{5.57}$$

The terms δ_α and δ_β are unknown, time-varying disturbance terms that account for the effects of unmodeled dynamics. Note that, in the case of a spinning TSS, the unmodeled dynamics include the tether elastic vibrations, variations in the orbit of the system, and attitude motion of the end bodies. The control objective is to determine expressions for u_α and u_β that drive the pendular motion to a desired planar motion in spite of the unknown disturbance terms. Specifically, we consider $\mathcal{H}$-tracking control in which we drive the out-of-plane motion to zero and $\mathcal{H}$ to a desired value of h^*. The method we use to determine these control laws is known as sliding mode control, a detailed description of which can be found in Refs. [58] and [28]. The fundamental concepts of sliding mode control are discussed as they are encountered in the developments presented below.

We first consider controlling the out-of-plane pendular motion to zero. Define the quantity

$$z_1 = \mathring{\beta} + k_\beta\beta \tag{5.58}$$

where k_β is a positive constant. From Eq. (5.58), if we could drive z_1 to zero in a finite time and hold it there for all time, then β and $\mathring{\beta}$ would exponentially approach 0 as τ approaches infinity. The surface $z_1 = 0$ is known as the sliding manifold or the sliding mode for the β dynamics, and the control developments presented below are geared toward driving the motion to the sliding manifold in a finite time. Moreover, we want to drive the motion to the sliding manifold in spite of the unknown disturbance terms. Differentiating Eq. (5.58) and using Eq. (5.57), the z_1 dynamics are governed by

$$\mathring{z}_1 = -[(\mathring{\alpha}+1)^2 + 3\cos^2\alpha]\sin\beta\cos\beta + k_\beta\mathring{\beta} + u_\beta + \delta_\beta \tag{5.59}$$

From Eq. (5.59), let the control input be

$$u_\beta = [(\mathring{\alpha}+1)^2 + 3\cos^2\alpha]\sin\beta\cos\beta - k_\beta\mathring{\beta} + v_\beta \tag{5.60}$$

such that Eq. (5.59) becomes

$$\mathring{z}_1 = v_\beta + \delta_\beta \tag{5.61}$$

Note that we have chosen u_β to cancel the known, nonlinear components of Eq. (5.59) while leaving the unknown disturbance term. The term v_β must now be chosen to account for δ_β.

Define the candidate Lyapunov function for the z_1 dynamics as

$$V_1 = \frac{1}{2}z_1^2 \tag{5.62}$$

which is positive definite about $z_1 = 0$. Differentiating Eq. (5.62) and using Eq. (5.61), the rate-of-change of V_1 along the system trajectory is

$$\begin{aligned}\mathring{V}_1 &= z_1\mathring{z}_1 \\ &= z_1(v_\beta + \delta_\beta) \\ &\leq z_1 v_\beta + |z_1||\delta_\beta|\end{aligned} \tag{5.63}$$

At this point, we make the assumption that the unknown disturbance δ_β is bounded, such that

$$|\delta_\beta| \leq \delta_\beta^* \tag{5.64}$$

where δ_β^* is a positive constant. Using this definition in Eq. (5.63), the function V_1 satisfies

$$\mathring{V}_1 \leq z_1 v_\beta + |z_1|\delta_\beta^* \tag{5.65}$$

Now, let v_β be given by

$$v_\beta = -(b_\beta + \delta_\beta^*)\mathrm{sgn}(z_1) \tag{5.66}$$

where $b_\beta > 0$ is a control gain and $\mathrm{sgn}(x)$ is the signum function. Using Eq. (5.66) in Eq. (5.65), we have

$$\begin{aligned}\mathring{V}_1 &\leq -z_1(b_\beta + \delta_\beta^*)\mathrm{sgn}(z_1) + |z_1|\delta_\beta^* \\ &= -b_\beta|z_1| \\ &\leq 0\end{aligned} \tag{5.67}$$

So, V_1 is nonincreasing, and is therefore a Lyapunov function for the z_1 dynamics. The control law given by the combination of Eqs. (5.60) and (5.66) therefore stabilizes the pendular motion about $z_1 = 0$. To gain further insight about the controlled motion of the system, we must consider two cases. First, if $|z_1| = 0$, then from the definition of V_1 we must have $V_1 = 0$. But, we also know that V_1 is nonincreasing, so if V_1 becomes 0, it must remain zero

for all time, implying that z_1 remains zero for all time as well. Next, consider the case when $|z_1| \neq 0$. Noting that $\mathring{V}_1$ can also be written as

$$\mathring{V}_1 = |z_1| \frac{d}{d\tau}(|z_1|) \tag{5.68}$$

from Eq. (5.67) we have

$$\frac{d}{d\tau}(|z_1|) \leq -b_\beta \tag{5.69}$$

Integrating Eq. (5.69), we obtain

$$|z_1| \leq -b_\beta \tau + |z_1(0)| \tag{5.70}$$

which implies that $|z_1|$ reaches 0 in a finite time, T_1, that satisfies

$$T_1 \leq \frac{|z_1(0)|}{b_\beta} \tag{5.71}$$

Once $|z_1|$ reaches zero, we know that it remains 0 for all time. The control therefore drives the out-of-plane pendular motion to the sliding mode in finite time, after which β and $\mathring{\beta}$ approach 0 according to $z_1 = 0$. This convergence is achieved in spite of the presence of the unknown disturbance term δ_β. Combining Eqs. (5.60) and (5.66), the composite control law is

$$u_\beta = [(\mathring{\alpha} + 1)^2 + 3\cos^2\alpha] \sin\beta \cos\beta - k_\beta \mathring{\beta} - (b_\beta + \delta_\beta^*)\text{sgn}(z_1) \tag{5.72}$$

To determine an expression for the control input u_α, define the quantity

$$z_2 = \mathcal{H} - h^* \tag{5.73}$$

The surface $z_2 = 0$ defines the sliding mode for the in-plane pendular motion. If we can drive z_2 to 0 and hold it there, $\mathcal{H}$ will remain at the desired value for all time. Because the control law given by Eq. (5.72) drives the out-of-plane pendular motion to 0, the pendular motion will therefore approach a natural planar trajectory with $h = h^*$. Differentiating Eq. (5.73) and using Eqs. (5.56) and (5.57), the z_2 dynamics are governed by

$$\mathring{z}_2 = 2[\mathring{\alpha}(u_\alpha + \delta_\alpha)\cos\beta + \mathring{\beta}(u_\beta + \delta_\beta)] \tag{5.74}$$

From Eq. (5.74), let u_α be given by

$$u_\alpha = \frac{1}{\mathring{\alpha}\cos\beta}\left(\frac{v_\alpha}{2} - \mathring{\beta} u_\beta\right) \tag{5.75}$$

such that the closed-loop dynamics for z_2 become

$$\mathring{z}_2 = v_\alpha + 2(\delta_\alpha \mathring{\alpha}\cos\beta + \delta_\beta \mathring{\beta}) \tag{5.76}$$

As done in the development of u_β, we have chosen u_α to cancel certain nonlinear terms in the z_2 dynamics, while also containing a term, v_α, that will be used to compensate for the uncertainties δ_α and δ_β.

Define the candidate Lyapunov function for the z_2 dynamics as

$$V_2 = \frac{1}{2} z_2^2 \tag{5.77}$$

which is positive definite about $z_2 = 0$. Differentiating Eq. (5.77) and using Eq. (5.76), the time rate-of-change of V_2 along the system trajectory is

$$\begin{aligned} \mathring{V}_2 &= z_2 \mathring{z}_2 \\ &= z_2 v_\alpha + 2 z_2 (\delta_\alpha \mathring{\alpha} \cos\beta + \delta_\beta \mathring{\beta}) \\ &\leq z_2 v_\alpha + 2|z_2|(|\delta_\alpha||\mathring{\alpha}| + \delta_\beta^* |\mathring{\beta}|) \end{aligned} \tag{5.78}$$

As done with δ_β, we assume that δ_α is bounded by

$$|\delta_\alpha| \leq \delta_\alpha^* \tag{5.79}$$

such that Eq. (5.78) becomes

$$\mathring{V}_2 \leq z_2 v_\alpha + 2|z_2|(\delta_\alpha^* |\mathring{\alpha}| + \delta_\beta^* |\mathring{\beta}|) \tag{5.80}$$

From Eq. (5.80), let v_α be given by

$$v_\alpha = -[b_\alpha + 2(\delta_\alpha^* |\mathring{\alpha}| + \delta_\beta^* |\mathring{\beta}|)]\text{sgn}(z_2) \tag{5.81}$$

where $b_\alpha > 0$ is a constant control gain, such that

$$\begin{aligned} \mathring{V}_2 &\leq -z_2[b_\alpha + 2(\delta_\alpha^* |\mathring{\alpha}| + \delta_\beta^* |\mathring{\beta}|)]\text{sgn}(z_2) + 2|z_2|(\delta_\alpha^* |\mathring{\alpha}| + \delta_\beta^* |\mathring{\beta}|) \\ &= -b_\alpha |z_2| \\ &\leq 0 \end{aligned} \tag{5.82}$$

The function V_2 is therefore nonincreasing, and is a Lyapunov function for the z_2 dynamics. The control law given by the combination of Eqs. (5.75) and (5.81) stabilizes z_2 about 0. Following similar logic as outlined previously for z_1, we can further state that the control law drives z_2 to 0 in a finite time, T_2, that satisfies

$$T_2 \leq \frac{|z_2(0)|}{b_\alpha} \tag{5.83}$$

and hold z_2 at zero for all time. The control law given by Eqs. (5.75) and (5.81) therefore drives $\mathcal{H}$ to the desired value and holds it at that value, in spite of the unknown disturbance terms. Combining Eqs. (5.75) and (5.81), the composite control law is

$$u_\alpha = \frac{-\mathring{\beta} u_\beta - \frac{1}{2}[b_\alpha + 2(\delta_\alpha^* |\mathring{\alpha}| + \delta_\beta^* |\mathring{\beta}|)]\text{sgn}(z_2)}{\mathring{\alpha} \cos\beta} \tag{5.84}$$

The control laws defined by Eqs. (5.72) and (5.84) drive the pendular motion to the desired reference motion in spite of the unknown disturbance terms. The only restrictions that we have to place of the system dynamics are that the disturbance terms are bounded, which is not a particularly restrictive assumption. However, we do note that the control laws are discontinuous because of their reliance on the signum function, which is discontinuous when its argument is 0. Such discontinuous control inputs can never be achieved by a real physical system, so we must modify the control laws to remove these discontinuities.

Following Refs. [58] and [28], let the control inputs have the modified form

$$u_\beta = [(\mathring{\alpha}+1)^2 + 3\cos^2\alpha]\sin\beta\cos\beta - k_\beta\mathring{\beta} - (b_\beta + \delta_\beta^*)\text{sat}\left(\frac{z_1}{\varepsilon_1}\right) \tag{5.85}$$

$$u_\alpha = \frac{-\mathring{\beta}u_\beta - \frac{1}{2}[b_\alpha + 2(\delta_\alpha^*|\mathring{\alpha}| + \delta_\beta^*|\mathring{\beta}|)]\text{sat}\left(\frac{z_2}{\varepsilon_2}\right)}{\mathring{\alpha}\cos\beta} \tag{5.86}$$

where ε_i are small positive constants and $\text{sat}(x)$ is the saturation function

$$\text{sat}(x) = \begin{cases} x, & |x| \leq 1 \\ \text{sgn}(x), & |x| > 1 \end{cases} \tag{5.87}$$

Because of the form of the saturation function, the control laws defined by Eqs. (5.85) and (5.86) are continuous; however, the use of the saturation function in place of the signum function means that the motion is not driven exactly to the sliding mode. Instead, the motion is driven to a small neighborhood of the sliding mode called the boundary layer, the size of which is determined by the ε_i. As the ε_i decrease, the boundary layer decreases in size, such that it vanishes when both ε_i are 0. Once the control drives the system to the boundary layer, z_1 and z_2 remain in it for all time. In light of this fact, using Eqs. (5.85) and (5.86) means that we can never exactly reach the desired reference motion, but we can come arbitrarily close to it by appropriate choice of ε_i.

The control gains for the sliding mode controller can be determined as follows. First, b_β and b_α can be determined from Eqs. (5.71) and (5.83) by specifying values for T_1 and T_2. The resulting values of b_α and b_β will ensure that z_1 and z_2 reach the boundary layer in times that satisfy Eqs. (5.71) and (5.83); however, we should note that the boundary layer may be reached in much faster times than T_1 and T_2. To determine an appropriate value for k_β, we note that the out-of-plane motion is governed by

$$\mathring{\beta} + k_\beta\beta = 0 \tag{5.88}$$

on the sliding mode. The solution to Eq. (5.88) is

$$\beta(\tau) = \beta(\tau*)e^{-k_\beta(\tau-\tau^*)} \tag{5.89}$$

where τ^* is the time that the boundary layer is reached. Defining the ratio $r = \beta(\tau)/\beta(\tau*)$, we can rewrite Eq. (5.89) as

$$k_\beta = -\frac{\ln(r)}{\tau - \tau^*} \tag{5.90}$$

So, we can use Eq. (5.90) to determine k_β such that β is reduced by a factor of r in a time $\tau - \tau*$ after the boundary layer is reached.

Figure 5.5 shows an example of the controlled system repsonse using the sliding mode controller, and the corresponding control inputs are shown in Fig. 5.6. The system parameters used to generate the plots in Figs. 5.5 and 5.6 are listed in Table 5.3, and the initial conditions are the same as those listed in Table 5.2. Note that specific values are assigned to δ_α and δ_β, despite the fact that they are "unknown" terms. Values for δ_α and δ_β must be set to generate the controlled system trajectories; however, the control laws have no specific knowledge of these terms, other than the fact that they are bounded by the parameters δ_α^* and δ_β^*. As Fig. 5.5 shows, the control laws are successful in driving the pendular motion to the desired planar motion with $h = h^*$. From Figs. 5.5(e) and 5.5(f), we see that the boundary layer (which is quite small for this particular example) is reached in a finite time, after which the system approaches the desired reference motion. Figure 5.6(b) shows that the magnitude of u_β is on par with the magnitudes required of all of the control laws considered previously, while the magnitude of u_α is the lowest we have seen thus far. However, we do note that the control inputs do not approach 0 as τ goes to infinity, and instead perform steady state oscillations about 0. These oscillations are due to the fact that the control laws must hold z_1 and z_2 in the boundary layer in spite of the disturbance terms, which requires continuous control actuation. Such continuous actuation could eventually wear out the control actuators, and is one of the primary disadvantages of using sliding mode control to control the pendular motion.

Table 5.3: Parameters used to generate controlled system response for sliding mode control

Parameter	Value
h^*	25
k_β	$\frac{\ln(100)}{2\pi}$
b_α	$\frac{\lvert\mathcal{H}(0)-h^*\rvert}{2\pi}$
b_β	$\frac{\lvert\mathring{\beta}(0)+k_\beta\beta(0)\rvert}{2\pi}$
δ_α	$0.01\cos(5\tau)$
δ_β	$0.01\cos(2\tau)$
δ_α^*	0.02
δ_β^*	0.02
ε_1	10^{-5}
ε_2	10^{-3}

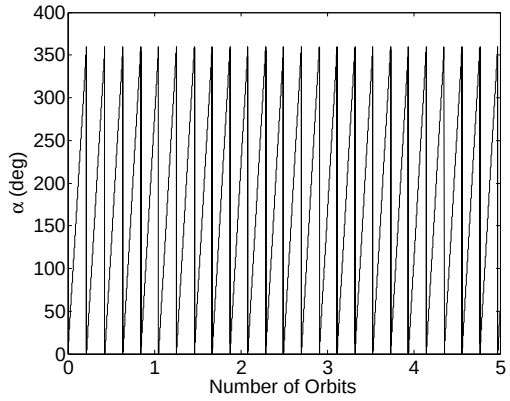

(a) In-plane angle

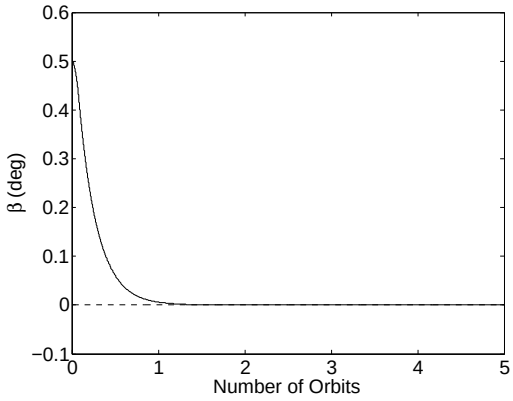

(b) Out-of-plane angle

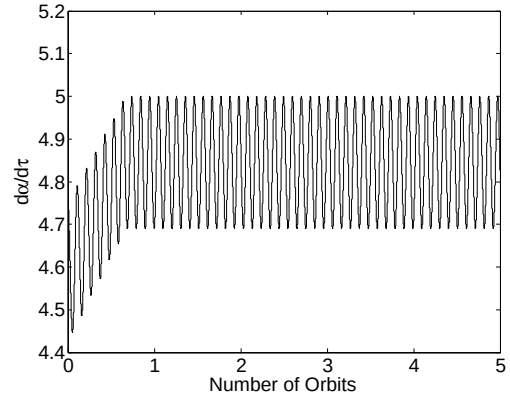

(c) In-plane angular rate

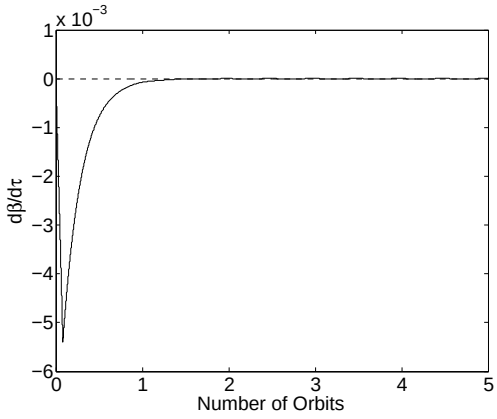

(d) Out-of-plane angular rate

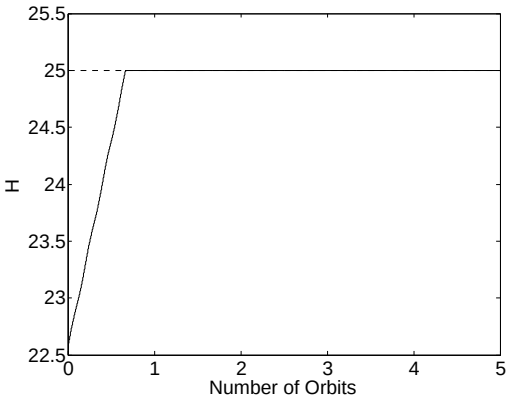

(e) $\mathcal{H}$

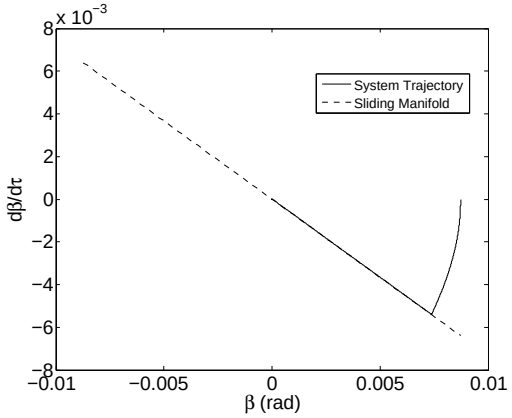

(f) Sliding Mode

Figure 5.5: System response for sliding mode control

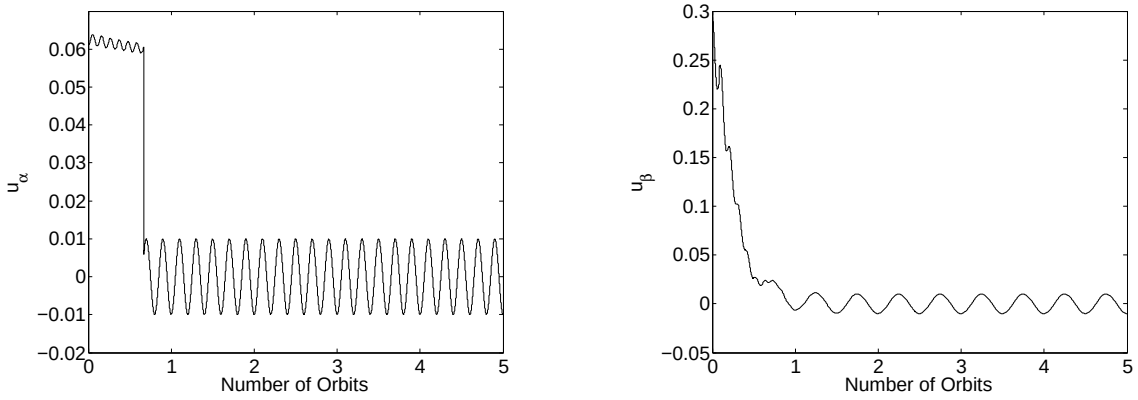

(a) In-plane control input

(b) Out-of-plane control input

Figure 5.6: Control inputs for sliding mode control

5.3.5 Adaptive Sliding Mode Control

The sliding mode control laws derived in §5.3.4 are successful in driving the pendular motion to the desired reference motion in spite of the unknown disturbance terms. However, the control laws require a priori knowledge of the disturbance terms in the form of the upper bounds δ_α^* and δ_β^*. For systems such as a spinning TSS, this type of knowledge may not be available, or it may be impractical to determine the upper bounds of the disturbances for the entire range of system parameters. We would therefore like to determine control laws that can account for the unknown disturbances without any a priori knowledge of them. To determine such control laws, we once again use the principles of sliding mode control used in §5.3.4, but also make use of some basic principles of adaptive nonlinear control.[58]

Returning to Eq. (5.63), recall that the time rate-of-change of the Lyapunov function for the z_1 dynamics satisfies

$$\mathring{V}_1 \leq z_1 v_\beta + |z_1||\delta_\beta| \tag{5.91}$$

In the sliding mode control law development, we assumed that we knew an upper bound on $|\delta_\beta|$ and proceeded to derive an expression for v_β using that knowledge. We now relax the assumption that we know anything about $|\delta_\beta|$ and determine an expression for v_β. Let v_β be given by

$$v_\beta = -b_\beta \text{sgn}(z_1) \tag{5.92}$$

where $b_\beta = b_\beta(\tau)$ is a positive, time-varying control gain. Using Eq. (5.92) in Eq. (5.91), we have

$$\mathring{V}_1 \leq -(b_\beta - |\delta_\beta|)|z_1| \tag{5.93}$$

If $b_\beta \geq |\delta_\beta|$, then $\mathring{V}_1 \leq 0$ and we have a sliding mode controller similar to the one developed previously. If $b_\beta < |\delta_\beta|$, however, then the Lyapunov rate will be positive and z_1 does not

approach the sliding mode. In light of these facts, let b_β be governed by the equation

$$\mathring{b}_\beta = (d_{\beta 1} b_\beta + d_{\beta 2} \mathring{V}_1) H(\text{sgn}(\mathring{V}_1)) \tag{5.94}$$

where $d_{\beta i} > 0$ are constant control gains and $H(x)$ is the Heaviside function

$$H(x) = \begin{cases} 1, & x \geq 0 \\ 0, & x < 0 \end{cases} \tag{5.95}$$

From Eq. (5.94), when $\mathring{V}_1 < 0$ we have $\mathring{b}_\beta = 0$, and b_β remains constant. When $\mathring{V}_1 \geq 0$ we have $\mathring{b}_\beta > 0$, and b_β increases; the positive constants $d_{\beta i}$ dictate the rate of growth of b_β, which is proportional to the current value of b_β and the current value of the Lyapunov rate. In this manner, b_β increases whenever the Lyapunov rate is positive until it reaches a value that is larger than the upper bound of $|\delta_\beta|$, after which it remains constant and the control laws acts like the sliding mode control law developed previously. The update expression given by Eq. (5.94) allows b_β to adapt according to the current behavior of the system. In a sense, Eq. (5.94) allows the control law to "learn" the value of b_β that results in a negative definite Lyapunov rate.

To ensure that the control law is continuous, let Eq. (5.92) be modified as

$$v_\beta = -b_\beta \text{sat}\left(\frac{z_1}{\varepsilon_1}\right) \tag{5.96}$$

When used with the adaptation mechanism of Eq. (5.94), this control law ensures that z_1 is driven to, and held within, the boundary layer. Once z_1 is held inside the boundary layer, there may be times at which the Lyapunov rate is positive, and b_β will be updated according to Eq. (5.94). However, because z_1 has already reached the boundary layer, we no longer need to update b_β. We therefore set $\mathring{b}_\beta = 0$ if $|z_1| \leq \varepsilon_1$. Combining Eqs. (5.72), the composite control law for the out-of-plane pendular motion is

$$u_\beta = [(\mathring{\alpha} + 1)^2 + 3\cos^2\alpha]\sin\beta\cos\beta - k_\beta \mathring{\beta} - b_\beta \text{sat}\left(\frac{z_1}{\varepsilon_1}\right) \tag{5.97}$$

Returning to Eq. (5.78), recall that the Lyapunov rate for the z_2 dynamics satisfies

$$\mathring{V}_2 \leq z_2 v_\alpha + 2|z_2|(|\delta_\alpha||\mathring{\alpha}| + |\delta_\beta||\mathring{\beta}|) \tag{5.98}$$

Similar to the procedure used to determine v_β, let v_α be given by

$$v_\alpha = -b_\alpha \text{sgn}(z_2) \tag{5.99}$$

where $b_\alpha = b_\alpha(\tau)$ is a positive, time-varying control gain. Using Eq. (5.99) in Eq. (5.98), we have

$$\mathring{V}_2 \leq -[b_\alpha - 2(|\delta_\alpha||\mathring{\alpha}| + |\delta_\beta||\mathring{\beta}|)]|z_2| \tag{5.100}$$

In light of Eq. (5.100), let b_α be governed by

$$\mathring{b}_\alpha = (d_{\alpha 1} b_\alpha + d_{\alpha 2} \mathring{V}_2) H(\mathrm{sgn}(\mathring{V}_2)) \tag{5.101}$$

where $d_{\alpha i} > 0$ are constant control gains. As discussed previously when considering b_β, Eq. (5.101) eventually results in a sliding mode controller that drives z_2 to 0. To ensure that the control input is continuous, however, we modify Eq. (5.99) as

$$v_\alpha = -b_\alpha \mathrm{sat}\left(\frac{z_2}{\varepsilon_2}\right) \tag{5.102}$$

such that the composite control law is

$$u_\alpha = \frac{-u_\beta \mathring{\beta} - \frac{1}{2} b_\alpha \mathrm{sat}\left(\frac{z_2}{\varepsilon_2}\right)}{\mathring{\alpha} \cos\beta} \tag{5.103}$$

Equations (5.97) and (5.103), in combination with the adaptation mechanisms of Eqs. (5.94) and (5.101), drive the pendular motion to the desired reference motion. Moreover, they do so in spite of the unknown disturbance terms, and without any a priori knowledge of the disturbance terms.

Figure 5.7 shows an example of the controlled system response for the adaptive sliding mode controller, and the corresponding control inputs and variable control gains are shown in Fig. 5.8. The system parameters used to generate the plots in Figs. 5.7 and 5.8 are listed in Table 5.4, and the initial conditions are the same as those listed in Table 5.2. Both of the variable control gains were initially set to zero. As Fig. 5.7 shows, the control laws are successful in driving the pendular motion to the desired reference motion; however, we do note that the control maneuver takes longer than any of the control maneuvers considered previously. A particularly interesting aspect of the controlled motion is illustrated in Fig. 5.7(f). The out-of-plane pendular motion is driven to the boundary layer rather early in the maneuver, but does not stay there initially. This behavior is due to the fact that the control gain b_β is not large enough to account for the unknown disturbances when the motion initially reaches the boundary layer, and the disturbances force the motion out of the boundary layer. The control law subsequently drives the motion back to the boundary layer, where it is once again forced out by the disturbances. Finally, b_β becomes large enough to fully counteract the effects of the disturbances, and the out-of-plane motion is driven to, and held inside of, the boundary layer. The behavior illustrated by Fig. 5.7(f) demonstrates the robustness of the adaptive sliding mode controller. Even though no knowledge of the disturbances is used in the control laws, they adapt to overcome the disturbances and drive the system to the reference motion.

From Fig. 5.8(b), we once again see that the out-of-plane control input is similar to those required by all of the control laws considered previously. The in-plane control input is the lowest required by all of the control laws. As with the regular sliding mode controller, the

control inputs for the adaptive sliding mode controller do not approach 0 as τ approaches infinity, and instead undergo steady-state oscillations. These steady-state oscillations are required to hold the motion in the boundary layer.

As shown by Figs. 5.8(c) and 5.8(d), both control gains start at 0 and quickly grow to larger positive values. As time progresses and the motion approaches the boundary layer, the values of both control gains level-off at constant values. Note, in particular, that b_β approaches a value that is very near 0.01. From Table 5.4, we see that this value is exactly the upper bound of the out-of-plane disturbance term. The behavior of b_β illustrates another advantage of the adaptive sliding mode controller over its non-adaptive counterpart: the adaptation mechanisms allow the control laws to "learn" the precise control gains required to make the Lyapunov rates negative definite, whereas the regular sliding mode control laws require estimates of these control gains. Such estimates may be overly conservative in some cases, resulting in unnecessarily large control inputs.

Table 5.4: Parameters used to generate controlled system response for adaptive sliding mode control

Parameter	Value
h^*	25
k_β	$\frac{\ln(100)}{2\pi}$
δ_α	$0.01\cos(5\tau)$
δ_β	$0.01\cos(2\tau)$
$d_{\alpha 1}$	1
$d_{\alpha 2}$	100
$d_{\beta 1}$	1
$d_{\beta 2}$	100
ε_1	10^{-5}
ε_2	10^{-3}

5.4 Validation of Computational Model

In this section the validity of the control laws developed in the previous section is assessed by applying them to the top-level computational model. From the examples presented in the previous section, the three control laws that resulted in the lowest magnitude control inputs are the $\mathcal{H}$-tracking control laws, the sliding mode control laws, and the adaptive sliding mode control laws. For this reason, only these control laws are applied to the top-level computational model in this section.

To apply the control laws developed using the lower-level computational model to the top-

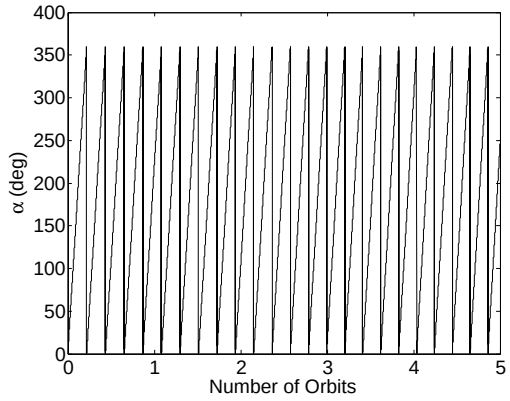

(a) In-plane angle

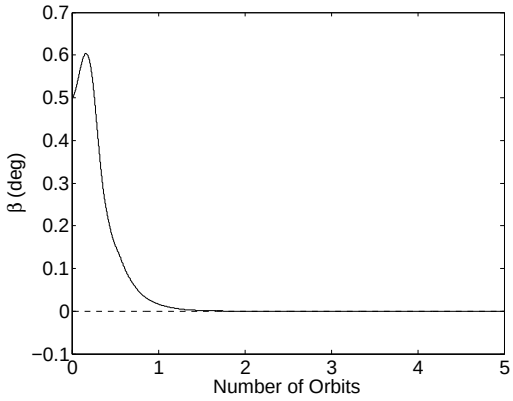

(b) Out-of-plane angle

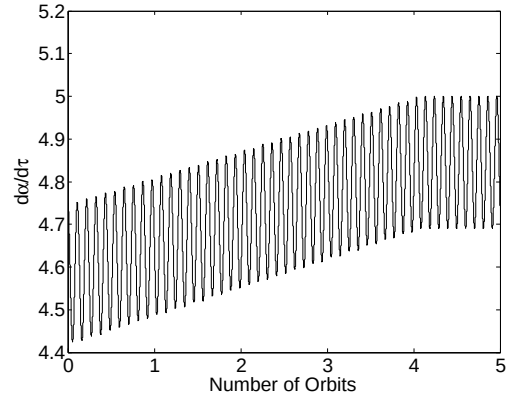

(c) In-plane angular rate

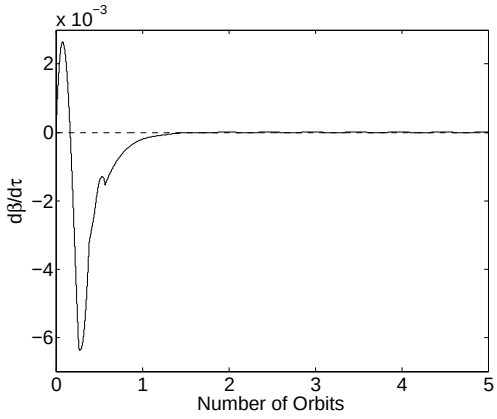

(d) Out-of-plane angular rate

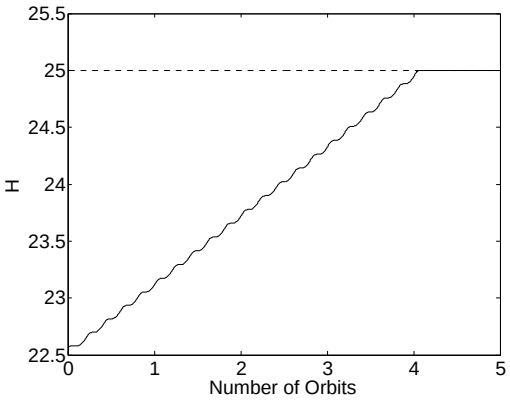

(e) $\mathcal{H}$

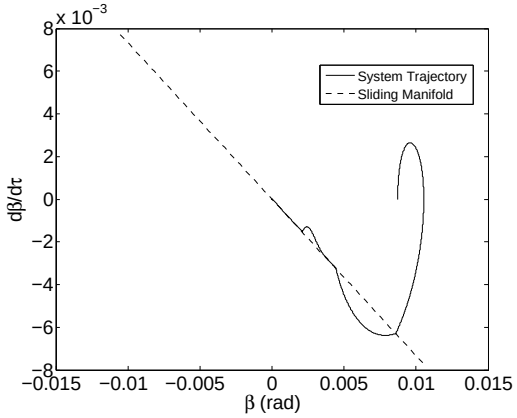

(f) Sliding Mode

Figure 5.7: System response for adaptive sliding mode control

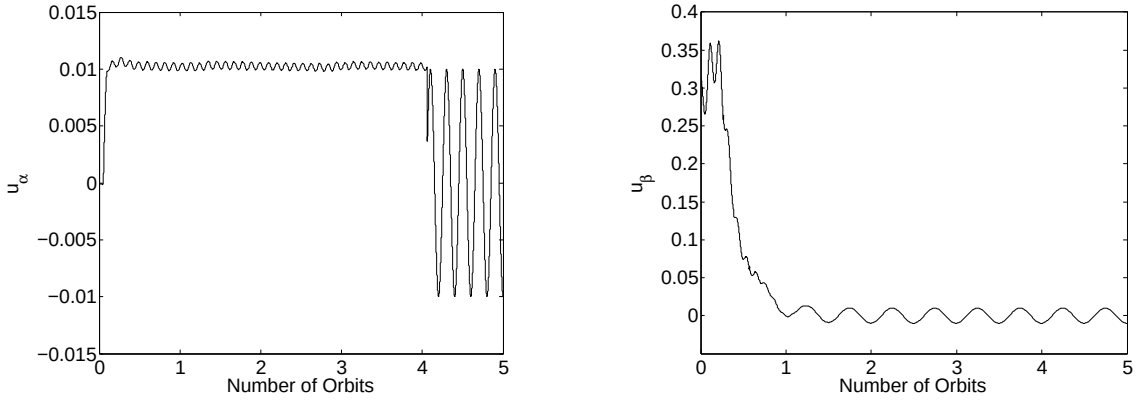

(a) In-plane control input

(b) Out-of-plane control input

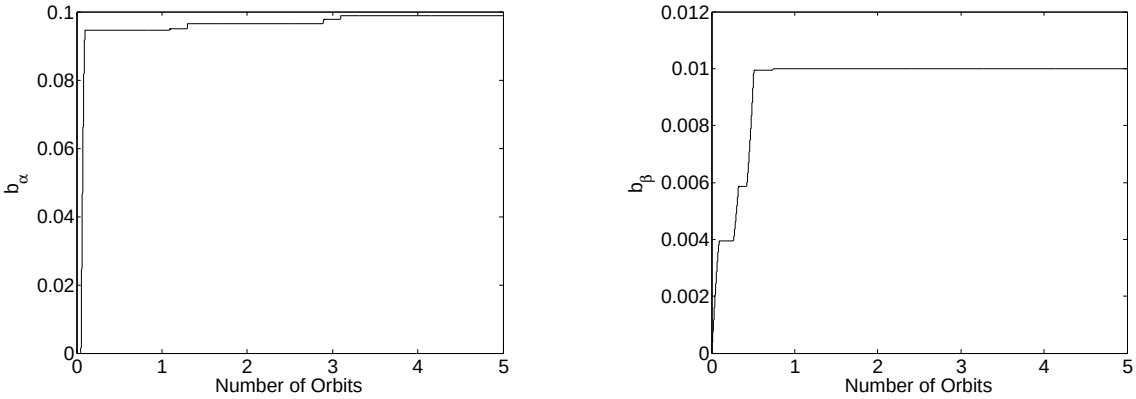

(c) In-plane control gain

(d) Out-of-plane control gain

Figure 5.8: Control inputs and gains for adaptive sliding mode control

level computational model, we note that the equations governing the pendular motion of the tether in the top-level computational model can be written as

$$\ddot{\alpha}\cos\beta - 2(\dot{\alpha}+\Omega_A)\dot{\beta}\sin\beta + 3\Omega_A^2\sin\alpha\cos\alpha\cos\beta = \frac{M_{A2}}{I_A} + \Delta_\alpha \tag{5.104}$$

$$\ddot{\beta} + [(\dot{\alpha}+\Omega_A)^2 + 3\Omega_A^2\cos^2\alpha]\sin\beta\cos\beta = \frac{M_{A1}}{I_A} + \Delta_\beta \tag{5.105}$$

where M_{Ai} are control moments acting about $\mathcal{A}$ in the $\hat{\mathbf{e}}_i$ direction, and Δ_α, Δ_β are terms that account for various aspects of the system dynamics. The Δ terms include effects due to the elastic vibrations of the tether, the variation of the orbit of $\mathcal{A}$, the attitude motion of the end bodies, and nonlinearities in the gravitational force acting along over the length of the system. If we assume that the control moments are applied using small thrusters on the secondary end body, $\mathcal{B}$, then we have

$$\begin{aligned}\vec{\mathbf{M}}_{\mathrm{A}} &= L\hat{\mathbf{e}}_3 \times (F_{B1}\hat{\mathbf{e}}_3 - F_{B2}\hat{\mathbf{e}}_2) \\ &= F_{B2}L\hat{\mathbf{e}}_1 + F_{B1}L\hat{\mathbf{e}}_2 \\ &= M_{A1}\hat{\mathbf{e}}_1 + M_{A2}\hat{\mathbf{e}}_2\end{aligned} \tag{5.106}$$

where F_{Bi} are the components of the thrust vector applied at $\mathcal{B}$. Note that a positive value of F_{B2} implies a force in the negative $\hat{\mathbf{e}}_2$ direction. This convention is used to ensure that a positive value of F_{B2} results in a positive value of M_{A1}. Using Eq. (5.106) in Eqs. (5.104) and (5.105) and placing the equations in nondimensional form, we have

$$\mathring{\alpha}\cos\beta - 2(\mathring{\alpha}+1)\mathring{\beta}\sin\beta + 3\sin\alpha\cos\alpha\cos\beta = \frac{F_{B1}L}{I_A\Omega_A^2} + \delta_\alpha \tag{5.107}$$

$$\mathring{\beta} + [(\mathring{\alpha}+1)^2 + 3\cos^2\alpha]\sin\beta\cos\beta = \frac{F_{B2}L}{I_A\Omega^2} + \delta_\beta \tag{5.108}$$

Comparing Eqs. (5.107) and (5.108) to Eqs. (5.56) and (5.57), the control forces acting at $\mathcal{B}$ are related to the nondimensional control inputs by

$$F_{B1} = \left(\frac{I_A\Omega_A^2}{L}\right)u_\alpha \tag{5.109}$$

$$F_{B2} = \left(\frac{I_A\Omega_A^2}{L}\right)u_\beta \tag{5.110}$$

Noting that

$$I_A = m_B L^2 + \frac{1}{3}\bar{\rho}L^3 \tag{5.111}$$

we can rewrite Eqs. (5.109) and (5.110) as

$$F_{B1} = \left(m_B + \frac{1}{3}\bar{\rho}L\right)L\Omega_A^2 u_\alpha \tag{5.112}$$

$$F_{B2} = \left(m_B + \frac{1}{3}\bar{\rho}L\right)L\Omega_A^2 u_\beta \tag{5.113}$$

Equations (5.112) and (5.113) are used to apply the control laws developed using the lower-level computational model to the top-level computational model.

5.4.1 Planar $\mathcal{H}$ Tracking

Figure 5.9 shows an example of the controlled system response for application of the $\mathcal{H}$-tracking control laws developed in §5.3.3 to the top-level computational model. The corresponding control inputs (in the form of forces applied at the secondary end body $\mathcal{B}$) are shown in Fig. 5.10. The system parameters and initial conditions used to generate the plots shown in Figs. 5.9 and 5.10 are listed in Tables 5.5 and 5.7, respectively. The parameters specific to the $\mathcal{H}$-tracking control law are listed in Table 5.6. As Fig. 5.9 shows, the control laws drive the pendular motion toward the desired reference motion, but the reference motion is not approached asymptotically. This fact can be seen in Figs. 5.9(b), 5.9(d), and 5.9(e) in which the out-of-plane motion and the quantity $\mathcal{H}$ undergo small amplitude oscillations about the desired reference motion. These steady-state oscillations are due to the unmodeled dynamics contained in the top-level model that are not accounted for by the control laws determined using the lower-level model. There may be certain situations in which the small steady-state oscillations seen in the controlled motion do not have a significant impact on the performance of the system. In such cases, the $\mathcal{H}$-tracking control laws are adequate for controlling the pendular motion of the tether. If more precise control of the pendular motion is required, then some other method of control that can account for the effects of the unmodeled dynamics must be employed.

Figure 5.10 shows that the maximum magnitude of both of the control forces required to control the pendular motion is on the order of 1 N. Such control forces could certainly be applied by small thrusters on the end bodies, however, the duration of the control maneuvers could mean that a significant amount of propellant may be required. The control forces do approach 0 as the maneuver is completed, meaning that the propellant required to perform the maneuver decreases significantly as the maneuver nears completion. The control forces do not approach 0 exactly, and instead undergo small amplitude steady-state oscillations due to the effects of unmodeled dynamics. Such steady-state oscillations could be avoided by switching off the inputs once the system is within a pre-specified range of the desired motion, thereby saving the propellant that would be consumed through the steady-state oscillations of the control forces.

Table 5.5: System parameters used when applying control laws to the top-level computational model

Primary End Body $\mathcal{A}$	
m_A (kg)	50,000
$\mathbf{I}_{\mathrm{A}}$ (kg-m^2)	diag(30,000 40,000 50,000)
$\mathbf{p}_{\mathrm{A}}$ (m)	$(0\ 0\ 1)^{\mathrm{T}}$
Secondary End Body $\mathcal{B}$	
m_B (kg)	100
$\mathbf{I}_{\mathrm{B}}$ (kg-m^2)	diag(300 400 500)
$\mathbf{p}_{\mathrm{B}}$ (m)	$(0\ 0\ 0)^{\mathrm{T}}$
Tether	
L (km)	20
$\bar{\rho}$ (kg/km)	2.5
EA (N)	55,000
c (s)	0.5
N_e	4
Central Body	
μ (km^3/s^2)	3.986×10^5

Table 5.6: Control parameters used when applying the $\mathcal{H}$-tracking control to the top-level computational model

Parameter	Value
h^*	25
$k_{\mathcal{H}}$	$\frac{\ln(100)}{2\pi}$
$k_{\beta 2}$	$\frac{\ln(100)}{2\pi}$
$k_{\beta 1}$	$\frac{k_{\beta 1}^2}{4}$

Table 5.7: Initial conditions used when applying control laws to the top-level computational model

System Orbital Motion	
a (km)	6,770
e	0.001
Ω (deg)	300
I (deg)	50
ω (deg)	45
ν (deg)	0
$\mathcal{A}$ Attitude Motion	
$\bar{\mathbf{q}}_{\mathrm{A}}$	$(1\ 0\ 0\ 0)^{\mathrm{T}}$
$\boldsymbol{\omega}_{\mathrm{A/O}}$ (deg/s)	$(0\ 4.75\Omega_{A0}\ 0)^{\mathrm{T}}$
$\mathcal{B}$ Attitude Motion	
$\bar{\mathbf{q}}_{\mathrm{B}}$	$(1\ 0\ 0\ 0)^{\mathrm{T}}$
$\boldsymbol{\omega}_{\mathrm{B/O}}$ (deg/s)	$(0\ 4.75\Omega_{A0}\ 0)^{\mathrm{T}}$
Pendular Tether Motion	
α (deg)	0
β (deg)	0.5°
$\dot{\alpha}$ (deg/s)	$4.75\Omega_{A0}$
$\dot{\beta}$ (deg/s)	0
Tether Elastic Vibrations	
$u(\bar{s},0)$ (m)	$20\sin\left(\frac{\pi\bar{s}}{L}\right)$
$\dot{u}(\bar{s},0)$ (m)	0
$v(\bar{s},0)$ (m)	$20\sin\left(\frac{\pi\bar{s}}{L}\right)$
$\dot{v}(\bar{s},0)$ (m)	0
$w(\bar{s},0)$ (m)	$\frac{c_A L}{EA} f(0)\left[\frac{\bar{s}}{L} - \frac{\gamma}{6}\left(\frac{\bar{s}}{L}\right)^3\right]$
$\dot{w}(\bar{s},0)$ (m)	$\frac{c_A L}{EA} \dot{f}(0)\left[\frac{\bar{s}}{L} - \frac{\gamma}{6}\left(\frac{\bar{s}}{L}\right)^3\right]$

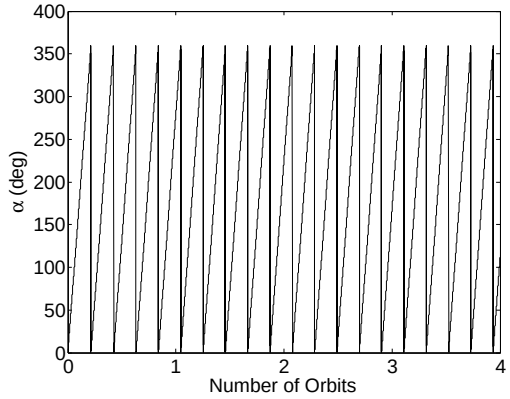

(a) In-plane angle

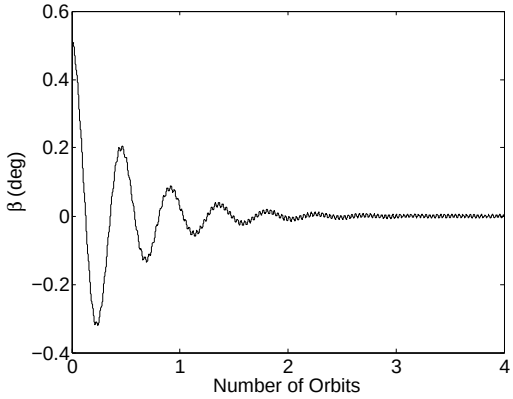

(b) Out-of-plane angle

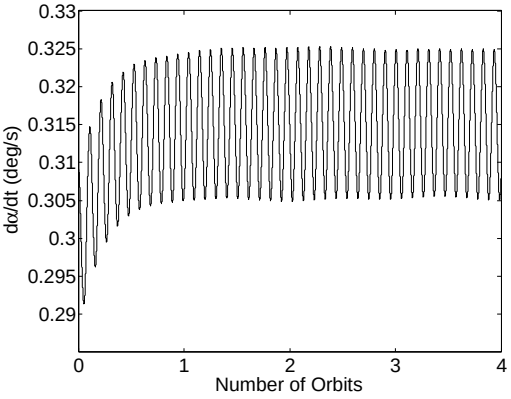

(c) In-plane angular rate

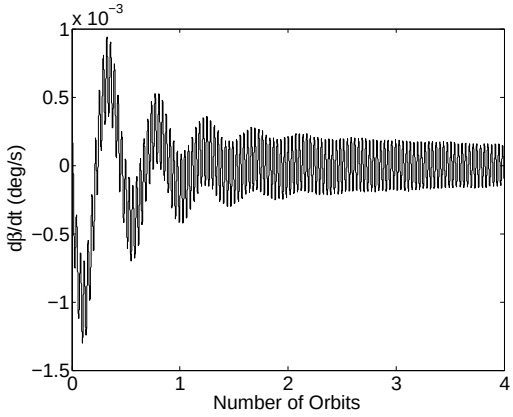

(d) Out-of-plane angular rate

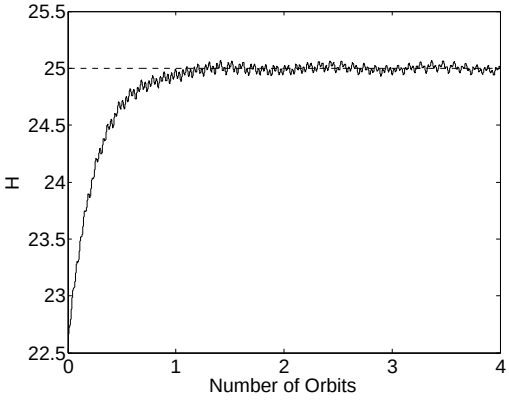

(e) $\mathcal{H}$

Figure 5.9: System response for planar $\mathcal{H}$-tracking control applied to the top-level computational model

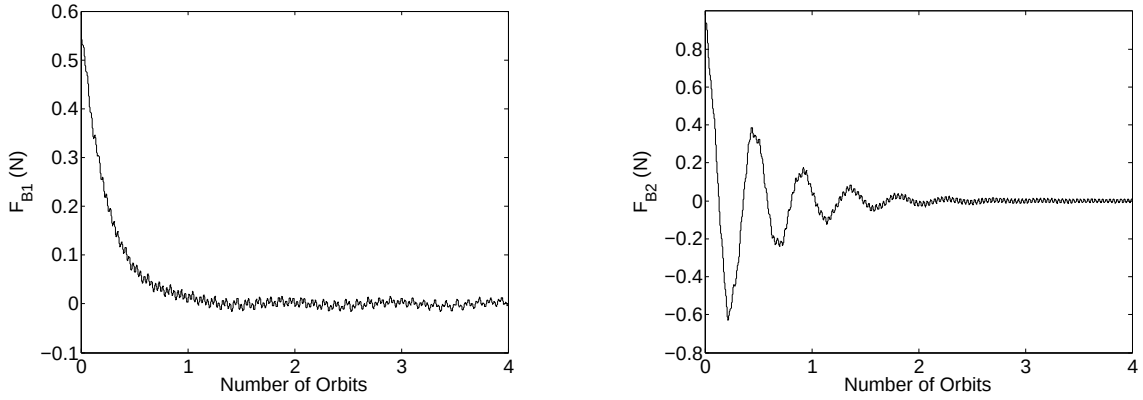

(a) In-plane control input

(b) Out-of-plane control input

Figure 5.10: Control inputs for planar $\mathcal{H}$-tracking control applied to the top-level computational model

5.4.2 Sliding Mode Control

Figure 5.11 shows an example of the controlled system response when the sliding mode control laws developed in §5.3.4 are applied to the top-level computational model. The corresponding control inputs are shown in Fig. 5.12. The system parameters and initial conditions used to generate the plots in Figs. 5.11 and 5.12 are the same as those listed in Tables 5.5 and 5.7. The parameters specific to the sliding mode control laws are listed in Table 5.8. As Fig. 5.11 shows, the sliding mode control laws are successful in driving the pendular motion of the tether to the reference motion. Recall, however, that the sliding mode control laws drive the motion to an arbitrarily small neighborhood of the reference motion called the boundary layer. In the example illustrated by Fig. 5.11, we have chosen the boundary layer to be quite small to demonstrate the fact that the pendular motion can be driven to the reference motion with a negligible error. This fact is most plainly seen in Figs. 5.11(b), 5.11(d), and 5.11(e) in which it appears that the motion is driven exactly to the reference motion.

Figure 5.12 shows that, like for the $\mathcal{H}$-tracking control, the maximum magnitude of both of the control forces required by the sliding mode controller is on the order of 1 N. However, the steady-state oscillations of the control inputs seen in the sliding mode controller are significantly larger than those seen in the $\mathcal{H}$-tracking controller. In the $\mathcal{H}$-tracking controller, the steady-state input oscillations are a result of the unmodeled dynamics that are not accounted for by the control laws. In the sliding mode controller, the steady-state input oscillations are due to the fact that the control laws hold the motion inside the boundary layer. These oscillations are therefore required to counteract the effects of the unmodeled dynamics.

As mentioned previously in this chapter, the large amplitude steady-state oscillations of the

inputs required by the sliding mode controller are one of its principle drawbacks. If precise tracking of the reference motion is not required, then it is most likely much more efficient to use the $\mathcal{H}$-tracking control laws because they would require significantly less propellant over extended periods of time. However, if precise tracking of the reference motion is required, then we have demonstrated that the sliding mode control laws are capable of providing such control, despite the fact that they are derived using a lower-level model that does not account for all of the relevant system dynamics. The cost of achieving such precise control of the pendular motion of the tether is that large steady-state control inputs may be required. In many situations it may be possible to control the pendular motion using a combination of the $\mathcal{H}$-based and sliding mode controllers. The majority of the time the $\mathcal{H}$-tracking control could be used to control the motion, and the sliding mode controller would be employed only in situations for which precise control is required. Such a combination of the two control methods would result in a more efficient use of the propellant required to provide the control forces.

Table 5.8: Control parameters used when applying the sliding mode control laws to the top-level computational model

Parameter	Value
h^*	25
k_β	$\frac{\ln(100)}{2\pi}$
b_α	$\frac{0.1}{2\pi}$
b_β	$\frac{0.001}{2\pi}$
δ_α^*	0.2
δ_β^*	0.2
ε_1	10^{-5}
ε_2	10^{-4}

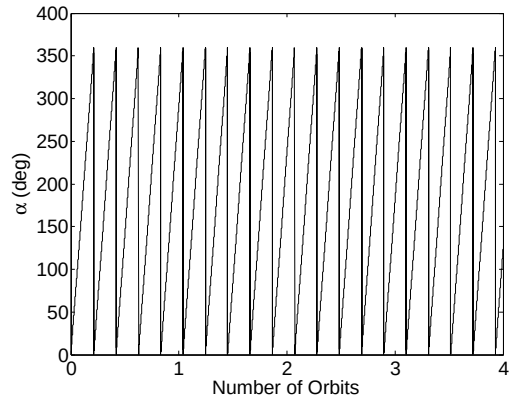

(a) In-plane angle

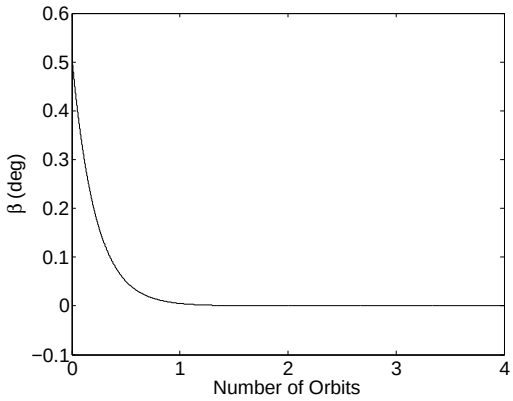

(b) Out-of-plane angle

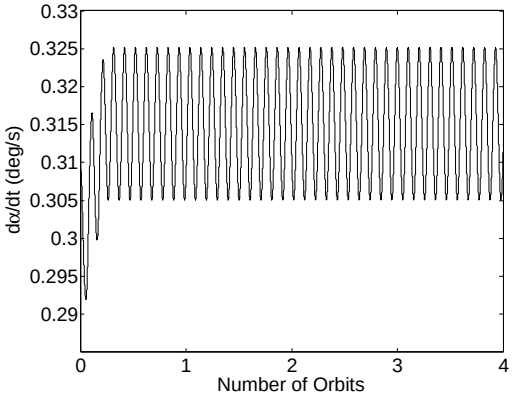

(c) In-plane angular rate

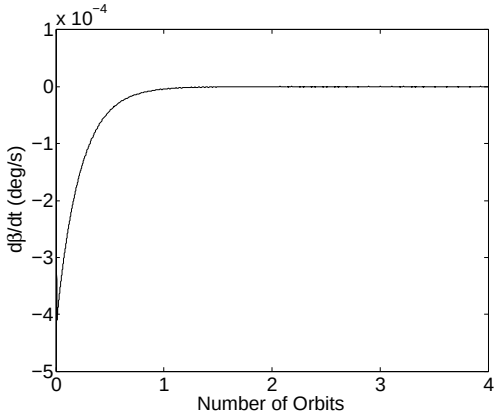

(d) Out-of-plane angular rate

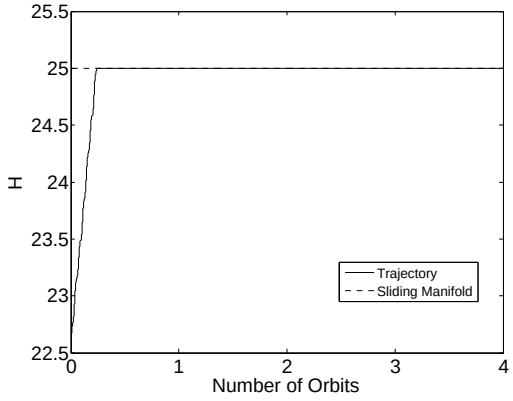

(e) $\mathcal{H}$

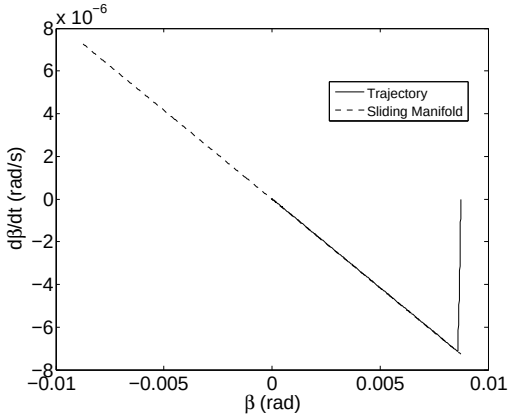

(f) Sliding Mode

Figure 5.11: System response for sliding mode control applied to the top-level computational model

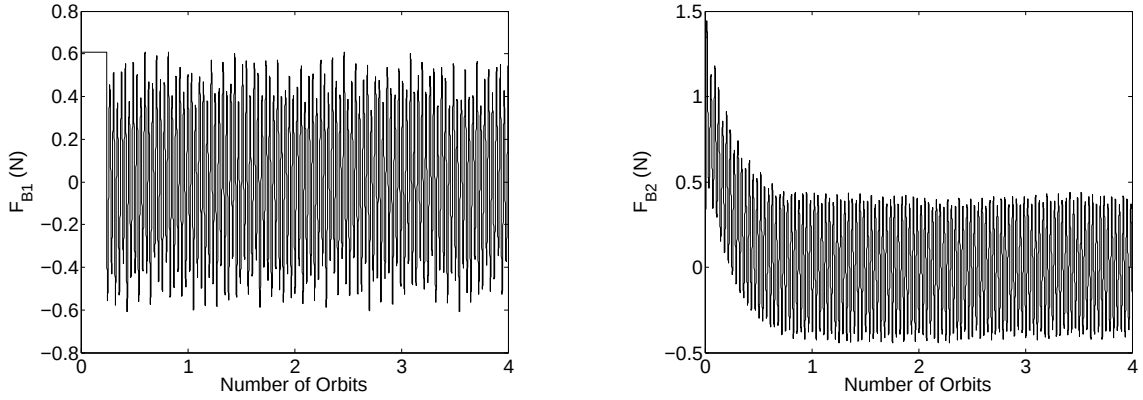

(a) In-plane control input

(b) Out-of-plane control input

Figure 5.12: Control inputs for sliding mode control

5.4.3 Adaptive Sliding Mode Control

We have seen that the sliding mode control laws developed using the lower-level computational model can be applied to the top-level computational model to precisely control the pendular motion to the reference motion. As discussed in §5.3.5, the sliding mode control laws require a priori knowledge of the upper bounds on the disturbances caused by the dynamics not accounted for by the control laws. For a TSS, these upper bounds depend on a number of different system parameters, and may vary greatly between particular systems. For this reason, we developed the adaptive sliding mode control laws in §5.3.5 that do not rely on any a priori knowledge of the disturbances due to the unmodeled dynamics.

Figure 5.13 shows an example of the system response when the adaptive sliding mode control laws are applied to the top-level computational model. The corresponding control forces and variable control gains are shown in Fig. 5.14. The system parameters and initial conditions used to generate the controlled response are once again listed in Tables 5.5 and 5.7, and the parameters specific to the adaptive sliding mode control laws are listed in Table 5.9. Both of the variable control gains are initially set to 0. From Figs. 5.13 and 5.14, we can see that the control laws are successful in controlling the pendular motion about the reference motion. As done for the regular sliding mode controller, we have chosen the boundary layer to be quite small, such that it appears that the motion exactly tracks the reference motion. One particular point to note about the controlled system response is that the out-of-plane motion is driven to the boundary layer several times before the control law has adapted sufficiently such that the motion can be held in the boundary layer. This type of behavior was also seen in §5.3.5, and is illustrated in Fig. 5.13(f).

Figure 5.14 shows that the maximum magnitude of both of the control gains required by the adaptive sliding mode controller is once again on the order of 1 N. We also once again see the large amplitude steady-state oscillations of the control forces that are required to hold

the motion in the boundary layer. These large magnitude steady-state control inputs could require an excessively large amount of fuel over extended periods of time, so the adaptive sliding mode controller should only be applied in situations for which precise control of the pendular motion is required. Figures 5.14(c) and 5.14(d) illustrate how the variable control gains change over time and eventually level-off at constant values. These figures illustrate how the adaptation mechanisms included in the control laws allow the laws to "learn" the appropriate values of the control gains.

Table 5.9: Control parameters used when applying the adaptive sliding mode control laws to the top-level computational model

Parameter	Value
h^*	25
k_β	$\frac{\ln(100)}{2\pi}$
$d_{\alpha 1}$	10^{-4}
$d_{\alpha 2}$	1
$d_{\beta 1}$	10^{-3}
$d_{\beta 2}$	1
ε_1	10^{-5}
ε_2	10^{-4}

5.5 Summary

In this chapter we used a number of nonlinear control design techniques to develop methods of controlling the pendular motion of the tether in a spinning TSS. Because of the relative simplicity of its mathematical model, the lower-level system model used in Ch. 4 to study the dynamics of spinning TSS was also used in this chapter to derive the control laws. A nonlinear controllability analysis was performed to demonstrate the inherent difficulty of controlling the pendular motion using only electrodynamic forcing, so the control laws were developed assuming that arbitary control inputs are available to control both the in- and out-of-plane pendular motion.

Four different sets of control laws were developed in this chapter. The first set of control laws allows for tracking of an arbitrary planar reference trajectory. The specific cases of tracking a linear growth of the in-plane angle (corresponding to a constant in-plane spin rate) and tracking of a specific natural in-plane motion were used to demonstrate the performance of the control laws. The second set of control laws allows for tracking of a natural planar motion with a specific value of the parameter h. The difference between these control laws and the first set is that they do not force the phase angle of the final in-plane motion to be mathced;

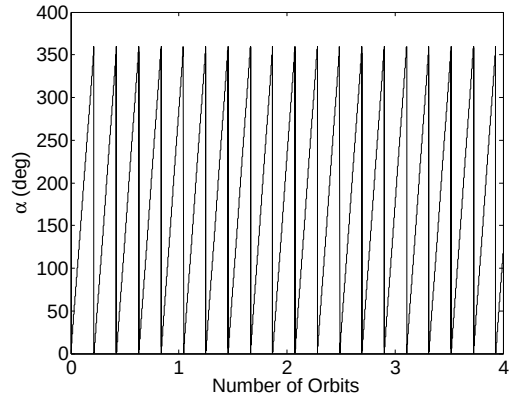

(a) In-plane angle

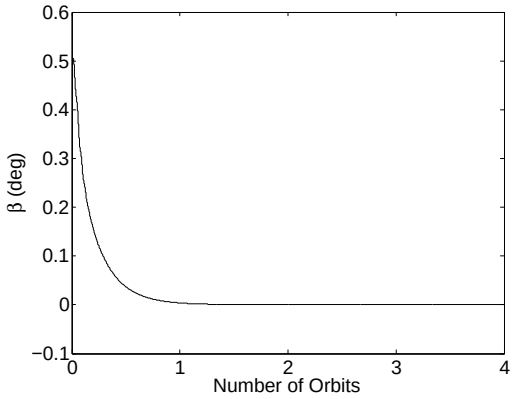

(b) Out-of-plane angle

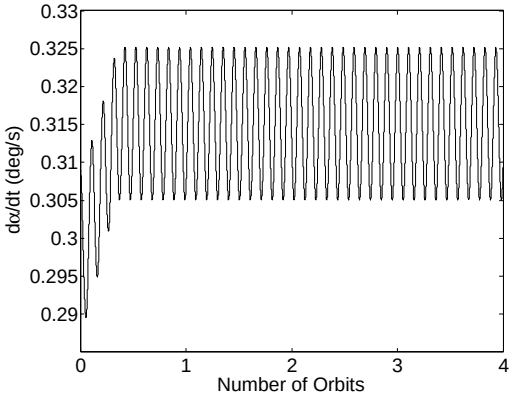

(c) In-plane angular rate

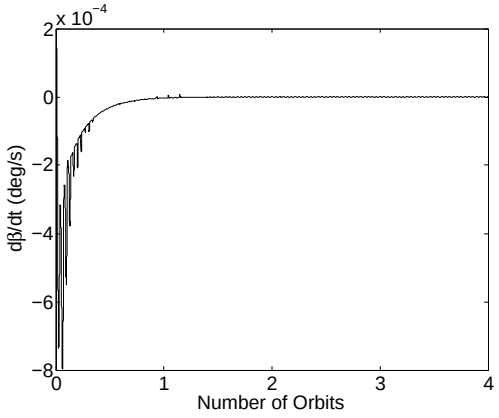

(d) Out-of-plane angular rate

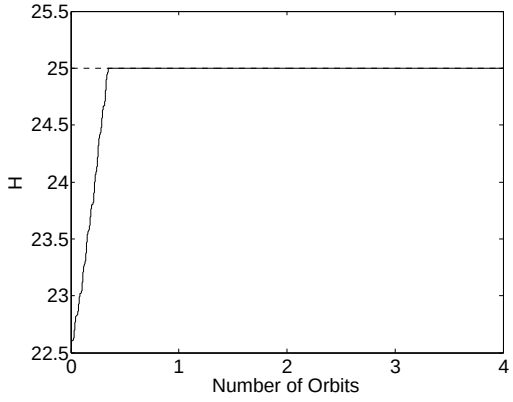

(e) $\mathcal{H}$

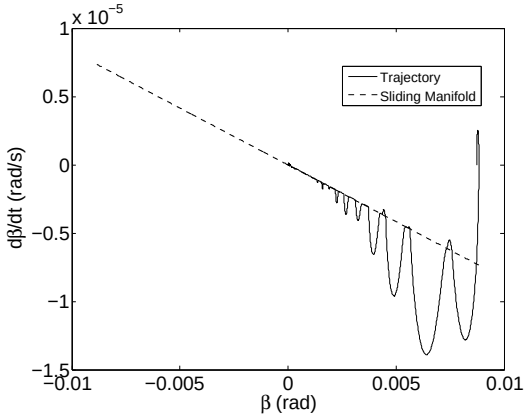

(f) Sliding Mode

Figure 5.13: System response for adaptive sliding mode control applied to the top-level computational model

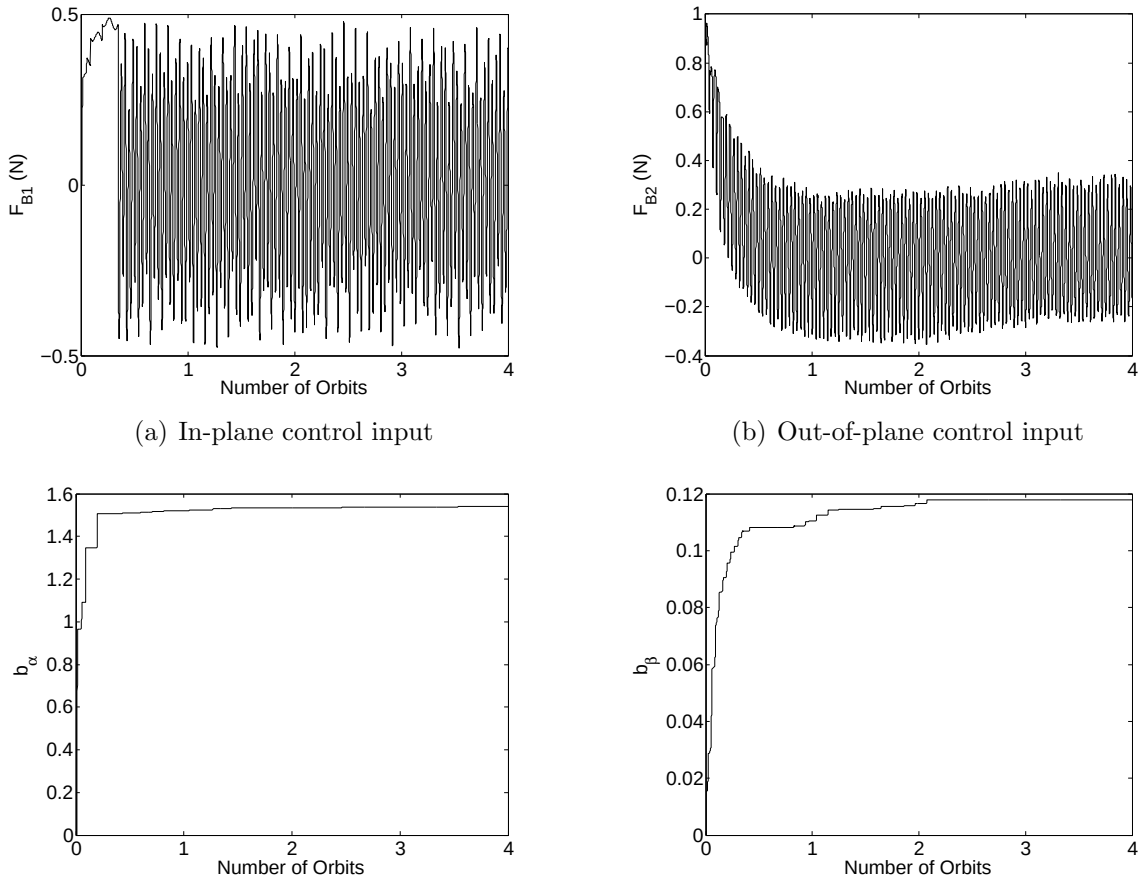

(a) In-plane control input

(b) Out-of-plane control input

(c) In-plane control gain

(d) Out-of-plane control gain

Figure 5.14: Control inputs and gains for adaptive sliding mode control

all that is matched is the value of h of the desired natural planar motion. In general, the fact that the phase angle is not matched results in lower control inputs than required when the phase angle is matched. The third set of control laws are based on principles of sliding mode control, meaning that they can control the pendular motion about a desired reference motion in spite of the presence of unknown disturbance terms due to unmodeled dynamics. The only constraint required of these control laws is that the unknown disturbances are bounded, and that these bounds are known a priori. One of the main drawbacks of using the sliding mode control laws is that they can require relatively large steady-state control inputs to hold the system at the reference motion. The magnitude of these steady-state control inputs depends on the magnitude of the disturbances, and they may become excessively large for some systems. The fourth and final set of control laws developed in this chapter is an extension of the third set to include some principles of adaptive control. For a typical TSS, it may be difficult or impractical to determine the bounds on the disturbance terms required by the sliding mode control laws. In light of this fact, the fourth set of control laws includes adaptation mechanisms that allow the control gains included in the laws to start at 0 and gradually "learn" what values they should be to compensate for the unknown disturbances and drive the system to the reference motion. In this manner, precise control of the pendular motion is achieved without any a priori knowledge of the disturbance terms. As with the regular sliding mode control laws, however, relatively large steady-state control inputs can be required to compensate for the unknown disturbance terms.

The second, third, and fourth sets of control laws derived in this chapter were applied to the top-level computational model to assess their applicability to an actual spinning TSS. The second set of control laws were successful in driving the pendular motion of the top-level computational model to the reference motion; however, the fact that the top-level model contains dynamics that are not accounted for by the lower-level model results in small steady-state oscillations about the reference motion. These steady-state oscillations can be quite small, and could most likely be tolerated for many applications. Both sets of sliding mode control laws were also successful in driving the pendular motion of the top-level computational model to the reference motion, but these control laws achieve much more precise tracking because of their ability to compensate for the effects of unmodeled dynamics. As mentioned previously, the main drawback of either set of sliding mode control laws is that they require relatively large steady-state control inputs to compensate for the effects of unmodeled dynamics. When applied to the top-level computational model, these large steady-state inputs translate to large propellant requirements for the thrusters on the secondary end body that provide the control forces. In practice, a combination control scheme incorporating the sliding mode control and the second set of control laws could be applied to more efficiently manage the propellant required to control the pendular motion. The second set of control laws would be used for most situations for which less precise control is needed, and the sliding mode control laws would only be used in situations that require precise control of the pendular motion.

Chapter 6

Summary and Recommendations for Future Work

Tethered satellite systems have a great deal of potential for a wide range of future space-based applications. Although a great deal of research has already been conducted on the dynamics and control of TSS, there remain a number of open areas of study that must be addressed before TSS can be widely put to use. The objective of the work presented in this dissertation is to address several of these open areas of study, and in the process identify new avenues down which TSS dynamics and control research should progress. The original contributions provided by this dissertation are summarized below, and we also present recommendations for future work on TSS dynamics and control.

6.1 Summary of Contributions

One of the main contributions provided by this dissertation is the computational model validation procedure presented in Ch. 2. In an ideal situation, the predictions made by the computational model for a particular physical system are compared to experimental data to assess the predictive capability of the computational model. For a TSS, such experimental data does not exist, so some other means of validating TSS computational models is required. The validation procedure presented in Ch. 2 uses the output of a top-level computational model in place of the non-existent experimental data. The conceptual model of the physical system used to develop the top-level computational model must therefore contain as few simplifying assumptions as possible, while still allowing for efficient determination of numerical solutions for the behavior of the system. The accuracy of the numerical solutions produced by the top-level computational model must also be rigorously verified before they can be used to assess the validity of any predictions made using lower-level computational models. The validation procedure presented in Ch. 2 is by no means ideal, most notably

because there is no guarantee that the top-level computational model itself makes accurate predictions about the behavior of the physical system. Only experimental data can be used to perform validation in the truest sense of the word, but we believe that the computational model validation procedure presented in this work is the best available option for systems, like a TSS, for which experimental data is not available.

Motivated by the validation procedure outlined in Ch. 2, a top-level computational model for the dynamics and control of TSS was developed in Ch. 3. The system was assumed to consist of two finite, rigid end bodies connected by a flexible tether. The tether is allowed to carry a constant electrical current, meaning that the model can be used to analyze electrodynamic tether systems. The mathematical model of the system was derived and used to develop two different computational models, each based on a different method of spatially discretizing the partial differential equations governing the elastic vibrations of the tether. The first method is the assumed modes method, and the second method is the finite element method. Computer codes were written to produce numerical solutions for both computational models, and the method of manufactured solutions was used to verify the accuracy of these numerical solutions. To the knowledge of the author, the work presented in Ch. 3 represents the first time that the MMS has been applied to a computational model for the dynamics and control of a TSS. A qualitative comparison of the two computational models was made and it was determined that the FEM-based computational model is better suited to the study of TSS dynamics and control. For this reason, the FEM-based computational model was used as the top-level computational model for TSS dynamics and control throughout this dissertation.

Because of the complicated nature of the top-level system model, studying the behavior of a TSS using the top-level computational model is impractical in most situations. Accurate numerical solutions can take a significant amount of time to produce using the top-level computational model, so studying the behavior of the system over the entire parameter space can be practically impossible. For this reason, it is entirely justifiable to use simplified system models that allow for much easier analysis of the system. In Ch. 4, a lower-level computational model was used to derive results related to the dynamics of the tether in a spinning TSS. The lower-level model treats the tether as two point mass end bodies connected by a flexible tether, with the primary end body constrained to an unperturbed circular orbit. The pendular motion of the tether is assumed to affect the transverse vibrations of the tether, but the transverse vibrations are assumed to have no influence on the pendular motion. The longitudinal elastic vibrations of the tether are assumed to be negligible.

The nominal pendular motion of a spinning TSS is in the orbit plane, so the equations governing the pendular motion of the tether in the lower-level mathematical model were linearized about a planar motion. The resulting equation for the in-plane pendular motion is decoupled from the equation governing the out-of-plane pendular motion, and a solution for the in-plane motion is determined in terms of Jacobi elliptic functions. When this solution for the in-plane motion is used in the equation governing the out-of-plane motion, the result is a Hill's equation, and Floquet theory was used to analyze the stability properties of the out-of-plane pendular motion. The Floquet analysis showed that the lower-level computational

model predicts that the out-of-plane pendular motion is unstable for some large-amplitude in-plane oscillatory motion, as well as ranges of rotational in-plane motion for systems with both positive and negative in-plane spin rates. The instability regions for systems with a negative in-plane spin rate correspond to systems for which the tether undergoes periods of slack, so they would likely not be used for an actual spinning TSS in spite of the unstable out-of-plane motion. However, the predicted instability regions for systems with a positive in-plane spin rate do not pass through periods of slackness, so they could have possible application for an actual spinning TSS. If such a system were used, a great deal of control effort would be required to counteract the effects of the unstable out-of-plane motion. The instabilities in the out-of-plane pendular motion derived in Ch. 4 have not been reported previously, and are an original contribution of this dissertation.

For spinning TSS with relatively large in-plane spin rates, the Hill's equation used to model the small out-of-plane pendular motion can be approximated with sufficient accuracy by a Mathieu's equation. Floquet's theorem was used to determine approximate solutions to the Mathieu's equation that are a linear combination of four simple harmonic oscillators. The two lowest-frequency oscillators contribute the greatest to the overall amplitude of the out-of-plane oscillations, and the frequency of all four of the oscillators increases as the in-plane spin rate increases. Like the predicted instabilities in the out-of-plane pendular motion, the approximate solutions for large in-plane spin rates have not been reported previously, and are an original contribution of this dissertation.

In addition to the pendular motion of the tether, the lower-level computational model was used to study the transverse elastic vibrations of a spinning TSS. The transverse vibrations are assumed to be small relative to the length of the tether, and the out-of-plane pendular motion is once again assumed to be small. The resulting equations governing the transverse elastic vibrations are a set of decoupled, linear, partial differential equations, and the method of separation of variables is used to analyze these equations. The mode shapes for the transverse vibrations are determined in terms of a hypergeometric function, and an expression for the eigenvalue corresponding to each mode shape is determined. The eigenvalues and the solution for the in-plane pendular motion are used in the equations governing the time-dependent portions of the assumed solution forms for the transverse vibrations, resulting in Hill's equations. Floquet theory was used to analyze these equations and show that the lower-level computational model predicts that the transverse vibrations are unstable for certain combinations of in-plane spin rate and system mass distribution. The largest instability regions correspond to systems with a relatively low in-plane spin rate and a secondary end mass that is small relative to the mass of the tether. The instability regions become progressively smaller as the in-plane spin rate and mass of the secondary end body are increased. Unlike the results related to the stability of the out-of-plane pendular motion, these results related to the instabilities in the transverse elastic vibrations of the tether are not new, and were previously reported in Refs. [5] and [8].

Because they were determined using a lower-level computational model, the results related to the motion of the tether in a spinning TSS presented in Ch. 4 were compared to predictions

made by the top-level computational model to assess their validity. Numerous validation tests were used to show that the instabilities in the out-of-plane pendular motion predicted by the lower-level computational model are also predicted by the top-level computational model, meaning that these predictions are validated. The approximate solutions for the out-of-plane motion compare favorably to the predictions made by the top-level computational model in a qualitative sense, but significant quantitative differences develop between the predictions over longer time spans. These differences are due to slight errors in the approximate frequencies that, over time, lead to significant phase differences. Despite these quantitative differences, however, the approximate solutions accurately reproduce the qualitative features of the out-of-plane pendular motion predicted by the top-level computational model.

A number of validation tests were used to show that the instabilities in the transverse elastic vibrations of the tether predicted by the lower-level computational model are not predicted by the top-level computational model. These results are therefore invalidated, and the lower-level system model must be altered to achieve better agreement with the top-level computational model. The main source of error in the lower-level predictions appears to stem from the assumption of a one-way coupling between the two modes of the tether motion. Any further study of the transverse vibrations of a spinning TSS should not use such an assumption, and should consider the transverse vibrations and pendular motion to be completely coupled.

The validation tests presented in Ch. 4 are one of the most significant contributions provided by this dissertation. They show that predictions made by lower-level computational models can both agree and disagree with those made by the top-level computational model. If the predictions made by the two models agree, then the lower-level predictions are given a weight and significance that they would not have if no kind of validation had been performed. If the predictions made by the two models do not agree, then the lower-level system model must be altered in some manner to achieve better agreement. The validation tests performed on the results pertaining to the transverse elastic vibrations of the tether clearly demonstrate that the mathematical correctness of a prediction does not mean that it can, or should, be applied to the physical system. Some form of validation must be performed to tie the predictions back to the actual physical system in order for the predictions to have any real significance.

The final significant contribution made in this dissertation is the control laws for the pendular motion of the tether developed in Ch. 5. All of these control laws were developed using a lower-level system model, and all drive the pendular motion to a desired planar reference motion. The control inputs used to control the pendular motion are assumed to be arbitrary control torques that are most likely due to thrusters on the end bodies. Two of the control laws developed in Ch. 5 are based on principles of sliding mode control, meaning that they can control the system about the reference motion in the presence of unknown disturbances. When applied to the top-level computational model, these unknown disturbances are due to the dynamics not accounted for by the lower-level model.

Several of the control laws were applied to the top-level computational model to assess their

applicability to an actual TSS. For the control laws that do not account for the unmodeled system dynamics, the pendular motion does not asymptotically approach the desired motion, but instead undergoes small amplitude oscillations about the desired reference motion due to the effects of the unmodeled dynamics. The sliding mode control laws were demonstrated to be capable of eliminating these steady-state oscillations about the reference motion at the cost of requiring relatively large magnitude steady-state control inputs. Because of this fact, the sliding mode controllers should only be used in situations for which precise control of the pendular motion is required. In most other situations, the control laws that do not account for unmodeled dynamics should prove sufficient in controlling the pendular motion of the tether.

6.2 Recommendations for Future Work

The work presented in this dissertation addresses only a handful of the open areas of research in TSS dynamics and control. Many issues have yet to be adequately addressed, and the work in this dissertation raises several new questions on its own. In this section, we make recommendations for ways in which the work presented in this dissertation can be extended in future TSS dynamics and control research.

The first way in which the work in this dissertation can be extended is to refine the top-level system model. Despite the fact that the system model presented in Ch. 3 is taken as the top-level system model, it contains several assumptions about the physical system that could be relaxed to make the model a better abstraction of reality. Most of these assumptions are related to the physical environment in which the TSS operates; recall that the only external forces acting on the system in the top-level system model are the gravitational force of the central body and the electrodynamic force. Other external forces, such as atmospheric drag and solar radiation pressure, could be added to the model, along with other effects like thermal expansion of the tether due to crossings between shadow and sunlight. The gravitational and electrodynamic force models can themselves be extended by using higher-order spherical harmonic expansions of the gravitational and magnetic fields of the central body. Modeling all of these external forces would make the top-level system model a better representation of an actual TSS, and would therefore provide an even better substitute for experimental data until it can be collected.

The fact that experimental data from an actual TSS is not readily available does not mean that data cannot be collected to validate some aspects of the system model. For example, the string model for the tether can be applied to any type of vibrating string, not just a TSS. In light of this fact, experimental data collected on an experimental setup as simple as a pendulum could be used to determine if a string model is adequate for modeling the vibrations of a TSS. Such experiments are conducted in Ref. [29]; however, comparison with the computational model is conducted by means of stop-motion photographs instead of physical measurements. More rigorous validation test than the ones conducted in Ref. [29]

would greatly enhance the level of confidence in modeling of TSS dynamics.

The dynamic analysis of spinning TSS presented in Ch. 4 can be extended in a number of ways. Many extensions of the system model used in Ch. 4 will result in equations that are small perturbations of those used in Ch.4. For example, orbital eccentricity and electrodynamic forcing introduce small perturbation terms into the equations governing the pendular motion of the tether. The effects of these additional influences can be studied using various perturbation methods (such as the method of averaging) with the solutions derived in Ch. 4 as the generating solutions for the perturbation analysis. The variation of the system orbit due to various external influences can also be studied by viewing the orbital motion as a small perturbation of a fixed orbit. Another way in which the dynamic analysis in Ch. 4 can be extended is to develop a new computational model for the elastic vibrations of the tether that takes into account the full coupling between the pendular motion and elastic vibrations of the tether. It may be possible to derive analytical results on the stability of the transverse vibrations using this new lower-level system model, but it is likely that any accurate study of the elastic vibrations of the tether will have to rely on numerical solutions.

One significant way in which the control analysis presented in Ch. 5 can be extended is to perform a more thorough controllability analysis of the system for the case in which the electrodynamic force is the only control input. It may be possible to perform certain types of control maneuvers using only the electrodynamic force, and knowing these maneuvers could prove useful because they would require no propellant. Along the same lines, it would be useful to determine optimal control laws that minimize the total control input required to control the pendular motion, thereby minimizing the required propellant. Both open- and closed-loop optimal control laws could be developed. Some hybrid control strategy could be developed that uses a combination of electrodynamic forcing and thrusters on the end bodies. The electrodynamic force could be used as the only control input for times when the pendular motion can be controlled adequately using only the electrodynamic force, and thrusters on the end bodies could be employed only in situations for which they are needed to make the system controllable. One final way in which the control analysis presented in Ch. 5 can be extended is to include the orbital motion in the system model and determine methods of controlling the orbital motion and the motion of the tether simultaneously, perhaps using only the electrodynamic force.

Lastly, we must note that the ultimate extension of the work presented in this dissertation would be to apply it to an actual TSS. All aspects of the work covered in Chs. 3–5, including the validity of the top-level computational model, could be rigorously verified by applying the various results and predictions to an operational TSS, or to experimental data obtained from an actual TSS.

Bibliography

[1] O. Axelsson and V.A. Barker. *Finite Element Solution of Boundary Value Problems*. Academic Press, Inc., Orlando, FL, 1984.

[2] P.M. Bainum and K.S. Evans. Three-dimensional motion and stability of two rotating cable-connected bodies. *Journal of Spacecraft and Rockets*, 12(4):242–250, 1975.

[3] P.M. Bainum and K.S. Evans. Gravity-gradient effects on the motion of two rotating cable-connected bodies. *AIAA Journal*, 14(1):26–32, 1976.

[4] R.H. Battin. *An Introduction to the Mathematics and Methods of Astrodynamics, Revised Edition*. AIAA, Reston, VA, 1999.

[5] V.V. Beletsky and E.M. Levin. *Dynamics of Space Tether Systems*. Univelt, San Diego, California, 1993.

[6] J.A. Bonometti, K.F. Sorensen, J.W. Dankanich, and K.L. Frame. 2006 status of the momentum exchance electrodynamic re-boost (mxer) tether development. In *42nd AIAA/ASME/SAE/ASEE Joint Propulsion Conference and Exhibit*, Sacramento, CA, 2006.

[7] W.E. Boyce and R.C. DiPrima. *Elementary Differential Equations and Boundary Value Problems, Seventh Edition*. John Wiley and Sons, New York, 2001.

[8] J.V. Breakwell and F.L. Janssens. On the transverse vibrations of a revolving tether. *Celestial Mechanics and Dynamical Astronomy*, 54:312–341, 1992.

[9] J.V. Breakwell and R. Pringle Jr. Nonlinear resonances affecting gravity-gradient stability. In *Proceedings of the XVI International Astronautics Congress*, pages 305–325, Athens, 1965.

[10] P.F. Byrd and M.D. Friedman. *Handbook of Elliptic Integrals for Engineers and Scientists: Second Edition, Revised*. Spinger-Verlag, New York, 1971.

[11] A. Celletti and V. Sidorenko. Some properties of the dumbbell satellite attitude dynamics. *Celestial Mechanics and Dynamical Astronomy*, 101:105–126, 2008.

[12] V. Chobotov. Gravitational excitation of an extensible dumbbell satellite. *Journal of Spacecraft and Rockets*, 4(10):1295–1300, 1967.

[13] G. Colombo, E. M. Gaposchkin, M. D. Grossi, and G. C. Weiffenbach. The skyhook: A shuttle-borne tool for low-orbital-altitude research. *Meccanica*, 10(1):3–20, 1975.

[14] J. Corsi and L. Iess. Stability and control of electrodynamic tethers for de-orbiting applications. *Acta Astronautica*, 48(5):491–501, 2001.

[15] M.L. Cosmo and E.C. Lorenzini (eds.). *Tethers in Space Handbook, Third Edition*. NASA, Washington, D.C., 1997.

[16] S.A. Crist and J.G. Eisley. Motion and stability of a spinning spring-mass system in orbit. *Journal of Spacecraft and Rockets*, 6(7):819–824, 1969.

[17] A.B. DeCou. Gravity gradient disturbances on rotating tethered systems in circular orbit. In *Proceedings of the 3rd International Conference on Tethers in Space: Toward Flight*, pages 343–351, Reston, VA, 1989. AIAA.

[18] J.R. Ellis and C.D. Hall. Model development and code verification for simulation of electrodynamic tether system. *Journal of Guidance, Control, and Dynamics*, 32(6):1713–1722, 2009.

[19] J.R. Ellis and C.D. Hall. Out-of-plane librations of spinning tethered satellite systems. *Celestial Mechanics and Dynamical Astronomy*, 106(1):39–67, 2010.

[20] S. Sasaki et al. Results from a series of tethered rocket experiments. *Journal of Spacecraft and Rockets*, 24(5):444–453, 1987.

[21] S.S. Gates, S.M. Koss, and M.F. Zedd. Advanced tether experiment deployment failure. *Journal of Spacecraft and Rockets*, 38(1):60–68, 2001.

[22] R.P. Hoyt. Stabilization of electrodynamic tethers. In *38th AIAA/ASME/SAE/ASEE Joint Propulsion Conference and Exhibit*, Indianapolis, Indiana, 2002. AIAA.

[23] P.C. Hughes. *Spacecraft Attitude Dynamics*. Dover Publications, Mineola, New York, 2004.

[24] L. Johnson et al. Nasa's in-space propulsion technology program: Update and overview. In *40th AIAA/ASME/SAE/ASEE Joint Propulsion Conference and Exhibit*, Fort Lauderdale, Florida, 2004.

[25] J.Pelaez and E.C. Lorenzini. Libration control of electrodynamic tethers in inclined orbit. *Journal of Guidance Control and Dynamics*, 28(2):269–279, 2005.

[26] T.R. Kane. Attitide stability of earth-pointing satellites. *AIAA Journal*, 3(4):726–731, 1965.

[27] T.R. Kane and D.J. Shippy. Attitide stability of a spinning unsymmetrical satellite in a circular orbit. *The Journal of the Astronautical Sciences*, 10(4):114–119, 1963.

[28] H.K. Khalil. *Nonlinear Systems*. Prentice Hall, Upper Saddle River, NJ, third edition, 2002.

[29] A. Kuhn, W. Steiner, J. Zemann, D. Dinevski, and H. Troger. A comparison of various mathematical formulations and numerical solution methods for the large amplitude oscillations of a string pendulum. *Applied Mathematics and Computation*, 67(1):227–264, 1995.

[30] K.D. Kumar. Review of dynamics and control of nonelectrodynamic tethered satellite systems. *Journal of Spacecraft and Rockets*, 43(4):705–720, 2006.

[31] E.L.M Lanoix, A.K. Misra, V.J. Modi, and G. Tyc. Effect of electrodynamic forces on the orbital dynamics of tethered satellites. *Journal of Guidance, Control, and Dynamics*, 28(6):1309–1315, 2005.

[32] D.F. Lawden. *Elliptic Functions and Applications*. Springer-Verlag, New York, 1989.

[33] E.M. Levin. Stability of the stationary motions of an electrodynamic tether system in orbit. *Cosmic Research*, 25:368–376, 1987.

[34] E.M. Levin. *Dynamic Analysis of Space Tether Missions*. Univelt, San Diego, California, 2007.

[35] K.K. Mankala and S.K. Agrawal. Equilibrium to equilibrium maneuvers of rigid electrodynamic tethers. *Advances in the Astronautical Sciences*, 119:1011–1023, 2004.

[36] K.K. Mankala and S.K. Agrawal. Equilibrium to equilibrium maneuvers of flexible electrodynamic tethers in equatorial orbits. *Journal of Spacecraft and Rockets*, 43(3):651–658, 2006.

[37] N.W. McLachlan. *Theory and Application of Mathieu Functions*. Oxford University Press, Oxford, 1947.

[38] L. Meirovitch. *Elements of Vibration Analysis*. McGraw-Hill, New York, 1975.

[39] L. Meirovitch. *Methods of Analytical Dynamics*. Dover Publications, Mineola, New York, 1998.

[40] L. Meirovitch and F. Wallace. Attitude instability regions of a spinning unsymmetrical satellite in a circular orbit. *The Journal of the Astronautical Sciences*, 14(3):123–133, 1967.

[41] A.K. Misra and V.J. Modi. A survey on the dynamics and control of tethered satellite systems. *Advances in the Astronautical Sciences*, 62:667–719, 1986.

[42] H. Nijmeijer and A. van der Schaft. *Nonlinear Dynamical Control Systems*. Springer-Verlag, New York, 19900.

[43] W.L. Oberkampf and C.J. Roy. *Verification and Validation in Scientific Computing*. Cambridge University Press, New York, 2010.

[44] J. Pearson, E. Levin, J.A. Carrol, and J.C. Oldson. Orbital maneuvering with spinning electrodynamic tethers. In *2nd International Energy Conversion Engineering Conference*, Providence, RI, 2004. AIAA.

[45] J. Pelaez and Y.N. Andres. Dynamic stability of electrodynamic tethers in inclinded elliptical orbits. *Journal of Guidance, Control, and Dynamics*, 28(4):611–622, 2005.

[46] J. Pelaez and M. Lara. Periodic solutions in electrodynamic tethers on inclined orbits. *Journal of Guidance, Control, and Dynamics*, 26(3):395–406, 2003.

[47] J. Pelaez, M. Ruiz, O. Lopez-Rebollal, E.C. Lorenzini, and M.L. Cosmo. A new kind of dynamic instability in electrodynamic tethers. *Journal of the Astronautical Sciences*, 48(4):449–476, 2000.

[48] J. Pelaez, M. Ruiz, O. Lopez-Rebollal, E.C. Lorenzini, and M.L. Cosmo. Two-bar model for the dynamics and stability of electrodynamic tethers. *Journal of Guidance, Control, and Dynamics*, 25(6):369–372, 2002.

[49] S. Pradhan. *Planar Dynamics and Control of Tethered Satellite Systems*. PhD thesis, The University of British Columbia, 1994.

[50] S. Pradhan, V.J. Modi, and A.K. Misra. On the offset control of flexible nonautonomous tethered two-body systems. *Acta Astronautica*, 38(10):783–801, 1996.

[51] P.J. Roache. *Verification and Validation in Computational Science and Engineering*. Hermosa Publishers, New Mexico, 1998.

[52] C.J. Roy. Review of code and solution verification procedures for computational simulation. *Journal of Computational Physics*, 205(1):131–156, 2005.

[53] M. Ruiz, O. Lopez-Rebollal, E.C. Lorenzini, and J. Pelaez. Modal analysis of the stability of periodic solutions in electrodynamic tethers. *Advances in the Astronautical Sciences*, 109:1553–1570, 2001.

[54] N. Sabey and S. Tragesser. Effects of libration on general electrodynamic tether orbital maneuvers. In *AIAA/AAS Astrodynamics Specialist Conference and Exhibit*, Honolulu, Hawaii, 2008.

[55] H. Schaub and J.L. Junkins. *Analytical Mechanics of Space Systems, Second Edition*. AIAA, Reston, VA, 2009.

[56] V.V. Sidorenko and A.I. Neishtadt. Investigation of the stability of long-periodic planar motion of a satellite in a circular orbit. *Cosmic Research*, 38(3):289–303, 2000.

[57] S. Singhvi and R.K. Kapania. Comparison of simple and chebychev polynomials in rayleigh-ritz analysis. *Journal of Engineering Mechanics*, 120(10):2126–2135, 1994.

[58] J.-J. Slotine and W. Li. *Applied Nonlinear Control*. Prentice-Hall, EngleWood Cliffs, NJ, 1991.

[59] L. Somenzi, L. Iess, and J. Pelaez. Linear stability analysis of electrodynamic tethers. *Journal of Guidance, Control, and Dynamics*, 28(5):843–849, 2005.

[60] P. Stabekis and P.M. Bainum. Motion and stability of a rotating space station-cable-counterweight configuration. *Journal of Spacecraft and Rockets*, 7(8):912–918, 1970.

[61] W. Steiner, A. Steindl, and H. Troger. Dynamics of a space tethered satellite system with two rigid end bodies. In *Fourth International Conference on Tethers in Space*, pages 1367–1379, Washington, D.C, 1995. Smithsonian Institute.

[62] R. Stevens and W. Wiesel. Large time scale optimal control of electrodynamic tether satellite. *Journal of Guidance, Control, and Dynamics*, 31(6):1716–1727, 2008.

[63] C.L. Tai and M.H. Loh. Planar motion of a rotating cable-connected space station in orbit. *Journal of Spacecraft and Rockets*, 2(6):889–894, 1965.

[64] S.G. Tragesser and H. San. Orbital maneuvers with electrodynamic tethers. *Journal of Guidance, Control, and Dynamics*, 26(5):805–810, 2003.

[65] T. Watanabe, T. Makida, H. Fujii, H. Kojima, and W. Singhose. An application of input shaping for electrodynamic tether system. In *AIAA/AAS Astrodynamics Specialist Conference and Exhibit*, Providence, Rhode Island, 2004. AIAA.

[66] P. Williams. Optimal orbital transfer with electrodynamic tether. *Journal of Guidance, Control, and Dynamics*, 28(2):369–372, 2005.

[67] P. Williams. Energy rate feedback for libration control of electrodynamic tethers. *Journal of Guidance, Control, and Dynamics*, 29(1):221–223, 2006.

[68] P. Williams. Simple approach to orbital control using spinning electrodynamic tethers. *Journal of Spacecraft and Rockets*, 43(1):253–256, 2006.

[69] P. Williams. Librations control of electodynamic tethers using predictive control with time-delayed feedback. *Journal of Guidance, Control, and Dynamics*, 32(4):1254–1268, 2009.

[70] P. Williams, T. Watanabe, C. Blanksby, P. Trivailo, and H.A. Fujii. Libration control of flexible tethers using electromagnetic forces and moveable attachment. *Journal of Guidance, Control, and Dynamics*, 27(5):882–897, 2004.

[71] X. Zhou, J. Li, H. Baoyin, and V. Zakirovx. Equilibrium control of electrodynamic tethered satellite systems in inclined orbits. *Journal of Guidance, Control, and Dynamics*, 29(6):1451–1454, 2006.